

# Laser Forming of Aerospace Alloys

by

J. W. A. Magee, B.Eng (Hons)

1999

A thesis presented for the degree of Doctor of  
Philosophy of the University of Liverpool

Mechanical Engineering, Department of Engineering,  
University of Liverpool, Liverpool L69 3GH

**VI ET ARTE**

**JM**

**MCMXCIX**

## Declaration

I declare that no part of this work has been submitted in support of any other qualification.

Jonathan Magee.

## Abstract

Laser forming is a complex thermal forming process which is relatively new to the field of laser materials processing. In order to implement laser forming for practical application the processing mechanisms must be understood, the geometrical constraints must be explored and the metallurgical implications must be investigated. This thesis investigates these factors. Two aerospace alloys and mild steel are examined. The investigation begins with an introduction to the process and the laser. The second chapter reviews previous work on laser forming process mechanics, experimental work, and currently developed applications. A synopsis for the present work is then given. In chapter three the relevant moments and forces acting in laser forming of sheet metal are examined theoretically using the method of inherent strain, and a finite volume heat conduction simulation for laser processing is used to evaluate the thermal field. This work describes the variables which affect the stability of the process and suitable thermal regimes for processing with certain mechanisms.

In chapter four the experimental methods and equipment used in the investigation are described. Chapter five describes the important results and discusses them in the context of previous work. The results are divided into three sections - energy, geometry, and material. The energy section critically analyses the bending of the sheet alloy as a function of the energy input and compares the results with models by previous authors. Then the model presented in chapter three is implemented and compared with the experimental results. In the geometrical section the longitudinal bending and stability of 2-D laser forming is investigated both experimentally and using the theory from chapter three. A dish shape is investigated experimentally to establish rules for axi-symmetrical shaping of 3-D structures. Important rules for the sequencing and positioning of the laser scan lines in relation to the geometry result from this work. The metallurgical and mechanical property implications of laser forming the aluminium alloy AA 2024 T3 and the titanium alloy Ti6Al4V are described. It is shown that it is possible to laser form the specified materials in the absence of detrimental metallurgical effects, but this may not always compliment the geometrical accuracy of the part. Finally the culmination of all these studies resulted in the demonstration of the process on a specified sheet metal geometry. Using processing parameters which resulted in an acceptable metallurgy the geometry of the part was

stabilised and measured.

The final chapter describes the important conclusions of the work on the energy, geometrical and materials aspects and provides a summary of the future work which would advance the process.

# Contents

<b>1</b>	<b>Introduction</b>	<b>1</b>
1.1	The process . . . . .	1
1.2	The laser . . . . .	2
1.2.1	Optical Resonator . . . . .	3
1.2.2	Active medium . . . . .	3
1.2.3	System to excite the active medium . . . . .	3
1.3	Principle of operation . . . . .	3
1.4	Characteristics of the energy source . . . . .	4
1.4.1	Monochromaticity . . . . .	4
1.4.2	Coherence . . . . .	4
1.4.3	Polarisation . . . . .	5
1.4.4	Diffraction . . . . .	5
1.4.5	Radiance . . . . .	5
1.5	Characteristics of the laser device . . . . .	5
1.5.1	Wavelength . . . . .	5
1.5.2	Spatial mode . . . . .	6
1.5.3	Divergence . . . . .	7
1.6	Laser Material Interaction . . . . .	7
1.6.1	Absorption . . . . .	7
<b>2</b>	<b>Literature Review</b>	<b>9</b>
2.1	Summary . . . . .	9
2.2	History . . . . .	9
2.3	Potential for application . . . . .	10
2.4	Mechanics of laser forming . . . . .	10
2.4.1	Temperature gradient mechanism . . . . .	10
2.4.2	Pointsource mechanism . . . . .	11
2.4.3	Buckling and upsetting mechanisms . . . . .	12
2.5	Mathematical models - Analytical . . . . .	15
2.5.1	Two layer models . . . . .	15

2.5.2	The residual stress model . . . . .	23
2.5.3	The buckling mechanism . . . . .	28
2.5.4	The upsetting mechanism . . . . .	30
2.6	Mathematical Models - Numerical . . . . .	31
2.6.1	Temperature Gradient Mechanism (TGM) . . . . .	31
2.6.2	Buckling Mechanism (BM) . . . . .	32
2.6.3	Upsetting Mechanism (UM) . . . . .	33
2.7	Previous experimental work . . . . .	35
2.7.1	Operating maps - Bend angle dependence on power and processing Speed . . . . .	35
2.7.2	Bend angle dependence on thermal and thermal-mechanical properties . . . . .	39
2.7.3	Development of temperature field and plastic strain . . . . .	42
2.7.4	Material and Metallurgy work . . . . .	42
2.7.5	Bend angle dependency on geometry of workpiece . . . . .	45
2.8	Applications of laser bending . . . . .	46
2.8.1	Primary forming operations . . . . .	46
2.8.2	Secondary forming operations . . . . .	48
2.8.3	Suggested Applications . . . . .	50
2.9	State of the art . . . . .	51
2.10	Synopsis for present research . . . . .	51
<b>3</b>	<b>Theoretical Analysis</b> . . . . .	<b>52</b>
3.1	Engineering theory of bending approximations . . . . .	52
3.1.1	Assumptions . . . . .	53
3.1.2	Co-ordinate system . . . . .	54
3.1.3	Transverse bending moment, $M_{tr}$ . . . . .	54
3.1.4	Longitudinal bending moment, $M_{lg}$ . . . . .	54
3.1.5	Transverse shrinkage force, $N_{tr}$ . . . . .	55
3.1.6	Longitudinal shrinkage force, $N_{lg}$ . . . . .	55
3.1.7	Inherent strain . . . . .	55
3.2	Thermal field . . . . .	57
3.2.1	Numerical solution to differential equations . . . . .	58
3.2.2	Extension to three dimensional case with a source . . . . .	61
3.2.3	The Tri Diagonal Matrix Algorithm ( <i>TDMA</i> ) solution to the algebraic equations . . . . .	64
3.2.4	Solution domain and Boundary conditions . . . . .	69
3.2.5	Thermal modelling outputs . . . . .	71

3.2.6	Temperature rise as the sheet moves under the hot spot, time( $x$ ), for $y = 0$ to the edge of the sheet $y$ , and $z = 0$ to the sheet thickness $z$ , or a combination ( $yz$ ), Temperature gradient mechanism . . . . .	75
3.2.7	Temperature rise as the sheet moves under the hot spot, time( $x$ ), for $y = 0$ to the edge of the sheet $y$ , and $z = 0$ to the sheet thickness $z$ , or a combination ( $yz$ ), Buckling mechanism . . . . .	79
3.2.8	Defining the shape function for the plastic strain zone, $b_z$ . . . . .	79
3.3	The Transverse and Longitudinal forces and moments evaluation for the thermal case presented in section 3.2.6 . . . . .	83
3.3.1	The combined thermo-mechanical analysis results . . . . .	87
3.3.2	Summary of theoretical analysis . . . . .	92
<b>4</b>	<b>Experimental Procedure</b> . . . . .	<b>93</b>
4.1	Summary . . . . .	93
4.2	Experimental strategy . . . . .	93
4.3	Bend angle measurement . . . . .	93
4.3.1	Measurement Method . . . . .	94
4.4	Materials and dimensions . . . . .	95
4.4.1	AA 2024 T3 alloy . . . . .	95
4.4.2	Ti6Al4V alloy . . . . .	95
4.4.3	Surface preparation of material . . . . .	98
4.5	Energy influences . . . . .	98
4.5.1	Heat source . . . . .	98
4.5.2	Laser beam characterisation . . . . .	98
4.5.3	Energy input . . . . .	99
4.5.4	Clamping . . . . .	100
4.5.5	Sheet Heating . . . . .	100
4.6	Geometry influences . . . . .	102
4.6.1	Sheet thickness . . . . .	102
4.6.2	Variation in bend angle along the length of the bending edge . . . . .	102
4.7	Laser forming a 3-D shape . . . . .	103
4.7.1	Sample preparation . . . . .	103
4.7.2	Clamping . . . . .	103
4.7.3	Laser scan patterns . . . . .	103
4.7.4	Energy input parameters . . . . .	104
4.7.5	Surface profiling of laser scanned geometries . . . . .	104

4.8	Metallurgical and mechanical property influences . . . . .	105
4.8.1	$\alpha - \beta$ Ti6Al4V sample preparation . . . . .	105
4.8.2	AA 2024 T3 sample preparation . . . . .	105
4.9	Integrated 2-D shape process demonstration . . . . .	107
4.9.1	Process Demonstration . . . . .	107
<b>5</b>	<b>Experimental Results and Discussion</b>	<b>110</b>
5.1	Energy input . . . . .	110
5.1.1	Laser beam diameter of the order of 12 times the sheet thickness . . . . .	110
5.1.2	Laser beam diameter of the order of 1-5 times the sheet thickness . . . . .	113
5.1.3	Comparison of Experimental results with other models and Magee 98 . . . . .	116
5.2	Geometry . . . . .	122
5.2.1	Decreasing bending rate . . . . .	122
5.2.2	Longitudinal bending and edge effects . . . . .	125
5.2.3	Laser forming a dish shape - A case study in 3-D geometry forming . . . . .	133
5.2.4	Discussion of dish forming work . . . . .	155
5.3	Metallurgy and Mechanical Properties . . . . .	156
5.3.1	The metallurgical changes which may occur to AA2024 - T3 due to laser forming . . . . .	156
5.3.2	AA 2024 T3 - Optical micrographs . . . . .	157
5.3.3	AA 2024 T3 - SEM images . . . . .	161
5.3.4	AA 2024 T3 - Microhardness graphs . . . . .	163
5.3.5	Discussion of the metallurgy and mechanical properties of laser bent AA 2024 . . . . .	166
5.3.6	Metallurgical changes which occur in $\alpha - \beta$ Ti6Al4V due to laser forming . . . . .	168
5.3.7	$\alpha - \beta$ Ti6Al4V - Optical micrographs . . . . .	168
5.3.8	Microhardness graphs . . . . .	172
5.3.9	Discussion of the metallurgy and mechanical properties of laser bent $\alpha - \beta$ Ti6Al4V . . . . .	173
5.4	Integrated 2D process demonstration . . . . .	175
5.4.1	The demonstrator part . . . . .	175
5.4.2	Initial forming strategy . . . . .	175
5.4.3	Influence of the part size . . . . .	176

5.4.4	2-D Laser forming system requirements . . . . .	185
5.4.5	Conclusion of 2-D process demonstration work . . . . .	185
<b>6</b>	<b>Conclusions and Future Work</b>	<b>187</b>
6.1	Conclusions . . . . .	187
6.1.1	Process Mechanics . . . . .	187
6.1.2	Energy Influences on laser forming of sheet material . . . . .	187
6.1.3	Geometrical influences on laser forming of sheet material . . . . .	188
6.1.4	Metallurgical and mechanical property implications . . . . .	190
6.2	Future work . . . . .	191
6.2.1	Spatial forming in 3D . . . . .	191
6.2.2	Closed loop control . . . . .	192
6.2.3	Other alloys . . . . .	192
	<b>Appendices</b>	<b>193</b>
<b>A</b>	<b>The Counterbending two layer model</b>	<b>194</b>
<b>B</b>	<b>Energy input parameters</b>	<b>198</b>
B.1	Energy input - bend angle tables . . . . .	198
B.2	Energy input - bend angle plots . . . . .	207
<b>C</b>	<b>G-Code program example</b>	<b>227</b>
<b>D</b>	<b>Metallurgy AA 2024 T3</b>	<b>229</b>
D.1	Processing parameters - AA 2024 T3 . . . . .	229
<b>E</b>	<b>Mechanical properties Ti6Al4V</b>	<b>234</b>
E.1	Processing Parameters . . . . .	234
E.2	Micro-hardness graphs . . . . .	236
	<b>References</b>	<b>240</b>

# List of Figures

1.1	Out of plane bending . . . . .	1
1.2	In-plane forming . . . . .	2
1.3	Components of a gas laser . . . . .	3
1.4	Laser beam coherence . . . . .	4
1.5	Laser beam modes . . . . .	6
1.6	Absorption dependencies for laser materials processing . . . . .	8
2.1	The temperature gradient mechanism . . . . .	11
2.2	The pointsource mechanism . . . . .	13
2.3	The buckling mechanism . . . . .	14
2.4	The upsetting mechanism . . . . .	14
2.5	Forces and moments acting in two layer model . . . . .	15
2.6	Sign convention in moment area theory, reading downwards: deflection, slope, curvature, bending moment, shear and load . . . . .	17
2.7	The first moment-area theorem . . . . .	18
2.8	Comparison of experimental results with the two layer model . . . . .	21
2.9	Comparison of solutions for two-layer models . . . . .	22
2.10	Counterbending angle from Yau's model . . . . .	23
2.11	Vollertsen's residual stress model for the TGM . . . . .	25
2.12	Critical operating region for temperature gradient mechanism . . . . .	28
2.13	Model geometry for the buckling mechanism . . . . .	29
2.14	Development of the bending angle during the buckling mechanism . . . . .	33
2.15	Distribution of upper and lower surface temperatures and displacements during the buckling mechanism . . . . .	34
2.16	Distribution of upper and lower surface strains during the buckling mechanism . . . . .	34
2.17	Plastic restraining in extrusion bending . . . . .	35
2.18	Bend angle dependence on laser power . . . . .	37
2.19	Bend angle dependence on processing speed, TGM . . . . .	38
2.20	Increase of process efficiency with increasing processing velocity, TGM . . . . .	38

2.21	Influence of the thermal conductivity on the bending angle . . . . .	40
2.22	Physical model of the influence of the thermal conductivity on the bend angle . . . . .	41
2.23	Increase of the material thermal properties on the bend angle . . .	42
2.24	Time run of the strain development . . . . .	43
2.25	Time run of the bend angle . . . . .	43
2.26	decreasing bend rate with increasing scans over an identical track .	45
2.27	Pipe and Tube forming . . . . .	47
2.28	Examples of laser formed rapid prototypes . . . . .	48
2.29	Distortion correction for car body shells . . . . .	49
2.30	Laser micro forming . . . . .	50
3.1	Co-ordinate system and relevant forces and moments . . . . .	54
3.2	1-D grid point cluster . . . . .	60
3.3	Solution domain . . . . .	69
3.4	Heat affected zone cross section for calculating local strain . . . . .	72
3.5	Heat affected zone cross section for the buckling mechanism . . . . .	73
3.6	Through thickness isotherms for the temperature gradient mechanism	74
3.7	Through thickness isotherms for the buckling mechanism . . . . .	74
3.8	Maximum temperature of hot spot at a given time, $y = 0$ mm, $z = 0$ to 1 mm . . . . .	75
3.9	Heating - cooling curve as the plate moves under the hot spot, $y = 0$ mm, $z = 0$ to 1 mm . . . . .	76
3.10	Heating - cooling curve as the plate moves under the hot spot, $y = 0$ mm, $z = 0.0$ mm . . . . .	76
3.11	Heating - cooling curve as the plate moves under the hot spot, $y = 0$ mm, $z = 0.6$ mm . . . . .	77
3.12	Heating - cooling curve as the plate moves under the hot spot, $y = 0$ mm, $z = 1.0$ mm . . . . .	77
3.13	Maximum temperature of hot spot, $z = 0$ mm, $y = 0$ to $n$ mm . . .	78
3.14	Maximum temperature of hot spot at a given time, $y = 0$ mm, $z = 0$ to 0.9 mm, Buckling mechanism . . . . .	79
3.15	Heating - cooling curve as the plate moves under the hot spot, $y = 0$ mm, $z = 0.1$ mm . . . . .	80
3.16	Heating - cooling curve as the plate moves under the hot spot, $y = 0$ mm, $z = 0.0$ mm . . . . .	80
3.17	Heating - cooling curve as the plate moves under the hot spot, $y = 0$ mm, $z = 0.5$ mm . . . . .	81

3.18	Heating - cooling curve as the plate moves under the hot spot, $y = 0$ mm, $z = 0.9$ mm . . . . .	81
3.19	Maximum temperature of hot spot, $z = 0$ mm, $y = 0$ to $n$ mm . . .	82
3.20	Yield strength as a function of temperature - AA2024 T3 (taken from private communication with Aluminium supplier - Appollo) . .	86
3.21	Elastic modulus as a function of temperature - AA2024 T3(taken from private communication with Aluminium supplier - Appollo) . .	86
3.22	Transverse bending moment with increasing sheet thickness . . . . .	88
3.23	Transverse curvature with increasing sheet thickness . . . . .	88
3.24	Transverse bend angle with increasing sheet thickness . . . . .	89
3.25	Pseudo transverse bend angle (allowing plastic zone to extend beyond sheet thickness)with sheet thickness . . . . .	90
3.26	Longitudinal bend angle with increasing sheet thickness . . . . .	90
3.27	Longitudinal curvature with increasing longitudinal moment . . . . .	91
3.28	Longitudinal bend angle with increasing sheet thickness for three sheet lengths in the direction of scanning . . . . .	91
4.1	Initial bend angle measurement device . . . . .	94
4.2	Phase diagram for aluminium copper based alloy . . . . .	96
4.3	Phase diagram for Ti6Al4V alloy . . . . .	97
4.4	Energy distribution across of raw beam . . . . .	99
4.5	Clamping arrangement in initial study . . . . .	100
4.6	Experimental arrangement in initial study . . . . .	101
4.7	Aluminium clamp for dish forming work . . . . .	104
4.8	Schematic of micro-hardness measurement set-up . . . . .	106
4.9	Photo - Mark I laser forming demonstrator system, <i>Sowerby Research centre</i> . . . . .	108
4.10	Schematic - Mark I laser forming demonstrator system . . . . .	109
5.1	Bend angle with increasing traverse velocity at constant beam diameter . . . . .	111
5.2	Bend angle with increasing traverse velocity at constant line energy	111
5.3	Bend angle with increasing traverse velocity at constant line energy	112
5.4	Double logarithmic plot of bend angle with increasing traverse velocity	113
5.5	Measured bend angle and calculated bend angle v traverse velocity	114
5.6	Measured bend angle and calculated bend angle v traverse velocity	115
5.7	Measured bend angle and calculated bend angle v traverse velocity	115
5.8	Comparison of analytical solutions and measured angles . . . . .	116

5.9	Measured bend angle and calculated Residual Model bend angle v traverse velocity . . . . .	117
5.10	Plastic isotherm cross-section for the case presented in figure 5.8 . .	118
5.11	Calculated bend angles with increasing sheet thickness for four pro- cessing velocities . . . . .	119
5.12	Experimental (Magee) and theoretical (Magee) bend angles with increasing processing velocity . . . . .	120
5.13	Experimental Peak temperatures on the reverse side of the Ti6Al4V sheet . . . . .	121
5.14	Experimental peak temperatures with calculated temperatures for the reverse side of the Ti6Al4V sheet, at a distance of up to 2 mm in the $y$ direction . . . . .	121
5.15	Experimental peak temperatures with calculated temperatures for the reverse side of the Ti6Al4V sheet, at a distance of up to 8 mm in the $y$ direction . . . . .	122
5.16	Increase in thickness of the material along the bending edge for 10, 20 and 30 scans; Power 250 W, Spot size 5mm, Velocity 15mm/s, Ti6Al4V . . . . .	122
5.17	Geometry of the bent zone of fig 5.16 after 30 scans . . . . .	123
5.18	Bend angle with increasing number of scans Ti6Al4V . . . . .	124
5.19	Bend angle with increasing number of scans AA 2024 T3 . . . . .	124
5.20	Bend angle with changing traverse velocity . . . . .	125
5.21	Bend angle with in plate location at low traverse velocity . . . . .	126
5.22	Bend angle with in plate location at medium traverse velocity . . .	126
5.23	Bend angle with in plate location at high traverse velocity . . . . .	127
5.24	Bend angle with in plate location at high traverse velocity . . . . .	127
5.25	Longitudinal bend angle for (for 1 scan) for the case presented in figure 5.23 (for 10 scans = 0.587 degrees) . . . . .	129
5.26	Bend angle with in plate location before and after sectioning, 10 scans	130
5.27	Bend angle with in plate location before and after sectioning, high traverse velocity, 10 scans . . . . .	131
5.28	Bend angle with varying line energy with location, Ti6Al4V alloy .	131
5.29	Bend angle with varying line energy with location, AA 2024 T3 alloy	132
5.30	3-star system with radial lines (outside-in) . . . . .	135
5.31	3-star system with circle bow lines (outside-in) . . . . .	136
5.32	5-star system with radial lines (outside-in) . . . . .	136
5.33	5-star system with circle bow lines (outside-in) . . . . .	137
5.34	7-star system with radial lines (outside-in) . . . . .	137

5.35	7-star system with circle bow lines (outside-in) . . . . .	138
5.36	3-star system with 27 radial lines (outside-in) . . . . .	139
5.37	5-star system with 30 radial lines (outside-in) . . . . .	139
5.38	7-star system with 28 radial lines (outside-in) . . . . .	140
5.39	Offset system with radial lines (outside-in) . . . . .	141
5.40	Offset system with circle bow lines (outside-in) . . . . .	141
5.41	Offset system with two radial line types (outside-in) . . . . .	142
5.42	Offset system with three circle bow line types (outside-in) . . . . .	142
5.43	Offset system with two radial line types . . . . .	143
5.44	Offset system with two circle bow line types 25 x 2 outside-in . . . . .	144
5.45	Offset system with three radial line types, 13x3 lines (outside-in) . . . . .	144
5.46	Offset system with three circle bow line types, 13x3 lines (outside-in) . . . . .	145
5.47	Dividing system with radial lines (outside-in) . . . . .	146
5.48	Dividing system with circle bow lines (outside-in) . . . . .	147
5.49	Dividing system with three radial line types (outside-in) . . . . .	147
5.50	Dividing system with three circle bow line types (outside-in) . . . . .	148
5.51	Dividing system with two radial line types, 24x 2 lines (outside-in) . . . . .	148
5.52	Dividing system with two circle bow line types, 24x 2 lines (outside-in) . . . . .	149
5.53	Dividing system with three radial line types, 12x 3 lines (outside-in) . . . . .	149
5.54	Dividing system with three circle bow line types, 12x3 lines (outside-in) . . . . .	150
5.55	Circle line system with linear radius increase (inside-out) . . . . .	151
5.56	Circle line system with square root radius increase (inside-out) . . . . .	152
5.57	Circle line system with quadratic radius increase (inside-out) . . . . .	152
5.58	Circle line system with linear radius increase, 10 lines (inside-out) . . . . .	153
5.59	Circle line system with square root radius increase, 10 lines (inside-out) . . . . .	154
5.60	Circle line system with quadratic radius increase, 10 lines (inside-out) . . . . .	154
5.61	The as-received material, x400 . . . . .	158
5.62	Recrystallisation of the upper region of the sheet under the clad layer, x200 . . . . .	159
5.63	Recrystallisation of the upper region of the sheet under the clad layer, x 400 . . . . .	159
5.64	Irregular Alclad-substrate interface and severe partial melting of recrystallised grains . . . . .	160
5.65	Fusion of the alclad with the substrate showing a dendritic cast structure and partial melting of recrystallised grains towards the lower regions . . . . .	160

5.66 Large recrystallised grains with precipitates at the grain boundaries, and constituent particles, visible as dark spots . . . . .	161
5.67 Microstructural changes at the interface of the resolidified material and the previous grain structure . . . . .	161
5.68 Partial melting and hot tearing of a grain . . . . .	162
5.69 Formation of a subgrain structure during the early stages of dynamic recrystallisation . . . . .	162
5.70 Hardness profile across the thickness of the as-received material . .	163
5.71 Hardness profile across the thickness of the material scanned 10 times, with an AED of $10.6 J/mm^2$ . . . . .	164
5.72 Hardness profiles across the thickness for samples with an AED of 17 and $20 J/mm^2$ . . . . .	164
5.73 Hardness increase due to finer grain size after recrystallisation for an AED of $25 J/mm^2$ . . . . .	165
5.74 Hardness profiles across the thickness for sample with an AED of 33.33 and $20 J/mm^2$ . . . . .	166
5.75 Hardness profiles across the thickness for a sample with an AED of $125 J/mm^2$ . . . . .	166
5.76 The as-received microstructure of the Ti6Al4V . . . . .	168
5.77 Formation of acicular plates for large energy input, processing in air	169
5.78 Formation of large acicular plates for large energy input, processing in air . . . . .	169
5.79 Length and depth of transformed zone v laser input energy . . . . .	170
5.80 Thickness increase in the laser irradiated zone, $\alpha - \beta$ Ti6Al4V alloy	170
5.81 Plate size with increasing line energy, $\alpha - \beta$ Ti6Al4V alloy . . . . .	170
5.82 Alpha case formation processing in air, Ti6Al4V . . . . .	171
5.83 Alpha case formation with increasing energy input and processing in air, Ti6Al4V . . . . .	171
5.84 Microstructure after the annealing treatment showing the typical Widmanstätten structure . . . . .	172
5.85 Increase in microhardness at the sample surface in the presence of an alpha case . . . . .	173
5.86 Required demonstrator part . . . . .	175
5.87 Required deflection at each point along the curvature . . . . .	176
5.88 Distortion of demonstrator part . . . . .	177
5.89 Schematic of longitudinal bending along bending edge from start to end of process . . . . .	178
5.90 Arresting the counterbending . . . . .	178

5.91 Force exerted by block underneath the sheet past the tangential point of contact . . . . .	179
5.92 Pneumatic clamping arrangement . . . . .	180
5.93 Geometrically accurate demonstrator part . . . . .	181
5.94 As received profile of the sheet . . . . .	182
5.95 Profile after 1 laser scan line . . . . .	182
5.96 Profile after 2 laser scan lines . . . . .	183
5.97 Profile after 3 laser scan lines . . . . .	183
5.98 Profile after 4 laser scan lines . . . . .	183
5.99 Profile after 5 laser scan lines . . . . .	184
5.100 Profile after 6 laser scan lines . . . . .	184
5.101 Profile after 7 laser scan lines . . . . .	184
5.102 Profile after 8 laser scan lines . . . . .	185
A.1 Geometry of Yau's two layer model . . . . .	194
B.1 Bend angle with decreasing energy input . . . . .	207
B.2 Bend angle with decreasing energy input . . . . .	208
B.3 Bend angle with decreasing energy input . . . . .	208
B.4 Bend angle with decreasing energy input . . . . .	209
B.5 Bend angle with decreasing energy input . . . . .	209
B.6 Bend angle with decreasing energy input . . . . .	210
B.7 Bend angle with decreasing energy input . . . . .	211
B.8 Bend angle with decreasing energy input . . . . .	211
B.9 Bend angle with decreasing energy input . . . . .	212
B.10 Bend angle with decreasing energy input . . . . .	213
B.11 Bend angle with decreasing energy input . . . . .	214
B.12 Bend angle with decreasing energy input . . . . .	214
B.13 Bend angle with decreasing energy input . . . . .	215
B.14 Bend angle with decreasing energy input . . . . .	216
B.15 Bend angle with decreasing energy input . . . . .	217
B.16 Bend angle with decreasing energy input . . . . .	217
B.17 Bend angle with decreasing energy input . . . . .	218
B.18 Bend angle with decreasing energy input . . . . .	219
B.19 Bend angle with decreasing energy input . . . . .	220
B.20 Bend angle with decreasing energy input . . . . .	220
B.21 Bend angle with decreasing energy input . . . . .	221
B.22 Bend angle with decreasing energy input . . . . .	222
B.23 Bend angle with decreasing energy input . . . . .	223

B.24 Bend angle with decreasing energy input . . . . . 223  
B.25 Bend angle with decreasing energy input . . . . . 224  
B.26 Bend angle with decreasing energy input . . . . . 225  
B.27 Bend angle with decreasing energy input . . . . . 226  
B.28 Bend angle with decreasing energy input . . . . . 226

# List of Tables

2.1	Boundary temperature increase for plastic yielding . . . . .	39
3.1	Width and depth of plastic zone, inherent strain and transverse bending moment for the case presented in figure 3.4 . . . . .	84
3.2	Moments, forces and curvatures for the case presented in figure 3.4 .	85
4.1	Elemental composition of AA 2024 - T3 . . . . .	95
4.2	Elemental composition of Ti6Al4V . . . . .	95
4.3	Materials and dimensions . . . . .	98
4.4	Laser process parameters for the 3-D forming . . . . .	104
4.5	Etchant composition . . . . .	105
4.6	Annealing conditions . . . . .	106
5.1	Expansion coefficients of the alloys . . . . .	110
5.2	Moments, forces and bend angles for the case presented in figure 5.23128	
5.3	Table of parameters used for AA2024 T3 micrographs . . . . .	158
5.4	Laser process parameters for the 2-D forming of demonstrator part	181

# List of Symbols

## S.I Units

$A$  - Absorption (constant)

$b$  - Breadth of plastic zone

$c_p$  - Specific heat capacity

$d_1$  - Laser beam diameter

$D$  - Ratio of depth of plastic zone to sheet thickness

$E$  - Elastic Modulus

$E_d$  - Elastic Modulus of disk

$E_{pl}$  - Elastic Modulus of plate

$F$  - Force

$F_o$  - Fourier number

$I$  - Moment of Inertia

$I_0$  - Intensity at centre of laser beam

$K$  - Spring constant

$k_f$  - Temperature dependent Yield stress

$k$  - Thermal conductivity, ( $\lambda$  p.40)

$l$  - Length

$l_h$  - Length of heated zone

$l_1$  - Length of plastically strained zone

$l_2$  - Length of elastically strained zone

$M$  - Bending moment

$m$  - Mass

$N$  - In-plane force

$$N_f = \frac{8Ap_1\sqrt{at}}{\pi kd_{12}}$$

$p_1$  - Laser power

$$P_f = \frac{d_1}{4\sqrt{at}}$$

$Q$  - Dimensionless power

$Q_1$  - Average energy input

$R$  - Radius of curvature

$r_{dim}$  - Radial dimension

$R_{hole}$  - Radius of hole

$r_1$  - Laser beam radius

$S$  - Dimensionless velocity

$S_h$  - Shear

$s_0$  - Sheet thickness

$s_1$  - Depth of plastic zone

$T$  - Temperature  
 $T_{amb}$  - Ambient temperature  
 $T_c$  - Critical temperature for plastic flow  
 $T_{int}$  - Initial temperature  
 $T_{end}$  - Final temperature  
 $t$  - time  
 $u$  - displacement  
 $u_d$  - displacement of disk  
 $u_{pl}$  - displacement of plate  
 $v_1$  - Velocity  
 $w$  - load  
 $x, y, z$  - Cartesian co-ordinates  
 $Y$  - Yield Strength  
 $a$  - Thermal diffusivity  
 $\alpha_B, \alpha_b$  - Bend angle  
 $\alpha_{th}$  - Coefficient of thermal expansion  
 $\Delta T$  - Time of heating  
 $\bar{\Delta T}$  - Average temperature of heated zone  
 $\Delta T'$  - Temperature increase  
 $\epsilon$  - Strain  
 $\epsilon_{in}$  - Inherent strain (maximum plastic strain less elastic strain during heating)  
 $\epsilon_{pm}$  - Maximum plastic strain  
 $\epsilon_r$  - Radial strain  
 $\epsilon_\theta$  - Tangential strain  
 $\kappa$  - Thermal diffusivity  
 $\rho$  - Mass density  
 $\sigma$  - Stress  
 $\sigma_d$  - Yield stress of disk  
 $\sigma_r$  - Radial stress  
 $\sigma_\theta$  - Tangential stress  
 $\nu$  - Poisson's ratio  
 $\nu_1$  - Poisson's ratio of disk  
 $\nu_2$  - Poisson's ratio of plate

# Chapter 1

## Introduction

### 1.1 The process

Laser forming is a non contact thermally induced forming process which may proceed by two primary forming mechanisms including out of plane and in plane strains. The mechanism activated is dependent on the laser processing parameters employed, the geometry of the workpiece and the material properties. Out of plane deformation is induced by the introduction of a steep thermal gradient to the surface of the material to be processed. A material with a low thermal conductivity, and a relatively small second moment of area (e.g. a sheet material), coupled with a rapid heat input facilitates this. Out of plane strain results in bending. (see figure 1.1) In plane strain occurs when the heat generated from the laser beam is fully penetrative through the sheet thickness, the heated width is large compared to the sheet thickness, and when the geometry (e.g. a box section material) resists out of plane bending. In plane strain results in shortening. (refer figure 1.2) The laser

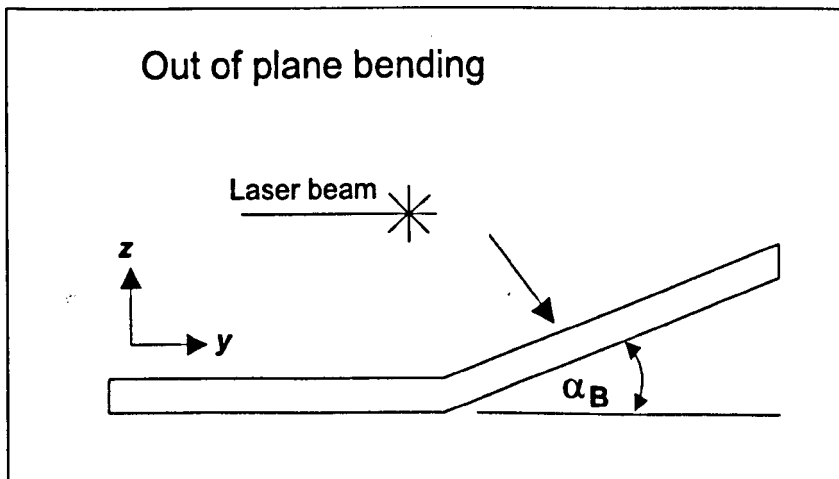


Figure 1.1: Out of plane bending

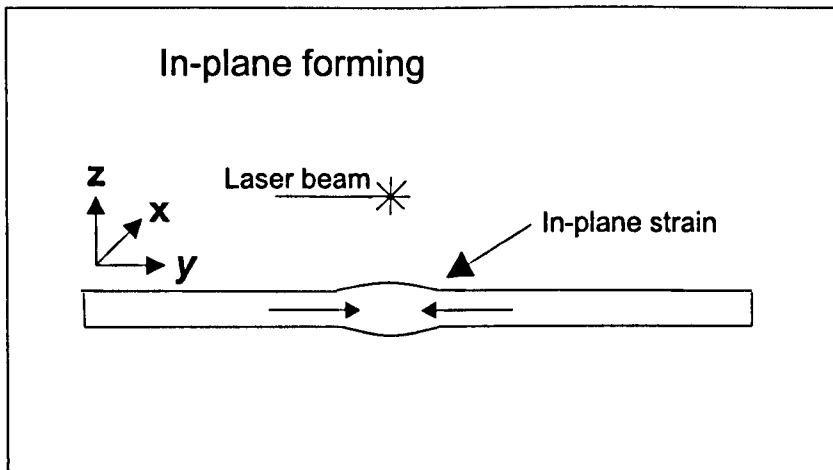


Figure 1.2: In-plane forming

is useful as a power source for forming as:-

1. Mechanical contact between the workpiece and the forming tool (the laser beam) is not required.
2. Potential for accuracy and controllability of this power source is great.
3. Material may be formed remotely.

## 1.2 The laser

Einstein laid down the principles by which lasers work. That principle is stimulated emission [1]. However it was not until some time after this that these principles were used to construct the first operational laser. In 1960 Maiman invented the ruby laser [2]. Since then many more devices have been developed including CO<sub>2</sub> [3], Excimer [4], Nd:YAG [5], and Diode lasers to name some of the most important in laser materials processing. The word laser refers to "Light Amplification by the Stimulated Emission of Radiation." The main components of a laser include (see figure 1.3) [1]:

- An optical resonator.
- An active medium.
- A system to excite the active medium.

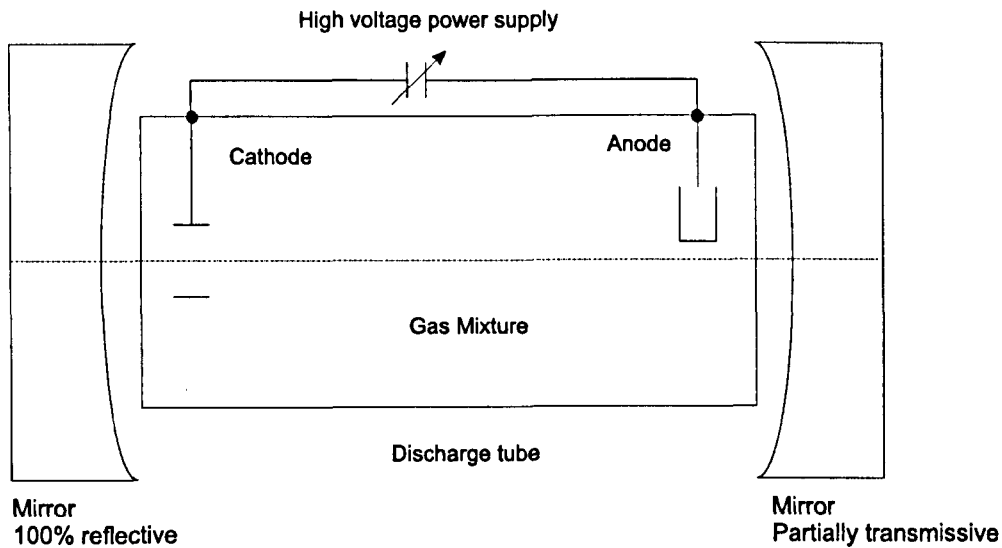


Figure 1.3: Components of a gas laser

### 1.2.1 Optical Resonator

This component of the laser generally consists of two mirrors with their reflective surfaces opposite and parallel to each other, and normal to the optical axis of the active medium so that light may oscillate between them.

### 1.2.2 Active medium

The active medium is chosen to amplify the light oscillations between the mirrors. In a gas laser the active medium may be a combination of gases such as carbon dioxide, helium and nitrogen.

### 1.2.3 System to excite the active medium

The medium must have enough energy to be active. Systems to excite the medium may take the form of a DC (Direct Current), a RF (Radio Frequency) power supply, or a focused light pulse depending on the laser type.

## 1.3 Principle of operation

Light inside the laser is amplified by the active medium. It oscillates between the mirrors due to its increased energy. Once the light is amplified sufficiently it can partially pass through one of the mirrors. This mirror is partially transparent. The opposite mirror is as reflective as possible and curved in a manner to reduce diffraction losses of the oscillating light. The light that emerges from the partially transparent mirror is the “laser beam” which is then guided along an optical

delivery system to the workpiece.

## 1.4 Characteristics of the energy source

Laser light possesses some unique properties compared to other forms of industrial light. These characteristics are responsible for the use of the laser as an effective power source. They are described next.

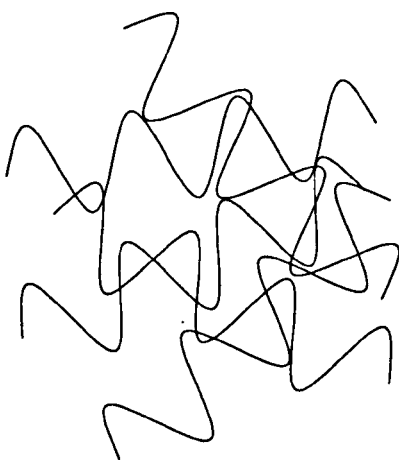
### 1.4.1 Monochromaticity

If light is highly monochromatic this implies that there is a small range of frequencies emitted by the light source. Spectral line width is a measure of this [2]. Laser light usually has a single or a few spectral lines which are very narrow. This is especially useful in applications such as interferometry and holography.

### 1.4.2 Coherence

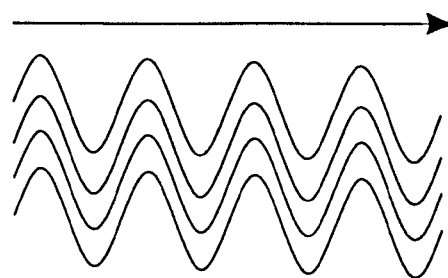
Electromagnetic waves have electric and magnetic components. Temporal and spatial coherence depends on the relationship between these components [4]. Temporal coherence refers to the direction parallel to the laser beam propagation. Spatial coherence refers to the direction perpendicular to the laser beam. If these components are aligned in phase the laser beam is deemed coherent as illustrated in figure 1.4.

Misaligned out of phase



(A) Incoherent light

Aligned in phase



(B) Coherent laser light

Figure 1.4: Laser beam coherence

### 1.4.3 Polarisation

A photon travelling in space has an oscillatory motion and this causes oscillations in its electric field which result in an electromagnetic wave. The wave represents the magnitude and direction of the photons electric field vector with respect to time. Incoherent light photons oscillate with different phases, frequencies and amplitudes which in turn produce electromagnetic waves with random orientations and phases. Laser light because of its monochromaticity and coherence has extremely similar phases, directions and amplitudes. The electric fields for the photons in the laser beam are aligned in the same direction and this leads to its linear polarisation [4].

### 1.4.4 Diffraction

Diffraction or scattering of light occurs when light is projected over increasing distances. This results in a loss of intensity. Laser beams have limited diffraction when compared to other light sources. A limited diffraction light beam is often termed “*collimated.*” Laser beams can be collimated and guided over quite large distances with small losses of intensity.

### 1.4.5 Radiance

At a given solid angle the amount of power emitted per unit area by the light source is called the radiance [5]. The solid angle refers to the angle over which the light is transmitted (the light cone). For a laser beam with limited divergence the solid angle is small over distance, therefore the area over which the beam impinges remains small and the radiance is very large. High power densities are possible which facilitate industrial materials processing.

## 1.5 Characteristics of the laser device

A particular laser device has a characteristic wavelength, spatial and temporal mode.

### 1.5.1 Wavelength

The wavelength is associated with the spatial distance over which a photon undergoes one cycle of vibration. Different lasing materials produce laser light with different wavelengths. The light should in principle have a narrow bandwidth. In practice proper design of the optical resonator is essential to minimise the bandwidth of the laser light. If any thermal expansion of the resonator components

occurs then the wavelength may change as the laser beam may not travel an integral number of half wavelengths of the required frequency. If that happens then the focal spot size of the laser beam cannot be minimised. This is because the refractive index of the focusing lens changes with changes in wavelength. This is referred to as chromatic aberration. Thus different wavelengths will focus at different points.

### 1.5.2 Spatial mode

Laser beam profiles are characterised by their transverse electromagnetic mode (TEM) [6]. When a laser beam exits the cavity it has a preferred intensity distribution due to the constraints imposed on it inside the cavity. These include the geometry of the cavity, the homogeneity of the medium, and the pumping power. TEM<sub>nm</sub> modes are described with the subscripts nm. The n denotes the number of nodes in the x or r direction and m denotes the number in the y or θ direction. The commonly used gaussian beam profile is denoted TEM<sub>00</sub>, (see figure 1.5).

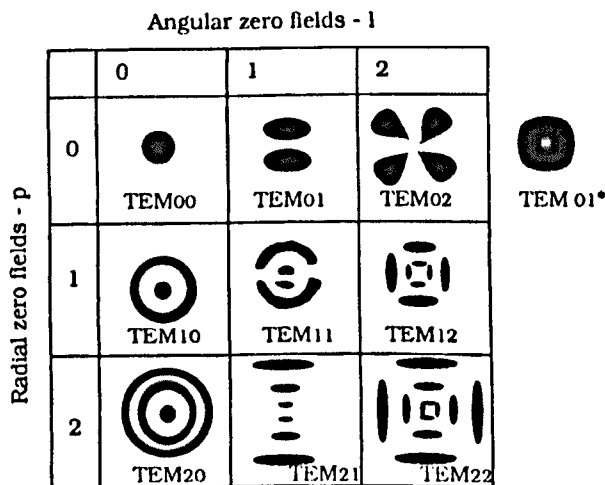
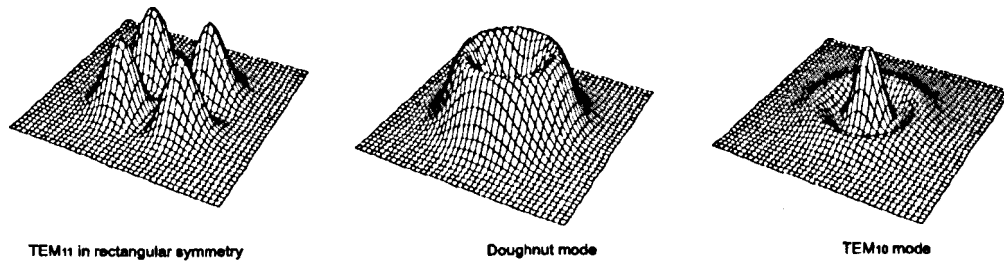


Figure 1.5: Laser beam modes

### 1.5.3 Divergence

Despite the coherence and monochromaticity of laser beams they do diverge to some extent. Coherent [6] introduced the  $M^2$  or  $Q$  factor to describe the degree of divergence of the beam by comparing a real laser beam with that of an ideal diffraction limited gaussian beam with the same beam waist.  $M^2$  is given by:

$$M^2 = \frac{\Theta_w}{\Theta_g} \quad (1.1)$$

$\Theta_w$  is the actual beam waist and  $\Theta_g$  is the beam waist of a diffraction limited beam.

## 1.6 Laser Material Interaction

When a laser beam impinges on a material part of the beam is absorbed, part of the beam is reflected and part of the beam transmits through the material. Transmission decays according to Beer Lambert's law. In metallic materials the absorption is via free electrons. These electrons can oscillate without disturbing the solid atomic structure of the material. Free electrons vibrate in phase but at 180 degrees out of phase with the impinging laser beam [1]. Metals are essentially opaque and the power is absorbed at the surface of the material. The reflectivity of metals is high in the infra-red region. The energy absorbed is equal to 1-R where R is the reflectivity of the material. The absorbed energy generates heat which is conducted through the material and which is lost from the surfaces by convection and radiation. With increasing energy input the material will melt or vaporise. In laser bending conduction is the dominant mode of heat transfer.

### 1.6.1 Absorption

Absorption is essential in laser materials processing techniques such as laser bending which rely on heat conduction. Absorption for a given material depends primarily on the wavelength of the laser light, the angle of incidence of the light and the temperature dependency of the materials absorption properties. Generally as the wavelength of the laser light decreases the ability of the material to absorb increases. (see figure 1.6) This is because at shorter wavelengths the more energetic photons are readily absorbed by a greater number of bound electrons and the reflectivity falls.[1] At elevated temperatures the phonon population increases which enhances phonon-electron energy transfer. Consequently the electrons will interact with the material structure rather than oscillate and reradiate [1]. The

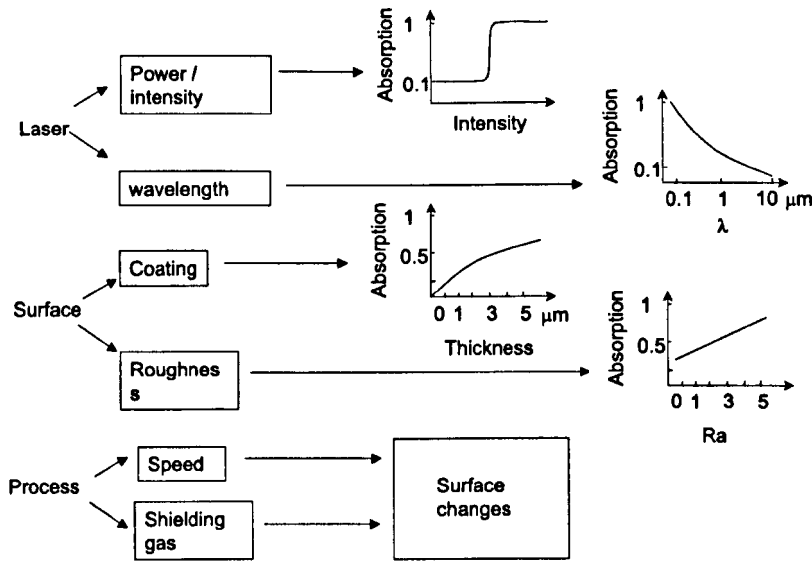


Figure 1.6: Absorption dependencies for laser materials processing

net result is that for metals the absorption increases with increasing temperature.

As the angle of incidence of the oncoming laser beam changes, the absorption behaviour changes. The absorption is maximised at the Brewster angle. At this angle reflection is at right angles to the angle of refraction. The electric vector in the plane of incidence cannot be reflected at this angle since there is no component at right angles to itself. Therefore the reflected ray of light will have an electric vector only at right angles to the plane of incidence. At this angle the angle of refraction is 90 degrees less the angle of incidence and using Snell's law, the refractive index,  $n$ , is given by: [1]

$$n = \tan(\text{Brewster angle}) \quad (1.2)$$

In laser forming absorption of light followed by conduction of heat are the most relevant transport phenomena. Laser forming is not carried out in the melting regime in this work. Therefore it is not necessary to describe the plasma-beam effects and interaction, commonly found in other laser materials processing techniques.

# Chapter 2

## Literature Review

### 2.1 Summary

This chapter presents the background to laser forming. It reviews the mechanisms and models for laser bending available in the literature, previous experimental work and the applications currently developed. A synopsis is given for the current research.

### 2.2 History

Laser forming originates from the similar process of flame bending or “line heating” which uses an oxy-acetylene torch as the heat source. Flame bending has been used extensively for curving and straightening heavy engineering components such as beams and girders for construction purposes [7]. The diffuse nature of the flame used in line heating makes the process rely heavily on operator skill. A flame heat source produces a constant temperature at the surface of the workpiece and it is difficult to establish a steep thermal gradient (which is often necessary for the process) in thin sections and materials with a high thermal conductivity. Consequently the operator must spend much time learning about the heating conditions which will produce the desired result by trial and error. The heating rates associated with laser beams impinging on metallic objects are high and steep thermal gradients are easily achieved. The laser beam can be applied to a very localised region in comparison with the flame as well. These advantages along with the potential for automation have led to research into laser forming.

## 2.3 Potential for application

In principle the generic nature of the CO<sub>2</sub> laser facilitates the cutting and bending of a component under the same set-up, whilst the Nd:YAG or diode laser beam can be guided to remote destinations for the adjustment and alignment of components. Dedicated micro-scale laser bending operations are already being carried out [8] and the realisation of flexible laser forming systems is evolving. The recent increase in laser bending research and development reflects the industrial interest in the process. Research programs span several areas including aerospace [9, 10], automotive [11] and electrical/electronic component manufacturing [8, 12].

## 2.4 Mechanics of laser forming

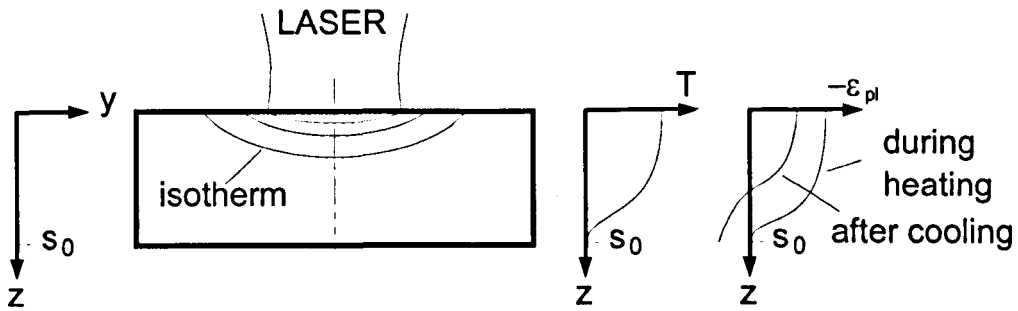
Once the laser beam has been absorbed at the surface of the material laser forming then involves two branches of engineering science including heat transfer and solid mechanics. In the following sections the process is described in terms of these sciences.

### 2.4.1 Temperature gradient mechanism

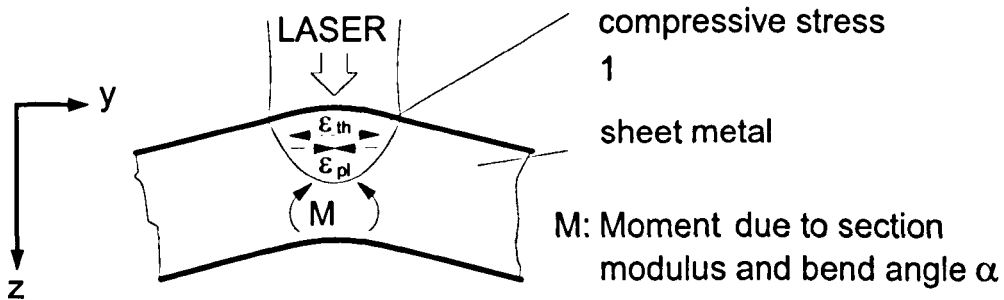
The Temperature Gradient Mechanism (TGM) is the most widely reported laser bending mechanism [13, 14, 15, 16, 17, 18, 19, 20]. This mechanism is used for bending the workpiece out of plane. The introduction of a steep thermal gradient into the material (see Fig 2.1) results in a differential thermal expansion through the thickness. Initially the plate bends in the direction away from the surface which is heated. This is called counter-bending (see Figure 2.1).

With continued heating the bending moment of the sheet opposes the counter-bending away from the laser beam and the mechanical properties of the material are reduced with the temperature increase. Once the thermal stress reaches the temperature dependent yield stress any further thermal expansion is converted into plastic compression. During cooling the material contracts again in the upper layers and because it has been compressed there is a local shortening of the upper layers of the sheet and the sheet bends towards the laser beam. The yield stress and Young's modulus return to a much higher level during this cooling phase and little plastic re-straining occurs.

**temperature-gradient**



**heating - counterbending**



**cooling - positive bending**

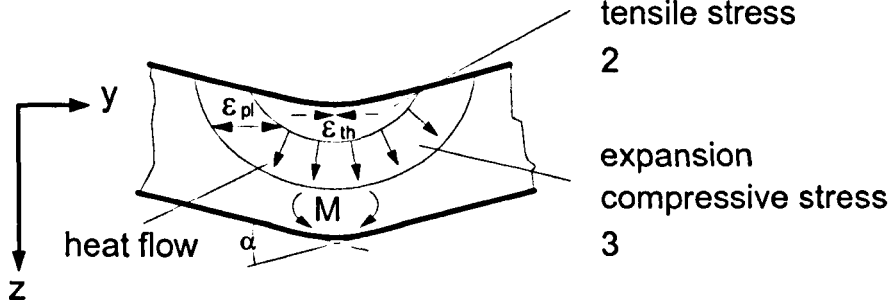


Figure 2.1: The temperature gradient mechanism

**2.4.2 Pointsource mechanism**

The pointsource mechanism [14] is the simplest of the phenomenological laser bending mechanisms. It is illustrated in figure 2.2. It proceeds by the following steps:

1. The start of irradiation of the sheet with a stationary laser beam. With a stationary laser spot switched on for a sufficient time the heating and cooling cycles are almost symmetrical.
2. Generation and conduction of heat from the irradiated spot into the surrounding material.
3. Local thermal expansion as the heated area is much smaller than the sheet

area. Due to the restricted thermal expansion a compressive stress is set-up within the locally expanding material.

4. Development of plastic strain once the temperature reaches a certain value. This happens because at some point the thermal expansion exceeds the maximum elastic strain which the material allows at that temperature.
5. End of laser irradiation.
6. Cooling of the plastic zone and conduction into surrounding material.
7. Contraction of the plastic zone and cancellation of the compressive stress.
8. Build up of tensile stresses in the previously irradiated zone.
9. Tensile stresses reach the yield stress of the material. Then one of two scenarios may happen:
  - (a) If the plastic compression during heating was smaller than the elastic strain at the room temperature yield stress no cancellation of plastic strain takes place.
  - (b) If the plastic strain during the heating stage was greater than the elastic strain at the room temperature yield stress a plastic restraining takes place which cancels part of the plastic compressive strain.

### 2.4.3 Buckling and upsetting mechanisms

These mechanisms are activated by the use of laser parameters which do not yield a temperature gradient in the  $z$  direction (depth)[14]. Usually in the case of the buckling mechanism (BM) the laser beam diameter on the surface of the sheet is much larger than the sheet thickness [20, 21, 22]. This results in a large amount of thermoelastic strain which results in a local thermoelastic - plastic buckling of the material. The buckle is traversed along the length of the sample and once the buckle reaches the exiting edge of the sheet the elastic strain dissipates and the remaining plastic strain causes a deflection (see Figure 2.3).

This mechanism is used for out of plane bending, and it may be accompanied by some in plane shrinkage as well. The part can be made to bend in either the positive or negative  $z$  directions. The direction depends on a number of factors including the pre-bending orientation of the sheet, pre-existing residual stresses and the direction in which any other elastic stresses are applied, for example a forced air stream acting on the bottom of the sheet. Some of these effects were investigated by Arnet

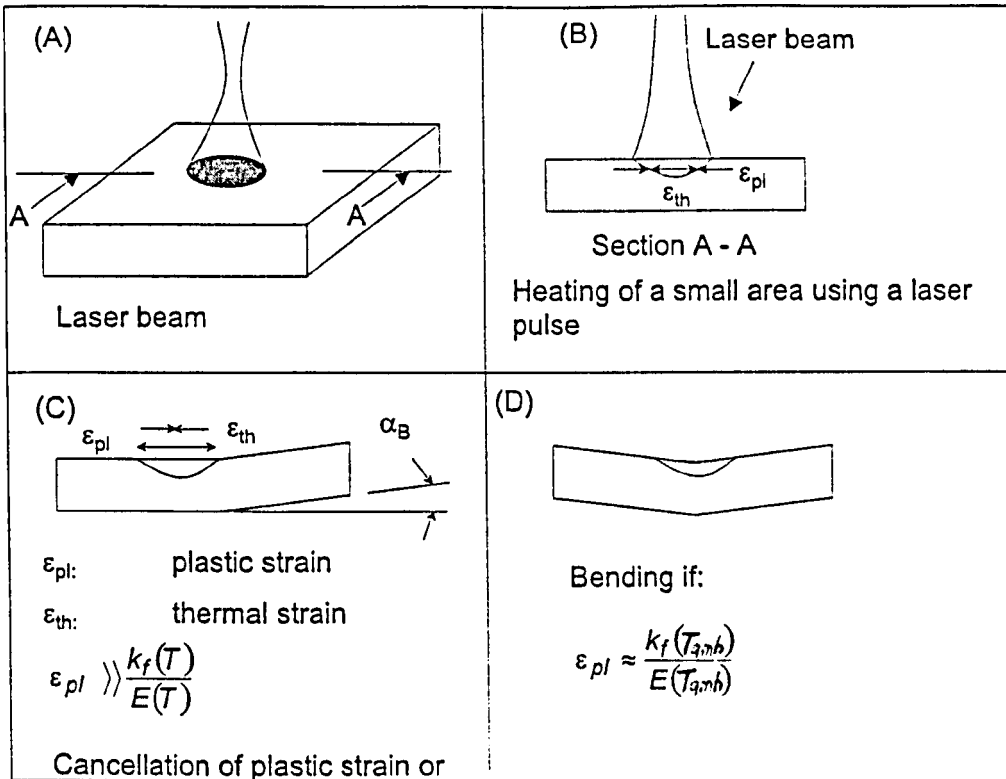


Figure 2.2: The pointsource mechanism

et al [21]. With the Upsetting Mechanism (UM) the geometry of the workpiece prevents buckling (because of its increased moment of inertia compared to a sheet). for example a box section and the irradiated sides of the workpiece can only become shorter. The mechanism is illustrated in figure 2.4. By careful selection of the sequence in which the sides of the geometry are heated the section can be made to step out of plane [23]. Some of these mechanisms can accompany each other to some extent as there is a transition region of laser processing parameters and geometries where a switch from one mechanism to another takes place. Additionally there is usually coupling between in plane and out of plane deformation in forming operations. [24]

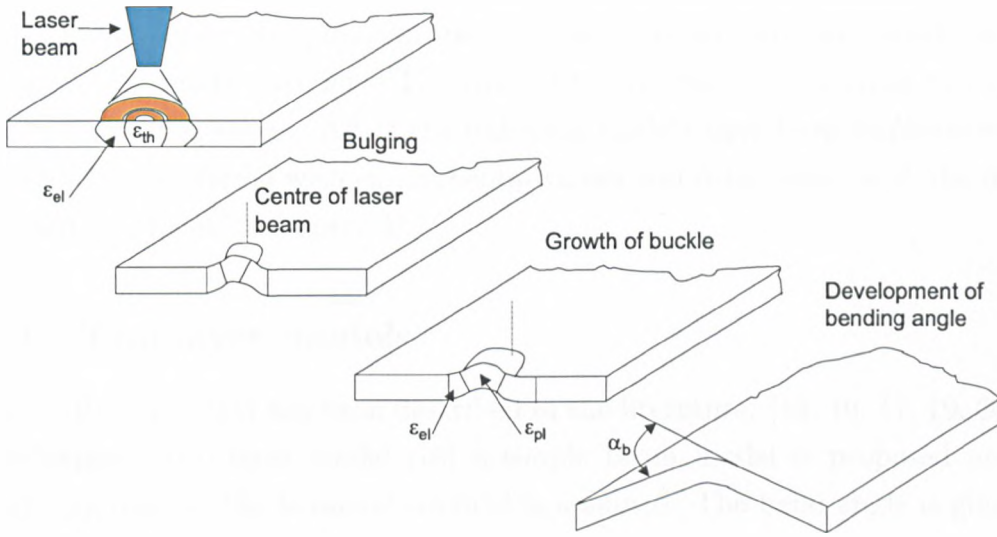


Figure 2.3: The buckling mechanism

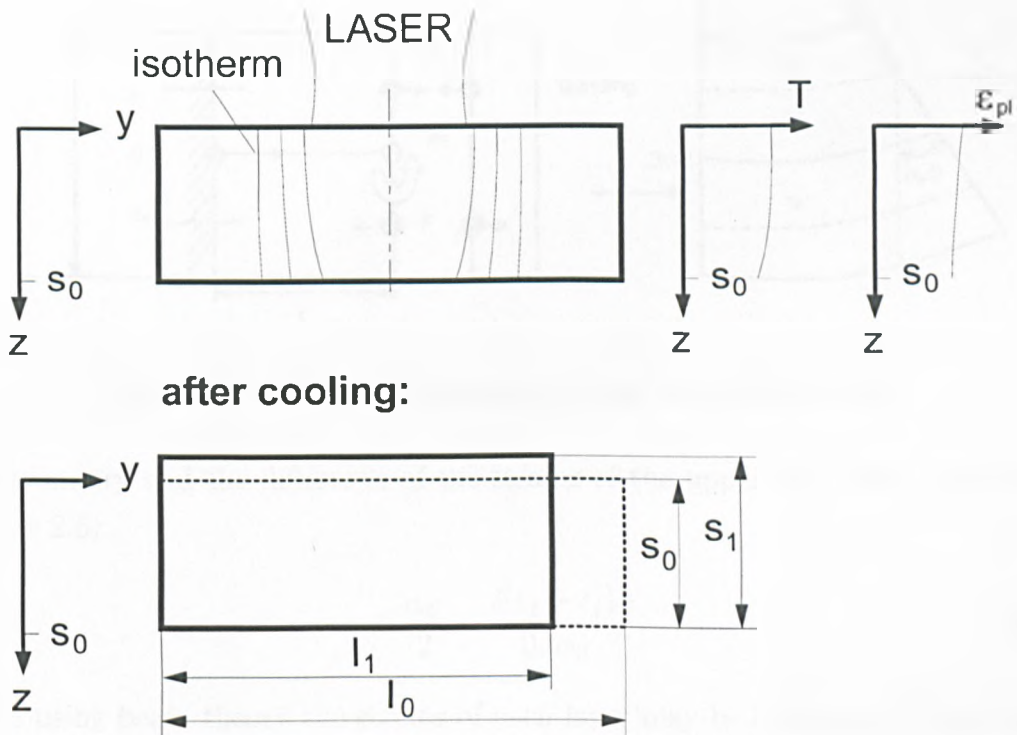


Figure 2.4: The upsetting mechanism

## 2.5 Mathematical models - Analytical

The previously described phenomenological mechanisms have been modelled analytically. The models are few. Therefore they are described in order to expand on the process mechanics. All of the following models have been implemented in chapter 5 for correlation with experimental values and comparison with the model presented by Magee in chapter 3.

### 2.5.1 Two layer models

In particular the TGM has been described in the literature. [14, 16, 17, 19, 20, 25] In Vollertsen's two layer model [16] a simple beam model is proposed and an energy approach to the temperature field is assumed. The bend angle is given by

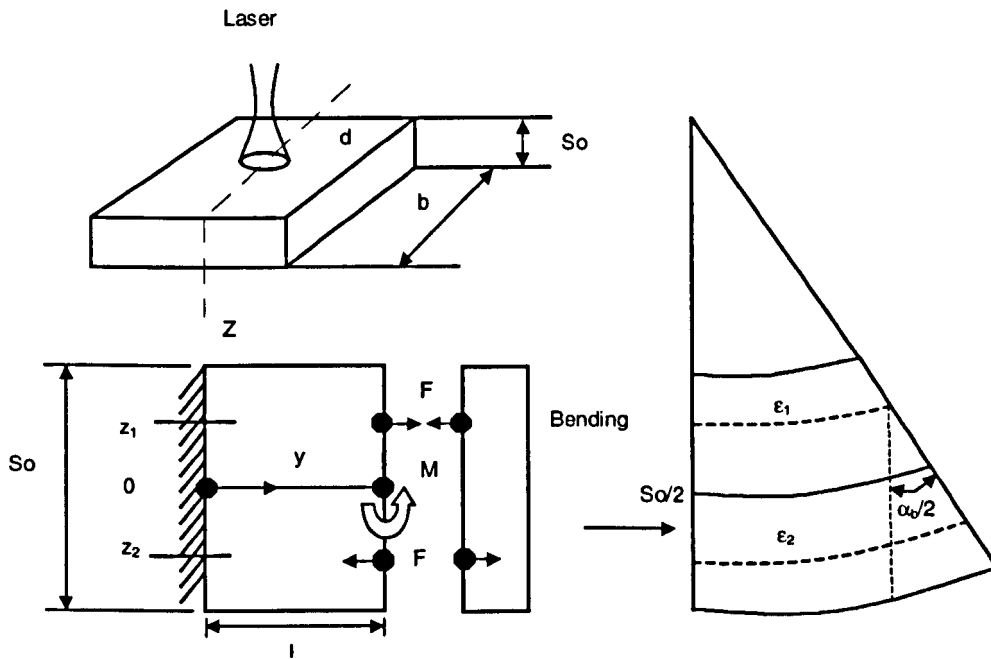


Figure 2.5: Forces and moments acting in two layer model

the geometry and the difference of the strains of the upper and lower layer (refer Figure 2.5):

$$\frac{\alpha_B}{2} = \frac{l(\epsilon_2 - \epsilon_1)}{0.5s_0} \quad (2.1)$$

Then using beam theory the strains of each layer may be calculated. From beam theory:

$$EIR = M \quad (2.2)$$

where:

$$I = \int_0^{\frac{h}{2}} B(z)z^2 dz \quad (2.3)$$

and  $R$  is the radius of curvature,  $I$ , the moment of inertia and  $E$ , the Elastic Modulus. At this point it is useful to define some of the basic parameters used in solid mechanics which will be used in the models described later, refer to figures 2.6 and 2.7. They are as follows.

$$y = \text{deflection} \quad (2.4)$$

$$\frac{dy}{dx} = \text{slope} \quad (2.5)$$

$$\frac{d^2y}{dx^2} = \text{curvature} \quad (2.6)$$

$$EI \frac{d^2y}{dx^2} = \text{bending moment} \quad (2.7)$$

$$-EI \frac{d^3y}{dx^3} = \text{shear } S_h = -\frac{dM}{dx} \quad (2.8)$$

$$EI \frac{d^4y}{dx^4} = \text{load } w = -\frac{dS}{dx} \quad (2.9)$$

where:

$$w = \text{load} \quad (2.10)$$

$$S_h = \text{Shear} = -\int w dx \quad (2.11)$$

$$M = \text{bending moment} = -\int S_h dx = \iint w dx dx \quad (2.12)$$

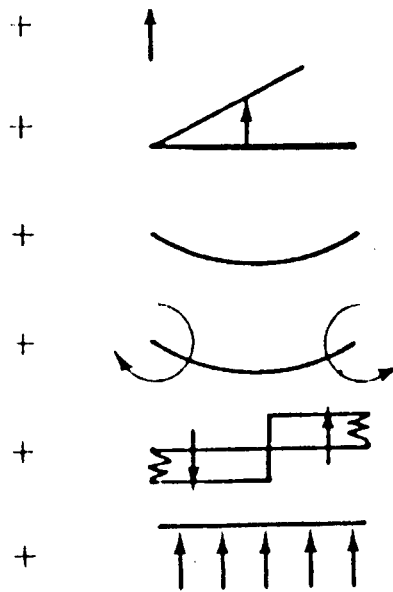


Figure 2.6: Sign convention in moment area theory, reading downwards: deflection, slope, curvature, bending moment, shear and load

$$\text{Curvature} = \frac{M}{EI} \quad (2.13)$$

$$\begin{aligned} \Theta &= \text{slope} \\ &= \int \frac{M}{EI} dx \\ &= \iiint \frac{w}{EI} dx dx dx \end{aligned} \quad (2.14)$$

$$\begin{aligned} y &= \text{deflection} \\ &= \iint \frac{M}{EI} dx dx \\ &= \iiint \frac{w}{EI} dx dx dx \end{aligned} \quad (2.15)$$

S and T are two points on the beam illustrated in figure 2.7. They are loaded at some points  $x_1$  and  $x_2$  from the origin. From the previously described equations the fraction of the moment and the flexural rigidity  $EI$  is equal to the curvature described in equation 2.6. The slope given by equation 2.5 is equal to the integral defined in equation 2.14. Integrating equation 2.14 with the limits of integration

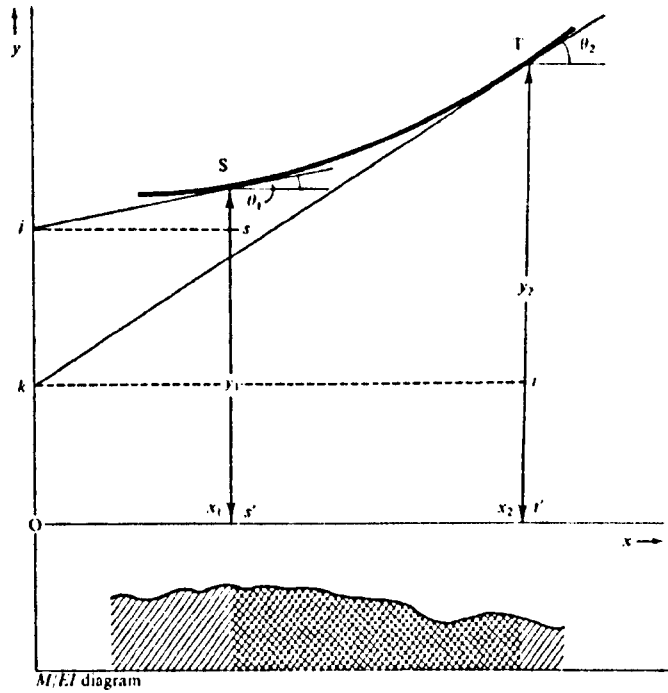


Figure 2.7: The first moment-area theorem

as the two points  $x_1$  and  $x_2$  yields:

$$\left[ \frac{dy}{dx} \right]_{x_1}^{x_2} = \int_{x_1}^{x_2} \frac{M}{EI} dx \tag{2.16}$$

and:

$$\Theta_2 - \Theta_1 = \int_{x_1}^{x_2} \frac{M}{EI} dx \tag{2.17}$$

This means that the change in the slope between the two points on the bent beam is the area of the  $M/EI$  diagram between those two points.

Having revised this notation the engineering beam theory models may now be described. Considering the geometry illustrated in figure 2.5 the strain of the upper layer (assuming it is compressed) is given by:

$$\epsilon_1 = \frac{F}{E_1 A_1} - \frac{M_1}{(EI)_1} z_1 + \alpha_{th} \Delta T \tag{2.18}$$

An important assumption made here is that all the thermal expansion of the upper layer given by  $\alpha_{th} \Delta T$  is converted into plastic compression. In reality this is not the case as some energy is used to elastically strain the material up to its temperature dependent yield point. However an appreciable amount of elastic straining does not occur because the free thermal expansion is greatly hindered by the cold and

rigid surrounding material. In addition the yield stress of the heated zone is reduced to almost zero during heating since it is temperature dependent. It may be acceptable under these conditions to omit these parameters and assume that all the thermal expansion is converted into plastic compression. During cooling as the heat flows into the surrounding regions there may be a tensile plastic restraining of the previously compressed zone.

After the plastic compression development the strain of the upper layer is given by:

$$\epsilon_1 = \frac{F}{E_1 A_1} - \frac{M_1}{(EI)_1} z_1 - \alpha_{th} \Delta T' \quad (2.19)$$

$\Delta T'$  is the maximum temperature difference between the upper and lower layers of the sheet. The strain of the lower layer is given by:

$$\epsilon_2 = -\frac{F}{E_2 A_2} - \frac{M_2}{(EI)_2} z_2 \quad (2.20)$$

Here  $I_2$  is the second moment of area. From the previously described beam theory the fraction of the moment  $M$  and the product  $EI$  yield the local curvature. For large curvatures it is assumed that:

$$\frac{M_1}{(EI)_1} = \frac{M_2}{(EI)_2} = \frac{M}{EI} = \frac{\alpha_B}{2l} \quad (2.21)$$

The bending angle  $\alpha_B$  can then be found by combining the equations for the upper and the lower layers (eq 2.19 and 2.20) along with equation 2.1:

$$\alpha_B = \frac{4l}{s_0} \left[ -\frac{F}{E_2 A_2} - \frac{\alpha_B z_2}{2l} - \frac{F}{E_1 A_1} + \frac{\alpha_B z_1}{2l} - \alpha_{th} \Delta T' \right] \quad (2.22)$$

where the force  $F$  is given by:

$$F = \frac{M}{2s_0} = \frac{\alpha_B EI}{s_0 l} \quad (2.23)$$

and substituting  $z_1 - z_2 = \frac{s_0}{2}$  into the previous two equations yields:

$$\alpha_B = \frac{4EI\alpha_B(E_1 A_1 + E_2 A_2)}{s_0^2(E_1 A_1 E_2 A_2)} + \alpha_B + \frac{4l\alpha_{th}\Delta T'}{s_0} \quad (2.24)$$

The cross sections of the beams are described by:

$$A_1 = b s_1 \quad (2.25)$$

and

$$A_2 = b(s_0 - s_1) \quad (2.26)$$

and the section moment is given by:

$$I = \frac{bs_0^3}{12} \quad (2.27)$$

Assuming  $E_1 = E_2$  the equation for the bend angle is then given by:

$$\alpha_B = 12\alpha_{th}\Delta T/l s_1(s_0 - s_1)/s_0^3 \quad (2.28)$$

To calculate the bend angle with this formula requires knowledge of the length of the heated zone,  $l$ , the depth of heating  $s_1$ , and the temperature rise of the upper layer  $\Delta T'$ . That requires the co-ordinates to be found as a function of the temperature, i.e. in the form of :

$$l = f(T) \quad (2.29)$$

For laser processing this is not possible analytically since the expressions for the temperature contain transcendental functions - Bessel functions which cannot be inverted suitably [22]. Vollertsen adopted an energy approach to the solution of the temperature field instead. In his energy approach all three factors  $l$ ,  $s_1$ , and  $\Delta T'$  are calculated simultaneously [16]. This factor is represented by:

$$\xi = \Delta T' l s_1 (s_0 - s_1) \quad (2.30)$$

This can be done because the parameters  $l$  and  $s_1$  determine the extent of the heated zone which is governed by the thermal conductivity. The temperature increase  $\Delta T'$  is controlled by the heated area, the heat capacity and the energy input from the laser beam. This approach was adopted because as the thermal conductivity increases, the extent of the heated area increases but the average temperature increase is lowered. From this it was assumed that the thermal expansion remains constant. Using these assumptions the energy input  $Q_1$  is given by the time of heating,  $\Delta t$ , the laser power,  $p_1$  and the absorption,  $A$ :

$$Q_1 = 0.5\Delta t p_1 A \quad (2.31)$$

0.5 is used as only one half of the heated area is used for the calculations. The heating time  $\Delta t$  is given by the fraction of the laser spot size and the processing

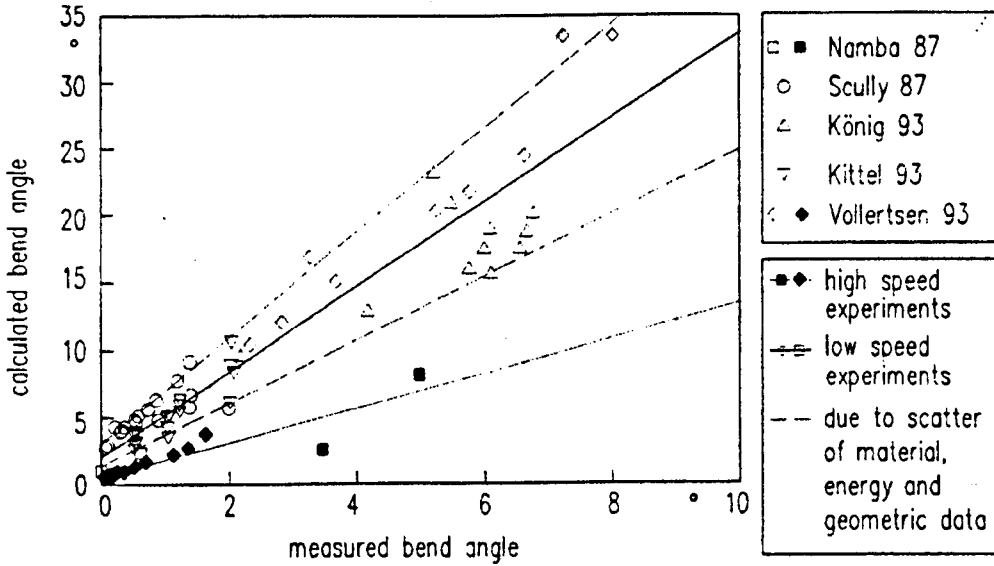


Figure 2.8: Comparison of experimental results with the two layer model

velocity:

$$\Delta t = \frac{d_1}{v_1} \tag{2.32}$$

The average temperature increase of the upper layer is given by the fraction of the energy input,  $Q$ , and the heat capacity,  $Cp$ . The mass of the heated area is determined from the volume of the heated zone and the density,  $\rho$ :

$$m = ld_1s_1\rho \tag{2.33}$$

Combining the last five equations results in:

$$\xi = \frac{p_1A(s_0 - s_1)}{2c_p v_1 \rho} \tag{2.34}$$

Introducing this equation into equation (2.28) gives an expression for the bend angle in terms of known parameters only:

$$\alpha_B = 3 \frac{\alpha_{th} p_1 A}{\rho c_p v_1 s_0^2} \tag{2.35}$$

Experimental data from other authors was presented and compared with the analytical results, (see figure 2.8) and Magee [9] has compared his results with this model in chapter 5.

Although substantial improvement in the agreement between this model and experimental work was achieved (compared to previous analytical models for the

flame forming process) some of the basic concepts were still omitted. The model assumed that all of the energy was used for plastic deformation and this ignored the energy used for the elastic straining.

In Yau's model [25] the two layer model approach was extended to include the counter-bending effect. This modification resulted in two equations, one for the counter-bending angle and one for the bend angle at the end of the cooling cycle. Details of the derivation may be found in Appendix A. The final equation for the bending angle including the temperature field equation in Yau's model is:

$$\alpha_B = 3 \frac{\alpha_{th} A p_1}{\rho c_p v_1} \frac{1}{s_0^2} \left( \frac{7}{2} \right) - 36 \frac{l Y}{s_0 E} \quad (2.36)$$

Comparing equation 2.35 with equation 2.36, Yau's solution (equation 2.36) includes some material and geometrical parameters which reduce the calculated bend angle compared to Vollertsen's solution. Both solutions were implemented and they differ only very slightly, and it is not really noticeable as illustrated in figure 2.9. This is because under the conditions of the temperature gradient mechanism the counterbending angle is very small and combined with the simplifying assumptions of the model the difference in the models is less than expected originally. Figure 2.10 illustrates the counterbending angle for the same conditions and it is of the order of  $10^{-5}$  to  $10^{-6}$  degrees. No account of the effect of the thermal

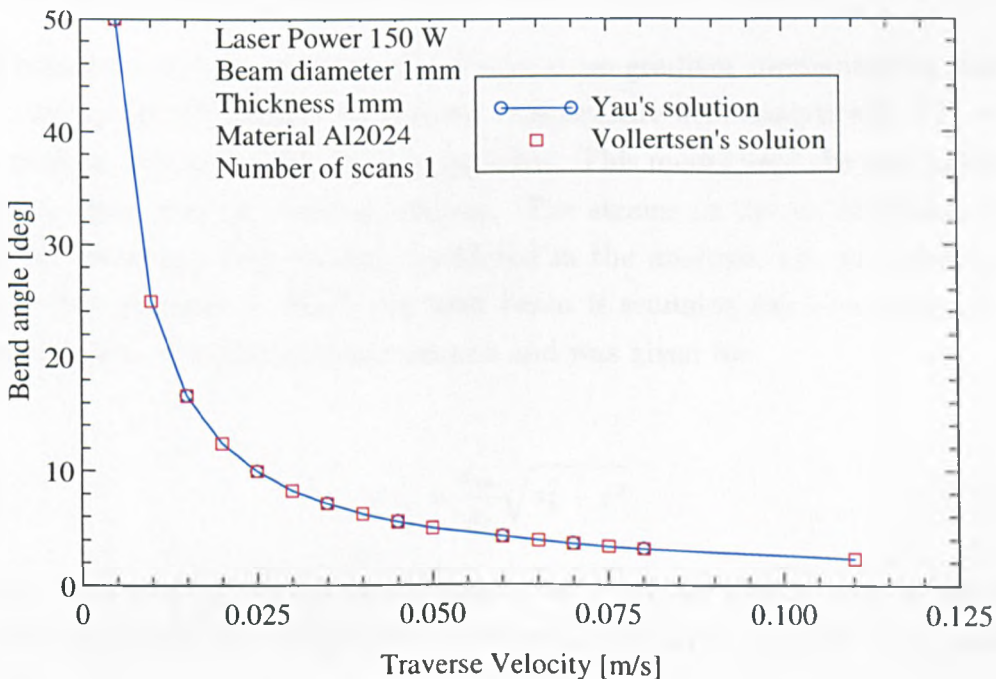


Figure 2.9: Comparison of solutions for two-layer models

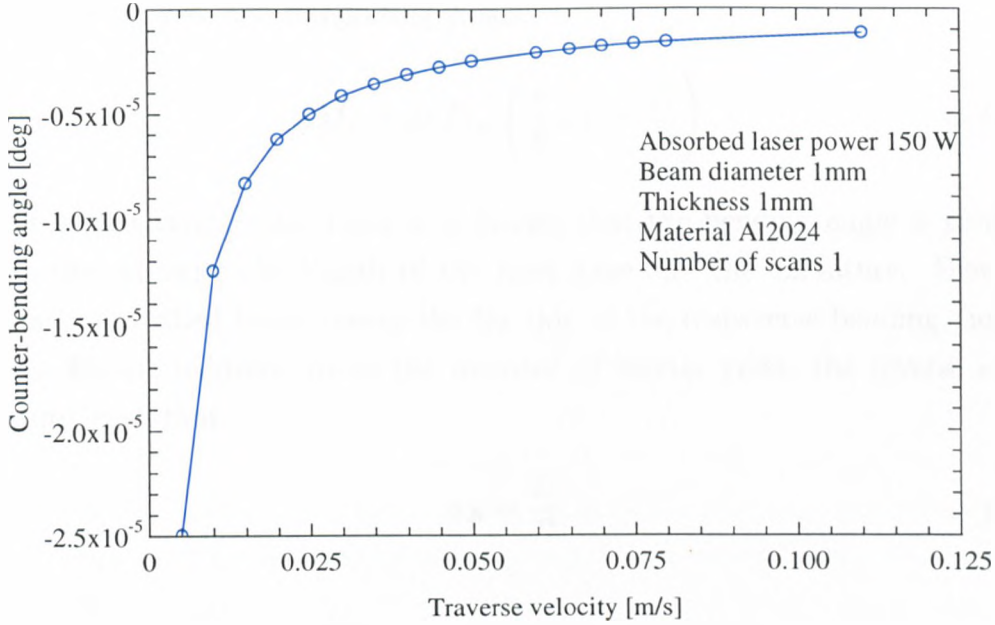


Figure 2.10: Counterbending angle from Yau's model

conductivity was included directly in either of these models and this implies that simplifications about the temperature field were made.

## 2.5.2 The residual stress model

Vollertsen extended the work on the temperature gradient mechanism in another model to include the effects of a realistic temperature field analytically [17], and a more realistic strain distribution was included. This model used the residual stress approach often used in welding analysis. The strains in the  $yz$  directions (refer figure 1.1) were the only strains considered in the analysis, i.e. an infinitesimal strip in the direction in which the laser beam is scanning ( $x$ ) is considered. An elliptical strain distribution was assumed and was given by:

$$\epsilon(z) = \frac{\epsilon_{in}}{s_1} \sqrt{s_1^2 - z^2} \quad (2.37)$$

Here  $s_1$  represents the depth of the plastic zone. If the plastic zone is less than the sheet thickness then integration of the local strains results in the local bending moment:

$$M_B = dx E \int_0^{s_1} \epsilon(z) \left( \frac{s_0}{2} - z \right) dz \quad (2.38)$$

Using equation 2.37 and integrating yields:

$$dM_B = dx E \epsilon_{in} \left( \frac{\pi}{8} s_0 s_1 - \frac{s_1^2}{3} \right) \quad (2.39)$$

From the geometrical conditions it is known that the bending angle is given by the fraction of twice the length of the bent zone and the curvature. From the previously described beam theory the fraction of the transverse bending moment and the Elastic modulus times the moment of inertia yields the inverse of the curvature, such that:

$$\alpha_B = \frac{2l}{R} \quad (2.40)$$

and

$$\frac{1}{R} = \frac{M_B}{EI} \quad (2.41)$$

and

$$dI = \frac{dx s_0^3}{12} \quad (2.42)$$

which leads to the equation for the bend angle:

$$\alpha_b = \frac{\epsilon_{in} l s_1}{s_0^3} (3\pi s_0 - 8s_1) \quad (2.43)$$

where:  $\epsilon_{in} = \alpha_{th} T(0, 0, 0, t) - \frac{k_f}{E}$

To calculate the bend angles with these formulas requires knowledge of the depth of the plastic zone and the length of the plastic zone which may be obtained from the temperature field calculation. The solution to the temperature field was an approximation of the Fourier equation of three dimensional heat conduction for a finite area source. As the length and depth of the plastic zone were required for the solution, the co-ordinates were required as a function of the temperature. An approximate solution in the range relevant to laser bending was used as it was not possible to invert this form of the heat equation in a suitable fashion analytically to give the depth co-ordinate. Details of this approximation can be found in reference.[17]

The depth of the plastic zone was given by:

$$s_1 = -\ln\left(\frac{4T_c}{3N_f} P_f^{-2/3}\right) \frac{\sqrt{2P_f at}}{2} \tag{2.44}$$

and the length of the heated zone was given by:

$$l = P_f \sqrt{4at} \sqrt{-\frac{1}{\sqrt{2P_f}} \ln\left(\frac{4T_c}{3N_f} P_f^{-2/3}\right)} \tag{2.45}$$

This model showed the importance of the thermal conductivity on the process. A slight change in the thermal conductivity changes the thermal expansion and the position of the elastic-plastic interface as the average temperature in the irradiated zone is sensitive to slight changes in the thermal conductivity. Consequently it is possible that the bend angle is sensitive to small changes in the thermal conductivity. This is contrary to what was reported in the two layer model. In addition with this model the contribution of the thermal strain to the plastic bending was found by subtracting the fraction of the yield stress and the elastic modulus from the thermal expansion (see  $\epsilon_{in}$  in equation 2.43). As both the yield stress and the elastic modulus are temperature dependent this required the function which related those parameters to temperature to be known in order to calculate this contribution accurately.

Provided with accurate information about the temperature dependent mechanical properties the model can predict the bend angles with reasonable accuracy for an analytical route, see figure 2.11.

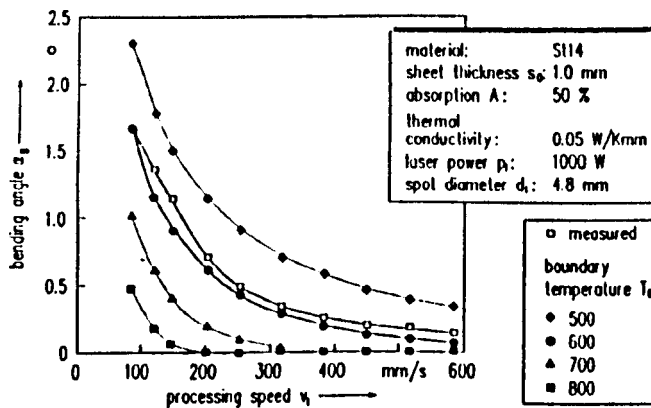


Figure 2.11: Vollertsen’s residual stress model for the TGM

Mucha et al [19] has also modelled the TGM and has provided solutions for rectangular, triangular, elliptical and circular shaped plastic zones, and these shapes depend on the material thermal properties and the laser processing parameters

used. Again the  $yz$  directions (assuming the same co-ordinate system as Vollertsen) are the only directions considered relevant for the analysis.

In common with Vollertsen's model the strain is described in terms of the  $z$  co-ordinate only.

$$\epsilon(y, z) = \epsilon_0(y) + zR(y) \quad (2.46)$$

where  $R(y)$  is the plate curvature. The function  $d(y)$  expresses the relationship between the zone depth  $s_1$  and the  $y$  co-ordinate. Each layer along the  $y$  direction contracts during cooling and it is assumed that outside this zone the strain is equal to zero. The thermal strain inside the zone was then found to be:

$$\epsilon_t(y, z) = -\alpha_{th}\Delta T\Theta(d(y) - z) \quad (2.47)$$

where the Heaviside step function  $\Theta(u) = 1$  for  $u \geq 0$  or  $\Theta(u) = 0$  for  $u < 0$ . The strain of each infinitesimal layer is described by:

$$\sigma(y, z) = E \left[ \epsilon_0(y) + zR(y) + \alpha_{th}\Delta T\Theta(d(y) - z) \right] \quad (2.48)$$

The equilibrium conditions for each layer of the plate are:

$$\int_0^{s_0} \sigma(y, z) = 0 \quad (2.49)$$

$$\int_0^{s_0} z\sigma(y, z) = 0 \quad (2.50)$$

Therefore:

$$\epsilon_0(y) = -\alpha_{th}\Delta Td(y) \left( 4s_0 - 3d(y) \right) \frac{1}{s_0^2} \quad (2.51)$$

$$R(y) = 6\alpha_{th}\Delta Td(y) \left( s_0 - d(y) \right) \frac{1}{s_0^3} \quad (2.52)$$

Mucha then presents equations for different shaped plastic zones determined by the function  $d(y)$ . The formulas for the bend angles for the different shaped plastic zones were found to be:

Rectangular:

$$\alpha_b = 6\alpha_{th}\Delta T l s_1 (s_0 - s_1) \frac{1}{s_0^3} \quad (2.53)$$

Triangular:

$$\alpha_b = \alpha_{th}\Delta T l s_1 (3s_0 - 2s_1) \frac{1}{s_0^3} \quad (2.54)$$

Elliptical:

$$\alpha_b = \alpha_{th}\Delta T l s_1 (3\pi s_0 - 8s_1) \frac{1}{2s_0^3} \quad (2.55)$$

Circular:

$$\alpha_b = \alpha_{th}\Delta T s_1^2 (3\pi s_0 - 8s_1) \frac{1}{s_0^3} \quad (2.56)$$

The temperature was then calculated from the solution for a moving point source (taken in [19] from Duley [26]):

$$T(x, y, z) = Ap_1 \exp(-v_1(r + y)/2\kappa)/(2\pi kr) \quad (2.57)$$

where:

$$r = (x^2 + y^2 + z^2)^{\frac{1}{2}} \quad (2.58)$$

$\kappa$  is the thermal diffusivity,  $k$  is the thermal conductivity and  $Ap_1$  is the absorbed laser power.

Then the bending angle was found for the case of semi-circular isotherms by introducing dimensionless variables for laser power and traverse velocity into the temperature field equation.

Dimensionless power:

$$Q = \frac{Ap_1}{(2\pi k \Delta T s_0)} \quad (2.59)$$

Dimensionless velocity:

$$S_{vl} = \frac{v_1 h}{2\kappa} \quad (2.60)$$

where  $D = s_1/s_0$  and  $R_{dim} = r/s_0$ . Introducing these enabled the calculation of

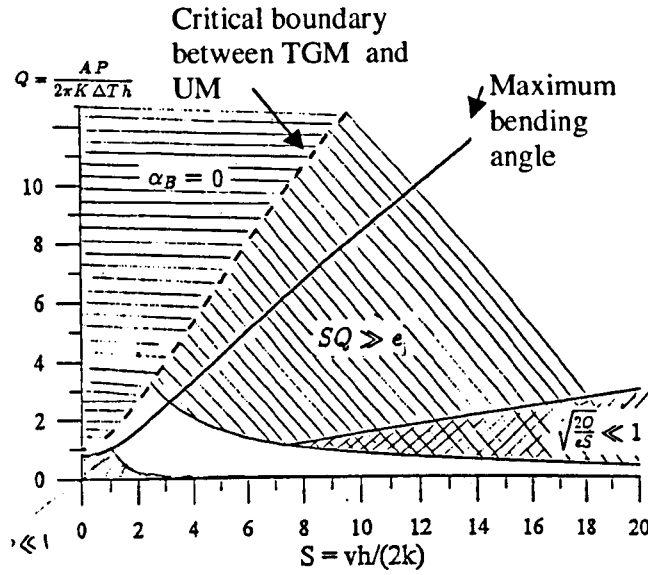


Figure 2.12: Critical operating region for temperature gradient mechanism

the maximum depth of an isotherm, and the bend angle was finally given by:

$$\alpha_B = \alpha_{th} \Delta T D^2 (3\pi - 8D) \tag{2.61}$$

The usefulness of this model is found in the trend it presents between the dimensionless laser power and traverse velocity and the resulting bend angle (see figure 2.12). This assists with determining the critical conditions which give rise to the temperature gradient mechanism. However this analytical route in common with the previously described models calculates the bend angle at the end of the process and does not describe the transient stages. A knowledge of the transient stages is useful for successful process control.

### 2.5.3 The buckling mechanism

As described previously the requirements for the initiation of the BM on sheet metal are that the laser beam diameter on the surface of the sheet is approximately an order of magnitude greater than the sheet thickness and that the material has a suitable thermal conductivity so that the laser processing parameters employed do not result in a temperature gradient in the depth direction of the sample. Using the large beam diameter results in a large amount of thermoelastic strain which initiates the growth of an elasto-plastic buckle. The strain near the centre of the laser beam is plastic and the strain away from the centre of the beam is considered elastic in Vollertsen's model. [22] The elastic strain is released when the laser beam traverses the exiting edge of the sample, and the plastic strain results in a

curvature and a bend angle. The model is derived from the geometrical conditions. Consider figure 2.13. The bend angle is given by:

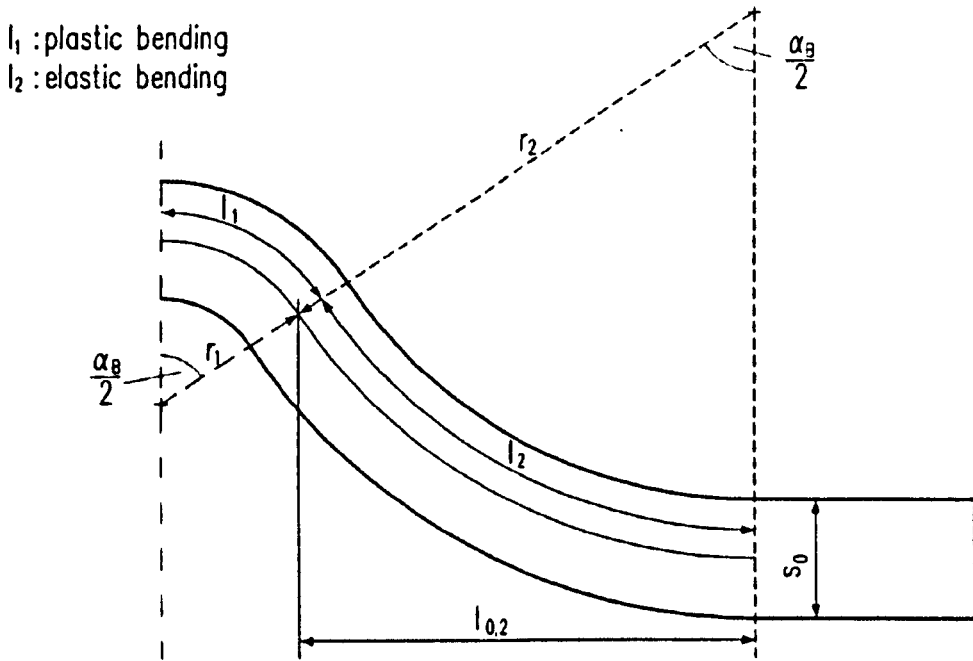


Figure 2.13: Model geometry for the buckling mechanism

$$\frac{\alpha_B}{2} = \frac{l_1}{r_1} = \frac{l_2}{r_2} \quad (2.62)$$

The radius  $r_2$  in region 2 is given by elastic bending theory:

$$M_{el} = Ebs_0^3/12r_2 \quad (2.63)$$

and for the region 1, i.e. the plastic zone

$$M_{pl} = \frac{1}{4}k_f(T_1)bs_0^2 \quad (2.64)$$

At the elastic plastic interface  $M_{el} = M_{pl}$  and  $r_2$  reduces to:

$$r_2 = \frac{Es_0}{3k_f(T_1)} \quad (2.65)$$

$l_2$  is then calculated from the new geometry:

$$l_2 = l_{0,2} + \Delta L \quad (2.66)$$

where:

$$l_{0.2} = r_2 \sin\left(\frac{\alpha_B}{2}\right) \quad (2.67)$$

and

$$\Delta l = \alpha_{th} \overline{\Delta T} l_h \quad (2.68)$$

where  $\overline{\Delta T}$  is the average temperature of the heated zone of dimensions  $l_h$ ,  $\Delta x$  and  $s_0$ .  $\overline{\Delta T}$  is calculated from the absorbed laser power  $Ap_1$ , the processing velocity  $v_1$ , and the heat capacity  $\rho c_p$  of the material.

$$\overline{\Delta T} = \frac{Ap_1}{2c_p \rho s_0 v_1} \quad (2.69)$$

$l_2$  may then be calculated from:

$$l_2 = r_2 \sin\left(\frac{\alpha_B}{2}\right) + f' \alpha_{th} Ap_1 / 2c_p \rho s_0 v_1 \quad (2.70)$$

$f'$  is the fraction of the thermal expansion that leads to an expansion of region 2. Using a value of 0.5 results in:

$$\frac{\alpha_B}{2} = \sin\left(\frac{\alpha_B}{2}\right) + \frac{3\alpha_{th} Ap_1 k_f(T_1)}{4E s_0^2 c_p \rho v_1} \quad (2.71)$$

Using the sine series expansion the last expression for the bend angle was simplified.

The final equation for the bending angle is:

$$\alpha_B = \left[ 36 \frac{\alpha_{th} k_f(T_1)}{c_p \rho E} \frac{Ap_1}{v_1} \frac{1}{s_0^2} \right]^{1/3} \quad (2.72)$$

Of note here is the much lower dependency of the bend angle on the temperature gradient, in this case the exponent  $n$  is only 1/3. Experimental data in chapter 5 will be compared with this exponent.

#### 2.5.4 The upsetting mechanism

Kraus has modelled box section laser bending. Using the upsetting mechanism box sections or extrusions can be made to bend out of plane by careful selection of the sequence of irradiations. A similar approach has been used to Vollertsen's models where a geometry / strain relationship is drawn between the processing

parameters and the bending angle. The final equation describing the bend angle in this case was found to be :

$$\alpha_b = \frac{1}{b} \left[ \frac{2\alpha_{th} A_{I_2} b}{v_l c_p \rho (2d_l s_0 - s_0^2)} - \frac{k_f(T_1) d_1}{E(T_1)} \right] \quad (2.73)$$

The model assumed that three of the four sides of the box section were heated simultaneously to initiate the bending. In reality the sides are usually irradiated sequentially. However for the purposes of an analytical model this effect would be very difficult to include. Numerical studies into the sequence of irradiations in extrusion bending have also been carried out by Kraus using finite element methods [23]. These studies and other author's numerical work are reviewed later.

## 2.6 Mathematical Models - Numerical

Given the complexity of analytically modelling forming processes such as laser bending where the workpiece temperatures, dimensions, and properties are changing both in time and space and which depend on many variables, the numerical approach is often more beneficial for modelling these situations. The improvement in computational efficiency in recent years has made such large scale numerical studies more viable. Numerical models have been available for a number of years for the flame forming process.[24, 28, 29, 30, 31] However it is only in recent times that emphasis has been placed on laser bending.

### 2.6.1 Temperature Gradient Mechanism (TGM)

Vollertsen developed a finite difference model [14, 32] for a two dimensional (2-D) analysis of the process. The temperature dependent material parameters were included in the model by taking values at particular temperatures of interest and linearly interpolating between them, and then those functions were used to relate the temperature to the material properties. A rectangular shaped source was used to represent the laser beam and the resultant two dimensional temperature (2-D) field was used to calculate the thermal expansion, strains and stresses in the elements. Then accounting for the stiffness of the whole sheet a calculation was made to assess in which elements the stress exceeded the temperature dependent yield stress. Then the elastic strain in those elements was reduced by the amount that exceeded the yield stress.

The amount of strain that exceeded the maximum elastic strain at the yield stress was converted into a plastic strain. A loop was initiated which continued

with this calculation until there was equilibrium of forces and moments. After the thermal field had finished being computed, the bending angle was calculated from the length of the upper and lower layers of an element in conjunction with the sheet thickness. This model provided a very fast means to calculate the effects of various process parameters, but the simple boundary conditions limiting this approach led to the modelling with the finite element method (FEM), see also reference. [33]

In Alberti et al's model [34] of the TGM the finite element method was used first to evaluate the temperature field and then the results of this analysis were inputted to the mechanical analysis. Illustrations for the temperature field and the deformation were provided at various stages of the process. Emphasis was placed on the importance of the temperature dependence of the yield stress of the material. A constant decay law was assumed for the relationship between increasing temperature and decreasing yield stress. Steel plates were considered in the analysis. Another numerical simulation by the same author looked at the combined process of thermal and mechanical bending. Details of this work can be found in reference.[35] As this is a combined process and not solely laser bending no further details are given here.

Hsiao et al have used the commercial package ABAQUS to model the process. They used the modelling in their work to emphasise the importance of the specimen size.[10] Their results state that the angular distortion obtained on a short specimen is much smaller than for a long specimen. This agrees with experimental results by Vollertsen.[14] They also studied the effect of the fraction of the laser power and the square root of the velocity times the plate thickness as a parameter:

$$\frac{p_1}{s_0\sqrt{v_1}} \quad (2.74)$$

In conjunction with this study Firth et al have used the code TOPAZ3D/NIKE3D for analysis. Details of their analysis can be found in. [4] Results from this study were compared with experimental results and it was reported that the model predicted the trends correctly, but the absolute angles predicted were considerably smaller (about a factor of 3) in some cases.

## 2.6.2 Buckling Mechanism (BM)

In work by Holzer et al [36] the BM was modelled using the commercial finite element package ABAQUS. Here it was assumed that the sheet was flat and free of residual stresses. The elements used in ABAQUS to model the heat yield were DC3D8 (8 -node cubic heat diffusion elements) and the stress analysis used C3D8 elements. A user defined FORTRAN function was used to model the heat input.

The intensity at the centre of the TEM<sub>00</sub> gaussian beam was given by:

$$I_0 = \frac{2p_l A}{\pi r_1^2} \tag{2.75}$$

where  $I_0$  is the laser beam intensity at the centre of a TEM<sub>00</sub> laser beam,  $p_l A$  is the absorbed power and  $r_1$  is the laser beam radius.

The intensity at a distance  $r$  from the centre of the laser beam was given by:

$$I(R) = I_0 e^{-\frac{2r}{r_1}} \tag{2.76}$$

Figure 2.14 illustrates the development of the bending angle from this analysis [36]. It is shown at times 0.88 s, 126 s, and at the end of the process. In figures 2.15 and 2.16 [36] the distributions of the upper and lower surface temperatures, and the elastic and plastic strains are shown. As may be seen in the case where the sheet bends in a convex direction away from the laser beam the plastic strain at the non irradiated side of the sheet is greater. [36]

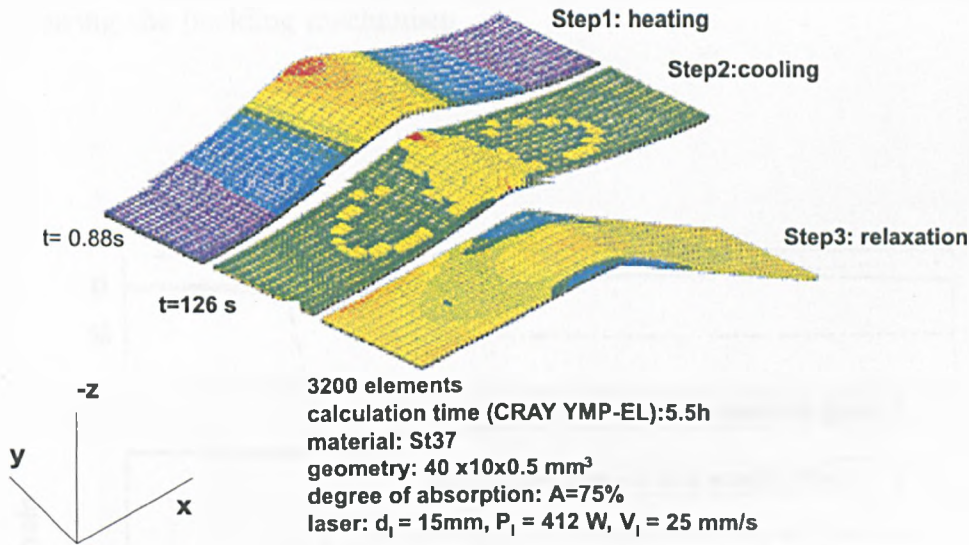


Figure 2.14: Development of the bending angle during the buckling mechanism

### 2.6.3 Upsetting Mechanism (UM)

Kraus has carried out a finite element analysis into extrusion forming. [17] Important information about the temporal development of the process resulted from this work which could not be determined experimentally. For example during the cooling phase a contraction in the irradiated zone takes place, and tensile stresses build up if the thermal contraction is hindered by the surrounding material and the workpiece stiffness. These stresses can reach the yield stress depending on

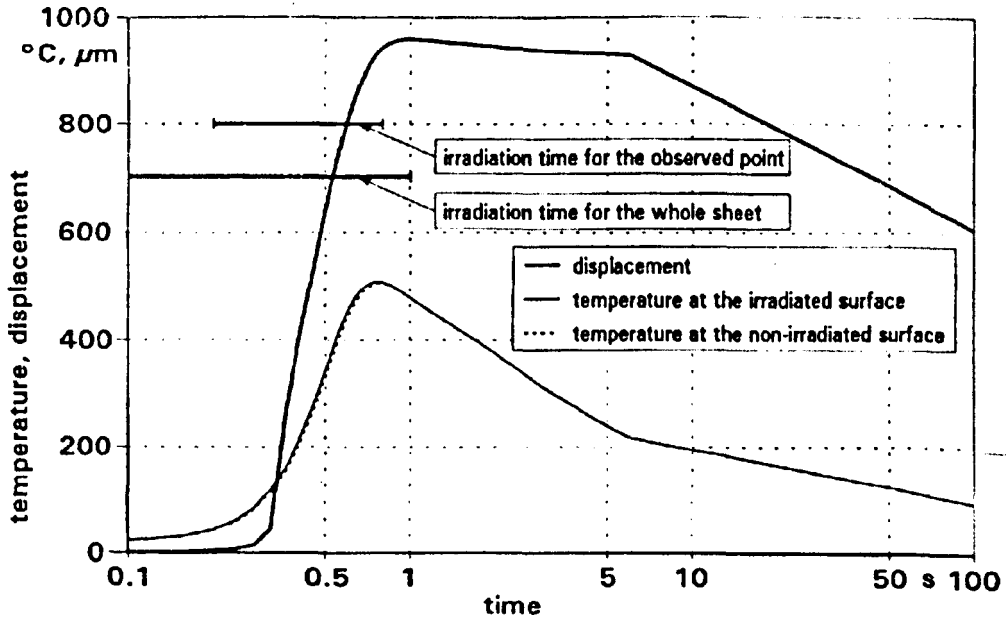


Figure 2.15: Distribution of upper and lower surface temperatures and displacements during the buckling mechanism

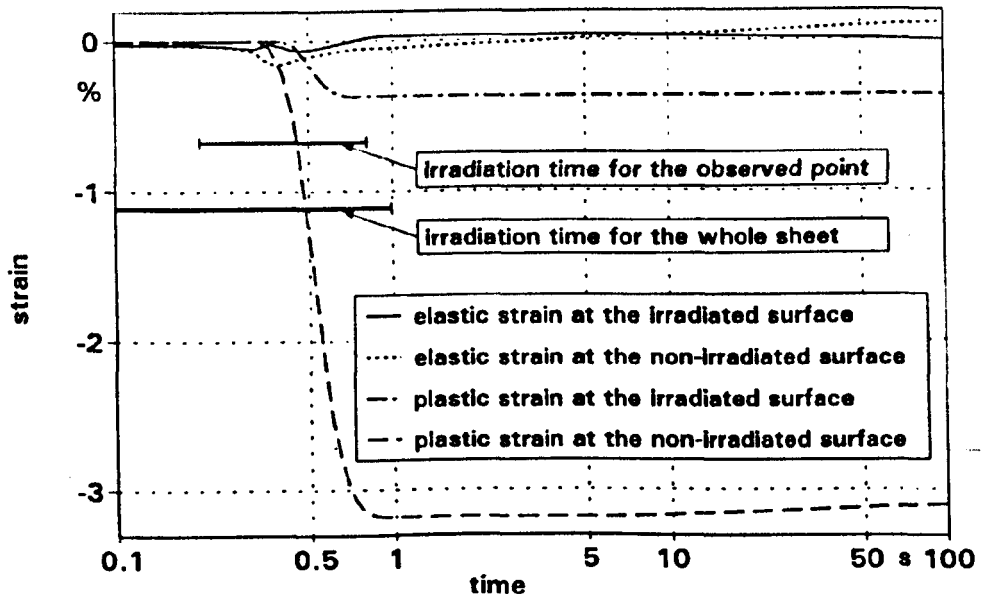


Figure 2.16: Distribution of upper and lower surface strains during the buckling mechanism

the process parameters employed and a plastic restraining may occur (see figure 2.17). This effect is particularly noticeable in extrusion bending where the moment

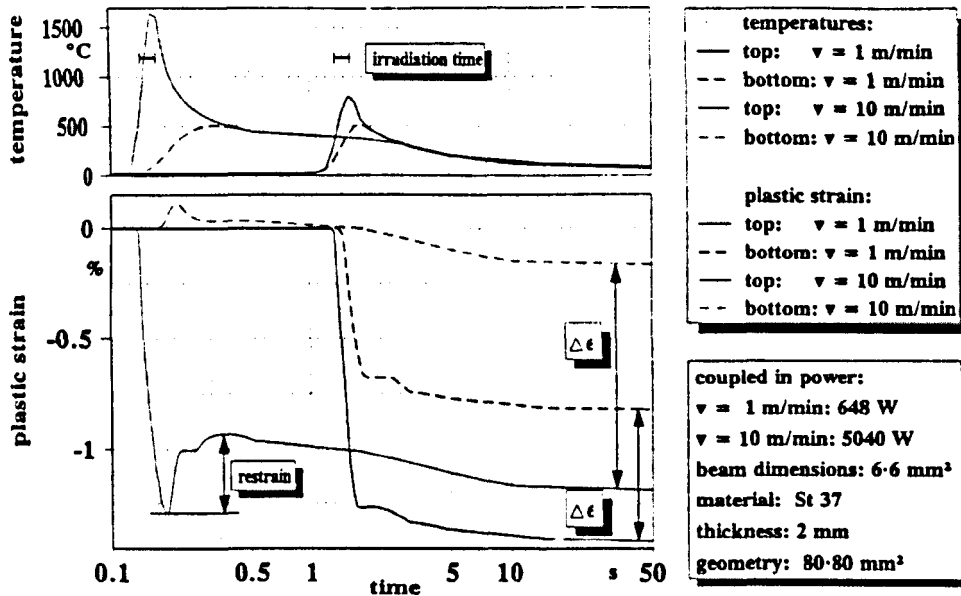


Figure 2.17: Plastic restraining in extrusion bending

of inertia of the workpiece is high. From this analysis Kraus found that there is an upper limit to the plastic strain which should be induced in order to minimise plastic restraining. The sequence of irradiations was also optimised using the finite element method (FEM).

## 2.7 Previous experimental work

The following sections summarise important experimental work that has been carried out to date in the field of laser forming. Empirical work has been carried out primarily for fundamental investigation. This has been done to verify mechanisms of laser forming and to determine materials effects on the bending process.

### 2.7.1 Operating maps - Bend angle dependence on power and processing Speed

In 1985 Namba [37] published one of the first experimental papers on laser forming. Materials investigated in this work included Ti, Al, AISI 304 stainless steel and carbon steel. The materials were irradiated with a 1.5kW CO<sub>2</sub> laser using a defocused beam with traverse speeds in the range of 5 - 15m/min. Namba claimed

that the deformation is caused by the steep thermal gradient which results in thermal expansion, thermal stress and plastic deformation. The following parameters were described as affecting the bend angle: [37]

- (a) Incident laser beam power
- (b) Laser beam diameter
- (c) Power density distribution of the laser beam
- (d) Absorptivity of laser beam on a material surface
- (e) Scanning speed of laser beam
- (f) Number of repetitions of laser beam scans
- (g) Density of the material, specific heat capacity of the material
- (h) Thermal expansion coefficient
- (i) Yield strength
- (j) Young's modulus
- (k) Poisson's ratio
- (l) Strain hardening coefficient
- (m) The dimensions of the workpiece
- (n) The melting temperature of the material and the fracture strength of the material.

In 1987 Scully determined that the bend angle is equal to the fraction of the Power and the square root of the traverse speed times the plate thickness. [38] That relationship was taken from earlier work by Masubuchi et al [39] on flame forming.

$$\alpha_B = \frac{p_1}{s_0 \sqrt{v_1}} \quad (2.77)$$

Later work in 1994 by Vollertsen has shown that there is a strong linear dependence of the bend angle on the laser power as shown in figure 2.18. The dependence of the bend angle on the processing speed has been reported in further work by Vollertsen as well. [14] In the experiments carried out a power law was assumed between the bend angle and the processing speed. The experimental data is plotted in double

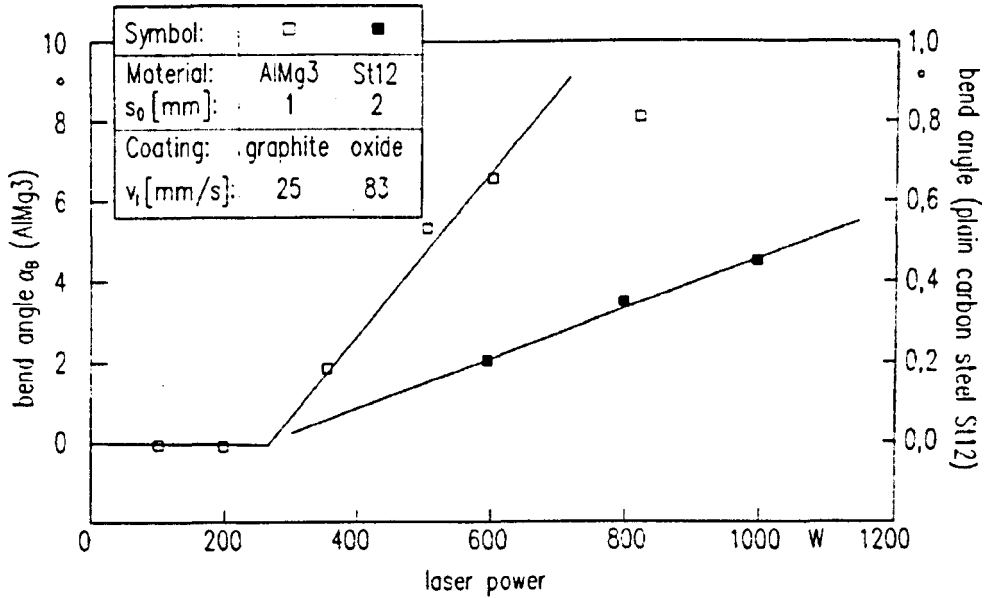


Figure 2.18: Bend angle dependence on laser power

logarithmic form. A linear dependence was obtained for 3.5mm sheet with scanning speeds in the range 7 -70 mm/s. The slope of the graph is  $-0.63$ , (refer to figure 2.19). Analytical model correlation with this is of the order of 63 percent [14], a slope of  $-1$  is expected from the analytical model. The bending angle was related to the processing velocity by:

$$\alpha_b \propto v_1^{-0.63} \tag{2.78}$$

The expected slope is derived from the notion that the increase in processing speed decreases the coupled energy. As the bend angle is proportional to the coupled energy it is expected that the bend angle should decrease linearly with increasing speed [14]. From Fig 2.20 it is obvious that this is not the case. It can be seen that the bend angle continues to increase with increasing traverse speed. This behaviour may be attributed to the fact that the temperature gradient is increased with increasing velocity and the time for heat conduction in the depth direction of the sheet is reduced. Ultimately this results in the difference of the plastic strains between the upper and the lower layer of the sheet being more pronounced and a greater bend angle per unit time may be achieved. Of course if the velocity is increased to a very high value then the temperature increase will be small and only an elastically reversible bending may occur. Also of note is the threshold energy for the process. It has been shown that no plastic deformation occurs below a given energy input. Therefore the boundary energy which will

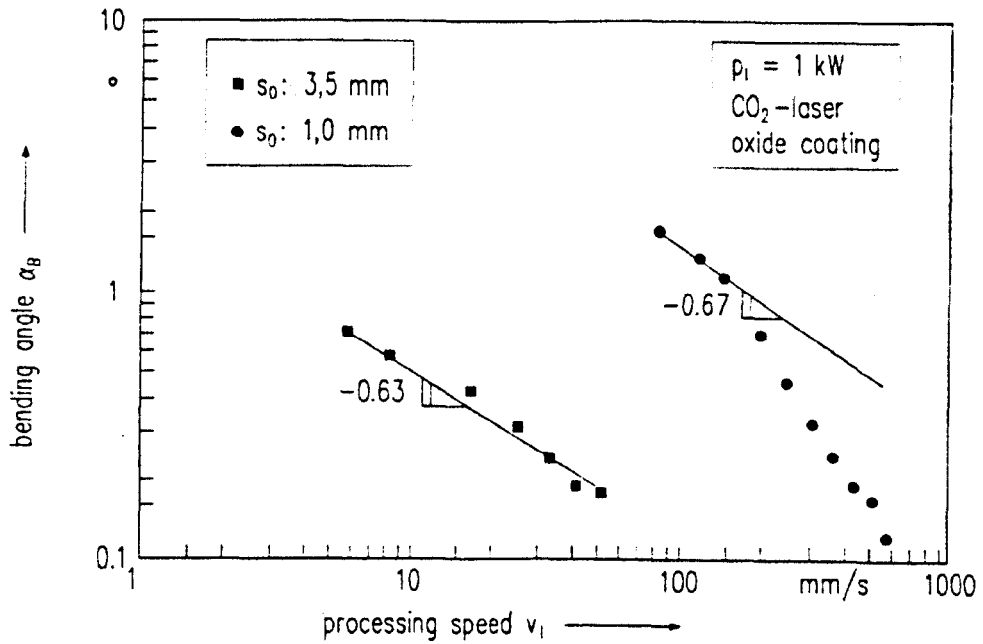


Figure 2.19: Bend angle dependence on processing speed, TGM

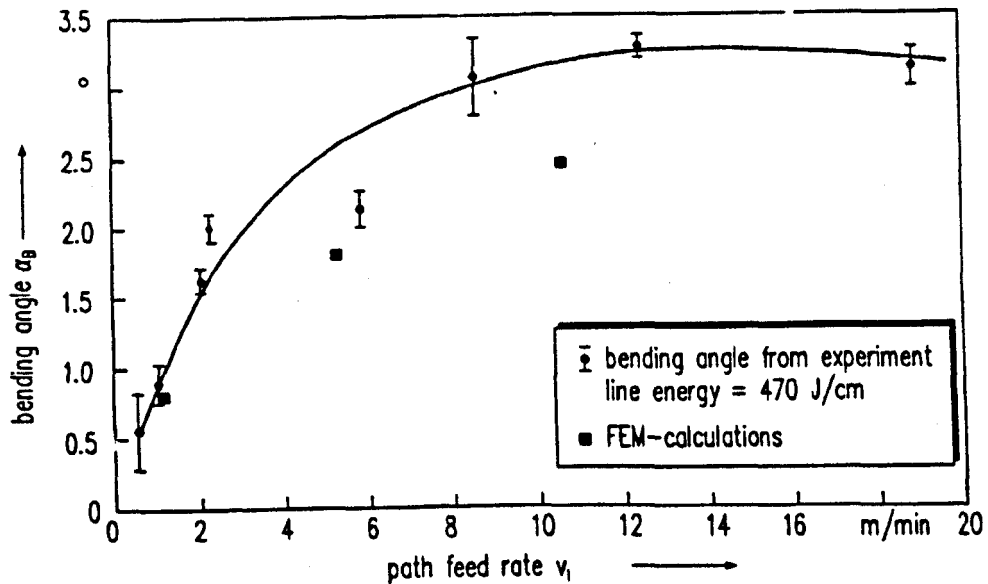


Figure 2.20: Increase of process efficiency with increasing processing velocity, TGM

Boundary temperature	(K)
Pure Aluminium	22
Aluminium Alloy	94
Pure Copper	32
Iron	49
Molybdenum	26
Low Alloyed Steel	71
Titanium	164

Table 2.1: Boundary temperature increase for plastic yielding

produce the onset of bending can be related to the temperature the material must reach at the limit of the thermal strain at the yield point stress [14]. Empirical analysis yields the temperature increases in table 2.1 for the given materials.

### 2.7.2 Bend angle dependence on thermal and thermal-mechanical properties

The thermal conductivity of the workpiece material is of vital importance in laser bending. The thermal conductivity determines the temperature field and hence the development of the thermal strain. If a material is a good conductor it is unlikely that a thermal gradient of sufficient magnitude can be created to initiate the bend with the temperature gradient mechanism unless the heat can be put into the sheet sufficiently fast. In general it is better that the material should be a relatively poor conductor in order for the temperature gradient mechanism to occur.

The role of the temperature gradient on the buckling and upsetting mechanisms is slightly different. [14] If the workpiece material has a high thermal conductivity then the size of the irradiated area will increase rapidly thus decreasing the average temperature of the material, the plastic straining and hence the bend angle. The distinction is drawn as forming will still occur for the latter mechanisms but no bending will occur in the former case if the temperature gradient is diminished to a large extent by a high thermal conductivity. (refer to figure 2.21) The effect has been physically modelled by Vollertsen. [14] It is considered of great importance not only due to the previously described factors but also due to the fact that the strength of the material changes with differing thermal conductivities. The conductivity can be related to the age hardening state of the material. The age hardenable state then has a role in influencing the thermal conductivity and the elastic reversible bending of the material, and ultimately the bend angle. Clearly there are complex dependencies for the thermal conductivity. The influence of the

thermal conductivity according to the literature is shown in figure 2.22. A physical

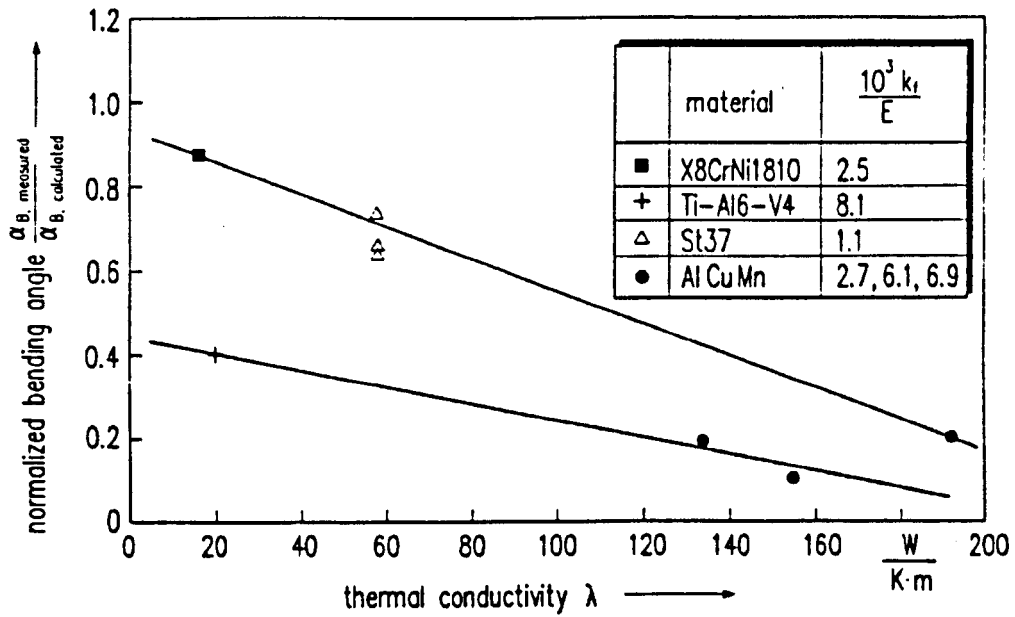


Figure 2.21: Influence of the thermal conductivity on the bending angle

model which uses the Fourier number shows that the temperature field is similar for similar Fourier numbers.

$$F_o = \frac{\kappa t}{x^2} \quad (2.79)$$

where:  $F_o$  is the Fourier number,  $\kappa$  is the thermal diffusivity,  $t$  is time and  $x$  is a length.

$$\kappa = \lambda / c_p \rho \quad (2.80)$$

where:  $\lambda$  is the thermal conductivity,  $c_p$  is the specific heat capacity and  $\rho$  is the mass density. The time,  $t$ , is given by the fraction of the length  $x'$  and the processing speed,  $v_1$ .

$$t = x' / v_1 \quad (2.81)$$

Combining  $x$ ,  $x'$ ,  $c_p$  and  $\rho$  into a constant  $c$  yields:

$$F_o = \frac{\lambda c}{v_1} \quad (2.82)$$

Using this model if the temperature field is altered by increasing the thermal conductivity or decreasing the scanning speed the effect of the increasing thermal conductivity can be approximated by the decreasing scan speed and holding the

power constant. The power is held constant by increasing it linearly with the increasing scan speed. Figure 2.22 illustrates this effect [14]. The material used was St37 steel, 2mm gauge, with a traverse speed of up to 320 mm/sec. The model as described above yielded a bend angle of 4 degrees for the given laser parameters. Experiments at the highest traverse speed were assumed to approximate the real thermal conductivity in this work. When lower traverse speeds were employed the higher thermal conductivities resulted.

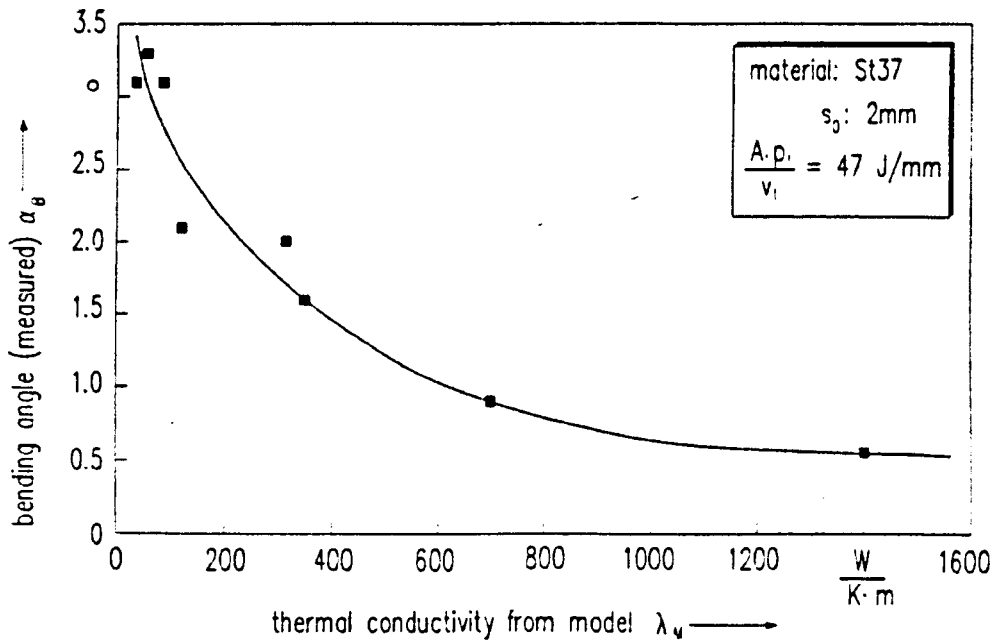


Figure 2.22: Physical model of the influence of the thermal conductivity on the bend angle

In figure 2.23 the influence of the fraction of the coefficient of thermal expansion and the specific heat times the mass density is plotted against the bend angle. This shows the influence of the material parameters on the bend angle. This is useful as the two layer model [16] assumes a relationship between these parameters of the form:

$$\alpha_b = \frac{c_1 \alpha_{th}}{c_p \rho} \quad (2.83)$$

The amount of forming depends critically on the thermal expansion. The thermal expansion is determined from the temperature increase and the coefficient of thermal expansion and the temperature increase of a volume is indirectly proportional to the volumetric heat capacity. [14] Using this analysis Vollertsen produced figure 2.23.

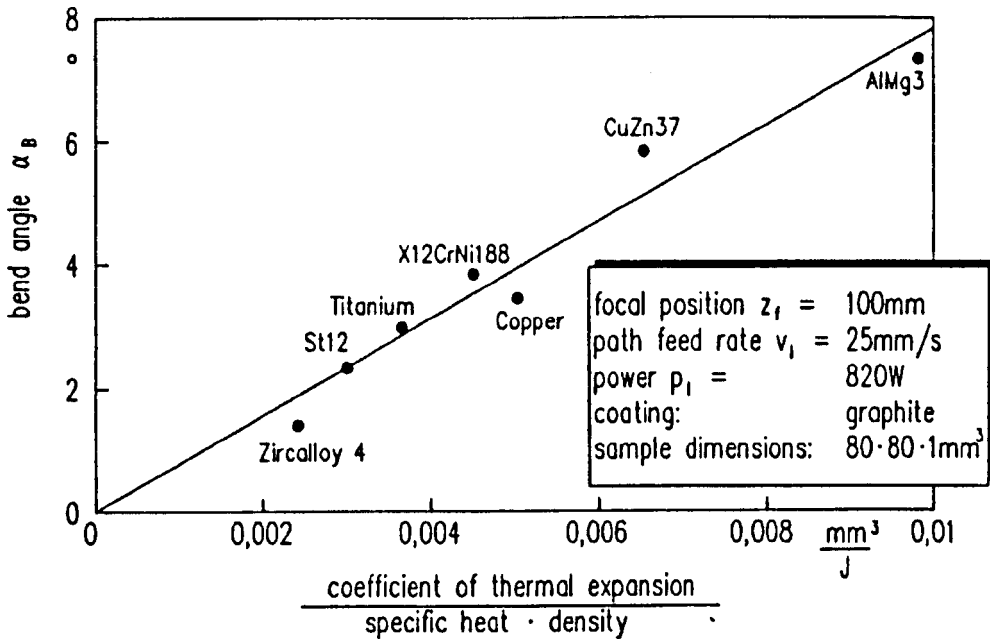


Figure 2.23: Increase of the material thermal properties on the bend angle

### 2.7.3 Development of temperature field and plastic strain

An early program in laser forming was that of the Laser line Heating (LLH) which formed part of the Navy Manufacturing Technology program (ManTech) in the U.S.A. The material investigated in this program was heavy duty 6.25 - 25 mm mild steel plate. [38] Important results from this work shows how the temperature changes as a function of time for the given material and how the micro strain changes as a function of time also. The micro strain was obtained by means of strain gauges mounted on the bottom of the plate surface. Scully noted the change in the strain between the heating and cooling cycles as shown in figure 2.24. The primary process parameters required for accurate control were identified as the laser power  $P$ , the traverse velocity  $V$ , and the plate thickness  $t$ . The Temperature Gradient Mechanism, although not specifically named was described as the driving force behind the bending in this instance. Vollertsen has studied the temporal development of the bend angle experimentally. Figure 2.25 illustrates this. It is in agreement qualitatively with the results by Scully described above.

### 2.7.4 Material and Metallurgy work

Scully reported that Masubuchi has reported a summary of a metallurgical analysis of the irradiated material.[38] This work forms part of an internal report at M.I.T. A series of Charpy V-notch tests was carried out on HY-80 steel. These tests were used to determine toughness, a micro hardness test was used to analyse the tensile

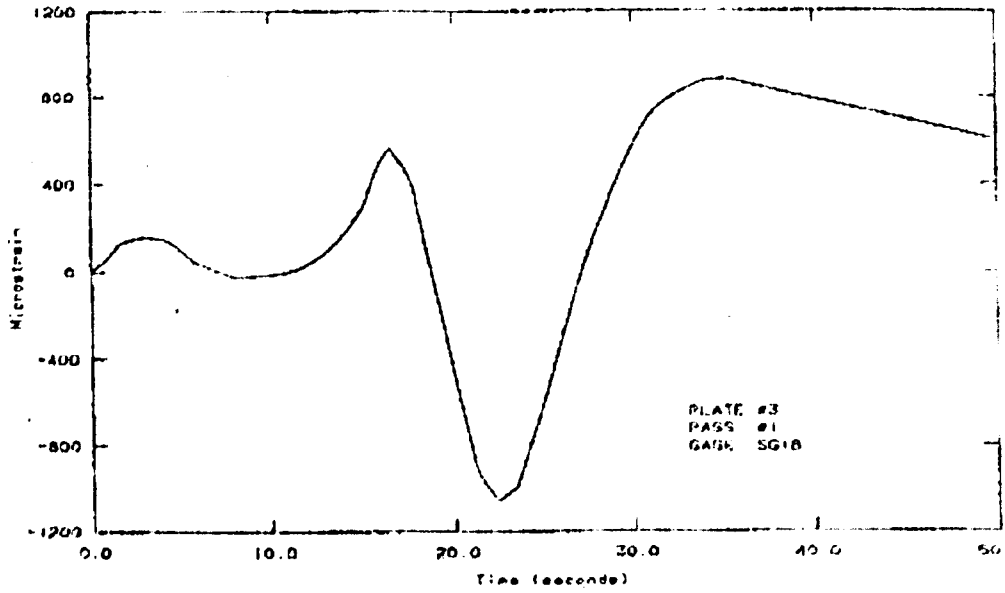


Figure 2.24: Time run of the strain development

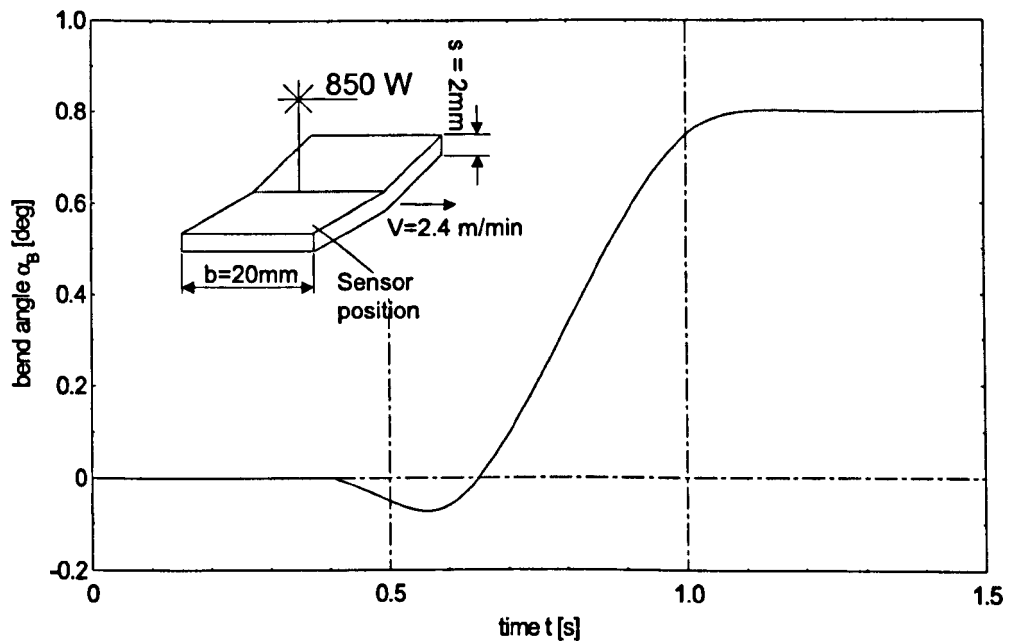


Figure 2.25: Time run of the bend angle

strength of the samples and optical microscopy was used to characterise the crystal structure and fracture surfaces present in the material. The fracture toughness of the heat affected zone is reported lower than that of the non - irradiated material.

A linear relationship between the number of passes over an identical track and the resultant bend angle is reported in this work. In later work the linear dependency of the bend angle on the number of passes has not been found for a range of materials.[40] Sprenger showed that there is a decreasing bend angle rate with increasing scans due to the strain hardening of the material. As the sheet deforms the outside of the bend cold works and the orientation of the dislocations in the material are changed. This results in strain hardening and each successive pass of the laser will increment the bend angle by a smaller amount than the previous scan. The work showed that the change in volume along the bend edge of the workpiece decreased the bend angle rate for subsequent scans. The coefficient of absorption changed and the bend angle achievable with further scans decreased. These influences are summarised next.

(a) Effect of the change in thickness along the bend edge

As described by Namba [37] the upper layer thickens as the material plastically compresses. The thermal expansion which is converted into plastic deformation is not cancelled during cooling and a bend angle results. However as the material has thickened due to the plastic compression the modulus of the section is augmented and for the same laser parameters for subsequent scans the angle achievable will diminish each time.

(b) Effect of strain hardening of the material

In materials with a large strain hardening coefficient and which are relatively thick it has been shown that the cold working of the underside of the sheet which causes strain hardening contributes significantly to the decreasing bending rate. Cold work occurs when the temperature gradient mechanism plastically compresses the upper layers of the sheet by thermal strain and cold works the outside of the bending edge. Cold working increases the strength of the material. In Sprenger's work it was shown that for AA2014 and for Ti6Al4V in the mill annealed condition that the lower layers of the sheet exceed the elastic limit after the fifth irradiation and the bend angle showed a greater linear dependence on the number of scans prior to this [40]. With subsequent passes the material will strain harden from the outside layer, layer by layer to the neutral layer of the material. The layer between the neutral layer and the heated layer is plastically compressed as well and consequently strain hardened. Figure 2.26 shows the decreasing

bend rate. Sprenger determined a parametric relationship for this behaviour

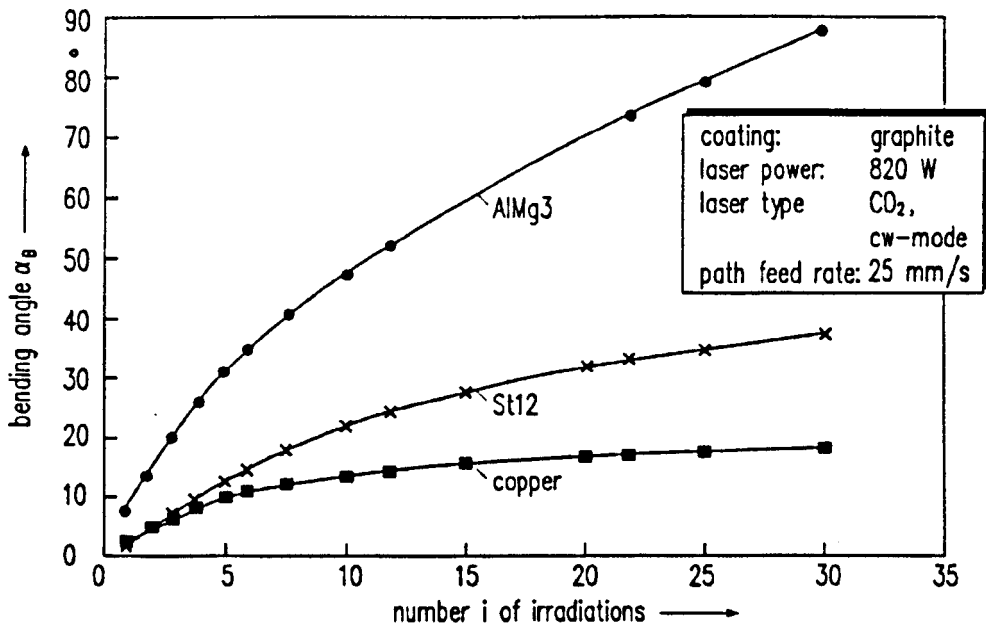


Figure 2.26: decreasing bend rate with increasing scans over an identical track

of the form:

$$\alpha_b \propto N^{c_{total}} \tag{2.84}$$

where:

$$c_{total} = -0.52n + \left[ 0.81 \frac{s_0^{-0.83}}{s_1^{-0.83}} \right] \tag{2.85}$$

and  $s_1 = 3mm$ . Sprenger obtained this expression for evaluating the bend angle after  $N$  scans of the beam. Assuming the absorptivity can be held constant, it yields a regression constant  $c_{total}$  which can be used with equation 2.84 to obtain the bend angle.

### 2.7.5 Bend angle dependency on geometry of workpiece

It has been shown that the thickness of the sheet is one of the major variables in the development of the bend angle. The bend angle is related linearly to the inverse of the square of the sheet thickness for the temperature gradient mechanism.[14] The volume of material to be heated increases with increasing thickness of the sheet. Even with one nominal thickness the thickness of the sheet increases with each pass. The increasing thickness is due to the plastic compression of the uppermost layer of the sheet.

The length of the bending edge is also of significance for the development of the bend angle. If the length of the bending edge is increased from 5 to 13 mm then the bend angle is increased by a factor of 3[14]. This is due to the changing section modulus with changing length and the difference in the temperature field due to the change of length in the lateral direction. The length of the bending leg also affects the bend angle achieved per unit time.

If the bending leg is short then the cooling of the workpiece is restricted to one side [14] and the temperature gradient decreases and hence the bending decreases. If the bending leg is long then the gravitational forces acting on the length will affect the bend angle. The weight of the leg results in tensile stresses in the surface of the sheet thus reducing the compressive stresses from heating and diminishing the bend angle.

Secondary geometrical effects were reported by Scully et al. [37] Less distortion occurs near the edges of plates according to this work. This is because the heat flow pattern is altered in comparison to the innermost part of the plate where the heat flow is to surrounding material. This results in less distortion near the edge of the workpiece. [38] This was also attributed to the rigidity of the plate becoming non symmetric near the plate edge. These effects have not been investigated in depth.

## **2.8 Applications of laser bending**

The range of uses for laser forming is growing steadily. Applications in industry can already be found in the production of electronics [8, 12] and in the straightening and aligning of automobile panels and structures[11]. In the following sections a brief overview of developed applications and a summary of the suggested applications is presented.

### **2.8.1 Primary forming operations**

The first application based laser forming research was found in primary forming. It was a natural progression that the laser should be investigated as a means of performing the tasks that flame forming is used for.

#### **Ship fabrication work**

Some research programs were set up to investigate the forming of ships panels and structures. Much of the flame forming research on ship work stems from Japan[28, 30, 31] In 1980 Masubuchi at M.I.T suggested using a high power laser

beam for this forming task[39]. Since the late 70's research programs with the US naval research have taken place. In Scully's paper [38] an investigation was made into using the laser as a line heat source for bending ships hull plate as a replacement for the conventional line heating process by flame. The reason for the interest in the application was the high controllability of the laser beam in comparison to the largely empirically understood flame heating method which is only viable using skilled operators.

Results from this study indicated that the method was very effective for forming steel plates, especially with thickness in the range of 6.25 to 12.50mm. The major advantages reported in comparison to the conventional flame heating used for forming hull plate included the accuracy and controllability of the heat source, and minimal material degradation as the material conformed to the U.S Military Specification MIL-S-16216J for high strength steel plates after laser processing. In conclusion Scully describes the process as most suitable for final processing of parts and that the bulk of the forming should be carried out by conventional methods, i.e. accurate forming in the final stages of production.

### Pipe and Tube Forming

Frackiewicz has presented laser formed pipe geometries which are difficult to form conventionally (see figure 2.27). The range of modifications include changing the shape of the pipe locally around the circumference, and bending the pipes out of plane.[18, 41] The range of materials that the process can be applied to is cited as extensive and the process is described as being suitable for processing hard and brittle alloys too[18, 41]. Frackiewicz has filed patents for the process in Poland, in 5 European Community (EC) countries (European patent application 0317 830 A2.- 1988 in[18]) and in the USA (US PAT. 5,228,324) [41]. Frackiewicz was one of the first authors outside Japan and America to investigate the process.

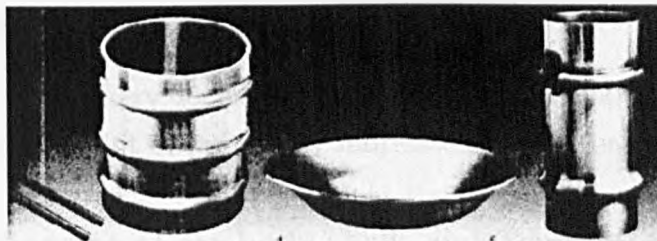


Figure 2.27: Pipe and Tube forming

### Dish or Spherical Cap shapes

Some authors have investigated the possibility for forming a bowl shape [10, 42] from sheet and plate material. The bowl has been investigated primarily as a case study for establishing some basic information about axi-symmetrical three dimensional (3-D) laser forming. Successful irradiation strategies have not yet been developed which satisfy the symmetry requirement totally, but progress is being made and it is an aim of the present work.

### Rapid prototyping

Vollertsen has presented some rapid prototypes of a lamp housing produced by laser cutting and then laser bending, and of spatially laser forming a spoon shape. The advantage reported for the technology in that work is that for prototyping no "hard-tools" are required to be produced, and this could be a time and cost saving technology at the prototyping stage. [43] Klocke et al has demonstrated using laser bending for rapid prototyping of an engine bracket and an air exhaust component [44](figure 2.28) that would have required special tooling to be manufactured had these operations been carried out conventionally. The part was laser cut and then laser bent which enhanced the process flexibility through the reduction of the number of set-ups required to produce the final component.

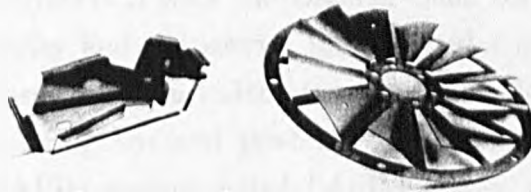


Figure 2.28: Examples of laser formed rapid prototypes

### 2.8.2 Secondary forming operations

In addition to the primary forming operations the laser could prove useful for adjustment and alignment of previously fabricated components.

#### Flexible straightening of car body shells and Tensioning of saw blades

The former project looked at the use of laser forming for the correction of post welding distortion in structural parts of car body shells, for example the 'A' posts [11]. Often during the welding process asymmetrical stresses build up with respect

to the part geometry and this results in an out of plane distortion, an in plane shrinkage or a combination. In many cases it is difficult to design out the distortion at the welding stage and manual re-work is often required. The advantage of laser forming for this task is the ease with which the distortion correction can be integrated into an automated welding system as shown in figure 2.29. This research

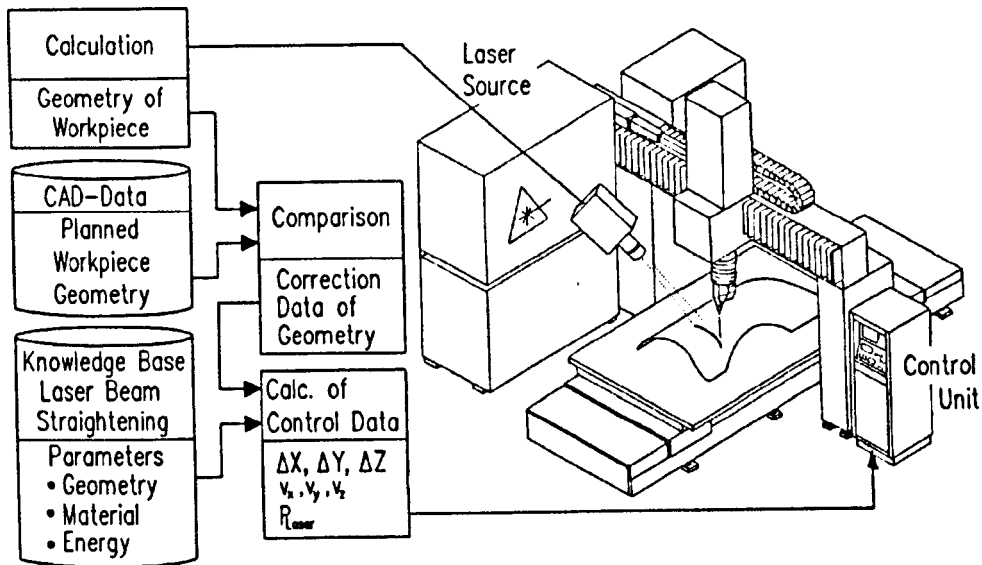


Figure 2.29: Distortion correction for car body shells

was carried out in conjunction with the Daimler-Benz corporation. In order to maximise the cut quality and the service life of circular saw blades Tonshoff et al [45] have used a laser beam to induce tangential tensile stresses in the tooth area of the blade to straighten and pre-tension the blade. A computer Aided Process Planning (CAPP) system called LASIM (Laser Assisted Straightening with Integrated Measurement) was developed to achieve this.

### Adjustment and alignment of electrical and electronic components

The miniaturisation of electrical and electronic devices has necessitated the development of robust manufacturing processes which can be implemented successfully on this scale. The use of mechanical means for adjusting the delicate components is often not possible. There are several reasons for this including the accessibility problems associated with the mechanical tooling, and the stress-strain behaviour of very tiny parts is not well understood. With laser adjustment very small deflections can be induced due to the accuracy with which the quantity and location of the laser energy can be delivered (see figure 2.30). On this scale of operation laser forming can offer a much faster process as well. This is particularly important for the mass production based electronics industry. Much of the research on

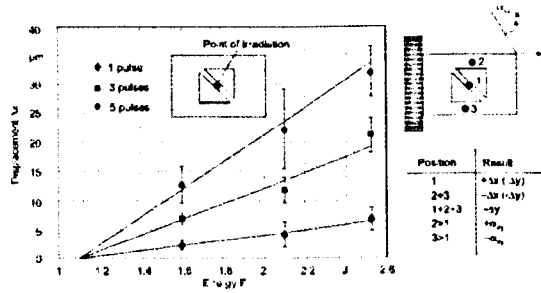


Figure 2.30: Laser micro forming

this application has originated in electronics manufacturers IBM, Siemens[12] and more recently Philips. [8, 46] A Brite - EuRam project (No BE95-1230) called AMULET (Accurate Manipulation Using Laser Technology) has been set up to develop the process on this scale. Details of the project activities may be found in various publications. [8, 12, 46, 47] Details of another project examining micro - laser induced deformations on 50HGSA spring steel at the Institute of Fundamental Technological Research (IPPT) in Poland may be found in reference[48]. In that work the transient stages of the micro deformation are presented.

### 2.8.3 Suggested Applications

#### Forming in space

One of the earlier papers on laser forming [38] suggested using laser forming for manipulating metal sheets in space. The background behind the idea was to reduce the space used by bulky structures being transported to space by transporting coiled sheet metal and then forming it in space to the required dimensions with a laser beam generated on earth. The laser could be guided remotely over a large distance and there would be no requirement to transport heavy press brakes to carry out this task.

#### Capacitance adjustment and Re - constructive surgery

Thomson and Pridham have suggested applications in the tuning of capacitance devices inside glass tubes which could not be accessed by conventional means and they have described the process as potentially suitable for manipulation of the human anatomy in re constructive surgery. Potentially this could be less harmful than using mechanical means as the method can be applied very locally and is non contact. [49, 50] They have shown some examples of Rapid Prototyping (RP) and have developed a feedback control system for straight line bends on small tokens of steel.[51]

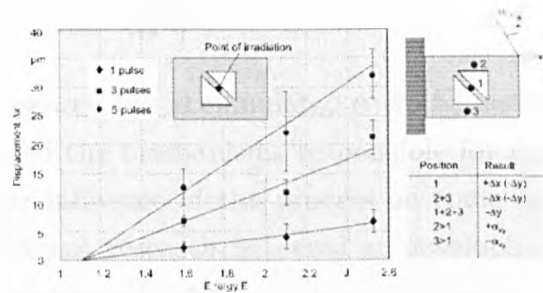


Figure 2.30: Laser micro forming

this application has originated in electronics manufacturers IBM, Siemens[12] and more recently Philips. [8, 46] A Brite - EuRam project (No BE95-1230) called AMULET (Accurate Manipulation Using Laser Technology) has been set up to develop the process on this scale. Details of the project activities may be found in various publications. [8, 12, 46, 47] Details of another project examining micro - laser induced deformations on 50HGSA spring steel at the Institute of Fundamental Technological Research (IPPT) in Poland may be found in reference[48]. In that work the transient stages of the micro deformation are presented.

### 2.8.3 Suggested Applications

#### Forming in space

One of the earlier papers on laser forming [38] suggested using laser forming for manipulating metal sheets in space. The background behind the idea was to reduce the space used by bulky structures being transported to space by transporting coiled sheet metal and then forming it in space to the required dimensions with a laser beam generated on earth. The laser could be guided remotely over a large distance and there would be no requirement to transport heavy press brakes to carry out this task.

#### Capacitance adjustment and Re - constructive surgery

Thomson and Pridham have suggested applications in the tuning of capacitance devices inside glass tubes which could not be accessed by conventional means and they have described the process as potentially suitable for manipulation of the human anatomy in re constructive surgery. Potentially this could be less harmful than using mechanical means as the method can be applied very locally and is non contact. [49, 50] They have shown some examples of Rapid Prototyping (RP) and have developed a feedback control system for straight line bends on small tokens of steel.[51]

## 2.9 State of the art

Basic laser forming research has accumulated over the last decade. Research programmes have identified the mechanisms responsible for the plastic deformation. Information about the influence of the process on some material properties has become available. Current research is aimed at developing laser forming into a robust manufacturing process[52, 53].

## 2.10 Synopsis for present research

Many questions remain to be answered if laser forming is to be implemented on full scale realistic parts. To date there is no published work reporting on symmetrical laser forming, either on straight line bends (1-D) or on spatial forming of 3-D parts. This work will examine uniform laser forming of straight line bends (1D), predefined radii of curvature (2D), and 3D forming. A dish shape will be used as a case study. Little attention has been paid to the suitability of laser forming aerospace alloys. The metallurgical and mechanical property implications will be expounded upon. There are moments and forces acting in laser forming other than transverse bending moments yet little information is available about them. A knowledge of them would improve 3D geometry processing capability and 2D geometry processing stability. The main themes of investigation here include:

- (a) Geometry - maintaining a uniform laser forming
- (b) Materials - maintaining materials integrity
- (c) Energy - Theoretical treatment of the deformation process - shape prediction, and correlation of analytical solutions with experimentally measured angles.

# Chapter 3

## Theoretical Analysis

### 3.1 Engineering theory of bending approximations

In the previous chapter the mechanics of laser bending were described using the engineering theory of bending and specifically beam theory. The transverse bending moment was used to find the curvature of the beam (sections 2.5.1 - 2.5.2). The temperature field was approximated using an energy approach, or by an approximation of the solution for the temperature field from a static laser beam impinging on a thin sheet (sections 2.5.1 - 2.5.2).

These models have advanced the understanding of the process mechanics at a rudimentary level, i.e. rational descriptions may now be given for why the plastic deformation in laser forming occurs. However the gross simplifications render them incomplete in terms of practical laser forming. It is hoped that some future laser forming operations will be concerned with forming an initially flat sheet into a final geometry which is three dimensional. Therefore a model which analyses transverse bending moments only, and predicts only an angular deformation is of limited use for practical forming. This is because the transverse bending moments are accompanied by other forces and moments, refer to figure 3.1. These may hamper uniform straight line angular deformation but facilitate 3-D shaping. What are they?

- (a) Transverse bending moments, (as described).
- (b) Transverse shrinkage forces
- (c) Longitudinal bending moments
- (d) Longitudinal shrinkage forces

Establishing these forces and moments would advance the “engineering theory of bending” approximations for laser forming. Then the superposition of the forces and moments would have to be considered to establish the final shape.

An alternative and rigorous analysis would require a full thermoelastic-plastic analysis which accounts for the temperature dependency of the mechanical properties of the material and geometrical non-linearity. This is expensive. However such an analysis could eventually provide a very accurate solution. Presently there is insufficient information about the mechanical properties (Yield stress, Elastic modulus) of the materials in question when subjected to high temperatures and quench rates. It is unlikely that there is a distinct elastic-plastic interface in laser forming. Instead it is probable that there is a boundary layer, analogous to a moving boundary problem such as the melting of ice. Unfortunately in laser forming there is no latent heat in the non-melting regime and thus it is not apparent how to implement a moving boundary approach. The amount of computational time involved in this type of analysis is substantial. Given these problems, a solution which predicts the shape trends but not the absolute values of the curvatures is proposed.

Instead of using the thermoelastic-plastic method, the elastic deformation theory is used here, with the appropriate forces and moments for a given heating pattern to predict the shape trend and determine what forces and moments are significant for a given set of processing parameters and material dimensions. Using the method of inherent strain for flame forming [54, 55] the bulk of the plastic deformation is assumed to occur within the heated region (i.e. in this case the region directly underneath the laser beam). The plastic strain of this zone is calculated from the maximum plastic strain less the elastic strain during heating. If the extents of the zone are known, the previously described forces and moments may be calculated for the section.

### 3.1.1 Assumptions

- (a) Plastic deformation is confined to the region directly underneath the laser beam.
- (b) Plastic loading occurs during heating, plastic unloading occurs during cooling.
- (c) Displacement of the irradiated zone is approximated by the circular hole in plate theory presented by Timoshenko [56].
- (d) The Engineering theory of bending is used to obtain forces and moments.

### 3.1.2 Co-ordinate system

The co-ordinate system used here is illustrated in figure 3.1. The transverse bending moment refers to the direction transverse to the heating line, the longitudinal bending moment refers to the direction the laser beam is scanning in,  $x$ . The co-ordinate system is identical for the shrinkage forces.

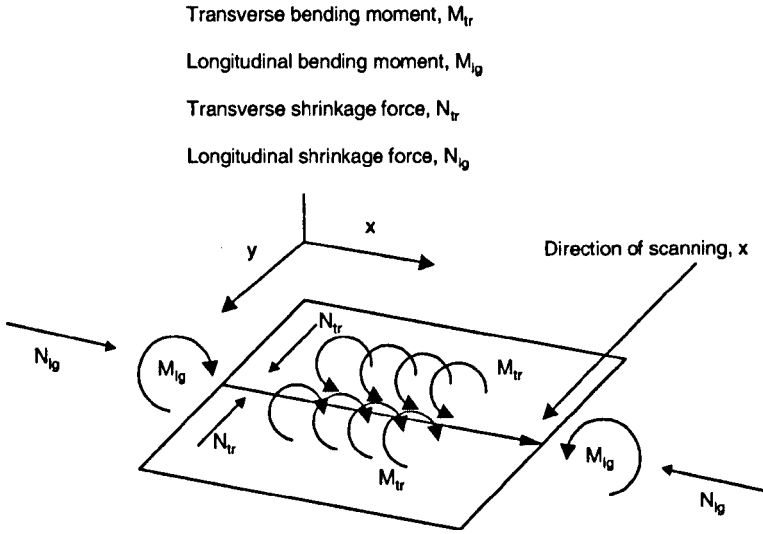


Figure 3.1: Co-ordinate system and relevant forces and moments

### 3.1.3 Transverse bending moment, $M_{tr}$

Using engineering beam theory the transverse bending moment can be found with a knowledge of the shape function for the local strain. It is given by:

$$M_{tr} = \int_{-s_0/2}^{s_0/2} E \epsilon_{in} b_z z dz \quad (3.1)$$

Integrating this equation results in the transverse bending moment per unit length of the sheet.

### 3.1.4 Longitudinal bending moment, $M_{lg}$

The longitudinal bending moment can be determined by including Poisson's ratio. Poisson's ratio is the ratio of the lateral to longitudinal strain. It is given by:

$$\nu = \frac{-\epsilon_{lateral}}{\epsilon_{longitudinal}} \quad (3.2)$$

The longitudinal bending moment is then given by:

$$M_{lg} = \int_{-s_0/2}^{s_0/2} E(1 - \nu)\epsilon_{in}b_z z dz \quad (3.3)$$

### 3.1.5 Transverse shrinkage force, $N_{tr}$

The transverse shrinkage or in plane force can be found by dropping the  $z$  dependency in the transverse bending moment equation. It is given by:

$$N_{tr} = \int_{-s_0/2}^{s_0/2} E\epsilon_{in}b_z dz \quad (3.4)$$

### 3.1.6 Longitudinal shrinkage force, $N_{lg}$

Similarly the longitudinal shrinkage force is given by dropping the  $z$  dependency in the equation for the longitudinal bending moment. It is given by:

$$N_{lg} = \int_{-s_0/2}^{s_0/2} E(1 - \nu)\epsilon_{in}b_z dz \quad (3.5)$$

In the equations describing the forces and moments the inherent strain  $\epsilon_{in}$  and the function describing the local strain  $b_z$  must be known, before the integral equations may be evaluated to get the components of the solution.

### 3.1.7 Inherent strain

Vollertsen described the maximum surface strain as:

$$\alpha_{th} * T(0, 0, 0, t) - \frac{k_f(T)}{E(T)} \quad (3.6)$$

In his analysis the maximum plastic strain was estimated by taking the co-efficient of thermal expansion times the temperature at the centre of the laser beam less the fraction of the yield stress and the elastic modulus at that temperature. Here the inherent strain is described using a mechanical analogy. The stress distribution surrounding a hole in a plate [56] is considered similar to the laser forming case. The mechanical properties are massively reduced in the ‘hole’ region, almost to zero, as in the case of the laser irradiated zone. Therefore the plate area surrounding the laser spot can be represented by the hole in plate theory. The actual laser spot itself can be represented by Timoshenko’s solution [56] for a disk subjecting a force around the edge. The ‘disk’ and the ‘hole in plate’ are then connected by the boundary condition that the stress at the edge of the disk must

equal the stress at the edge of the hole and then the elastic-plastic interface may be established if an average temperature for plastic yielding can be specified. This is the major limiting assumption of the model. To circumvent this assumption the full thermoelastic-plastic is required. However it is expensive, complex and often not accurate, due to the uncertainty surrounding the input data such as thermo-mechanical properties. The method here allows a relatively simple and powerful analysis which may be appropriate as a design tool.

### Strain representation of the region directly underneath the laser beam

Proceeding from Timoshenko [56] (pages 65..149) the stress strain relationship for radial strain in a circular disk which is exerting a force around the edge and which is constrained is described by:

$$\begin{aligned}\epsilon_r &= \frac{du_d}{dr} \\ &= \frac{1}{E_d}(\sigma_r - \nu\sigma_\theta) + \epsilon_r^{in}\end{aligned}\quad (3.7)$$

The tangential strain is given by:

$$\begin{aligned}\epsilon_\theta &= \frac{u_d}{r} \\ &= \frac{1}{E_d}(\sigma_\theta - \nu\sigma_r) + \epsilon_\theta^{in}\end{aligned}\quad (3.8)$$

For the plate with the circular hole the displacement relationship given by Timoshenko [56] when uniform pressure is acting around the hole is:

$$u_{pl} = \frac{p}{E_{pl}} \frac{R^2}{r} (1 + \nu_2) \quad (3.9)$$

Evaluating the spring constant around the disk yields:

$$\begin{aligned}K &= \frac{p}{u_{pl}} \\ &= \frac{E_{pl}}{R(1 + \nu_2)}\end{aligned}\quad (3.10)$$

As described previously the stress at the edge of the “disk” must equal the stress at the edge of the “hole”. Therefore the stress may be expressed by:

$$\sigma = -Ku_d (R_{hole} = r_{dim}) \quad (3.11)$$

Re-arranging this equation yields:

$$\sigma = \frac{-\epsilon_{in} K R_{hole}}{1 + \frac{(1-\nu_1)}{E_1} K R_{hole}} \quad (3.12)$$

When the plate is heated to the high temperature which induces plastic strain, the plastic strain of the “disk” is given by:

$$\sigma_d = -\frac{(\alpha_{th} T_c + \epsilon_{pm}) K R_{hole}}{1 + \frac{(1-\nu_1)}{E_d} K R_{hole}} \quad (3.13)$$

where:

$$\epsilon_{pm} = \alpha_{th} T_c \quad (3.14)$$

Subtracting the elastic strain from the maximum plastic strain during heating yields the inherent strain  $\epsilon_{in}$ :

$$\epsilon_{in} = \alpha_{th} T_c - \sigma_d \left( \frac{1}{R_{hole} K} + \frac{1 - \nu_1}{E_d} \right) \quad (3.15)$$

The previous expression will be used for the calculation of the inherent strain. Next it is necessary to evaluate the temperature field in order to calculate the shape of the local strain zone through the sheet thickness. That is the aim of the next section.

## 3.2 Thermal field

The shape function for describing the local strain depends on the thermal regime in which the forming is taking place. If the laser beam diameter is large, the processing velocity low, and the thermal conductivity reasonably high, it may be expected that the local strain could be idealised as a rectangular to circular region directly underneath the laser spot. If the processing velocity is high, a more elliptical isothermal zone would be expected and the local strain through the sheet thickness could be idealised with an elliptic function.

First it is necessary to check this hypothesis. The three dimensional (3D) temperature field around a laser beam impinging on a moving substrate must be evaluated in order to show this. This is necessary anyway, as the temperatures must be evaluated also, in order to determine the thermal expansion of the irradiated zone and the loading arising from this expansion.

The three dimensional equation for time dependent heat conduction with a

source is evaluated to achieve this. It is:

$$\frac{\partial}{\partial t}(\rho CT) + u \frac{\partial}{\partial x}(\rho CT) = \frac{\partial}{\partial x} \left( k \frac{\partial}{\partial x} \right) + \frac{\partial}{\partial y} \left( k \frac{\partial}{\partial y} \right) + \frac{\partial}{\partial z} \left( k \frac{\partial}{\partial z} \right) \quad (3.16)$$

The Finite Volume Method, prescribed by Patankar [57] has been used to numerically evaluate the previously described equation. The solution originally adopted by Ducharme is used here, [58].

### 3.2.1 Numerical solution to differential equations

Numerical solutions to differential equations usually divide a domain of interest into a number of subdomains, discretization equations are applied, the equations for the unknowns at each point chosen in the domain are established, and the equations are subsequently solved with an appropriate algorithm. The finite volume method divides the domain of interest into a number of non-overlapping control volumes so that one control volume encloses one grid point. This is one of a number of numerical techniques. Other commonly applied methods include the finite difference and finite element methods. In the finite volume method the differential heat conduction equation is integrated over each control volume. Let the differential equation be represented by a general variable  $\phi$ . To illustrate the method simply, assume that the variable  $\phi$  is a function of one independent variable,  $x$ .

Then the numerical solution of the differential heat conduction equation is evaluated from a set of numbers from which the distribution of the dependent variable  $\phi$  can be assessed. If the distribution of  $\phi$  is represented by a polynomial in  $x$ , then the equation may have the form:

$$\phi = a_0 + a_1x + a_2x^2 + \cdots a_mx^m \quad (3.17)$$

A numerical method could then be used to find the number of coefficients  $a_0, a_1, a_2, \cdots a_m$ . Then  $\phi$  may be evaluated at any point  $x$  by substituting the  $x$  value and the value of the  $a$ 's into the previous equation. However the overall objective is to determine the value of  $\phi$ , and the values of  $a_1..a_m$  in themselves have no meaning. As a result numerical schemes have been set up which have the values of  $\phi$  at the various grid points as the unknowns. Therefore a numerical method treats the dependent variable as the unknown at a number of grid points in the discretized domain of interest. Usually algebraic equations are used to represent the unknowns and the system of equations must then be solved with a suitable algorithm.

It is necessary to pay attention now to the discretization equation and tech-

nique. The discretization equation is algebraic. It connects the values of  $\phi$  for a group of grid points. The equation is derived from the differential equation for  $\phi$  and thus expresses the same information. Then an assumption must be made for how  $\phi$  varies between the grid points. A *piecewise* profile is usually employed for this. That is in and around a small region in the domain of interest a single algebraic equation may be used to represent the behaviour of  $\phi$  and then a large number of small regions or subdomains may be defined with different profiles. This is done because it is unlikely that one profile assumption could represent accurately the whole domain of interest. Of course this technique also results in the fact that only a few grid points need participate in the discretization equation. Therefore the value of  $\phi$  influences its immediate neighbours only. It may then be expected that as the number of grid points increases the numerical solution will approach the exact solution of the differential equation. This is because as the grid points get denser the change in  $\phi$  between the points gets very small and the *piecewise profiles* decrease in importance.

If that is the case it also indicates that the discretization equations are not unique, because although different piecewise profiles may be employed, if the grid point density increases to a very large number all the solutions approach the exact solution of the differential equation.[57]

### Finite Volume Formulation

As stated in the previous section the finite volume method divides the domain of interest into a number of non-overlapping control volumes so that one control volume encloses one grid point. The differential equation is then integrated over each control volume. The piecewise profiles expressing the relationship for  $\phi$  between grid points are used to evaluate the integrals. Then the discretization equation containing the values of  $\phi$  for a group of grid points is found. With the control volume method the conservation principle is applied to a finite volume as opposed to the differential equation which applies it to an infinitesimal volume. The method is useful as the integral formulation conserves the quantity of energy over any group of control volumes exactly and over the whole domain of interest. Even a low density of grid points yields exact integral balances [57].

To illustrate the method for the simplest of cases, consider one dimensional steady state heat conduction, given by:

$$\frac{d}{dx} \left( k \frac{dT}{dx} \right) + S = 0 \quad (3.18)$$

where:  $S$  is the source term,  $k$  is the thermal conductivity,  $T$  is the temperature. Considering figure 3.2 and integrating the last equation over the control volume

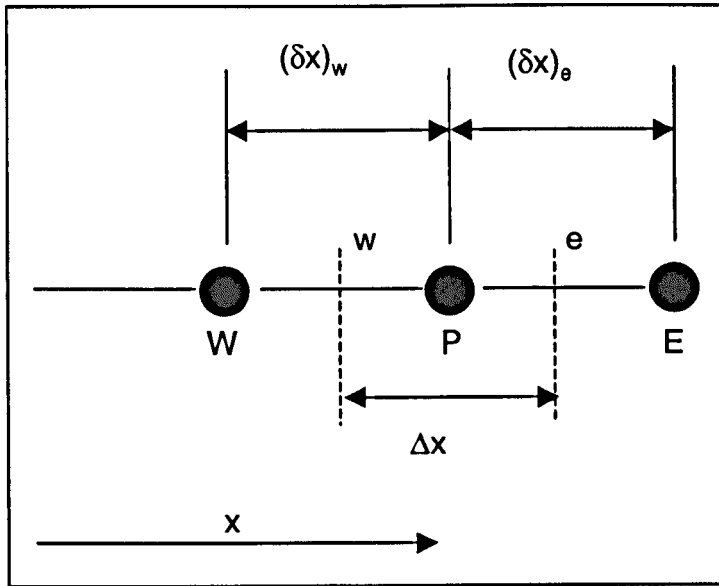


Figure 3.2: 1-D grid point cluster

yields:

$$\left(k \frac{dT}{dx}\right)_e - \left(k \frac{dT}{dx}\right)_w + \int_w^e S dx = 0 \quad (3.19)$$

Then assuming a piecewise linear profile for the interpolation function and evaluating the derivatives  $\frac{dT}{dx}$ , the equation becomes:

$$\frac{k_e(T_E - T_P)}{(\delta x)_e} - \frac{k_w(T_P - T_W)}{(\delta x)_w} + \bar{S}\Delta x = 0 \quad (3.20)$$

where:  $\bar{S}$  is the average value of  $S$  over the control volume.

Equation 3.20 may be recast in a neater form as:

$$a_p T_p = a_E T_E + a_W T_W + b \quad (3.21)$$

where:

$$a_E = \frac{k_e}{(\delta x)_e} \quad (3.22)$$

and:

$$a_W = \frac{k_w}{(\delta x)_w} \quad (3.23)$$

and:

$$a_p = a_E + a_W \quad (3.24)$$

and:

$$b = \bar{S}\Delta x \quad (3.25)$$

Equation 3.21 is the standard form used by Patankar to express the discretization equation. On the left hand side of the equation  $T_p$  expresses the temperature at the central grid point. The temperature points on either side of  $T_p$  appear on the right hand side of the equation, along with the constant  $b$ .

### 3.2.2 Extension to three dimensional case with a source

Using the previously described method of discretization the method of Patankar can be extended to three dimensions and to the unsteady case with a source. Let the equation to be solved be:

$$\rho c_p \left( \frac{\partial T}{\partial t} + u \frac{\partial T}{\partial x} \right) = k \left( \frac{\partial^2 T}{\partial x^2} + \frac{\partial^2 T}{\partial y^2} + \frac{\partial^2 T}{\partial z^2} \right) + \text{source term} \quad (3.26)$$

Then applying Patankar's method as in the previous example:

$$\frac{\partial T}{\partial x} = \frac{T_E - T_W}{\delta x_e + \delta x_w} \quad (3.27)$$

Then:

$$\begin{aligned} \frac{\partial^2 T}{\partial x^2} &= \frac{\left(\frac{\delta T}{\delta x}\right)_e - \left(\frac{\delta T}{\delta x}\right)_w}{\Delta x} \\ &= \frac{\frac{T_E - T_P}{\delta x_e} - \frac{T_P - T_W}{\delta x_w}}{\Delta x} \end{aligned} \quad (3.28)$$

and,

$$\frac{\partial^2 T}{\partial y^2} = \frac{\frac{T_N - T_P}{\delta x_n} - \frac{T_P - T_s}{\delta x_s}}{\Delta y} \quad (3.29)$$

and,

$$\frac{\partial^2 T}{\partial z^2} = \frac{\frac{T_u - T_p}{\delta x_u} - \frac{T_p - T_D}{\delta x_d}}{\Delta z} \quad (3.30)$$

$$\frac{\partial T}{\partial t} = \frac{T_p - T_p^{old}}{\delta t} \quad (3.31)$$

where:

$$\begin{aligned} T_p &\equiv T(x, y, z) \\ T_E &= T(x + 1, y, z) \\ T_W &= T(x - 1, y, z) \\ T_N &= T(x, y + 1, z) \\ T_S &= T(x, y - 1, z) \\ T_U &= T(x, y, z + 1) \\ T_D &= T(x, y, z - 1) \end{aligned}$$

Substituting equations 3.27 to 3.31 into equation 3.26 yields:

$$\begin{aligned} \rho c_p \left( \frac{T_p - T_p^{old}}{\delta t} U \frac{T_E - UT_W}{\delta x_e + \delta x_w} \right) & - k \left( \frac{\frac{T_E}{\delta x_e} + \frac{T_W}{\delta x_w}}{\Delta x} + \frac{\frac{T_u}{\delta z_u} + \frac{T_D}{\delta z_d}}{\Delta z} \right. \\ & + \frac{\frac{T_N}{\delta y_n} + \frac{T_s}{\delta y_s}}{\Delta y} - \frac{\frac{T_p}{\delta x_e} + \frac{T_p}{\delta x_w}}{\Delta x} \\ & \left. - \frac{\frac{T_p}{\delta x_u} + \frac{T_p}{\delta x_d}}{\Delta z} - \frac{\frac{T_p}{\delta x_n} + \frac{T_p}{\delta x_s}}{\Delta y} \right) \end{aligned}$$

– source term = 0 (3.32)

multiplying by  $\Delta x \Delta y \Delta z$  and grouping:

$$\begin{aligned} \rho c_p U \frac{(T_E \Delta x \Delta y \Delta z - T_W \Delta x \Delta y \Delta z)}{\delta x_e + \delta x_w} & - \frac{(k \frac{\Delta y \Delta z T_E}{\delta x_e} + k \frac{\Delta y \Delta z T_W}{\delta x_w} + k \frac{\Delta x \Delta y T_u}{\delta z_u} + k \frac{\Delta x \Delta y T_D}{\delta z_d} + k \frac{\Delta x \Delta z T_N}{\Delta y_n} + k \frac{\Delta x \Delta z T_S}{\delta y_s})}{\Delta x \Delta y \Delta z} \\ & + \frac{T_p}{\Delta x \Delta y \Delta z} \left( \frac{k \Delta y \Delta z}{\Delta x_e} + \frac{k \Delta y \Delta z}{\delta x_w} + \frac{k \Delta x \Delta y}{\delta z_u} + \frac{k \Delta x \Delta y}{\delta z_d} + \frac{k \Delta x \Delta z}{\Delta y_n} + \frac{k \Delta x \Delta z}{\delta y_s} \right) \\ & - \frac{T_p^{old} \rho c_p \Delta x \Delta y \Delta z}{\delta t \Delta x \Delta y \Delta z} - \frac{\text{sourceterm}}{\Delta x \Delta y \Delta z} = 0 \quad (3.33) \end{aligned}$$

However it is possible to let:

$$a_E = \frac{k}{\delta x_e} \quad (3.34)$$

$$a_W = \frac{k}{\delta x_w} \quad (3.35)$$

$$a_U = \frac{k}{\delta z_u} \quad (3.36)$$

$$a_D = \frac{k}{\delta z_d} \quad (3.37)$$

$$a_N = \frac{k}{\delta y_n} \quad (3.38)$$

$$a_S = \frac{k}{\delta y_s} \quad (3.39)$$

Therefore:

$$\begin{aligned} T_p = & \left( a_e \Delta y \Delta z T_E + a_w \Delta y \Delta z T_W + a_n \Delta x \Delta z T_N + a_s \Delta x \Delta y T_s \right. \\ & + a_U \Delta x \Delta y T_U + a_D \Delta x \Delta y T_D - \frac{\rho c_p U}{2} \Delta y \Delta z T_E + \frac{\rho c_p U}{2} \Delta Y \Delta z \Delta u \\ & \left. + \text{source term} \Delta x \Delta y \Delta z + \frac{\rho c_p \Delta x \Delta y \Delta z T_p^{\text{old}}}{(\delta t)} \right) \end{aligned}$$

divided by:

$$\begin{aligned} & \left( a_E \Delta y \Delta z + a_W \Delta y \Delta z + a_N \Delta x \Delta z + a_S \Delta x \Delta z + a_U \Delta x \Delta y \right. \\ & \left. + a_D \Delta x \Delta y + \frac{\rho c_p \Delta x \Delta y \Delta z}{(\delta t)} \right) \quad (3.40) \end{aligned}$$

Using the hybrid scheme prescribed in Patankar (pages 88-91)  $a_E$  is re written as:

$$\begin{aligned} a_E &= \frac{k}{\delta x_e} \\ &= \frac{k}{\delta x_e} \left( 1 - 0.1 \left| \frac{\rho c_p u \Delta y \Delta z}{k \Delta y \Delta z / \delta x_e} \right| \right)^5 \\ &\quad + ||0, -\Delta z \rho c_p u|| \end{aligned} \quad (3.41)$$

and for  $a_w$ :

$$a_w = \frac{k}{\delta x_w} \left( 1 - 0.1 \left| \frac{\rho c_p u \Delta y \Delta z}{k \Delta y \Delta z / \delta x_w} \right| \right)^5 + || + \Delta y \Delta z \rho c_p u, 0 || \quad (3.42)$$

$\Delta x, \Delta y, \Delta z, \rho, c_p, u$  are always positive, so  $a_e$  and  $a_w$  may be re-written as:

$$a_E = \frac{k}{\delta x_e} \left( 1 - 0.1 \left| \rho c_p u \frac{\delta x_e}{k} \right| \right)^5 \quad (3.43)$$

and:

$$a_w = \frac{k}{\delta x_w} \left( 1 - 0.1 \left| \rho c_p u \frac{\delta x_w}{k} \right| \right)^5 + \rho c_p u \Delta y \Delta z \quad (3.44)$$

### 3.2.3 The Tri Diagonal Matrix Algorithm (*TDMA*) solution to the algebraic equations

In order to solve the algebraic equations and evaluate the temperature field it is necessary to employ a stable algorithm to achieve this. The aim of this section is to show how the *TDMA* is a suitable algorithm when compared with the analytical solution. Solving the 1-D equation for  $z$  we have:

$$k \frac{\partial^2 T}{\partial z^2} + S \cos\left(\frac{\pi z}{10}\right) + R = 0 \quad (3.45)$$

where  $R$  and  $S$  are constants.

This equation is solved for  $0 \leq Z \leq 5$  with the boundary conditions:

$$T(z = 0) = T_{int} = 300K \quad (3.46)$$

and:

$$T(z = 5) = T_{end} = 500K \quad (3.47)$$

The analytical solution applying these boundary conditions is:

$$T = T_{int} + z \left( \frac{T_{end} - T_{int}}{5} + \left( \frac{20z}{\pi^2} + \frac{100}{\pi^2} \left( \cos\left(\frac{\pi z}{10}\right) - 1 \right) \right) \frac{S}{k} + \left( \frac{5z}{2} - \frac{z^2}{2} \right) \frac{R}{k} \right) \quad (3.48)$$

This holds as long as  $k$  is assumed constant throughout the  $Z$  direction.

For each position in  $z$  the equations for 300, 340, 380, 420, and 460K become:

$$T(z = 0) = T_{int} = 300K - \text{Boundary condition} \quad (3.49)$$

$$T(z = 1) = T_{int} + \frac{T_{end} - T_{int}}{5} + \frac{15.1S}{k\pi^2} + \frac{4R}{2k} = 340 + 1.53\frac{S}{k} + 2\frac{R}{k} \quad (3.50)$$

$$T(z = 2) = T_{int} + \frac{2}{5}(T_{end} - T_{int}) + \frac{20.9S}{k\pi^2} + \frac{6R}{2k} = 380 + 2.12\frac{S}{k} + 3\frac{R}{k} \quad (3.51)$$

$$T(z = 3) = T_{int} + \frac{3}{5}(T_{end} - T_{int}) + \frac{18.8S}{k\pi^2} + \frac{6R}{2k} = 420 + 1.90\frac{S}{k} + 3\frac{R}{k} \quad (3.52)$$

$$T(z = 4) = T_{int} + \frac{4}{5}(T_{end} - T_{int}) + \frac{10.95S}{k\pi^2} + \frac{4R}{2k} = 460 + 1.10\frac{S}{k} + 2\frac{R}{k} \quad (3.53)$$

$$T(z = 5) = T_{end} = 500K - \text{Boundary condition} \quad (3.54)$$

### The numerical solution which approximates the analytical solution

Consider the 1-D equation again, as described in equation 3.45. It may be re-written as:

$$\left( k \frac{\partial T}{\partial z} \right)_u - \left( k \frac{\partial T}{\partial z} \right)_d + S \int_d^u \cos\left(\frac{\pi z}{10}\right) dz + R \int_d^u dz = 0 \quad (3.55)$$

The domain of interest is illustrated in figure 3.2 with the exception now that the example refers to the  $Z$  direction rather than the  $X$  direction and the notation has to be changed accordingly. Re-writing equation 3.45 once more according to this arrangement yields:

$$\frac{k_u(T_u - T_p)}{(\delta z)_u} - \frac{k_d(T_p - T_w)}{(\delta z)_d} + S\bar{C}\Delta z + R\Delta z = 0 \quad (3.56)$$

Here  $\bar{C}$  is an average value of  $\cos\left(\frac{\pi z}{10}\right)$  over the range  $d \rightarrow u$ . The average value is chosen as:

$$\frac{1}{2} \left[ \cos\left(\frac{\pi z_d}{10}\right) + \cos\left(\frac{\pi z_u}{10}\right) \right] \quad (3.57)$$

To simplify this example let  $(\delta z)_u = (\delta z)_d = \Delta z$  and  $k_u = k_d = k$ . Then:

$$\frac{k(T_u - T_p)}{\Delta z} - \frac{k(T_p - T_w)}{\Delta z} + S \frac{1}{2} \left[ \cos\left(\frac{\pi z_u}{10}\right) + \cos\left(\frac{\pi z_d}{10}\right) \right] \Delta z + R \Delta z = 0 \quad (3.58)$$

Therefore:

$$2T_p = T_u + T_w + \frac{S}{k} (\Delta z)^2 \frac{1}{2} \left[ \cos\left(\frac{\pi z_u}{10}\right) + \cos\left(\frac{\pi z_d}{10}\right) \right] + \frac{R}{k} (\Delta z)^2 \quad (3.59)$$

Rewriting the last equation in the form of  $a_i T_i = b_i T_{i+1} + C_i T_{i-1} + d_i$  results in six equations which have to be solved:

$$a_0 T_0 = b_0 T_1 + c_0 T_{-1} + d_0 \quad (3.60)$$

Note as  $T_0$  is a boundary condition,  $a_0 = 1$ ,  $b_0 = 0$ ,  $c_0 = 0$ ,  $d_0 = T_{int}$ .

Applying the TDMA let  $d_1$  to  $d_4$  be:

$$d_1 = s_1 S + r_1 R \quad (3.61)$$

$$d_2 = S_2 S + r_2 R \quad (3.62)$$

$$d_3 = S_3 S + r_3 R \quad (3.63)$$

$$d_4 = S_4 S + r_4 R \quad (3.64)$$

$a_0, a_1, b_1, c_1$  and  $a_5$  are as before.

$$r_1 = r_2 = r_3 = r_4 = \frac{1}{k} \quad (3.65)$$

so:

$$s_1 = \frac{1}{2} \left( 1 + \cos \frac{\pi}{10} \right) \quad (3.66)$$

$$s_2 = \frac{1}{2} \left( \cos \frac{\pi}{10} + \cos \frac{2\pi}{10} \right) \quad (3.67)$$

$$s_3 = \frac{1}{2} \left( \cos \frac{2\pi}{10} + \cos \frac{3\pi}{10} \right) \quad (3.68)$$

$$s_4 = \frac{1}{2} \left( \cos \frac{3\pi}{10} + \cos \frac{4\pi}{10} \right) \quad (3.69)$$

Proceeding from Patankar, pages 52 and 53 results in:

$$P_0 = \frac{b_0}{a_0} = 0 \quad (3.70)$$

$$P_1 = \frac{b_1}{a_1 - c_1 P_0} = \frac{1}{2} \quad (3.71)$$

$$Q_0 = \frac{d_0}{a_0} = T_{int} = 300K \quad (3.72)$$

$$Q_1 = \frac{d_1 + c_1 Q_0}{a_1 - c_1 P_0} = \frac{s_1 S + r_1 R + 300}{2} \quad (3.73)$$

$$P_2 = \frac{b_2}{a_2 - c_2 P_1} = \frac{2}{3} \quad (3.74)$$

$$\begin{aligned} Q_2 &= \frac{d_2 + c_2 Q_1}{a_2 - c_2 P_1} \\ &= \frac{(2s_2 + s_1)S + (2r_2 + r_1)R + 300}{3} \end{aligned} \quad (3.75)$$

$$P_3 = \frac{b_3}{a_3 - c_3 P_2} = \frac{3}{4} \quad (3.76)$$

$$\begin{aligned} Q_3 &= \frac{d_3 + c_3 Q_2}{a_3 - c_3 P_1} \\ &= \frac{(3s_3 + 2s_2 + s_1)S + (3r_3 + 2r_2 + r_1)R + 300}{4} \end{aligned} \quad (3.77)$$

$$P_4 = \frac{b_4}{a_4 - c_4 P_3} = \frac{4}{5} \quad (3.78)$$

$$\begin{aligned} Q_4 &= \frac{d_4 + c_4 Q_3}{a_4 - c_4 P_3} \\ &= \frac{(s_4 S + r_4 R) + (3s_3 + 2s_2 + s_1)S + (3r_3 + 2s_2 + s_1)R + 300}{5} \end{aligned} \quad (3.79)$$

It is now necessary to evaluate  $T_4, T_3, T_2$ , and  $T_1$  using the following equations:

$$T_4 = P_4 T_5 + Q_4 \quad (3.80)$$

$$T_3 = P_3 T_4 + Q_3 \text{ using } T_4 \text{ just found} \quad (3.81)$$

$$T_2 = P_2 T_3 + Q_2 \text{ using } T_3 \text{ just found} \quad (3.82)$$

$$T_1 = P_1 T_2 + Q_1 \text{ using } T_2 \text{ just found} \quad (3.83)$$

$$T_5 \text{ is fixed at } 500K - \text{Boundary condition} \quad (3.84)$$

This leads us towards the solutions for  $T_4 - T_1$ . They are as follows:

$$\begin{aligned} T_4 &= \frac{4}{5} 500 + \frac{(4s_4 + 3s_3 + 2s_2 + s_1)S + (4r_4 + 3r_3 + 2r_2 + r_1)R + 300}{5} \\ &= 460 + 1.32 \frac{S}{k} + 2 \frac{R}{k} \end{aligned} \quad (3.85)$$

By the same procedures  $T_3$  to  $T_1$  are found to be:

$$T_3 = 420 + 2.20 \frac{S}{k} + 3 \frac{R}{k} \quad (3.86)$$

$$T_2 = 380 + 2.38 \frac{S}{k} + 3 \frac{R}{k} \quad (3.87)$$

$$T_1 = 340 + 1.68 \frac{S}{k} + 2 \frac{R}{k} \quad (3.88)$$

$T_0$  is fixed at 300K as it is a boundary condition.

Comparing the *TDMA* with the analytical solution, they are identical except

for the approximation:

$$\int_d^u \cos\left(\frac{\pi z}{10}\right) dz \tag{3.89}$$

Additionally it only took one sweep of the equations to get the exact answer, that is because the *TDMA* gives the exact solution.

That completes the description of the solution method. The actual boundary conditions used in the model are outlined in the next section.

### 3.2.4 Solution domain and Boundary conditions

The code solves the heat equation in the domain as shown in figure 3.3. The

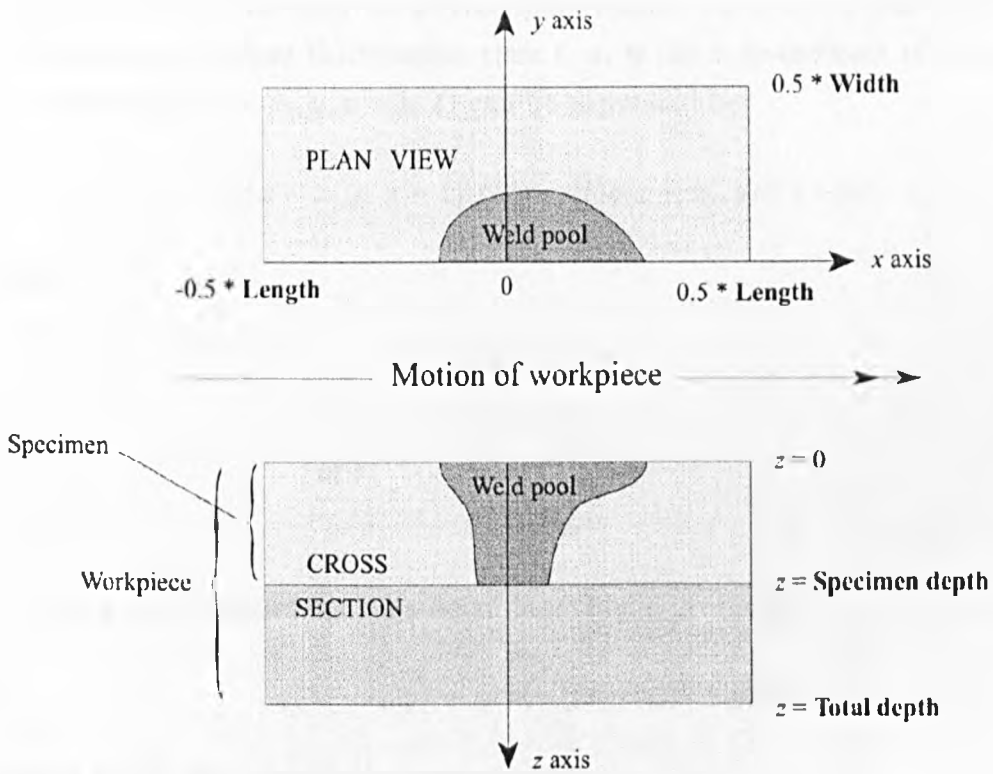


Figure 3.3: Solution domain

domain is described by:

$$-\frac{1}{2} \text{Length} \leq x \leq \frac{1}{2} \text{Length}$$

$$0 \leq y \leq \frac{1}{2} \text{Width}$$

$$0 \leq z \leq \text{Total depth}$$

The length and width refer to the zone where output is generated rather than the extents of the workpiece. They are chosen so that the temperature in that region does not extend much greater than ambient, otherwise the extents have to be moved further out. The length is from minus half to plus half the grid length, therefore there is a period of time before the workpiece reaches the laser beam as it translates underneath it, as the beam is located at zero.

### Heat flux Representation

The solution allows for up to ten sources and sinks, since many problems involve either multiple sources (e.g. dual wavelength processing, arc augmented welding) or sinks (e.g. clamping arrangements, chiller bars etc). The heat flux of one of the ten sources is represented by a function  $f_i(x - x_i, y, z - z_i, t)$ , ( $i = 1$  to 10). The position of the source may be at the upper surface ( $z_i = 0$ ), or the lower surface of the sheet ( $z_i = \text{sheet thickness}$ ) at time  $t$ .  $x_i$  is the  $x$  co-ordinate of the source  $i$ . The function  $f_i(x - x_i, y, z - z_i, t)$  can be expressed by:

$$f_i(x - x_i, y, z - z_i, t) = q_0(t)q(x - x_i, y)\delta(z - z_i) \quad (3.90)$$

where:

$$\begin{aligned} & \delta(z - z_i) = 1 \\ & \quad \text{if } z = z_i \\ \text{or: } & \delta(z - z_i) = 0 \\ & \quad \text{if } z \neq z_i \end{aligned} \quad (3.91)$$

$q(x - x_i)$  is defined for a gaussian laser beam profile as:

$$q(x - x_i, y) = \exp(-((x - x_i)^2 + y^2)/a^2) \quad (3.92)$$

Here  $a$  is the gaussian radius of the beam.

### Total heat flux on surfaces

The total heat flux is defined by the summation of the sources and sinks and the radiative and convective losses from the surfaces.

**Top boundary,  $z = 0$**

$$Q_T = f_0(x, y, 0, t) + \sum_{i=1..9} f_i(x - x_i, y, -z_i, t) + A_T(T - T_0) + \epsilon_T \sigma (T^4 - T_0^4) \quad (3.93)$$

where:  $\sigma$  is the Stefan-Boltzmann constant,  $\epsilon_T$  is the radiative emission coefficient of the top surface,  $A_T$  is the convective loss coefficient of the top surface.

**Bottom boundary,  $z =$  sheet thickness**

$$Q_B = \sum_{i=1..9} f_i(x - x_i, y, d - z_i, t) + A_B(T - T_0) + \epsilon_B\sigma(T^4 - T_0^4) \quad (3.94)$$

where:  $\epsilon_B$  is the radiative emission coefficient of the bottom surface,  $A_B$  is the convective loss coefficient of the bottom surface.

### Boundary conditions

The heat equation is solved according to the following boundary conditions:

**Top boundary,  $z=0$**

$$k \frac{\partial T}{\partial z} = Q_T(x, y, t) \text{ for } T(z, y, 0) \leq T_{\text{boiling}} \quad (3.95)$$

and for all other cases:

$$T = T_{\text{boiling}} \quad (3.96)$$

**Bottom boundary,  $z =$  sheet thickness**

$$k \frac{\partial T}{\partial z} = Q_b(x, y, t) \quad (3.97)$$

At the extents of the grid in the lateral directions, i.e.  $x$  and  $y$ , a no heat loss condition is applied:

$$k \frac{\partial T}{\partial z} = 0 \quad (3.98)$$

Alternatively the temperature at large distances from the laser spot can be fixed to ambient temperature:

$$T = T_{\text{ambient}} \quad (3.99)$$

### 3.2.5 Thermal modelling outputs

Using the finite volume code which numerically solved the heat equation, a number of outputs were produced. They included:

- (a) Heat affected zone cross section,  $yz$ .
- (b) Isotherms,  $xy$ , for  $z = 0$  to  $z =$  the sheet thickness.

- (c) Temperature rise as the sheet moves under the hot spot, time( $x$ ), for  $y = 0$  to the edge of the sheet,  $y$ , and  $z = 0$  to the sheet thickness,  $z$ , or a combination ( $yz$ ).

### Heat affected zone cross section, $yz$

The output of the heat affected zone cross section from the thermal code is used for describing the strain zone for the mechanical calculations. The heat affected zone cross section in the  $yz$  plane indicates the shape and extent of the zone, if a boundary temperature for plastic yielding can be specified. In this study aluminium was chosen as the material of interest and analytical calculations by Vollertsen, [14] suggests that the boundary temperature rise for plastic yielding of the material is 94 K.

The following figure illustrates the heat affected zone cross section for laser parameters which result in the temperature gradient mechanism. The 500 K isotherm is chosen as it is higher than the analytical calculation by Vollertsen (367 K) and this is always required in practice as the analytical calculation assumes a total conversion of energy for plastic straining, and this is not the case in reality. When the temperature gradient mechanism is active an elliptical function seems appropriate for the local strain definition. As may be seen from figure 3.4 the maximum

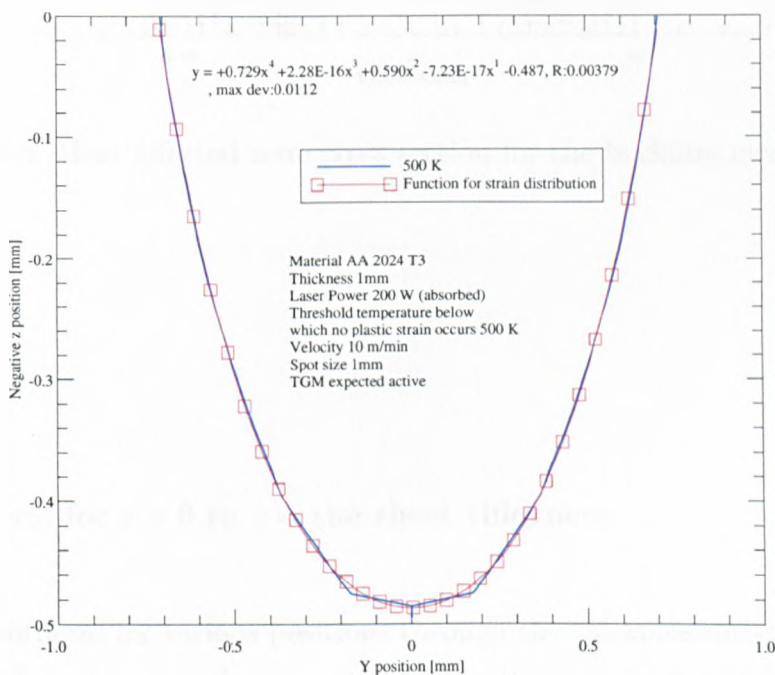


Figure 3.4: Heat affected zone cross section for calculating local strain

depth of the isotherm is approximately half the sheet thickness and under these conditions the temperature gradient mechanism is active.

Increasing the spot size to approximately ten times the sheet thickness and increasing the laser power results in a radically different thermal field and heat affected zone cross section as shown in figure 3.5. In this case the isotherms are rectangular, fully penetrating through the sheet thickness and the “plastic isotherm” is much wider than in the previous case.

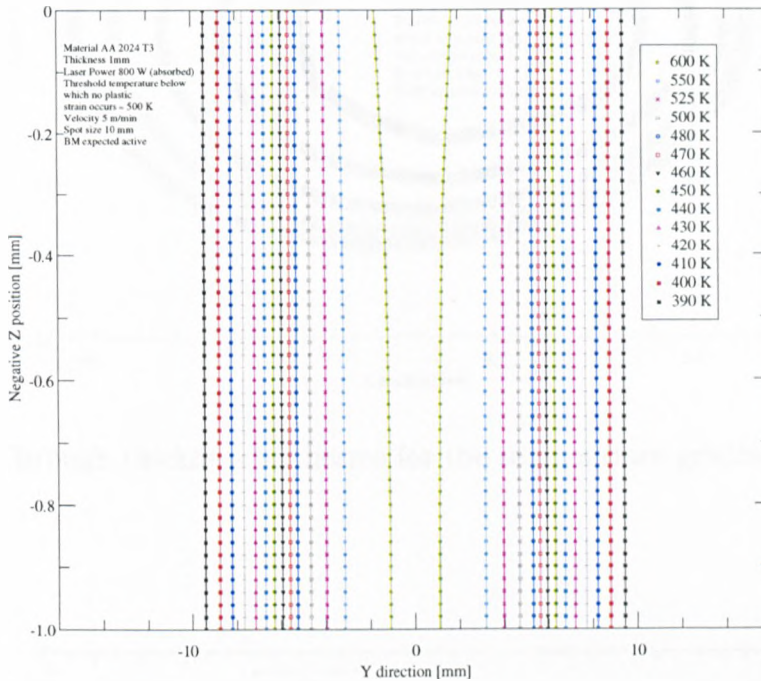


Figure 3.5: Heat affected zone cross section for the buckling mechanism

**Isotherms,  $xy$ , for  $z = 0$  to  $z =$  the sheet thickness**

The 500 K isotherm for various positions through the thickness direction is shown in figure 3.6. It is apparent that they are elliptical in nature when the temperature gradient mechanism is active. This indicates that for these conditions the plastic zone is similar in shape to that of a half ellipsoid. Alternatively when the buckling mechanism conditions are applied the isotherms are again elliptical but the extents of the zone are greater in the lateral  $xy$  directions, as illustrated in figure 3.7.

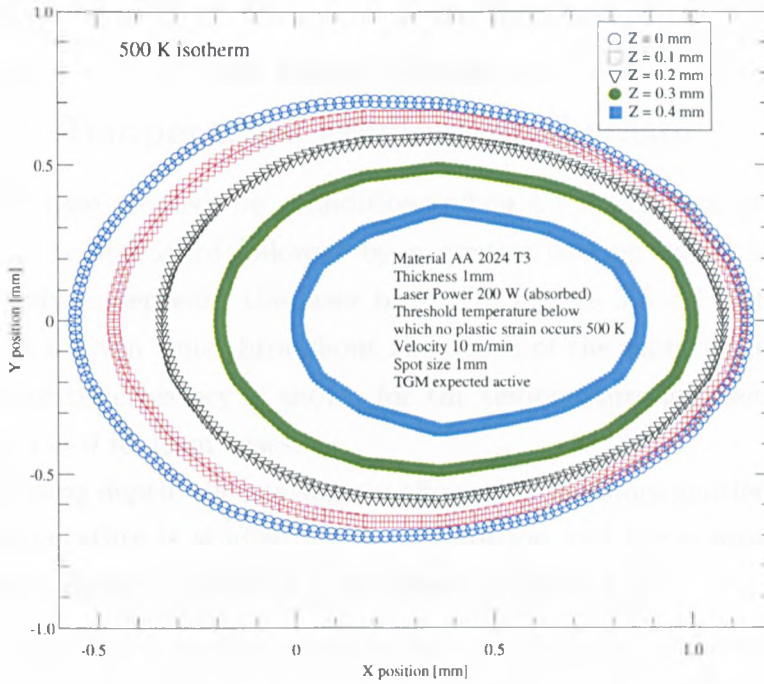


Figure 3.6: Through thickness isotherms for the temperature gradient mechanism

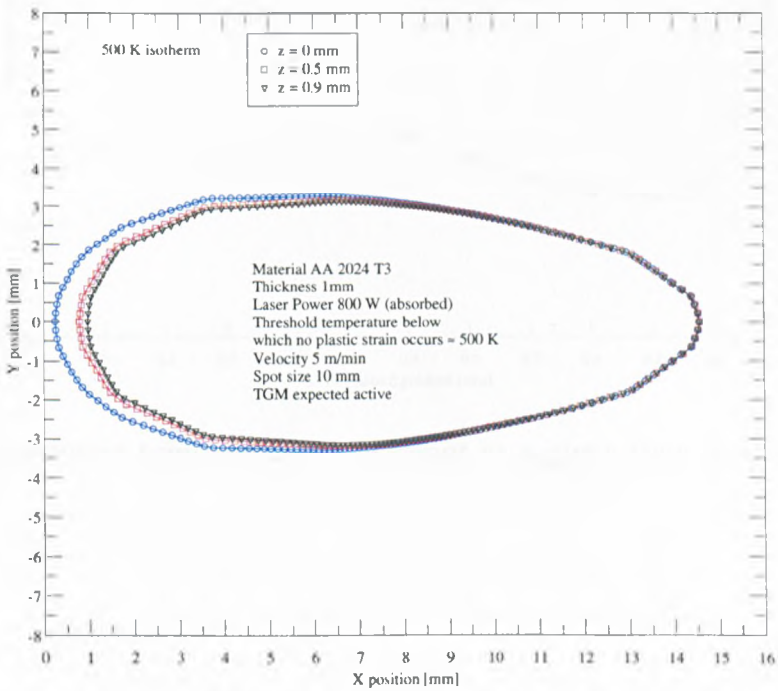


Figure 3.7: Through thickness isotherms for the buckling mechanism

### 3.2.6 Temperature rise as the sheet moves under the hot spot, time( $x$ ), for $y = 0$ to the edge of the sheet $y$ , and $z = 0$ to the sheet thickness $z$ , or a combination ( $yz$ ), Temperature gradient mechanism

For the former case studied, i.e. conditions when a temperature gradient exists, a sharp rise in temperature followed by a gentler cooling curve is expected at positions directly underneath the laser beam. In figures 3.8 - 3.12 the maximum temperature at a given time throughout the depth of the material is plotted, and the temperature time history is shown for the temperature gradient mechanism, for the  $y = 0$ ,  $z = 0$  to 1mm cases.

With increasing depth, the heating - cooling curve becomes gentler, as expected. When the temperature is studied for one  $z$  position and the  $y$  position is varied the temperature decays quickly in  $y$ , as shown in figure 3.13.

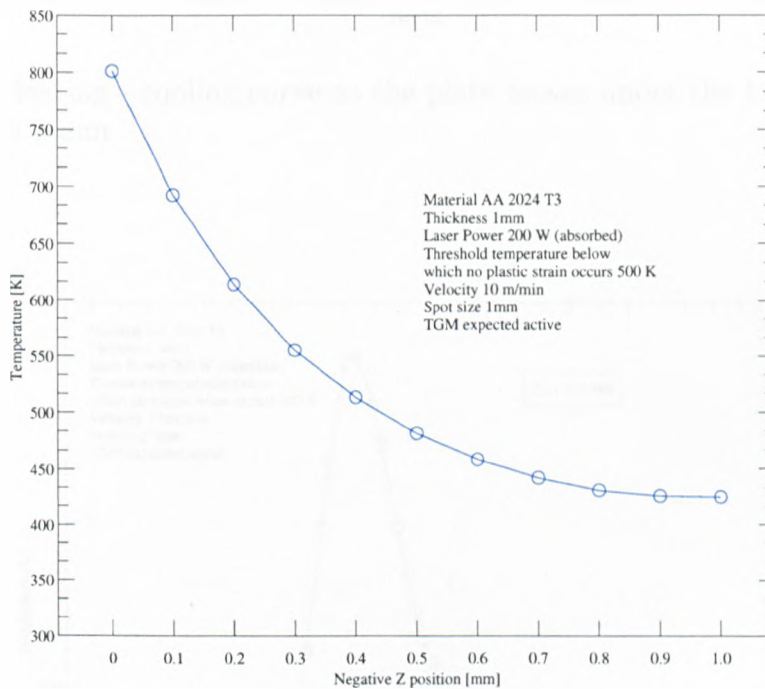


Figure 3.8: Maximum temperature of hot spot at a given time,  $y = 0$  mm,  $z = 0$  to 1 mm

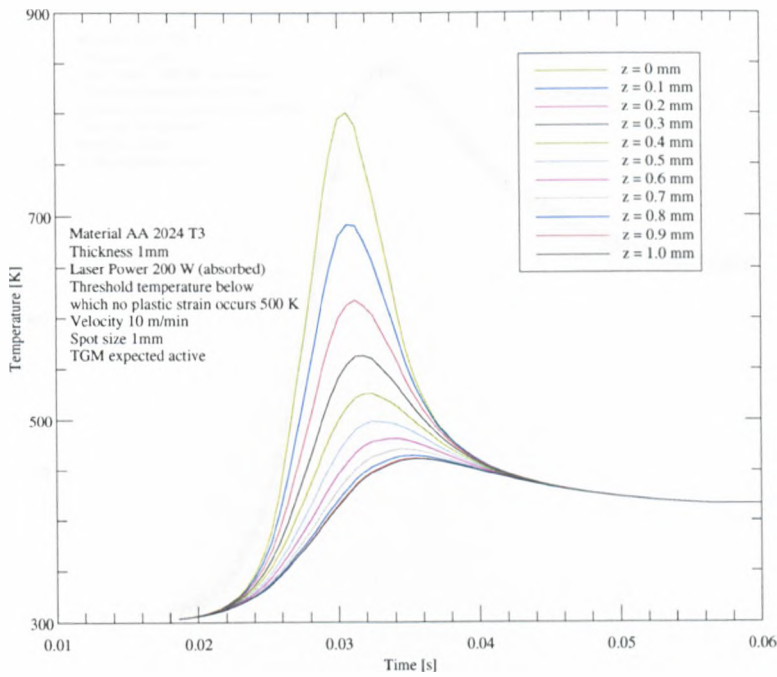


Figure 3.9: Heating - cooling curve as the plate moves under the hot spot,  $y = 0$  mm,  $z = 0$  to 1 mm

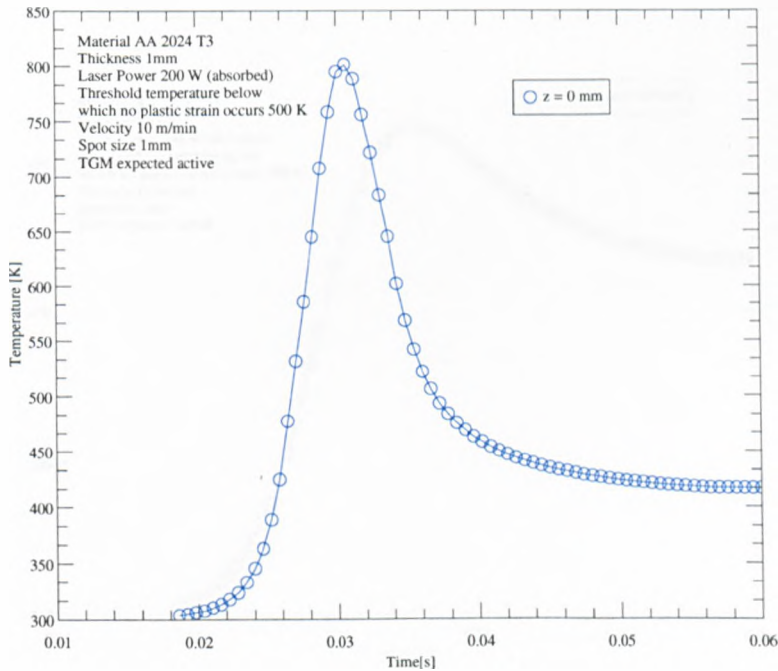


Figure 3.10: Heating - cooling curve as the plate moves under the hot spot,  $y = 0$  mm,  $z = 0.0$ mm

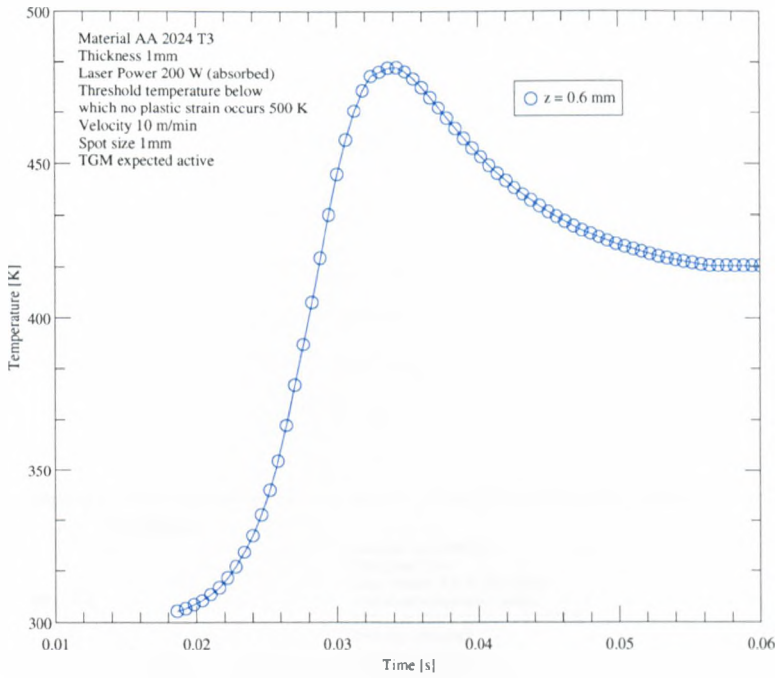


Figure 3.11: Heating - cooling curve as the plate moves under the hot spot,  $y = 0$  mm,  $z = 0.6$ mm

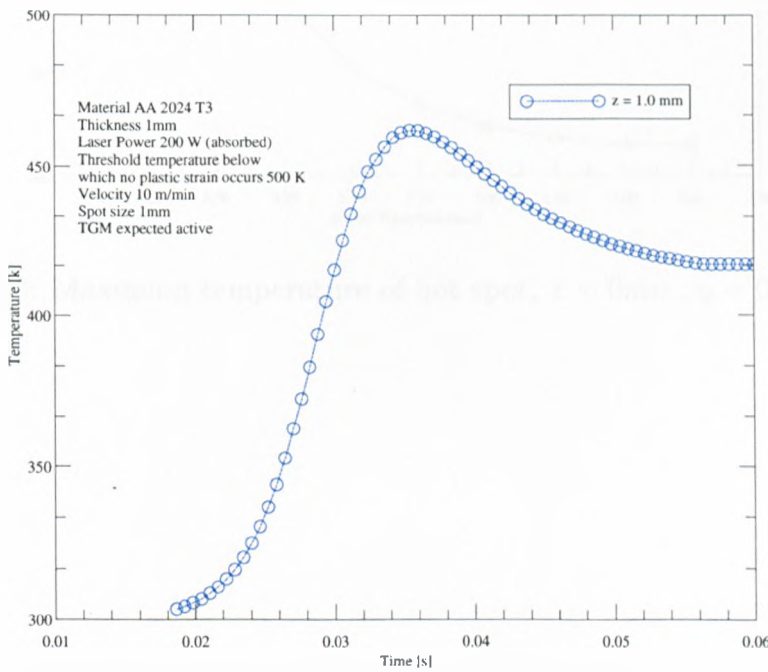


Figure 3.12: Heating - cooling curve as the plate moves under the hot spot,  $y = 0$  mm,  $z = 1.0$ mm

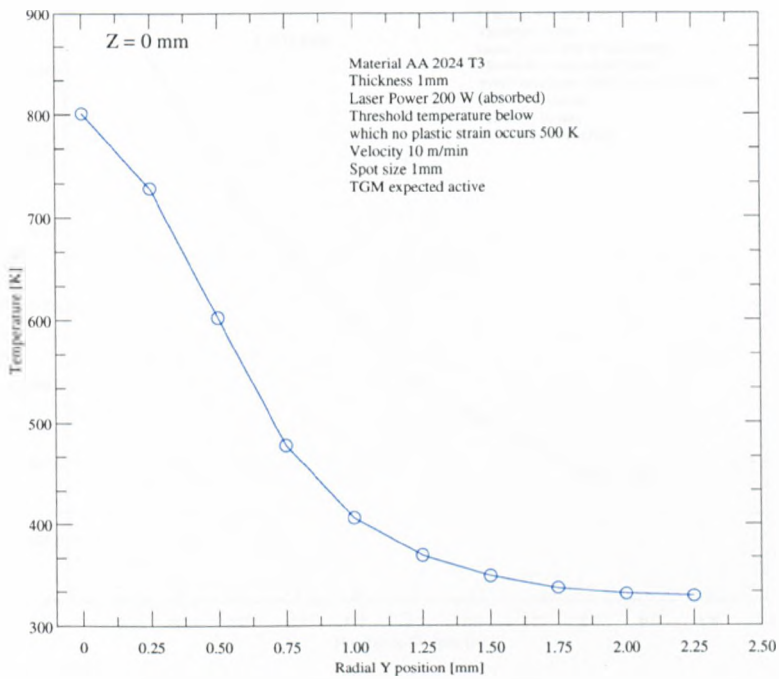


Figure 3.13: Maximum temperature of hot spot,  $z = 0\text{mm}$ ,  $y = 0$  to  $n$  mm

### 3.2.7 Temperature rise as the sheet moves under the hot spot, time( $x$ ), for $y = 0$ to the edge of the sheet $y$ , and $z = 0$ to the sheet thickness $z$ , or a combination ( $yz$ ), Buckling mechanism

Under conditions which initiate the buckling mechanism it would be expected that there would be a much smaller variation of the temperature through the thickness direction than in the case of the temperature gradient mechanism. Figures 3.14 - 3.18 illustrate this. Additionally the more gradual decay of the temperature in the radial  $y$  direction is shown in figure 3.19.

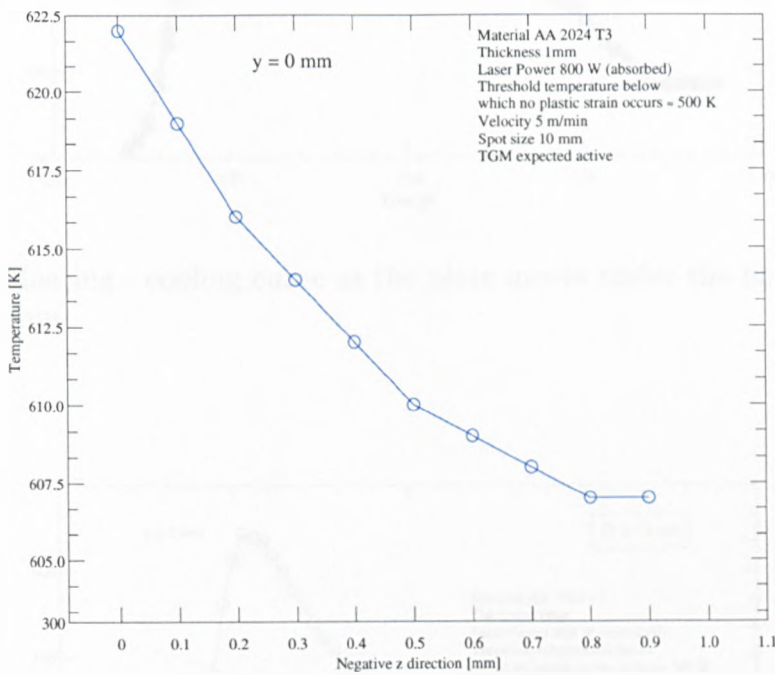


Figure 3.14: Maximum temperature of hot spot at a given time,  $y = 0$  mm,  $z = 0$  to 0.9 mm, Buckling mechanism

### 3.2.8 Defining the shape function for the plastic strain zone, $b_z$

It is reasonable to assume that under laser forming conditions (non-melting regime) with a gaussian laser beam that the resultant isotherms are elliptical in nature when the temperature gradient mechanism is active. If forming is taking place in the high energy to melting regime with a large defocused laser spot, a circular or rectangular profile for the plastic strain distribution seems appropriate. Here the former case is studied and the strain profile is idealised with an elliptic shape

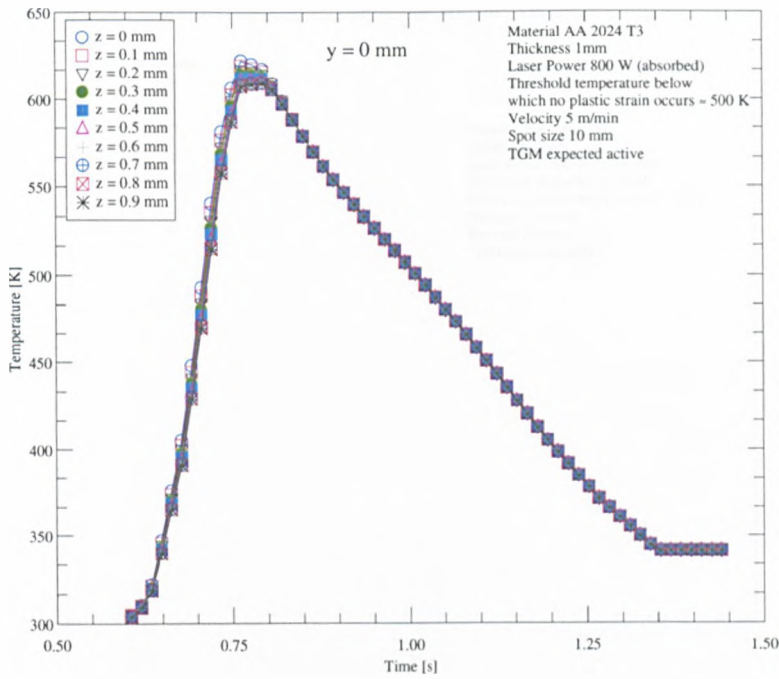


Figure 3.15: Heating - cooling curve as the plate moves under the hot spot,  $y = 0$  mm,  $z = 0..1$ mm

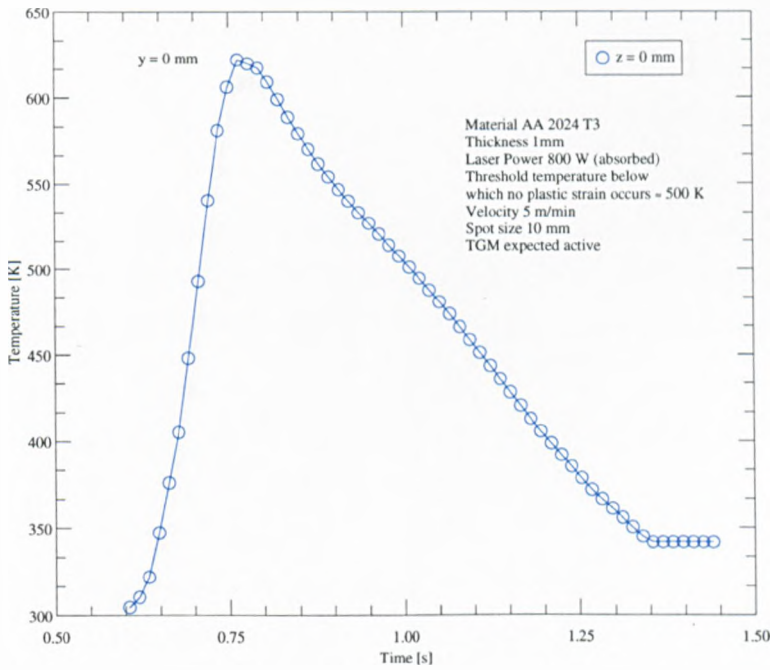


Figure 3.16: Heating - cooling curve as the plate moves under the hot spot,  $y = 0$  mm,  $z = 0.0$ mm

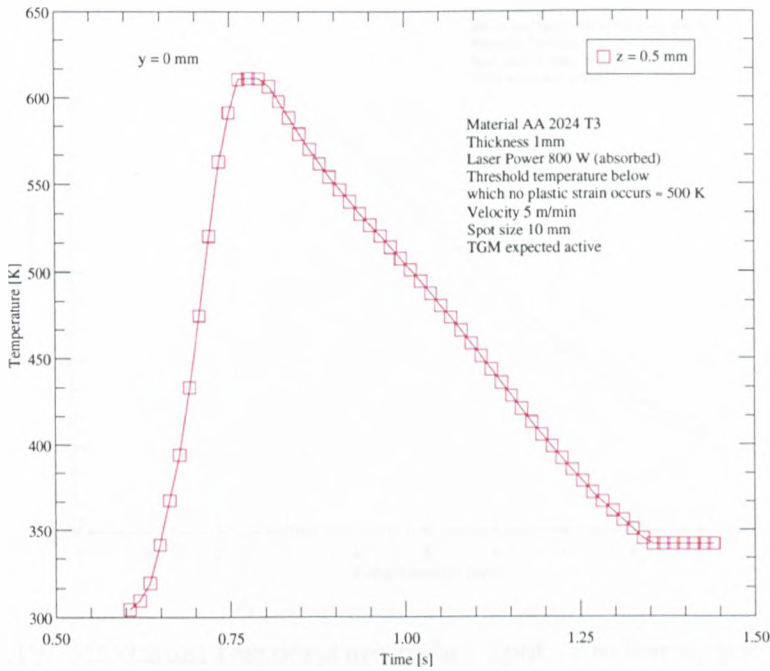


Figure 3.17: Heating - cooling curve as the plate moves under the hot spot,  $y = 0$  mm,  $z = 0.5$ mm

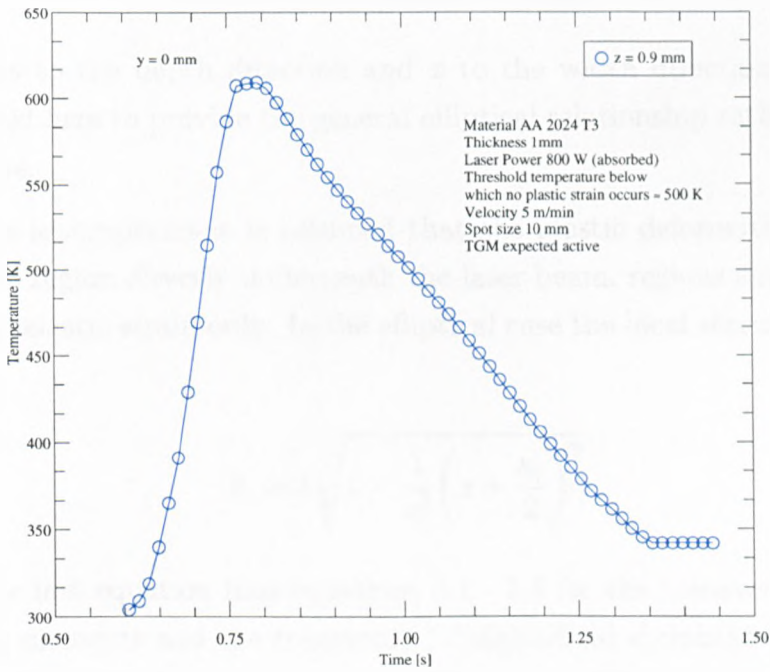


Figure 3.18: Heating - cooling curve as the plate moves under the hot spot,  $y = 0$  mm,  $z = 0.9$ mm

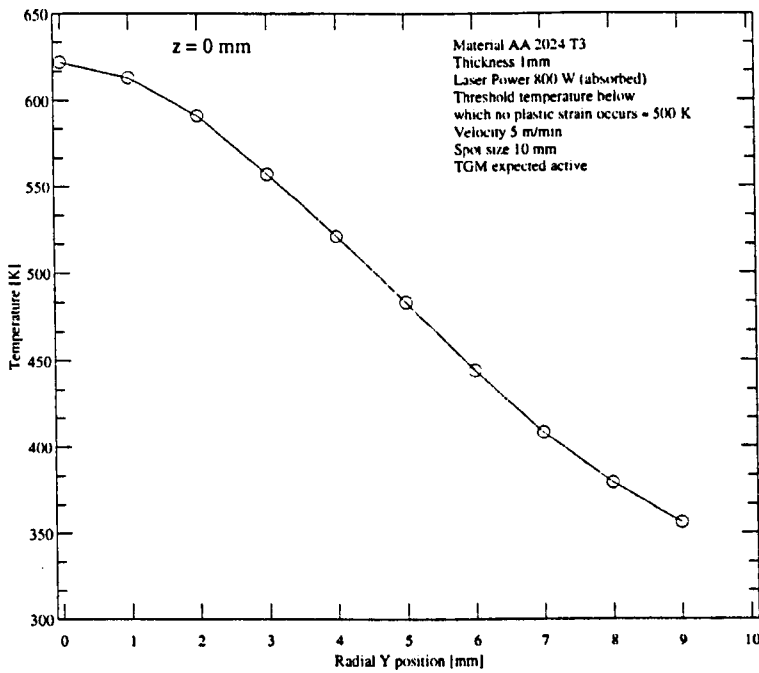


Figure 3.19: Maximum temperature of hot spot,  $z = 0\text{mm}$ ,  $y = 0$  to  $n$  mm

function. Alternatively the parametric equation given in figure 3.4 could be used. It is given by:

$$y = 0.729x^4 + 0.59x^2 - 0.487 \quad (3.100)$$

Here  $y$  refers to the depth direction and  $x$  to the width direction. The former case is studied here to provide the general elliptical relationship rather than a case specific shape.

From the assumptions it is assumed that the plastic deformation occurs primarily in the region directly underneath the laser beam, regions outside this zone experiencing elastic strain only. In the elliptical case the local strain function  $b_z$  is defined by:

$$b_z = b \sqrt{1 - \frac{1}{s_1^2} \left( z + \frac{s_0}{2} \right)^2} \quad (3.101)$$

Inserting the last equation into equations 3.1 - 3.5 for the transverse / longitudinal bending moments and the transverse / longitudinal shrinkage forces, and the equation for the inherent strain and then integrating yields:

$$M_{tr} = \frac{E\epsilon_{in}}{6} s_1 s_0 \left( \frac{3\pi}{4} - 2 \frac{s_1}{s_0} \right) \quad (3.102)$$

$$M_{lg} = E\epsilon_{in} \frac{(1-\nu)}{2} b s_1 \left( \frac{s_0}{2} - \frac{s_1}{3} \right) \quad (3.103)$$

and for the in plane forces:

$$N_{tr} = \frac{E\epsilon_{in}\pi}{4} R_{hole} \quad (3.104)$$

$$N_{lg} = E(1-\nu)\epsilon_{in} \frac{b}{2} R_{hole} \quad (3.105)$$

These equations are numerically evaluated to examine their significance in the next section.

### 3.3 The Transverse and Longitudinal forces and moments evaluation for the thermal case presented in section 3.2.6

Setting the boundary temperature for plastic flow and evaluating the forces and moments tables 3.1 - 3.2 were produced.

What is very important in the evaluation of these equations is the function relating the temperature to the mechanical properties. These functions are plotted in figures 3.20 and 3.21 (\*private communication with Aluminium supplier - Appollo), which show Yield Strength and Elastic modulus respectively. As may be seen from the table the value of the bending moment changes as the plate thickness increases, whereas there is no dependency on the in plane shrinkage on the material thickness. Obviously this ignores the coupling between the in plane and the out of plane deformation, but this is omitted as it is a first attempt to apply this analysis to laser forming.

#### Superposition of the bending moments in perpendicular directions

Given the difficulty with combining the in plane and the out of plane deformation solution, the out of plane deformation is assumed here to cause the bending. Therefore to calculate the out of plane bend angles in perpendicular directions only the superposition of bending moments is considered. Proceeding from Timoshenko [57] pp.288-290 in pure bending with bending moments in two perpendicular directions superposition must be considered. Let  $R_1$  and  $R_2$  be the curvatures in the planes parallel and transverse to the laser scan line, and let  $M_1$  and  $M_2$  be

Width of Plastic zone [m]	Inherent Strain	Depth of plastic zone [m]	Sheet thickness [m]	Transverse Bending Moment [Nm]
0.0014	0.0062	0.0005	0.0010	51.51
0.0014	0.0062	0.0005	0.0010	47.03
0.0014	0.0062	0.0005	0.0009	46.14
0.0014	0.0062	0.0005	0.0009	45.24
0.0014	0.0062	0.0005	0.0009	44.35
0.0014	0.0062	0.0005	0.0009	43.45
0.0014	0.0062	0.0005	0.0009	42.56
0.0014	0.0062	0.0005	0.0009	41.66
0.0014	0.0062	0.0005	0.0009	40.77
0.0014	0.0062	0.0005	0.0009	39.87
0.0014	0.0062	0.0005	0.0009	38.98
0.0014	0.0062	0.0005	0.0009	38.08
0.0014	0.0062	0.0005	0.0008	37.19
0.0014	0.0062	0.0005	0.0008	36.30
0.0014	0.0062	0.0005	0.0008	35.40
0.0014	0.0062	0.0005	0.0008	34.51
0.0014	0.0062	0.0005	0.0008	33.61
0.0014	0.0062	0.0005	0.0008	32.72
0.0014	0.0062	0.0005	0.0008	31.82
0.0014	0.0062	0.0005	0.0008	30.93
0.0014	0.0062	0.0005	0.0008	30.03
0.0014	0.0062	0.0005	0.0008	29.14
0.0014	0.0062	0.0005	0.0007	28.24
0.0014	0.0062	0.0005	0.0007	27.35
0.0014	0.0062	0.0005	0.0007	26.45
0.0014	0.0062	0.0005	0.0007	25.56
0.0014	0.0062	0.0005	0.0007	24.66
0.0014	0.0062	0.0005	0.0007	23.77
0.0014	0.0062	0.0005	0.0007	22.87
0.0014	0.0062	0.0005	0.0007	21.98
0.0014	0.0062	0.0005	0.0007	21.08
0.0014	0.0062	0.0005	0.0007	20.19
0.0014	0.0062	0.0005	0.0006	19.29
0.0014	0.0062	0.0005	0.0006	18.40
0.0014	0.0062	0.0005	0.0006	17.50
0.0014	0.0062	0.0005	0.0006	16.61
0.0014	0.0062	0.0005	0.0006	15.71
0.0014	0.0062	0.0005	0.0006	14.82
0.0014	0.0062	0.0005	0.0006	13.92
0.0014	0.0062	0.0005	0.0006	13.03
0.0014	0.0062	0.0005	0.0006	12.13
0.0014	0.0062	0.0005	0.0006	11.24
0.0014	0.0062	0.0005	0.0005	10.34

Table 3.1: Width and depth of plastic zone, inherent strain and transverse bending moment for the case presented in figure 3.4

Transverse Shrinkage force [N]	Longitudinal bending moment [Nm]	Longitudinal shrinkage force [N]	Transverse Curvature [m]	Longitudinal Curvature [m]
501146.28	0.037	312.67	0.118	163.30
501146.28	0.034	312.67	0.111	151.36
501146.28	0.033	312.67	0.108	146.76
501146.28	0.033	312.67	0.107	144.50
501146.28	0.032	312.67	0.105	142.26
501146.28	0.032	312.67	0.104	140.05
501146.28	0.031	312.67	0.103	137.87
501146.28	0.031	312.67	0.102	135.71
501146.28	0.030	312.67	0.100	133.58
501146.28	0.034	312.67	0.109	149.05
501146.28	0.029	312.67	0.099	131.48
501146.28	0.029	312.67	0.098	129.40
501146.28	0.028	312.67	0.097	127.35
501146.28	0.028	312.67	0.096	125.33
501146.28	0.027	312.67	0.095	123.34
501146.28	0.027	312.67	0.094	121.38
501146.28	0.026	312.67	0.093	119.44
501146.28	0.025	312.67	0.092	117.54
501146.28	0.025	312.67	0.091	115.66
501146.28	0.024	312.67	0.090	113.82
501146.28	0.024	312.67	0.089	112.01
501146.28	0.023	312.67	0.088	110.23
501146.28	0.023	312.67	0.087	108.48
501146.28	0.022	312.67	0.086	106.77
501146.28	0.022	312.67	0.086	105.09
501146.28	0.021	312.67	0.085	103.44
501146.28	0.020	312.67	0.085	101.84
501146.28	0.020	312.67	0.084	100.27
501146.28	0.019	312.67	0.084	98.74
501146.28	0.019	312.67	0.083	97.26
501146.28	0.018	312.67	0.083	95.81
501146.28	0.018	312.67	0.083	94.41
501146.28	0.017	312.67	0.083	93.06
501146.28	0.017	312.67	0.083	91.76
501146.28	0.016	312.67	0.083	90.51
501146.28	0.015	312.67	0.083	89.31
501146.28	0.015	312.67	0.084	88.18
501146.28	0.014	312.67	0.084	87.11
501146.28	0.014	312.67	0.085	86.11
501146.28	0.013	312.67	0.086	85.19
501146.28	0.013	312.67	0.088	84.35
501146.28	0.012	312.67	0.090	83.60
501146.28	0.012	312.67	0.093	82.95

Table 3.2: Moments, forces and curvatures for the case presented in figure 3.4

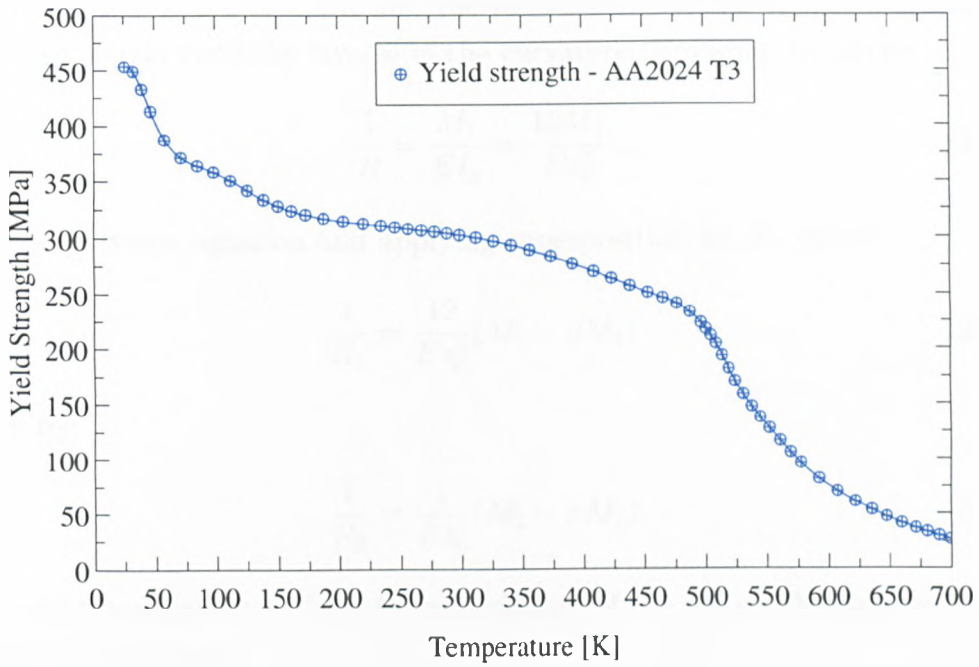


Figure 3.20: Yield strength as a function of temperature - AA2024 T3 (taken from private communication with Aluminium supplier - Appollo)

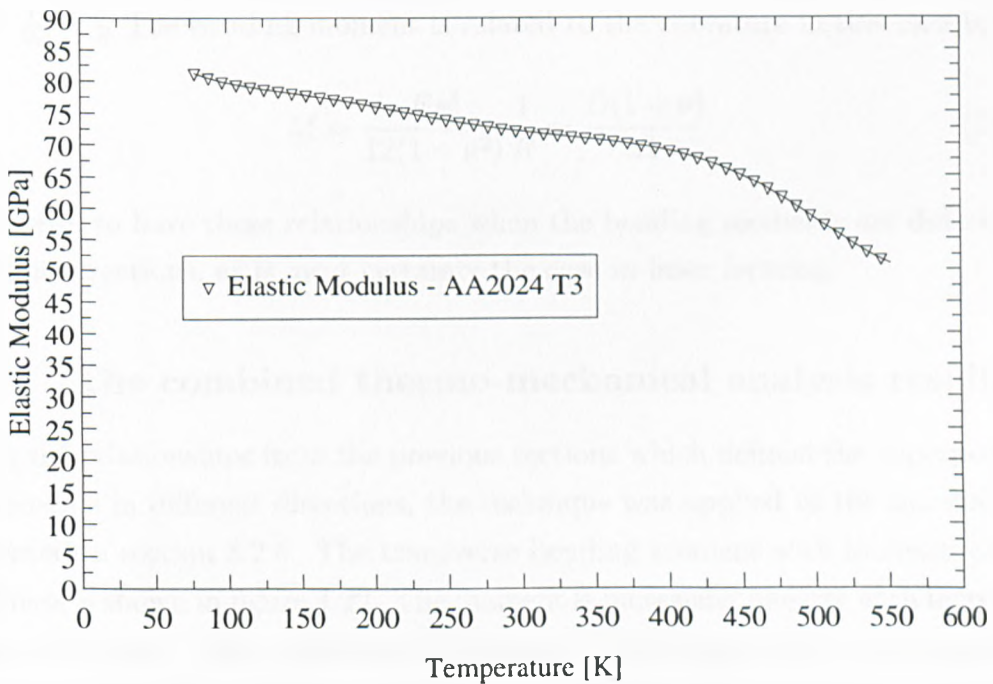


Figure 3.21: Elastic modulus as a function of temperature - AA2024 T3(taken from private communication with Aluminium supplier - Appollo)

the bending moments in these directions. From previous discussions in chapter two the fraction of the moment and the product of the elastic modulus and the moment of inertia yield the inverse of the curvature. Revising this gives:

$$\frac{1}{R} = \frac{M_1}{EI_y} = \frac{12M_1}{Es_0^3} \quad (3.106)$$

Using the previous equation and applying superposition for  $R_1$  yields:

$$\frac{1}{R_1} = \frac{12}{Es_0^3}(M_1 - \nu M_2) \quad (3.107)$$

and for  $R_2$ :

$$\frac{1}{R_2} = \frac{1}{Es_0^3}(M_2 - \nu M_1) \quad (3.108)$$

These equations make use of the flexural rigidity of the plate. The *flexural rigidity* of a plate is given by:

$$\frac{Es_0^3}{12(1 - \nu^2)} = \text{Flexural rigidity} = D \quad (3.109)$$

If the applied bending moment is the same in both directions, then the curvatures are the same as well, and a spherical surface results: If  $M_1 = M_2 = M$  then  $\frac{1}{R_1} = \frac{1}{R_2} = \frac{1}{R}$  The bending moment is related to the curvature in this case by:

$$M = \frac{Es_0^3}{12(1 - \nu^2)} \frac{1}{R} = \frac{D(1 + \nu)}{R} \quad (3.110)$$

It is useful to have these relationships when the bending moments are different in different directions, as is most certainly the case in laser forming.

### 3.3.1 The combined thermo-mechanical analysis results

Using the relationships from the previous sections which defined the superposition of moments in different directions, the technique was applied to the thermal case presented in section 3.2.6. The transverse bending moment with increasing sheet thickness is shown in figure 3.22. The moment is increasing linearly with increasing sheet thickness. The transverse curvature and bend angle with increasing sheet thickness have been calculated and are shown in figures 3.23 and 3.24. Interestingly there is a minimum point for the transverse curvature. It occurs at a sheet thickness of 0.63 mm. This may be due to the fact that the bending moment is the integral value from zero to the thickness of the plastic zone. However when the thickness

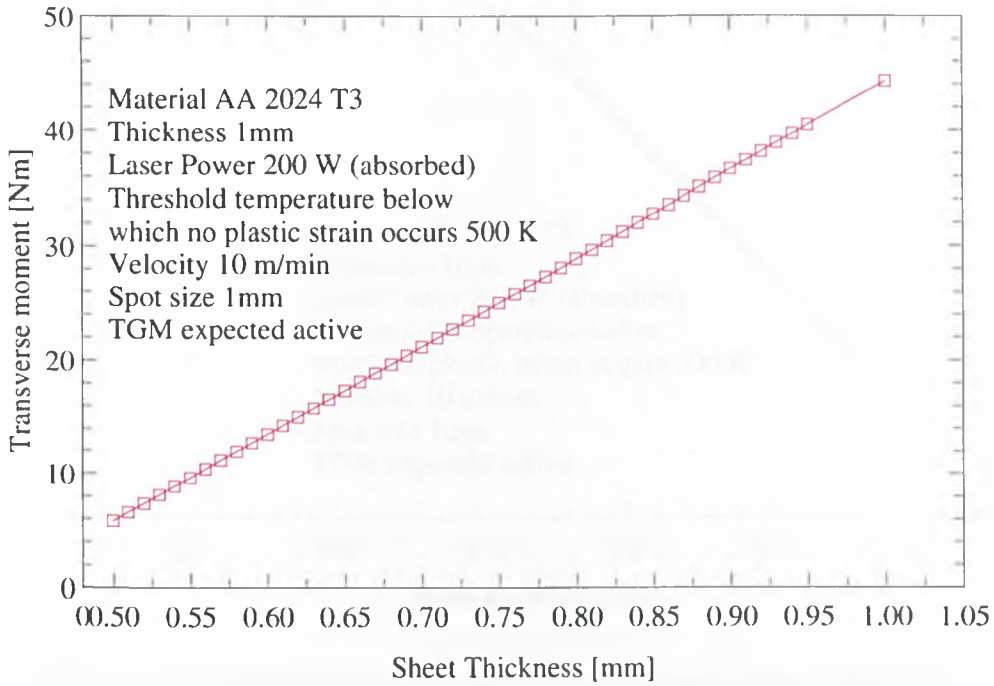


Figure 3.22: Transverse bending moment with increasing sheet thickness

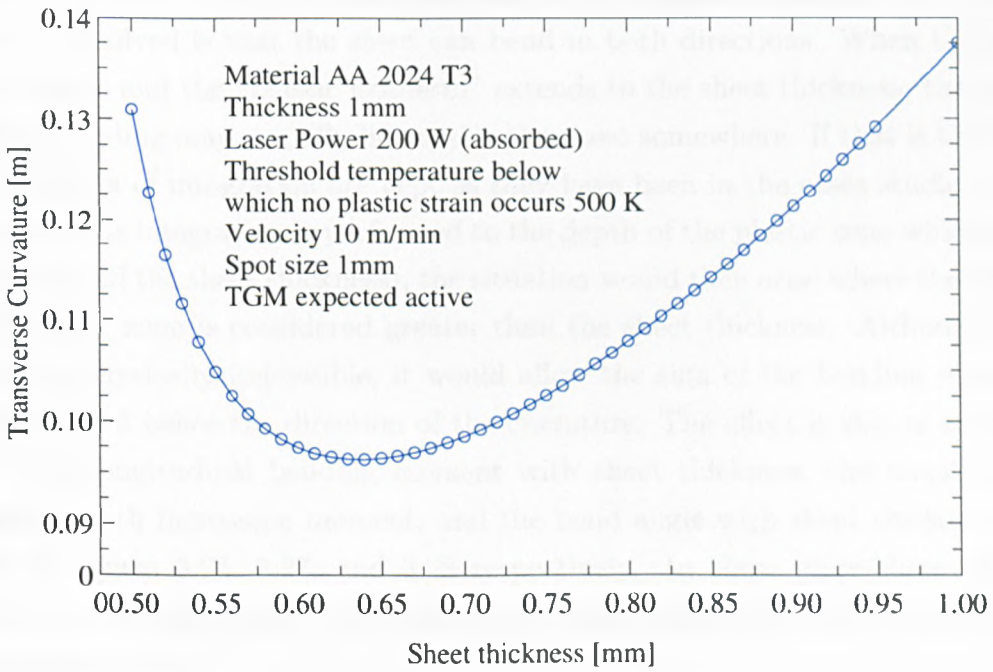


Figure 3.23: Transverse curvature with increasing sheet thickness

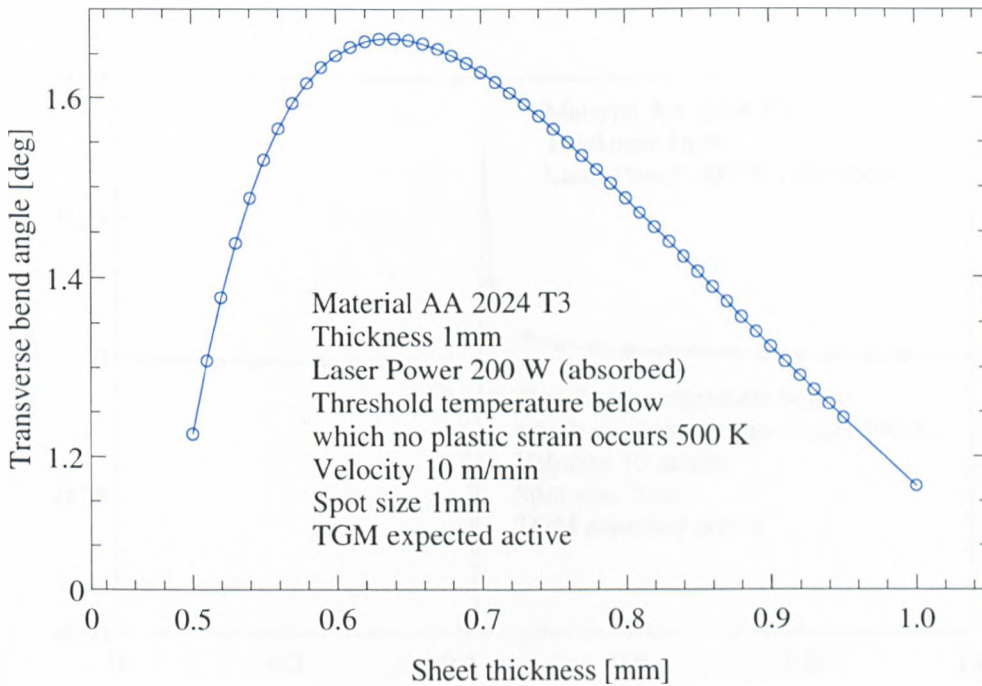


Figure 3.24: Transverse bend angle with increasing sheet thickness

of the plastic zone approaches that of the sheet thickness the curvature goes up. Probably the limits of integration should then be changed from zero to the sheet thickness (in equation 3.1), rather than the depth of the plastic zone, as they are now both the same. This is a moot point and as yet remains un-solved. The reason why it is unsolved is that the sheet can bend in both directions. When the heat input is large and the “plastic isotherm” extends to the sheet thickness, the pivot point for bending may actually lie outside the sheet somewhere. If that is the case and the limits of integration are kept as they have been in the cases studied here (i.e. where the integration is performed to the depth of the plastic zone which may extend beyond the sheet thickness), the situation would then arise where the depth of the plastic zone is considered greater than the sheet thickness. Although this does seem physically impossible, it would allow the sign of the bending moment to change, and hence the direction of the curvature. The effect is shown in figure 3.25. The longitudinal bending moment with sheet thickness, the longitudinal curvatures with increasing moment, and the bend angle with sheet thickness are shown in figures 3.26, 3.27, and 3.28 respectively. In these plots there are no pronounced turning points. As expected the longitudinal bending is less than in the transverse case.

In figure 3.28, the longitudinal bending as described by equation 3.3 is presented. As the length of the zone taken for the bend angle calculation is increased, the curvature becomes greater as shown for the three sheet lengths. The calculation

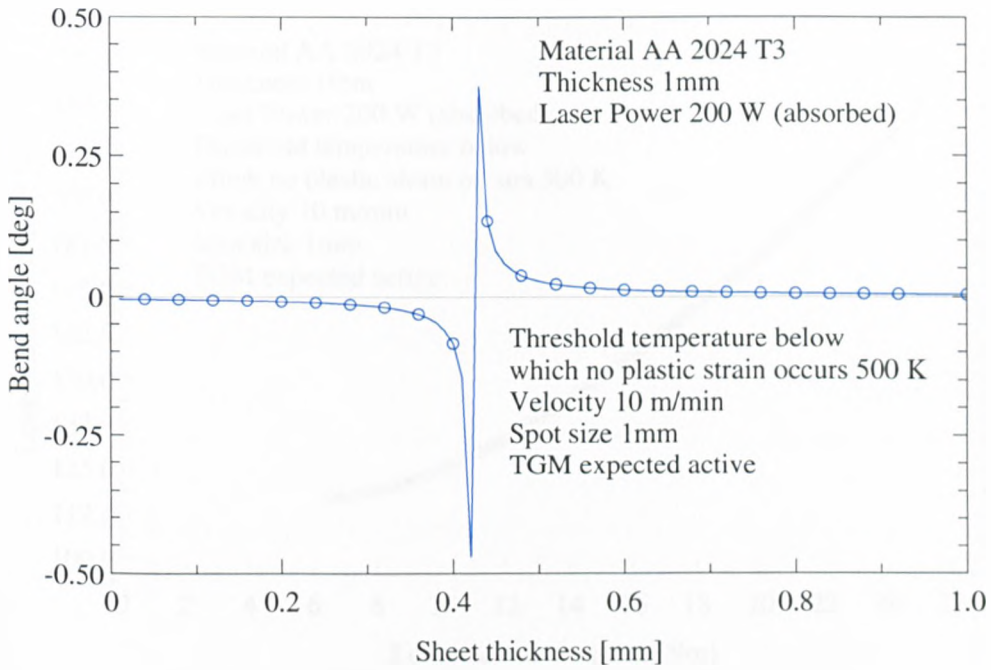


Figure 3.25: Pseudo transverse bend angle (allowing plastic zone to extend beyond sheet thickness)with sheet thickness

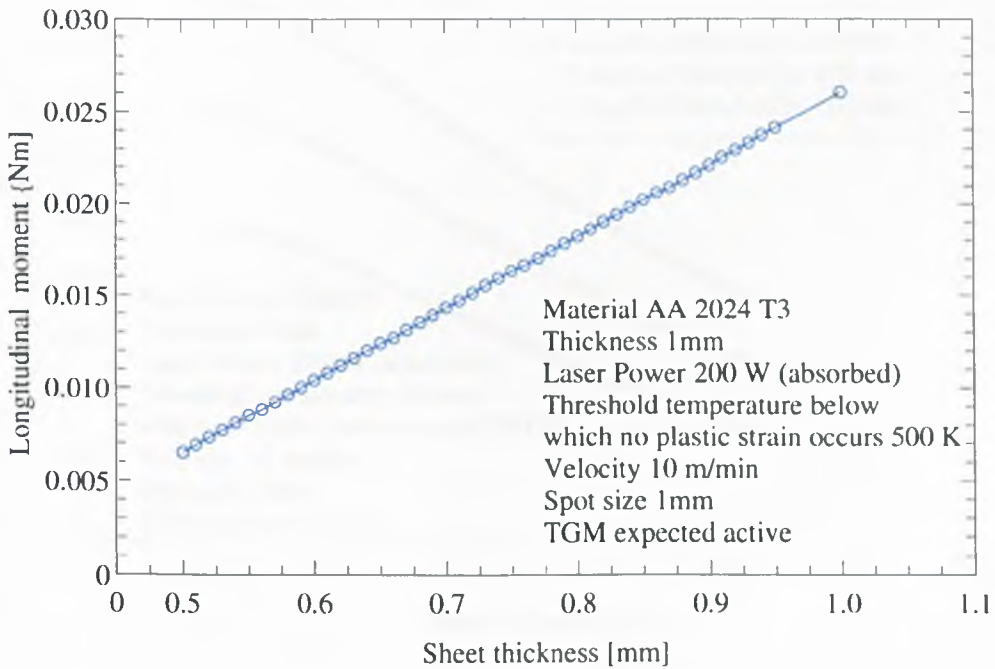


Figure 3.26: Longitudinal bend angle with increasing sheet thickness

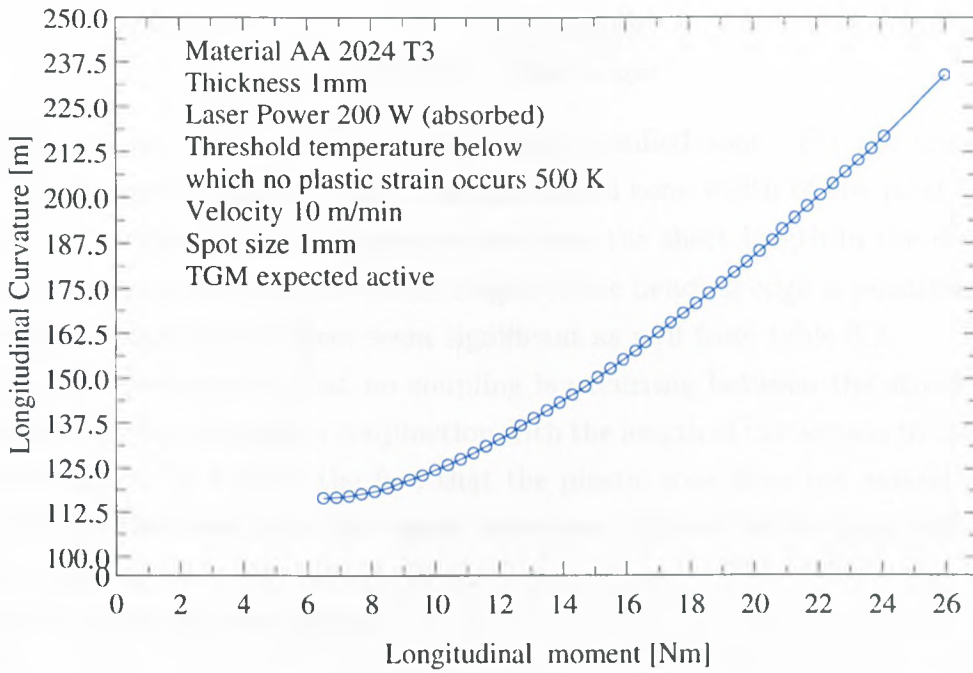


Figure 3.27: Longitudinal curvature with increasing longitudinal moment

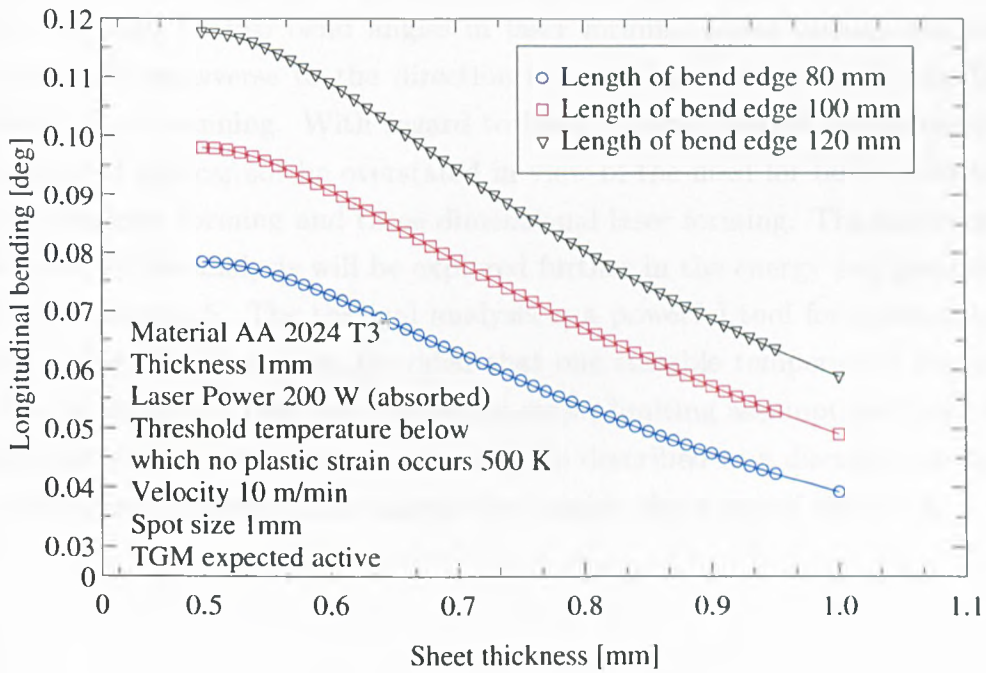


Figure 3.28: Longitudinal bend angle with increasing sheet thickness for three sheet lengths in the direction of scanning

for the curvature is related to the bend angle by:

$$\frac{1}{\text{curvature}} = \frac{2 * \text{length}}{\text{bend angle}} \quad (3.111)$$

The "length" is related to the extent of the plastified zone. For the transverse case, this is approximated as twice the isothermal zone width of the plastic zone. For the longitudinal case it is taken to be twice the sheet length in the direction of scanning, assuming that the entire length of the bending edge is plastified. The forces in the plane of the sheet seem significant as well from table 3.2.

Using the assumption that no coupling is occurring between the stresses, the inherent strain can be used in conjunction with the length of the section to calculate the new length. In view of the fact that the plastic zone does not extend all the way through the sheet, only the upper layers can shorten, which must add to the applied bending moment, taking the sheet out of plane. This will have to be the subject of a future investigation.

### 3.3.2 Summary of theoretical analysis

In summary, it may be seen that there are other forces and moments acting in laser forming apart from the transverse bending moment which has been the subject of several previous investigations [14, 16, 17, 19, 21, 25]. This indicates that there should in theory be two bend angles in laser forming under certain conditions, i.e. the angle transverse to the direction of scanning and the angle parallel to the direction of scanning. With regard to laser forming process development the importance of this cannot be overstated in view of the need for both uniform one dimensional laser forming and three dimensional laser forming. The experimental application of this analysis will be explored further in the energy and geometrical sections of chapter 5. The thermal analysis is a powerful tool for estimating the extents of the plastified zone, provided that one suitable temperature for plastic flow can be specified. That was one of the major limiting assumptions made here, as the elastic-plastic interface cannot really be described as a discrete isotherm in time and space. However that analysis lies outside the scope of this work.

# Chapter 4

## Experimental Procedure

### 4.1 Summary

The experimental procedures used in the study on laser forming of the aerospace alloys are described in this chapter. The themes of investigation included energy, geometry, and material. Additionally the procedures used in the development study on integrated 2D process demonstration are presented.

### 4.2 Experimental strategy

There were too many variables for a full orthogonal set of experiments. Instead the experiments were arranged as far as possible so that groups of laser bends had all controlled parameters constant except for the one being investigated. This enabled the parametric investigation of the governing variables on the materials being studied.

### 4.3 Bend angle measurement

Critical to the success of the experimentation was the ability to measure accurately the deflection of the samples at various locations over the surface, and in a non-intrusive manner. In the fundamental investigation a simple optical device composed of a CCD camera, a moveable cross-hairs generator and a monitor was used in conjunction with the CNC (Computer Numerical Control)x-y tables as illustrated in figure 4.1. Subsequently a laser stripe system comprising of a laser, a CCD camera and image processing software was integrated into the laser forming demonstrator system and used for surface profiling. This system is shown in figure 4.9.

The deflection was measured prior to processing to calculate any initial bend angle. In the majority of cases the bend angle measurement was carried out after processing for scans 1 to 5 and after 10. In the study examining the bend angle with increasing number of laser scans this number was extended to 30 scans.

### 4.3.1 Measurement Method

A CCD camera was focused on the edge of the plate mounted in the clamp. It was ensured that the camera and the clamp were perfectly horizontal. The moveable cross-hairs which were visible via a monitor were brought to a point tangential to the top surface of the plate edge. Since the xyz stages of the workpiece handling system could be moved in 1 micron steps this was achieved to a high degree of accuracy. The base co-ordinates of the cross hairs at that point were recorded from the motion control unit monitor or the xyz stages. After the plate had been irradiated, strained plastically and had deflected, the moveable cross hairs were brought to a point tangential to the top surface of the plate edge again by moving the yz stages. The co-ordinates of the new point were recorded and the process

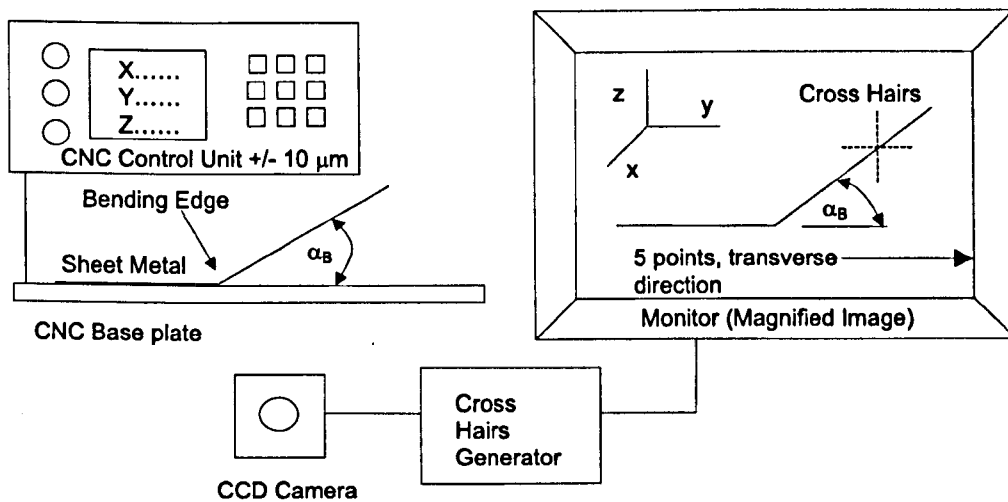


Figure 4.1: Initial bend angle measurement device

was repeated five times along the plate length. Then the relative displacement of the sample in the yz directions was calculated. The slope of the line through these co-ordinates yielded the tan of the angle and hence the bend angle was obtained by taking the arctan of the slope. The accuracy of the measurement depended on the success with which the crosshairs could be brought to a point tangential to the deflected surface. The camera which magnified the image of the sheet edge assisted with this. The accuracy was found to be within 10 microns. The system was calibrated against samples which had a known bend angle and it

showed excellent agreement.

## 4.4 Materials and dimensions

The alloy sheet used in each of the experiments was aluminium Al2024 T3 or hot rolled Ti6Al4V titanium alloy, see tables 4.1 and 4.2 for percentages of the alloying elements added to the aluminium and titanium respectively.

Element	Cu	Mg	Mn	Fe	Zn	Si	Cr	Ti	V	Zr	Other
%	4.61	1.39	0.60	0.21	0.14	0.11	0.01	0.01	0.01	0.001	0.05

Table 4.1: Elemental composition of AA 2024 - T3

Element	C	Fe	N	O	Al	V	H
%	0.08	0.25	0.05	0.20	5.50-6.65	3.5-4.5	0.015

Table 4.2: Elemental composition of Ti6Al4V

### 4.4.1 AA 2024 T3 alloy

The AA 2024 T3 alloy is an aluminium copper magnesium alloy. It has a clad layer of pure aluminium on both the upper and lower surfaces. It is solution heat treated and cold rolled. Solution heat treatment proceeds by heating a wrought metal to the required temperature, maintaining it at that temperature until constituents can enter into solid solution, and finally cooling it at the required rate to hold the constituents in solution. The AA 2024 solution heat treatment increases the level of hardening solutes such as copper, magnesium and silicon entering the solid solution in the aluminium matrix. The temperature at which the maximum amount is soluble corresponds to the eutectic temperature. Temperatures are usually restricted to below the maximum level in order to avoid overheating and partial melting. Cold work after the solution heat treatment improves the strength and toughness of the AA 2024 alloy. A phase diagram typical of aluminium-copper alloys is illustrated in figure 4.2.

### 4.4.2 Ti6Al4V alloy

The production of titanium alloys is complex and thus it is necessary to introduce a small amount of background on the compositional details in order to make the metallurgical analysis of laser forming meaningful. Titanium is an allotropic element and at a temperature of 1155 K it transforms from a hexagonal close packed

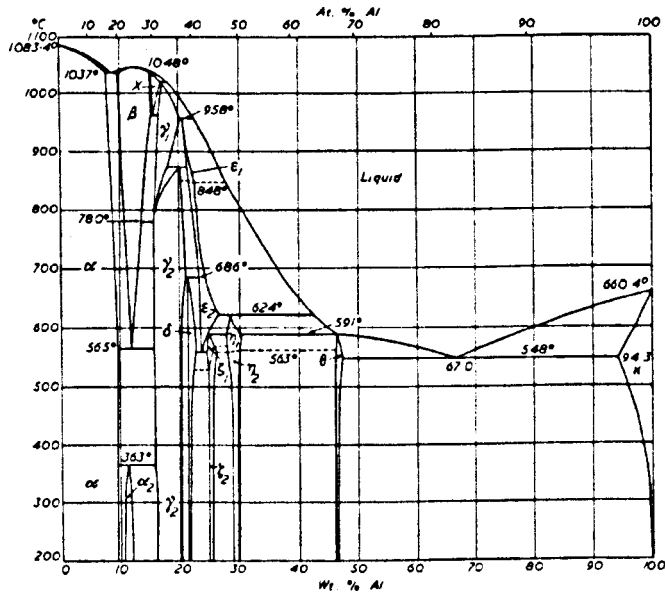


Figure 4.2: Phase diagram for aluminium copper based alloy

crystal structure, called the alpha phase ( $\alpha$ ), to a body centered cubic structure, called the beta phase ( $\beta$ ). With a high powered laser beam this temperature is achievable with ease. Elements may be added to produce alloys with an alpha, beta or mixed alpha-beta microstructure. Titanium alloys are classified into three categories: alpha alloys, beta alloys and alpha-beta alloys. The category does not refer to the equilibrium constitution. It corresponds to the principal room temperature microstructure after heat treatment. Alloying elements can be either alpha or beta stabilisers. The temperature for transformation from  $\alpha$ , and  $\beta$  or from  $\alpha$  to all  $\beta$  is known as the  $\beta$  transus temperature. It is the lowest equilibrium temperature at which the material is 100 %  $\beta$ . Below the  $\beta$  transus temperature, titanium is a mixture of  $\alpha$  and  $\beta$  if the material contains some  $\beta$  stabilisers. The  $\beta$  transus is important as processing is often carried out just above or below it. Alpha stabilisers, for example, aluminium and oxygen, dissolve in the  $\alpha$ -phase and increase the temperature at which this phase is stable. They do this by raising the  $\alpha$ - $\beta$  transus. There are two types of beta stabilisers; isomorphous elements, for example, vanadium and molybdenum, which stabilise the  $\beta$ -phase at lower temperatures, by lowering the  $\alpha$ - $\beta$  transus. The second type of beta stabilisers form a beta eutectoid.

The alloy in this investigation is Ti6Al4V. It is an alpha-beta alloy containing an  $\alpha$  stabiliser (aluminium) and a  $\beta$  stabiliser (vanadium). When this alloy is slow cooled from the beta region, alpha begins to form below the  $\beta$  transus. (1253 K) The phase diagram in figure 4.3 illustrates the formation of  $\alpha$  on cooling at the 4 % Al section. The microstructure then consists of parallel plates of  $\alpha$  delineated by

the  $\beta$  between them. This microstructural morphology is called a “Widmanstatten” structure. A significant amount of the  $\beta$  structure is retained between the  $\alpha$  plates giving rise to the characteristic “Basket-weave” structure. The final microstructure consists of plates of the white  $\alpha$  separated by the dark  $\beta$  phase. On

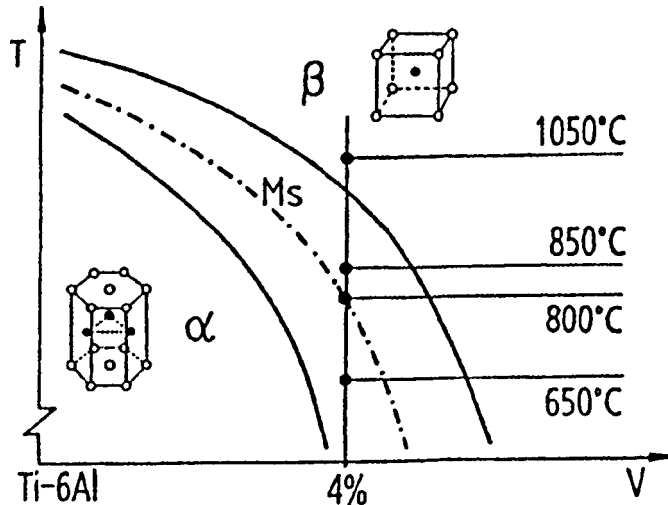


Figure 4.3: Phase diagram for Ti6Al4V alloy

rapid cooling the  $\beta$ -phase in the  $\alpha$ - $\beta$  alloy decomposes by a martensitic transformation to form martensite. Martensite is formed by a diffusionless transformation and leads to an acicular (plate-like) structure. The cooling rates associated with the laser forming process may promote such a formation. There are two types of this non-equilibrium microstructure -  $\alpha'$  has a hexagonal crystal structure and  $\alpha''$  has an orthorhombic structure.  $\alpha'$  can only be formed by quenching, whereas  $\alpha''$  can also be formed by applying an external stress, both of which are available with the laser forming process. When the alloy is rapidly cooled from above the  $\beta$ -transus, i.e. 1250 K, the structure becomes martensitic with some beta. This retained beta is due to the fact that the temperature for the end of the martensite transformation is below room temperature (298 K) for this alloy. This is because vanadium is a beta stabiliser and adding 4% V to a Ti6Al alloy is enough to put the  $M_f$  below 298 K. Therefore on quenching to 298 K not all of the beta is converted to martensite.

Generally titanium alloys are not used in the conditions described above, but are hot worked in the  $\alpha$  and  $\beta$  region of the phase diagram in order to break up the structure and distribute the alpha phase in a finely divided equiaxed form. This is usually followed by annealing at 973 K which produces a structure of mainly  $\alpha$  with finely distributed retained beta. This structure has the advantage of being more ductile than when the alpha is in the Widmanstatten form. When additional strength is needed, the alloys are hardened by heating to high temperatures of

about 1213 K in the  $\alpha$  and  $\beta$  field. This produces a large volume fraction of beta. The material is then water quenched so the transformation  $\beta$  to  $\alpha'$  takes place. The martensite is then heated so that it is precipitation hardened. If the alloy was held at a lower temperature in the  $\alpha$  and  $\beta$  field before quenching, then the beta phase that forms may be so rich in vanadium that the  $M_s$  temperature is decreased to below room temperature. After quenching the beta is retained.

The alloy in this work is mill annealed to produce a microstructure of globular crystals of beta in an alpha matrix. This places the alloy in a soft and machineable condition.

### 4.4.3 Surface preparation of material

The material was not given any treatment other than spraying with a graphite coating to improve the coupling of the laser beam energy into the sheet. For the process demonstration the aluminium alloy AA 2024 in the T3 (solution heat treated, cold rolled) condition was chosen. This material was black anodised to improve the laser beam absorption characteristics. The dimensions of the sheets investigated in the energy influence study are shown in table 4.3.

Material	Length (mm)	Width (mm)	Thickness (mm)
Ti6Al4V	80	80	0.8 - 3.0
AA2024 T3	80	80	0.8 - 1.0
AA2024 demonstration (1)	450	450	0.8
AA2024 demonstration (2)	450	225	0.8

Table 4.3: Materials and dimensions

## 4.5 Energy influences

### 4.5.1 Heat source

A fast axial flow (FAF) PRC Oerlikon CO<sub>2</sub>-laser (wavelength: 10.6  $\mu\text{m}$ ) in the continuous wave mode was used in all cases as the heat source. The output laser power was varied in the 250 - 1300 W range. The spot size was varied in the 1 - 12 mm range.

### 4.5.2 Laser beam characterisation

The nominal TEM<sub>00</sub> laser beam mode of the CO<sub>2</sub>-laser (wavelength: 10.6  $\mu\text{m}$ ) was checked for power distribution. A laser beam analyser was not used for this task

since there are subtle complications when attenuating a high power CO<sub>2</sub> laser beam for these devices. Instead the “knife edge” method was used. A “Coherent” digital power meter was used to record the output power of the apertured raw beam at the end of the optical beam delivery. The chosen power was 250 W, according to the laser controller. The actual absorbed power was verified from the power meter.

A perfectly horizontal “Stanley knife blade” was progressively stepped into the path of the laser beam by the CNC system which could be moved in 10  $\mu\text{m}$  steps. The laser was fired and the power level allowed to settle. The new absorbed power was recorded from the power meter. This measurement was repeated at eight points along the laser beam axis in the radial direction. Laser power was plotted against radial position and found to follow gaussian theory as shown in figure 4.4. The raw laser beam diameter ( $1/e^2$ ) was measured as 7.8 mm. This was found to be in agreement with the manufacturers information.

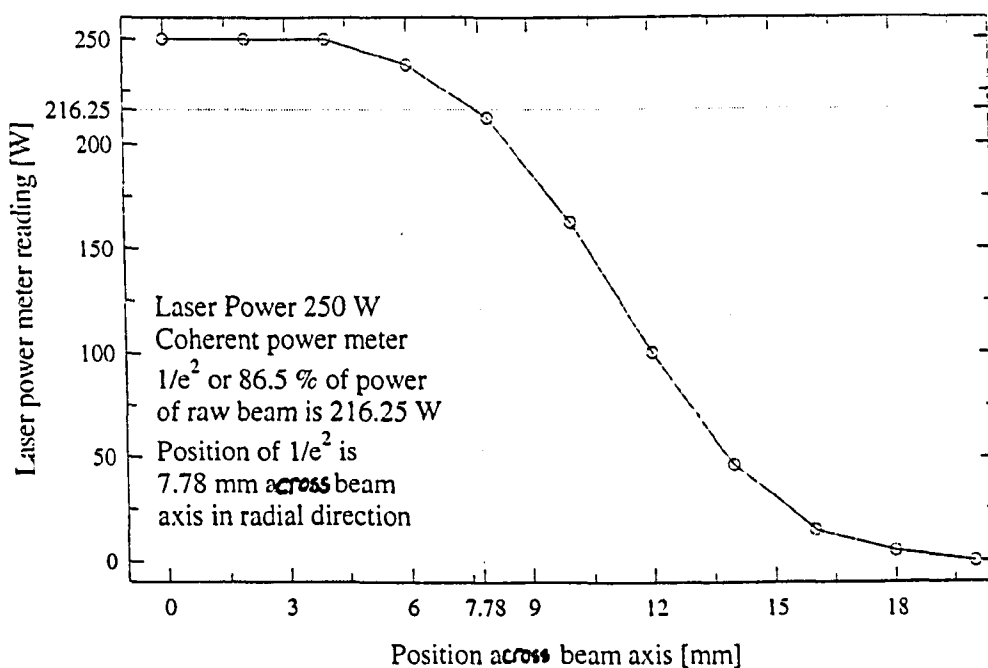


Figure 4.4: Energy distribution of raw beam

### 4.5.3 Energy input

The energy input to the sample was varied by adjusting the power, incident spot size and traverse velocity. A full description of the parameters used may be found in Appendix B. The chosen beam diameters were verified for all power settings by firing the laser beam onto the surface of a perspex block and measuring the diameter of the indentation nearest the surface. This gave a good estimate of the

$1/e^2$  value since the perspex vaporises almost immediately and does not appreciably conduct the heat from the beam. The Z stage (vertical displacement) of the workpiece handling system was adjusted until the desired laser spot diameter was achieved. All experiments were carried out with a “Coherent” ZnSe 178 mm focal length lens for this study. The spot size position was set up outside the focus in all cases.

#### 4.5.4 Clamping

The clamping device used in the initial investigation on the small tokens is illustrated in figure 4.5. The samples were free to move in the positive and negative Z directions but were restrained in all other directions. The laser scan lines were positioned sufficiently far away from the aluminium clamp so that the clamp would not act as a heat sink. The clamp restrained the sample up to a distance of 20mm from the edge, and the laser scan line was at 40mm from the edge. Therefore for all spot sizes used, i.e. 1-12mm, there was at least a gap of 14mm from the clamp to the outer edge of the laser beam.

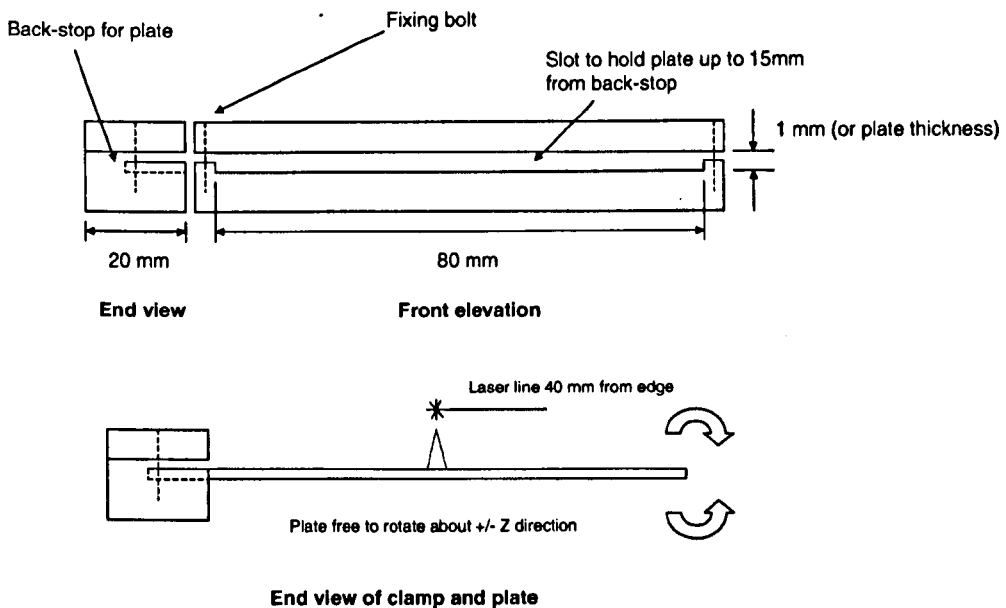


Figure 4.5: Clamping arrangement in initial study

#### 4.5.5 Sheet Heating

The sheets were heated with various energy inputs (Appendix B) and were cooled to ambient temperature by a forced air stream after plastic strain development.

This ensured that there was no influence of a partially warm sheet on the temperature gradient for subsequent scans using the same laser parameters (assuming no metallurgical changes). The effectiveness of the forced air stream was verified by means of a K-Type thermocouple connected to a digital voltmeter for an initial case. It showed that a sample which was heated to just below the melting point of the material, i.e. 1975k in the case of Ti6Al4V returned to ambient temperature when subjected to the forced air stream after plastic straining in less than two minutes. The overall arrangement for the initial experiments is illustrated in figure 4.6.

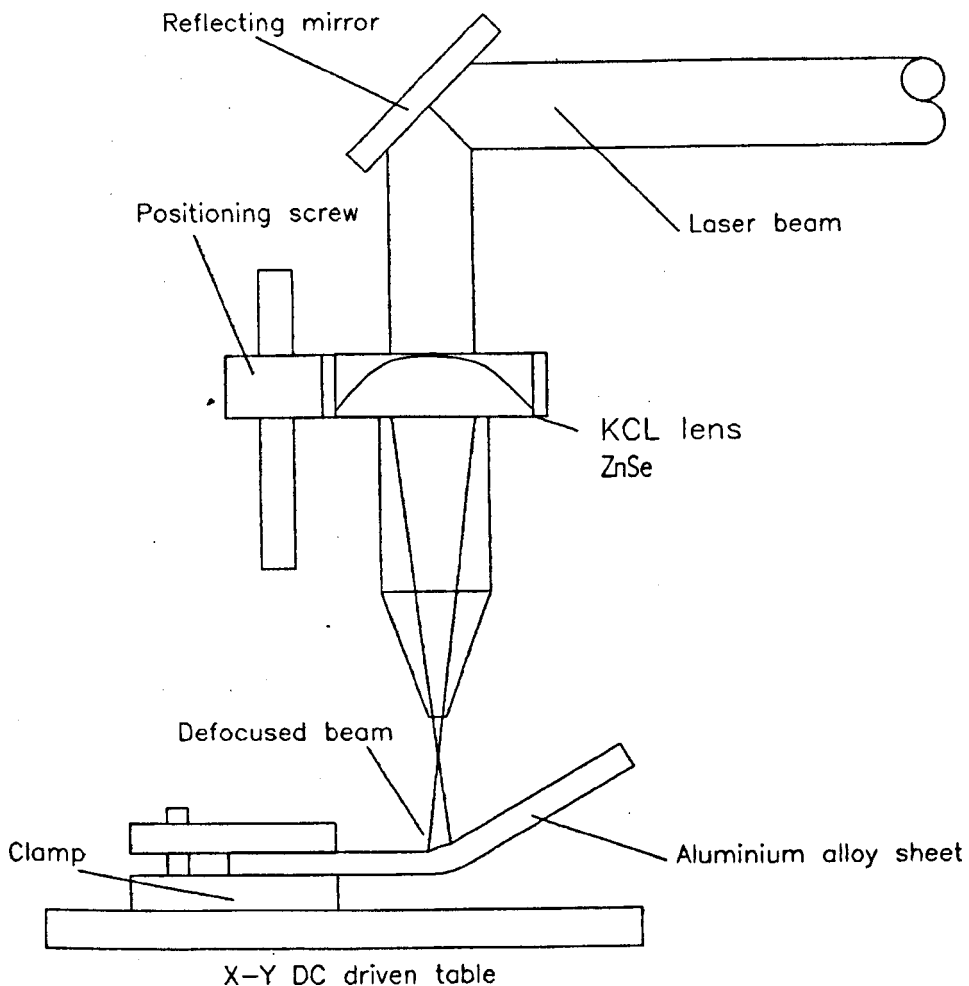


Figure 4.6: Experimental arrangement in initial study

## 4.6 Geometry influences

### 4.6.1 Sheet thickness

The sheet thickness was examined as a parameter. The thickening of the sheet due to the bending process itself facilitated this study.

### 4.6.2 Variation in bend angle along the length of the bending edge

The initial geometrical study examined sheets of dimensions 80 x 80 x 0.8mm. As a continuation to this study the effect of the local bending along the length of the bending edge was studied as a parameter. This was because there was variation in the bending angle along the length of the bending edge.

In this study the dimensions of the sheets were maintained at 80 x 80 x 0.8 mm. The sheets were annealed in order to relieve any residual stresses from upstream processes such as guillotining and the rolling process. Some of the post annealed samples exhibited slight curvatures of large radii. The average curvature of the sheets was measured before the process. The sheets with the initial curvature were processed with the concave side up. The deflection was measured after the bending at eight locations along the sheet length in the direction the laser beam had scanned. In each experiment the energy input to the sample was varied only by changing the velocity of the sample relative to the laser beam.

This velocity was varied in the range from where just no melting occurred to where no measurable deflection could be recorded. For further analysis the aluminium alloy plates were cut into strips perpendicular to the direction the laser beam had scanned and the deflection of each strip was measured once again. The backs of these plates were supported along the curvature in order to avoid further plastic deformation, and sectioning was performed with a low speed bandsaw using coolant. Finally, in an attempt to control the curvature along the plate, samples were produced by varying the traverse velocity along the length of the bending edge. The velocity was recorded for each position that the bend angle was measured at, and was monitored from the signal produced by the encoder on the servo motors that drove the xy motion stages. This ensured that the actual velocity at each position was known.

## 4.7 Laser forming a 3-D shape

The objective of the study on laser forming dish shapes was to establish basic rules about the conditions necessary for axi-symmetric 3-D laser forming. The strategy was to work initially from parameters which were perceived to yield an asymmetric forming and then progressively towards a regular symmetric forming. By doing so the parameter - symmetry relationship could be established. A shallow dish shape was chosen as the case study. It possesses axi-symmetry and this simplified the objective as this was one of the first attempts in structured 3D laser forming.

### 4.7.1 Sample preparation

The samples were CR4 (Cold rolled) mild steel in the 2mm gauge. The diameter of the flat circular plates was 120mms. A circular hole of 6mm diameter was laser cut at the centre of the plates and used for a clamping screw, as illustrated in figure 4.7. These diameters were laser cut to avoid the build-up of residual stresses around the edges. Other processes such as trepanning, milling or drilling would have resulted in these stresses. The sample surfaces were cleaned with a mild acetone solution to remove the protective oil film from the steel surface in preparation for graphite coating. Graphite from an aerosol was sprayed onto the surface to enhance the absorption of the laser beam to the surface of the material.

### 4.7.2 Clamping

The clamp which mounted the samples on the CNC system was made of pure aluminium. This material was chosen to assist the heat removal process as no time for cooling between laser scans on the samples was allowed. The diameter of surface contact between the clamp and the sample was 30mm. The samples were irradiated to within a radius of 20mm which meant that no area of the sample directly over the aluminium clamp was heated (which could act as a heat sink). A stainless steel M6 screw fixed the sample to the clamp. The clamp is illustrated in figure 4.7.

### 4.7.3 Laser scan patterns

In order to examine the effect of various scan patterns on the geometry many part programs had to be written and executed. ISO G-Code was the language used to write these programs. An example program is listed in Appendix C.

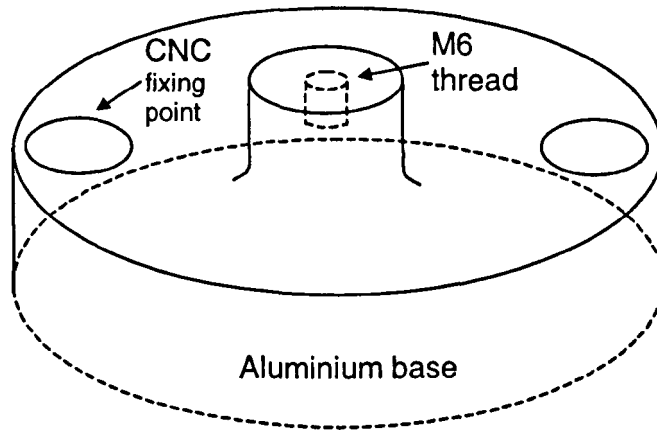


Figure 4.7: Aluminium clamp for dish forming work

#### 4.7.4 Energy input parameters

The irradiation experiments were made on CR4 mild steel samples and Al7075 T6 aluminium alloy samples. The process parameters are displayed in Table 4.1. It should be noted that the process parameters were tuned primarily for the upsetting mechanism to occur on the mild steel and the aluminium alloy.

Parameter	Steel CR4	AA7075
Spot size	5.3mm	5mm
Laser power	820 W	500 W
Velocity	1 m/min	6 m/min
Graphite coating	yes	yes

Table 4.4: Laser process parameters for the 3-D forming

#### 4.7.5 Surface profiling of laser scanned geometries

The post-irradiation graphite remaining on the sample surface was cleaned off with acetone. A co-ordinate measuring machine was used to measure the height of many points on the samples. The output from the co-ordinate measuring machine was grid data in IGES format. This data was normalised and converted into a useable ASCII format. The grid point co-ordinates were sorted into columns. These columns corresponded to the grid point of each row. The computer software Maple V.3 was used to prepare the grid data for viewing with the software Matlab 5.1. Contour plots of the samples were produced. These plots illustrated the degree of symmetry of the formed samples.

## 4.8 Metallurgical and mechanical property influences

This section details the metallographic preparation of the laser bent samples.

### 4.8.1 $\alpha - \beta$ Ti6Al4V sample preparation

The 80 x 80 mm samples were cut into eight strips. The cut lines were made transverse to the direction the laser beam had scanned. Each strip was 10mm wide. For the metallurgical analysis the centre strip was chosen. The heat affected zone (HAZ) and material extending to approximately 1 cm on either side of it was hot-mounted in resin mounts for the investigation. The samples were then ground manually with silicon carbide papers of various grades, ranging from 180 to 1200 grit. A high speed, cloth covered polishing wheel in conjunction with 6 micron and then 1 micron diamond particles were employed for polishing. Etching was performed with Kroll's reagent. Table 4.5 shows its composition.

The mounts were held in this solution for between 15 and 20 seconds. Then the mounts were washed with soap and rinsed with water and alcohol. The mounts were held for a further 2 minutes in a 4% HF solution in order to reveal the formation of any alpha case. The microstructures were characterised using the Nomarski microscopy technique and a range of magnifications from x50 to x1000 were employed.

Volume (ml)	Etchant
1	Hydrofluoric acid (HF)
5	60 percent Nitric acid (HNO <sub>3</sub> )
194	De-ionised water

Table 4.5: Etchant composition

Some microhardness measurements were carried out using a Vickers testing machine. Approximately 12 measurements were made across the sample thickness. For these tests a 300g load was used.

The effect of annealing the laser bent specimens was addressed. Laser formed samples were annealed under the conditions in table 4.6.

### 4.8.2 AA 2024 T3 sample preparation

This section details the preparation of the aluminium alloy for microscopy.

Temperature(C)	Air/Furnace Cooling	Time(h)
1065	Furnace	1
1065	Air	1
955	Furnace	1
955	Air	1

Table 4.6: Annealing conditions

### Etching

Keller's reagent was chosen for etching the AA 2024-T3 samples. It is suitable for revealing the grain size and shape through grain contrast or grain boundary lines. It can also provide a means of examination for incomplete recrystallisation and subgrains. Examination of overheating (partial melting) throughout grain boundary eutectic formations can be achieved as well. The examination of general constituent size and distribution through coarse insoluble particles and precipitates is possible. The Keller's reagent consisted of a mixture of 2 ml of hydrofluoric acid (HF of concentration 48 %), 3 ml of hydrochloric acid, 5 ml of nitric acid (HNO<sub>3</sub> concentrated) and 175 ml of H<sub>2</sub>O. This is usual practice and can be found in the ASM Metals Handbook, 1985.

### Characterisation

A Nikon optical microscope was used to observe the etched samples. Then using a photographic camera, black and white exposures (ASA 125) were taken of the samples using green light. Afterwards, an Hitachi S-246N SEM machine was used to obtain high resolution images of the etched samples. A Leitz Vickers micro-hardness tester was employed to measure the hardness across the depth of the bent elbow of the mounted samples. A schematic diagram of the location of the hardness measurements across the samples is shown in figure 4.8. The loads used for measurements of the Alclad layer and the core alloy were 50 and 200 grams respectively.

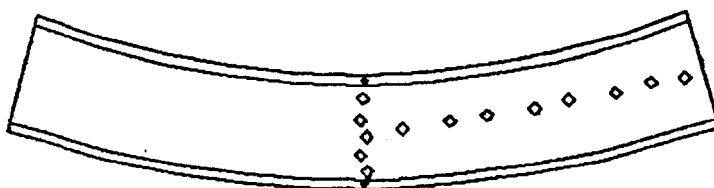


Figure 4.8: Schematic of micro-hardness measurement set-up

## 4.9 Integrated 2-D shape process demonstration

The culmination of the basic information was the demonstration of the process on a large thin 2-D component.

### 4.9.1 Process Demonstration

The demonstrator part was chosen as a flat rectangular sheet of dimensions 450 x 450 x 0.8 mm of the AA2024 T3 alloy which is formed into a cylinder of radius 900mm. The sheet was black anodised to ensure a uniform coating to enhance the absorptivity of the beam into the material. This part is large in terms of laser forming operations to date, and the shallow radius of curvature is almost at the spring-back limit of conventional forming operations. The primary objectives of the demonstration were to obtain:

- Geometrical accuracy,
- Surface smoothness and reproducibility.

The main components of the Mark 1 (MK1) demonstrator system included:

- PRC Oerlikon CO<sub>2</sub>, 2.0KW laser,
- Up to 4 axes CNC motion. Naples Coombe Translation and Rotational stages,
- Galil DMC-1040 controller,
- Automated bend angle measurement and surface profiling using the 3-D CAM laser stripe measurement system,
- Host PC interfaced to other components,
- Pneumatic clamping and plate support arrangements.

With this system the scan conditions were set and then the program instructions were executed, a cooling system then helped to return the part to room temperature quickly and uniformly. It consisted of a high pressure forced air stream in the processing cabinet. The surface was then profiled using the 3-D CAM laser stripe and this information was used to give the heights at various points over the sheet surface. This data was used to give a measure of:

- The radius of curvature,

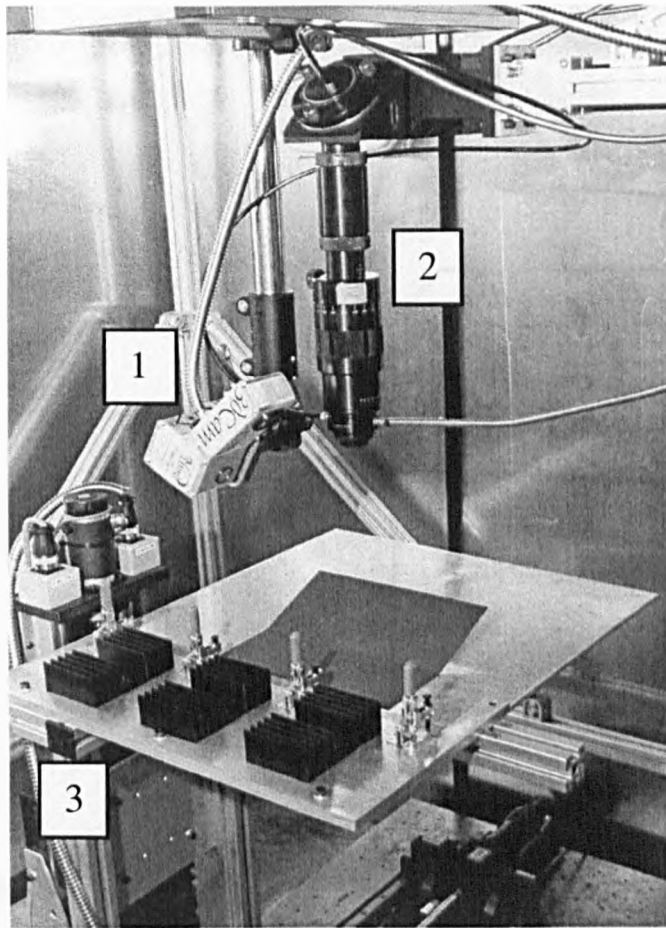


Figure 4.9: Photo - Mark I laser forming demonstrator system, *Sowerby Research centre*

- Any deviations in the radius of curvature along the length of the bending edge, i.e. any longitudinal distortion or curvatures in the wrong direction.

The system itself is illustrated in figure 4.9 and schematically in figure 4.10. Box 1 labels the laser stripe measurement system, box 2 labels the laser beam delivery system and manual focus control, and box 3 labels the translational stages. The laser stripe measurement system was obtained directly from outside and was not developed within the programme. It came with the associated software to carry out the processing of the image data and the calibration of the system. It consists of a laser diode and a CCD camera. The camera and stripe are offset from each other by an angle, and the system determines the distance to the sample by the method of triangulation which is detailed in numerous publications [1, 59].

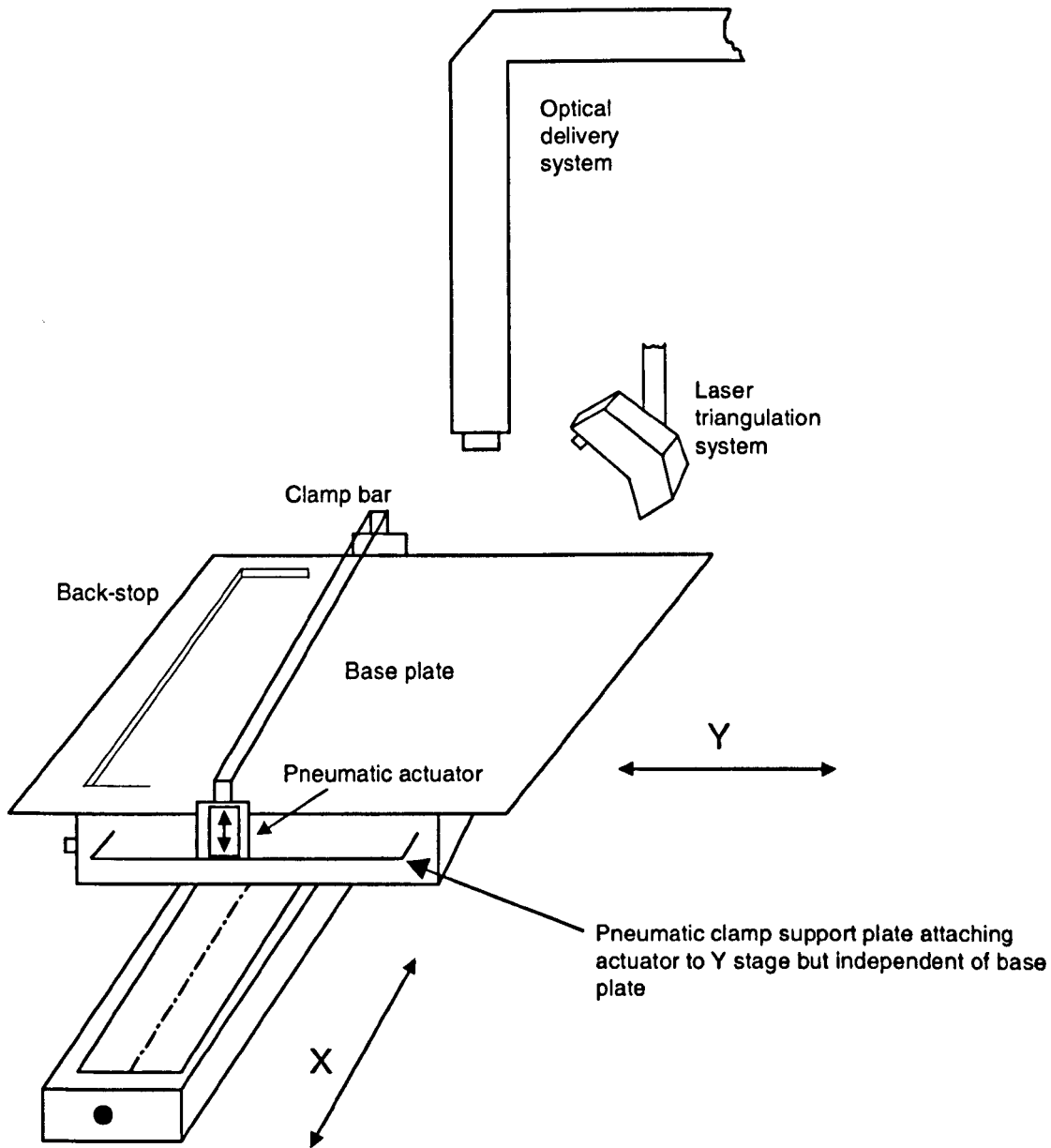


Figure 4.10: Schematic - Mark I laser forming demonstrator system

# Chapter 5

## Experimental Results and Discussion

### 5.1 Energy input

The results of this study are presented in two parts. Firstly, the results of the cases where the laser beam diameter to sheet thickness was large are shown. Then the cases where the laser beam diameter to sheet thickness ratio was small are presented.[61]

#### 5.1.1 Laser beam diameter of the order of 12 times the sheet thickness

$\alpha - \beta$  titanium alloy

For the titanium alloy it was found that a traverse velocity exists where the bend angle per laser scan is maximised for a given laser power (figure 5.1). In this study given the low coefficient of thermal conductivity and thermal expansion of the titanium alloy (see table 5.1) the temperature gradient mechanism (TGM) was expected to be active at the higher velocities. Below the optimum traverse

Coefficient of thermal expansion	Coefficient of thermal conductivity
Ti6Al4V - $9 \times 10^{-6}$ K	30 W/mK
AA2024 T3 - $24 \times 10^{-6}$ K	104 W/mK

Table 5.1: Expansion coefficients of the alloys

velocity, there was a loss of efficiency from overheating the material through the thickness direction. This resulted in less differential straining in this direction,

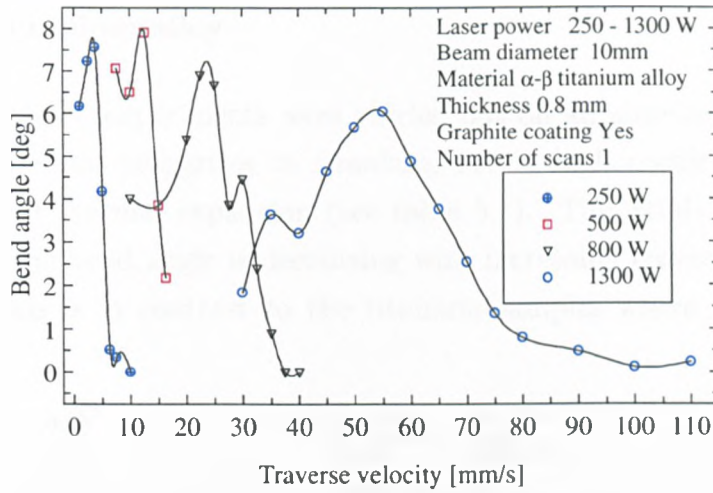


Figure 5.1: Bend angle with increasing traverse velocity at constant beam diameter

and hence a smaller bend angle. A phase transformation occurred at the very high temperatures (slow velocities) which had a negative effect on the bend angle. This effect is discussed in the metallurgical section. When the energy supplied to the surface was held constant at 33 J/mm the bend angle increased with increasing velocity up to a maximum, at higher velocities it decreased (figure 5.2).

These results support the idea that the temperature gradient, and the efficiency of the process increases as the processing speed increases [14], and that the increase in the efficiency is offset by a reduction in the bend angle after the optimum point (see figures 5.1, and 5.2). This is because increasing the velocity further results in less coupled energy, less thermal expansion, and a smaller reduction of the yield point stress in the heated zone. Since all of these factors contribute to overcoming the elastic share of the bending, the bend angle begins to drop off again.

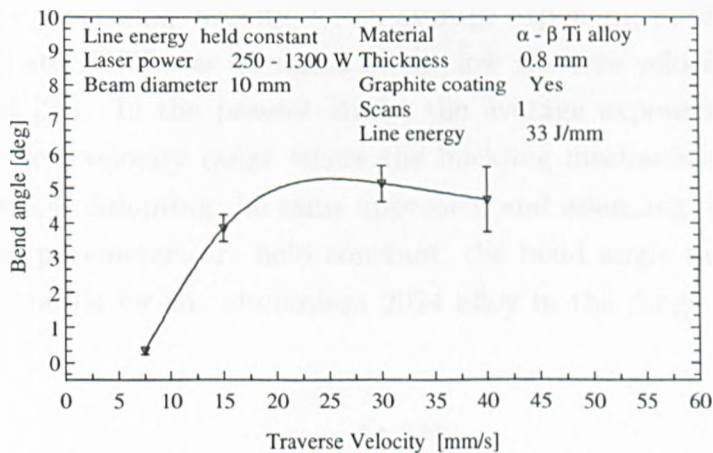


Figure 5.2: Bend angle with increasing traverse velocity at constant line energy

## 2024 - T3 aluminium alloy

For further analysis, experiments were carried out on an aluminium alloy which has different thermal properties to titanium, i.e. a high coefficient of thermal conductivity and thermal expansion (see table 5.1). This study shows that for one laser scan the bend angle is decreasing with increasing traverse velocity, (see figure 5.3). This is in contrast to the titanium samples where there is a peak

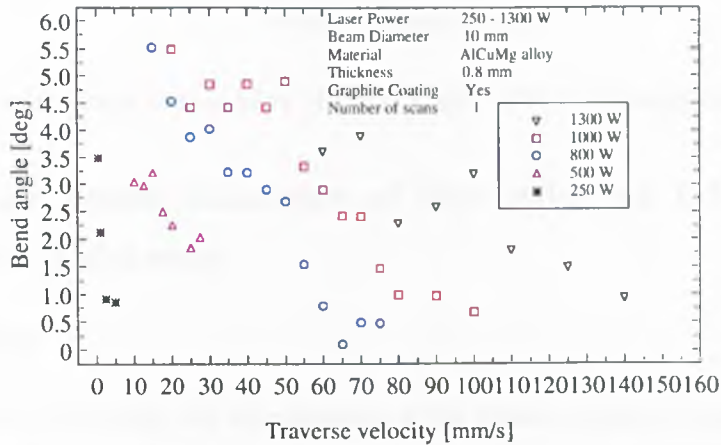


Figure 5.3: Bend angle with increasing traverse velocity at constant line energy

in the velocity - bend angle curve due to the metallurgical influences. Since the thermal conductivity of the aluminium alloy is high, the temperature gradient in the depth direction of the samples was small. Under these conditions, the buckling mechanism is expected to be active. Using a power law which relates the final bend angle,  $\alpha_b$ , to the processing velocity,  $V$ ; an average exponent,  $n$ , of approximately 0.45 for carbon steel C75 was obtained at the low traverse velocities in work by Vollertsen et al [22]. In the present study, the average exponent was found to be 0.54 for the low velocity range where the buckling mechanism was active, as shown in figure 5.4. Adopting the same approach, and assuming that all material and geometrical parameters are held constant, the bend angle can be related to low processing speeds for the aluminium 2024 alloy in the range of the buckling mechanism by:

$$\alpha_b \propto V^{-0.54} \quad (5.1)$$

In the higher velocity range, where a pronounced temperature gradient may have started to emerge in the depth direction, the bend angle continued to drop sharply. This is attributed again to the reduction in the coupled energy.

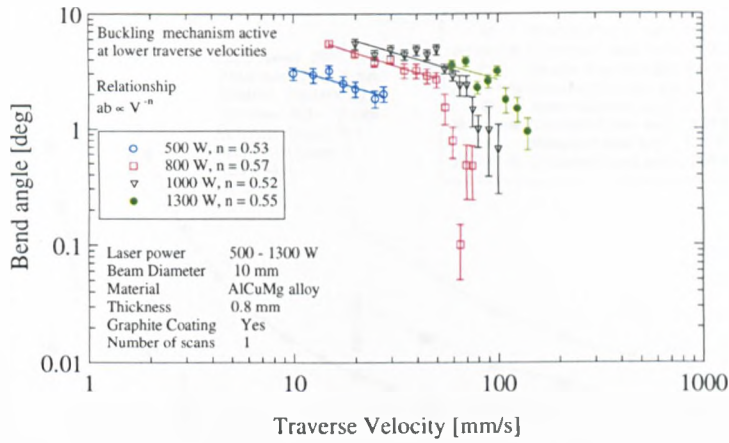


Figure 5.4: Double logarithmic plot of bend angle with increasing traverse velocity

### 5.1.2 Laser beam diameter of the order of 1-5 times the sheet thickness

#### Titanium alloy

The temperature field and the dimensions of the plastic zone are changed by varying the power density, the processing velocity, or both. In this experiment the beam diameter was reduced from 10mm to 5mm and the processing velocity was increased for the power range 250-1000W. These parameters altered the temperature field and hence the extent of the plastic zone, in comparison with the earlier cases (section 5.1.1). From figure 5.5 it may be seen that the measured bend angles are much smaller than in the previous study (on the titanium alloy).

This may not be surprising given that a smaller volume of material was heated and the reduced plastic region had to overcome the bending moment of the entire sheet. In addition, as the temperature gradient mechanism was active here, the bend angle decayed quickly with increases in the processing velocity. This was because the elastic effects became very pronounced at the higher velocities. The second set of curves in figure 5.5 shows the calculated bend angle. This calculation was taken from the two layer model described in chapter 2 [16], which relates the bend angle to the material properties, the energy input, and the sheet thickness, by the following expression:

$$\alpha_b = 3 \frac{\alpha_{th} p_1 A}{\rho c_p v_1} \frac{1}{s_0^2} \quad (5.2)$$

In figure 5.5 the calculated value of the bend angle differs from the measured angle in that it is much larger, but the trends of both the theoretical and experimental curves are similar. Two main reasons why the measured angles differ from the

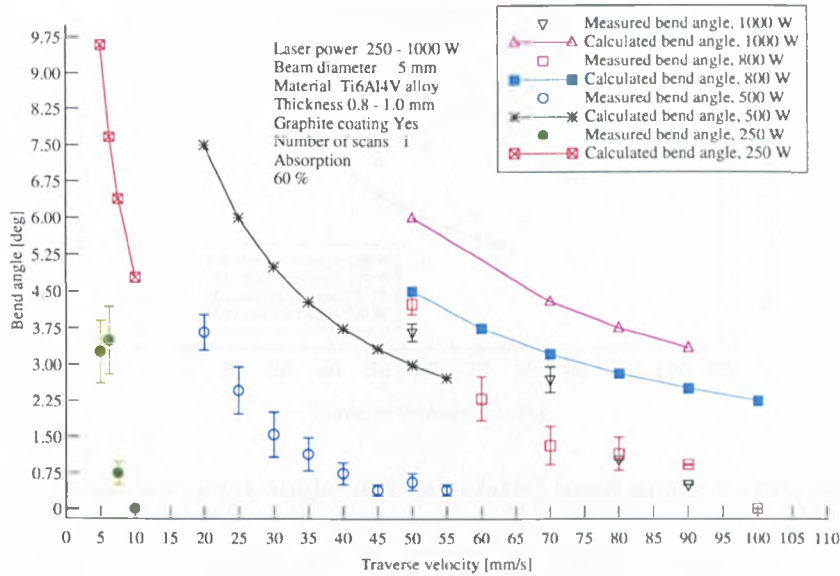


Figure 5.5: Measured bend angle and calculated bend angle v traverse velocity

calculated angles are as follows. Firstly, the two layer model assumes a constant temperature in the top layer of the sheet and a step to ambient temperature at the bottom layer. As a result the effect of the thermal conductivity is ignored. It would be necessary to include the thermal conductivity in order to determine the realistic temperature field, the size of the plastic zone and the mechanical properties of the material at elevated temperatures. Two of the most important mechanical properties which affect the bend angle are the yield strength and the Young's modulus, both of which are temperature dependent. Secondly, the counter-bending effect is ignored in the model. This assumes that there is a total conversion of the thermal expansion of the top layer into plastic compression. By accounting for these parameters, the absolute bend angles and the trend could be calculated with improved accuracy.

### 2024 T3 aluminium alloy

Further experiments were carried out on the aluminium alloy and the bend angles were compared with the two layer model reported in [16]. For this study the laser beam diameter was 1.25 times the sheet thickness. For figure 5.6 the bend angles were calculated in the high velocity range, where the temperature gradient mechanism was most likely to be active, i.e. from 45 - 75 mm/s at 250 W, and from 60 - 110 mm/s at the higher power of 500 W. Again the predicted bend angles are some orders too high, for the reasons stated previously. In the model no account of the yield strength of the material is taken. The amount of elastic strain required to reach the yield point is high for the materials studied. This requires that the

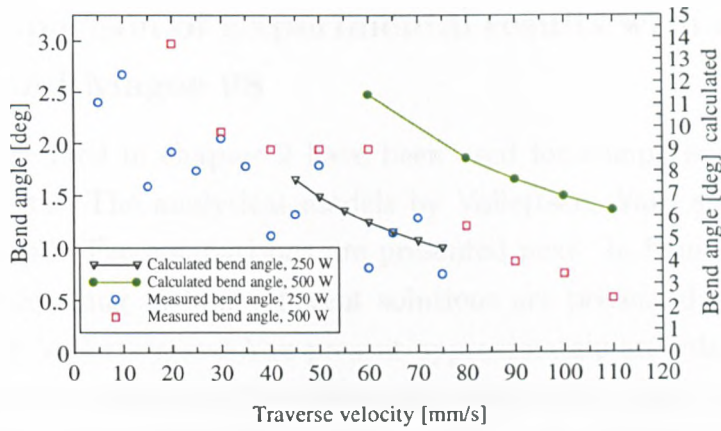


Figure 5.6: Measured bend angle and calculated bend angle v traverse velocity

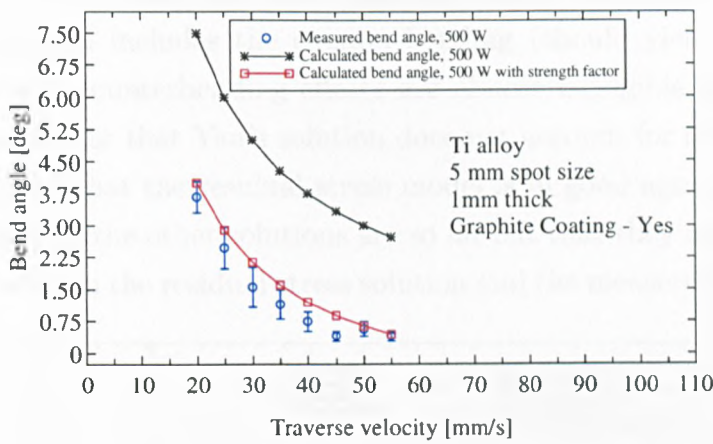


Figure 5.7: Measured bend angle and calculated bend angle v traverse velocity

elastic strain at the yield point should be subtracted from the thermal expansion in order to calculate more accurately what the contribution of the thermal strain is to the plastic bending. A function which relates the absorbed power to the previously described factors could be used in conjunction with the two layer model in order to predict the bend angle more accurately [16]. In figure 5.7 the factor accounting for the strength was taken as 50% of the power at the lowest velocity. This factor was decreased linearly with increasing velocity. The calculated bend angles are now of the same order as the measured angles. The background behind this is that the elastic effects become increasingly pronounced with increasing velocity, so the actual energy used for plastic straining is also reduced with increasing velocity. Since the two layer model assumes a total conversion of thermal expansion of the upper layer to plastic strain, the elastic effects can be approximated by a factor which reduces the absorbed power with increasing velocity.

### 5.1.3 Comparison of Experimental results with other models and Magee 98

The models described in chapter 2 have been used for comparison with the experimental results. The analytical models by Vollertsen, Yau, and Mucha have been implemented. The comparisons are presented next. In figure 5.8 the angles as calculated according to four different solutions are presented. The two layer models, both by Vollertsen and Yau present approximately an order of magnitude greater angles at the lower velocities and angles which are 4 times greater than the measured values at the very high velocities. Of note is the fact that Vollertsen's solution and Yau's solution yield almost identical values. As described in chapter 2 Vollertsen's two-layer model ignores the energy used for counterbending up to the temperature dependent yield point (therefore should predict angles too high) whereas Yau's model includes the counter-bending (should yield lower angles). This indicates that counterbending effects are almost negligible in the temperature gradient regime or that Yau's solution does not account for them adequately. It may be observed that the residual stress model is in good agreement from this graph. In actual fact the other solutions are so far out that they mask the scale of the difference between the residual stress solution and the measured values. Figure

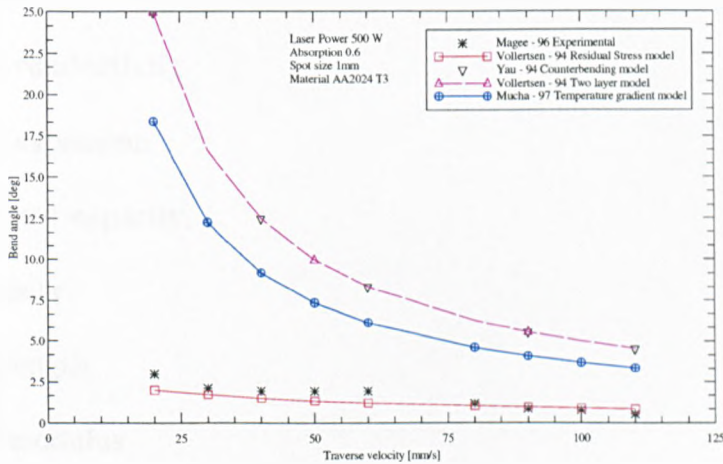


Figure 5.8: Comparison of analytical solutions and measured angles

5.9 presents the residual stress model predictions and the measured angles only for the titanium alloy (to reveal the differences masked in the previous case), for conditions which are within the model range (TGM). The difference is huge. The problem with this solution is the determination of the thermo-mechanical properties of the material. In the model the Yield strength and the Elastic modulus must be chosen *a priori*. The values are usually chosen based around the value of the average temperature of the heated zone during the heating cycle. However

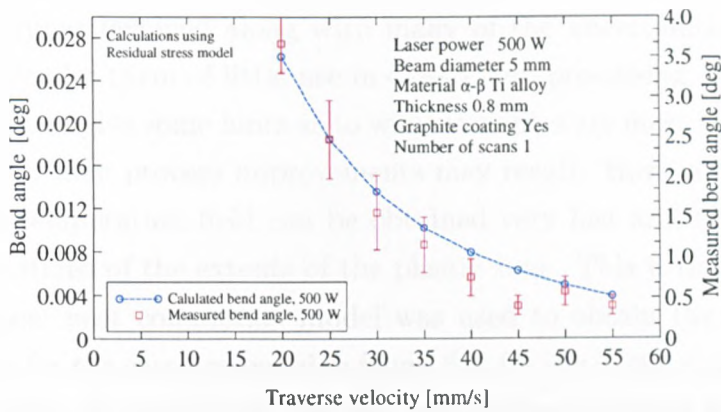


Figure 5.9: Measured bend angle and calculated Residual Model bend angle v traverse velocity

this ignores the heating-cooling rate. In the previous models analytical solutions with simple boundary conditions were used to evaluate the temperature field and this lead to an error in determining the temperature of interest as well. Tables are available for the thermo-mechanical properties, but they have not been measured using a laser as the heat source. They are usually carried out using furnace heated samples. The following properties are temperature dependent:

- (a) Absorption
- (b) Thermal conductivity
- (c) Thermal expansion
- (d) Specific heat capacity
- (e) Mass density
- (f) Yield Strength
- (g) Young's modulus

This results in great difficulty for the analytical route, as these functions may be complicated and probably a numerical scheme is the only possible method of solution. The contribution of the thermal expansion to the plastic straining is multi-dependent.

The correlation of the experimental data with the models available in the literature was not in good agreement. It is unlikely that an analytical solution can act as a panacea for all process problems. Clearly analytical models available in the literature would be too crude to implement as a starting point in a closed loop laser forming system. Complicated numerical solutions can be performed but the

computational times involved along with many of the uncertainties surrounding the input data render them of little use in closed loop processing. To this end the analytical route can give some hints as to what variables are most important, most sensitive etc, and then process improvements may result. However the numerical solution to the temperature field can be obtained very fast and this may lead to improved estimations of the extents of the plastic zone. This is discussed next.

The numerical heat conduction model was used to obtain the extents of the plastic isotherm for the case presented in figure 5.8, for use in the mechanical model from chapter three. It was found that the temperature gradient mechanism was not really sustainable below 80 mm/s with these parameters, if the 500K isotherm is taken as the elastic-plastic interface. The extents of the zone are shown in figure 5.10 Then using the mechanical model the bend angles for a range of sheet thick-

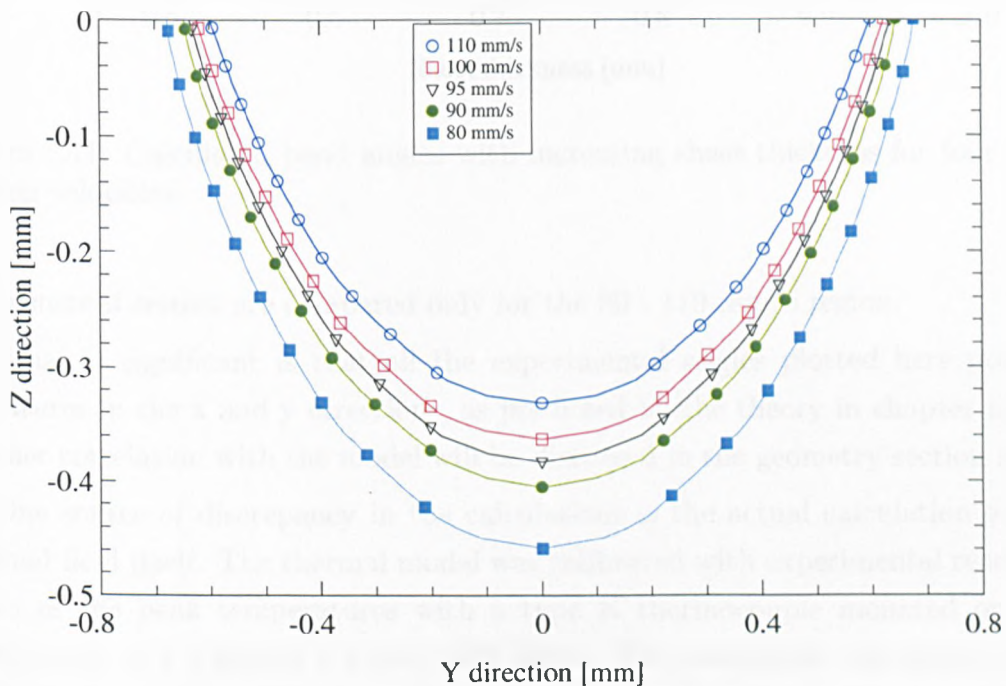


Figure 5.10: Plastic isotherm cross-section for the case presented in figure 5.8

nesses were calculated. They are plotted in figure 5.11. Finally the bend angle relating to the sheet thickness of 0.8mm is plotted in figure 5.12 for the velocity range of 80 to 100 mm/s. There is reasonable agreement between the experimental results and the calculated angles in this instance. Comparing the results of models from other authors which are plotted against the experimental data in figure 5.8, there is improvement. The model is sensitive to the temperature dependent material properties and the characteristic length taken for the curvature-bend angle calculation. Additionally the numerical heat transfer model showed that the TGM was only sustainable at speeds of around 80 mm/s or greater. That is why the

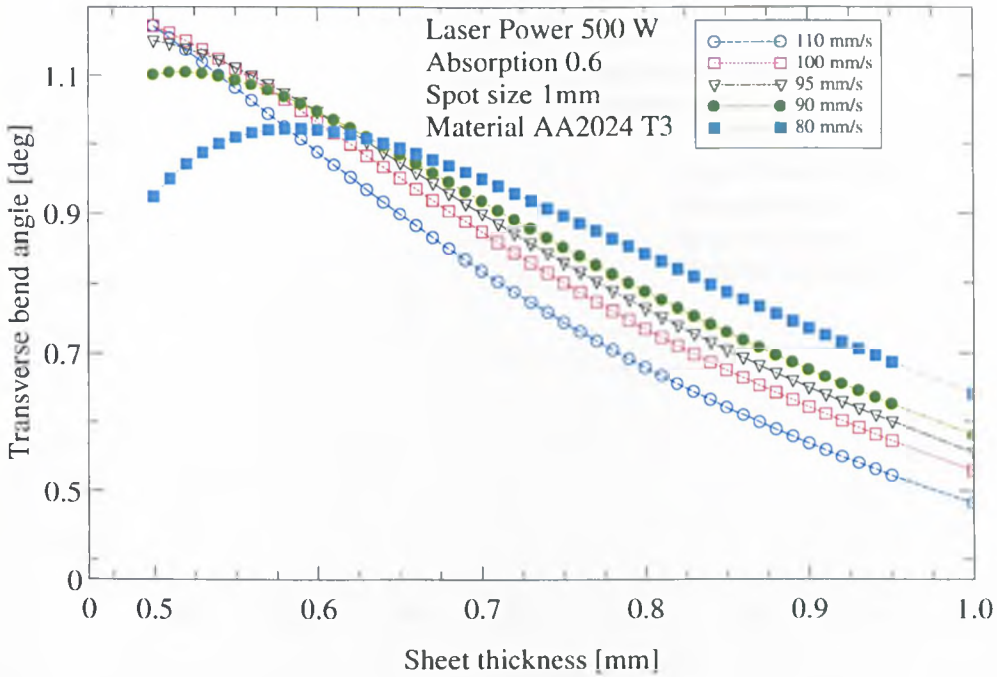


Figure 5.11: Calculated bend angles with increasing sheet thickness for four processing velocities

experimental results are compared only for the 80 - 110 mm/s region.

What is significant is that all the experimental angles plotted here possess curvatures in the  $x$  and  $y$  directions, as predicted by the theory in chapter three. Further correlation with the model will be discussed in the geometry section next.

One source of discrepancy in the calculations is the actual calculation of the thermal field itself. The thermal model was calibrated with experimental readings taken of the peak temperatures with a type K thermocouple mounted on the reverse side of a Ti6Al4V 0.8 mm thick sheet. The calibration was made solely with titanium. Figure 5.13 shows the peak temperature as the position of the laser beam is moved in relation to the thermocouple. The thermocouple was mounted at the centre of the sheet on the bottom (non irradiated side) with a heat resistant epoxy resin. The laser beam was stepped in  $200 \mu\text{m}$  steps in the direction parallel to the thermocouple. If the laser beam is considered to be scanning in  $x$ , the thermocouple may be considered to give the temperatures in the  $y$  direction at  $z=0.8 \text{ mm}$ . As expected the temperature was greatest when the laser beam was directly over the thermocouple ( $y=0$ ) and least when the beam was farthest away (at the edge of the sheet on either side of the thermocouple,  $\pm 17 \text{ mm}$ , refer figure 5.13). The  $y$  direction was used for the readings as it refers to the maximum “width” of the plastic zone which was intended for calculating the predominant transverse bending moment. Up to a distance of about 2 mm on either side of the

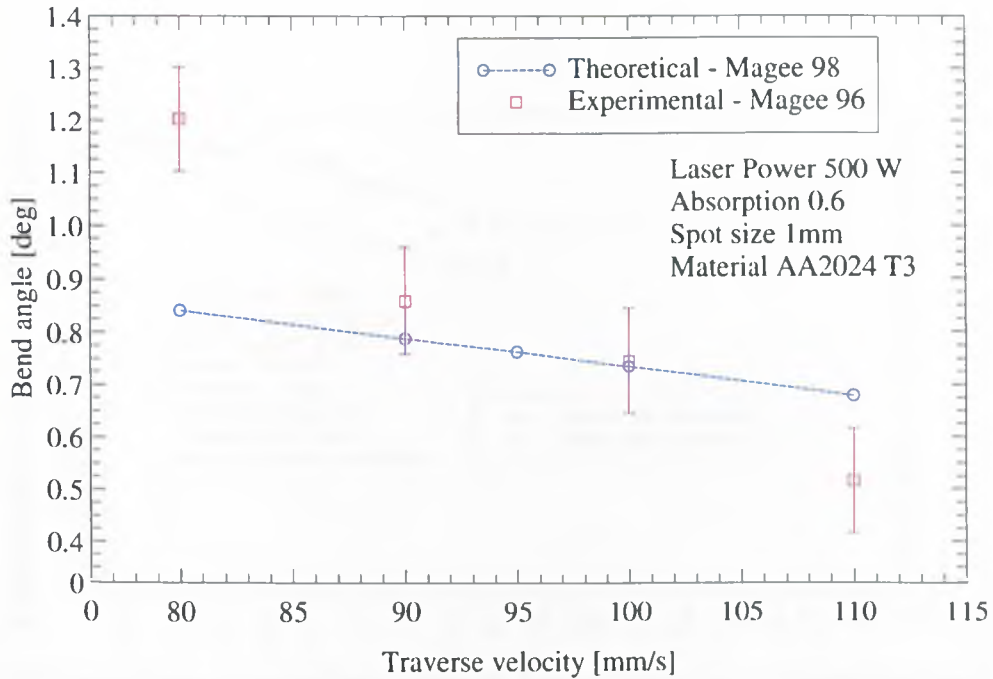


Figure 5.12: Experimental (Magee) and theoretical (Magee) bend angles with increasing processing velocity

thermocouple the model was in excellent agreement using a constant value for the absorption efficiency, as shown in figure 5.14.

However beyond this distance in the  $y$  direction the experimental values are higher. This may have been due to the growth of an oxide layer on the titanium alloy due to the repeated scanning over the sample which enhanced the absorption. The temperatures have been calculated out to a distance of 8 mm on one side of the thermocouple, and from figure 5.15, it may be seen that there is 100K discrepancy at these distances. However for the purposes of the temperature gradient mechanism which is concerned with temperatures close to the laser beam and a small heat affected zone, the model may be considered promising.

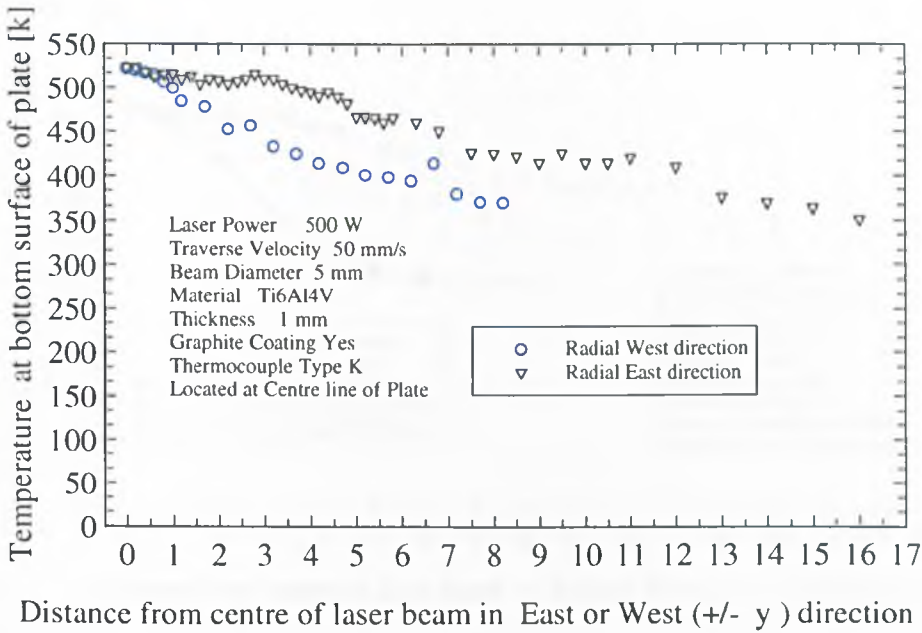


Figure 5.13: Experimental Peak temperatures on the reverse side of the Ti6Al4V sheet

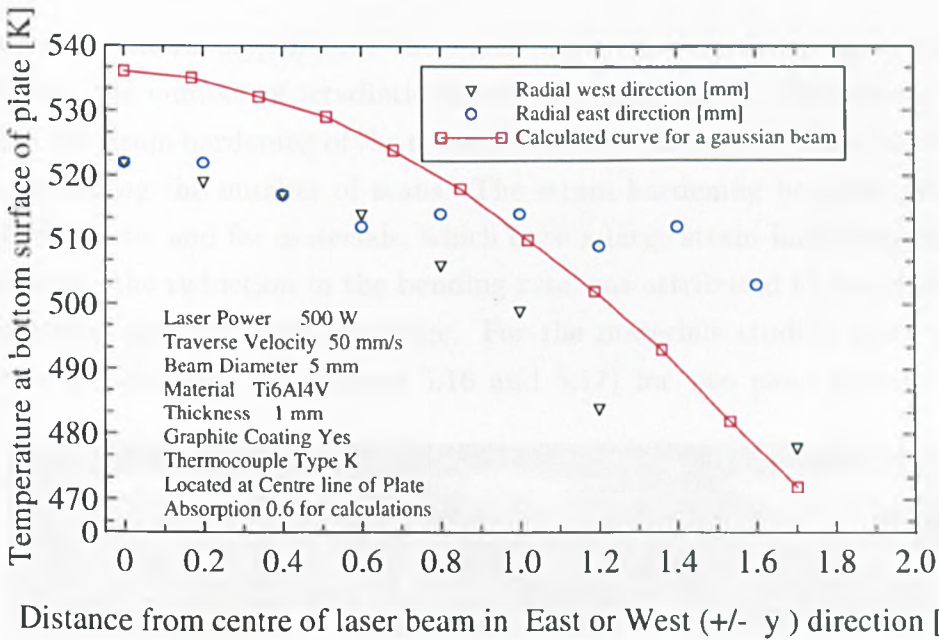


Figure 5.14: Experimental peak temperatures with calculated temperatures for the reverse side of the Ti6Al4V sheet, at a distance of up to 2 mm in the  $y$  direction

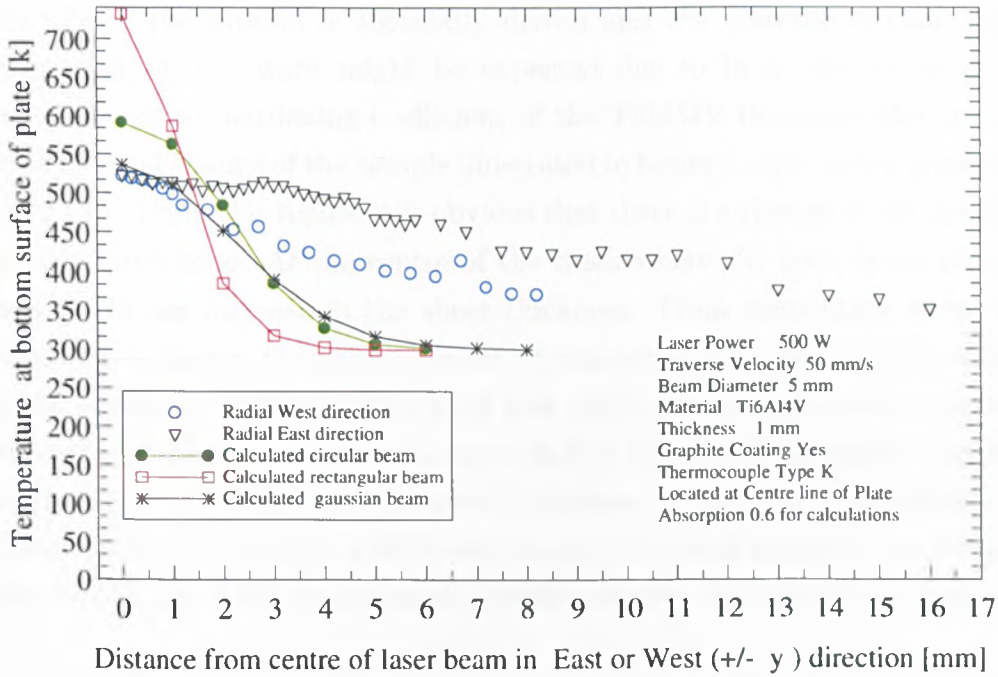


Figure 5.15: Experimental peak temperatures with calculated temperatures for the reverse side of the Ti6Al4V sheet, at a distance of up to 8 mm in the  $y$  direction

## 5.2 Geometry

### 5.2.1 Decreasing bending rate

It has been shown in [40] that the bend angle shows a decaying increase with increasing the number of irradiations over the same track. The causes reported include the strain hardening of the material, and the changing absorption behaviour with increasing the number of scans. The strain hardening becomes pronounced for thick sheets, and for materials, which have a large strain hardening coefficient. In addition, the reduction in the bending rate was attributed to the thickening of the material along the bending edge. For the materials studied here, the latter effect is predominant (see figures 5.16 and 5.17) for two main reasons. Firstly,

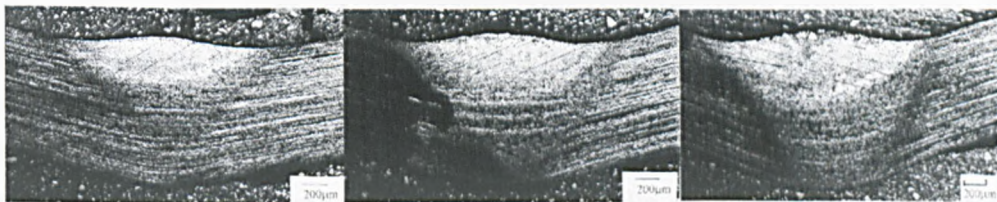


Figure 5.16: Increase in thickness of the material along the bending edge for 10, 20 and 30 scans; Power 250 W, Spot size 5mm, Velocity 15mm/s, Ti6Al4V

the sheets of  $\alpha - \beta$  titanium and AA2024 T3 alloy were in most cases 1mm thick

or less. Since the process is thermally driven and the material is thin, only a small amount of cold work might be expected due to heat conduction effects. Secondly, the strain hardening coefficient of the Ti6Al4V titanium alloy is small. The dimensional change of the sample illustrated in figure 5.16 is shown graphically in figure 5.17. From this figure, it is obvious that there is a change in the geometry of the irradiated zone. At the centre of the track where the laser beam scanned, there is a  $475 \mu\text{m}$  increase in the sheet thickness. From elementary strength of materials, it is known that the moment of resistance increases as the sectional thickness increases. Therefore, the bend rate drops for the same energy input, as the thickness increases. It has been shown in [14] that the bend angle is inversely proportional to the square of the sheet thickness. Using this relationship, the two-layer model [16] predicts a 53% reduction in the bend angle for the thickness increase of  $475 \mu\text{m}$ , if the energy input is held constant. The situation is somewhat

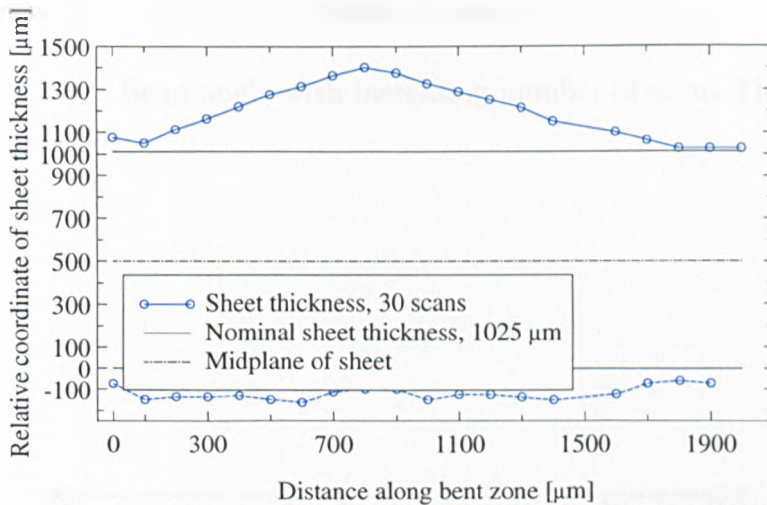


Figure 5.17: Geometry of the bent zone of fig 5.16 after 30 scans

more complex in the case of the AA 2024 T3, solution heat treated, cold rolled alloy. Although the thickness of the sample increases, the hardness generally drops from the heat input. The AA 2024 T3 re-ages to the original hardness a relatively long time afterwards at room temperature (this is discussed in section 5.3.4). Since the ultimate tensile strength is proportional to the hardness, as the hardness drops with increasing the number of scans, the strength drops. In that case, an increase in the section modulus that would reduce the bend angle is offset to some extent by the reduction of the strength. Then the decay of the bending rate with increasing the number of scans over the same track is less pronounced. (see figures 5.18 and 5.19) This argument is contrary to what was reported in [40]. In that work the increase of micro hardness was attributed to the strain hardening. What was most likely occurring in that work was that there was a phase transformation

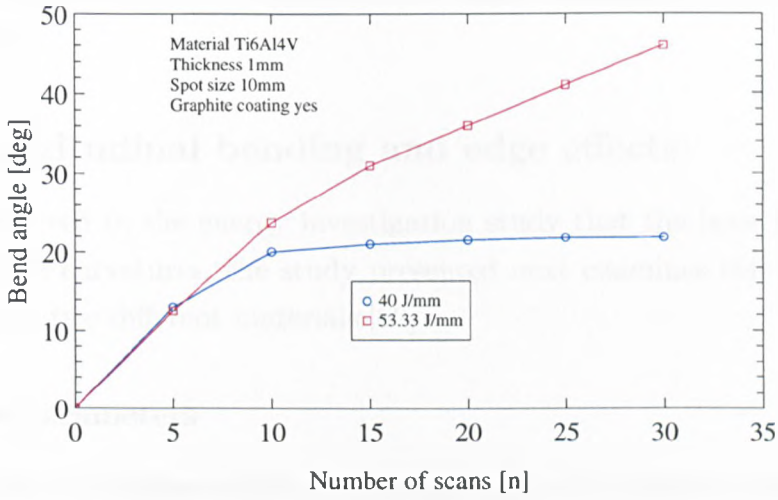


Figure 5.18: Bend angle with increasing number of scans Ti6Al4V

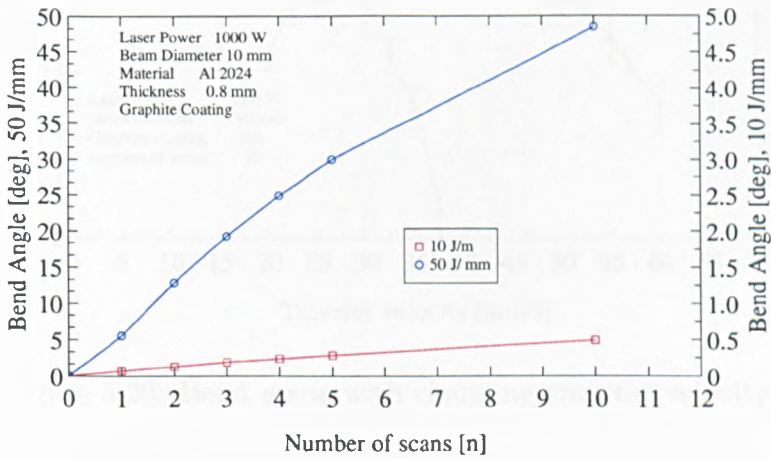


Figure 5.19: Bend angle with increasing number of scans AA 2024 T3

to martensite of the titanium, formation of a hard and brittle alpha case on the surface of the material due to the uptake of oxygen, and the thickening of the material along the bending edge from the laser forming process. Additionally the materials studied here are of a lighter gauge. Strain hardening is more pronounced for thick sheets.

### 5.2.2 Longitudinal bending and edge effects

As it was observed in the energy investigation study that the laser formed samples had double curvatures, the study presented next examines this longitudinal bending for the two different materials.[62]

#### Initial laser parameters

The initial laser parameters which were used to verify the existence of the changing bend angle along the bending edge are illustrated in figure 5.20. Given the large beam diameter and the high thermal conductivity, under the conditions employed the buckling mechanism was expected to be active on the AA2024 T3 samples. In the case of the Ti6Al4V alloy, due to its lower thermal conductivity, at higher velocities the temperature gradient mechanism may have played a role.

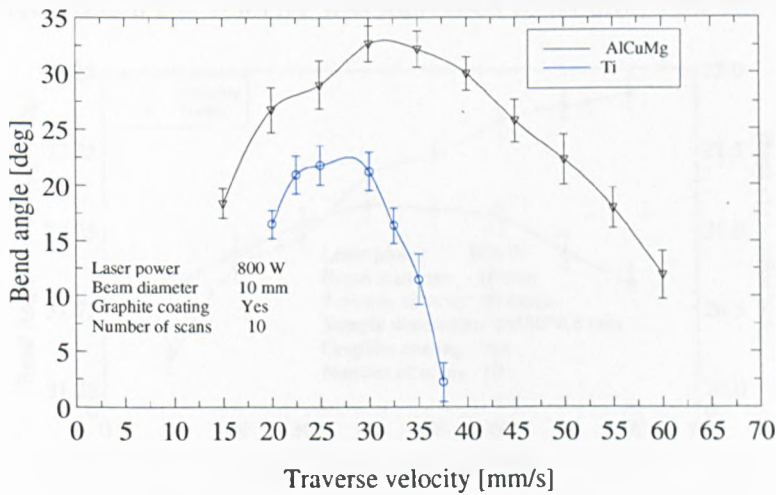


Figure 5.20: Bend angle with changing traverse velocity

#### Changing bend angle along the length of the bending edge

For each case, the bend angle was measured at eight positions along the length of the bending edge. In the case of the AA 2024 T3 the angle increased almost in a linear fashion with increasing distance along the bending edge as shown in figure

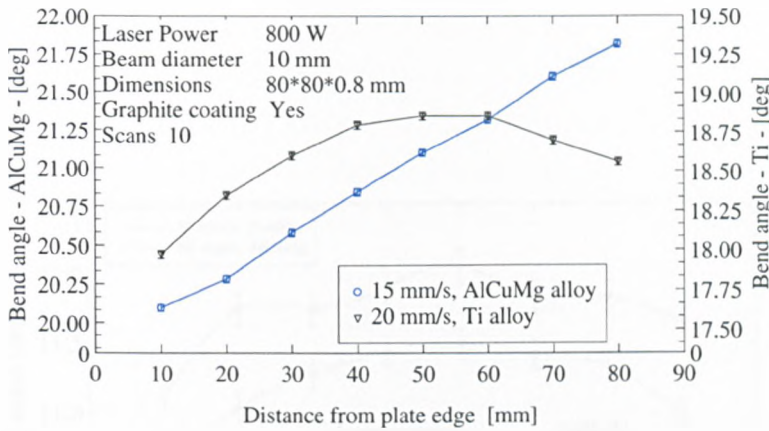


Figure 5.21: Bend angle with in plate location at low traverse velocity

5.21. For the titanium alloy the angle increased over the length of the bending edge until 3/4 of the length of the bending edge was reached where the angle dropped off again. In both cases the bend angle where the laser beam exited the plate was greater than where it entered. Similar behaviour was evident when the traverse velocity was increased from 15 and 20 mm/s to 30 mm/s, in figure 5.22. In this instance the bend angle of the titanium alloy was more symmetrical about the midpoint of the bending edge. However the angle for the aluminium alloy continued to increase in an almost linear fashion with increasing distance towards the exiting edge. When the velocity was increased to 60 mm/s for the AlCuMg and

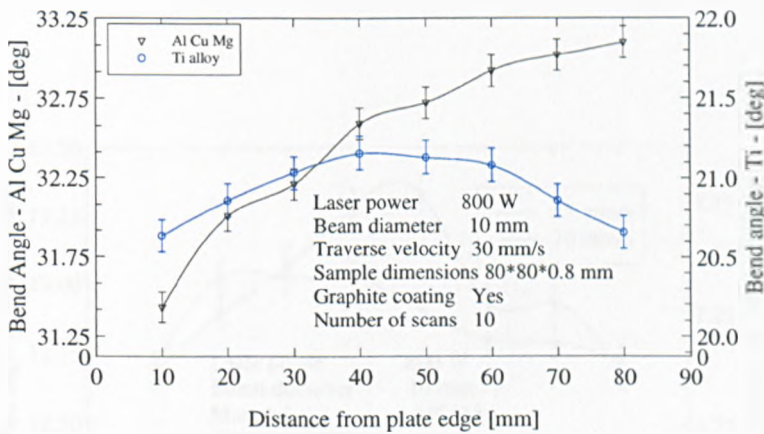


Figure 5.22: Bend angle with in plate location at medium traverse velocity

to 35 mm/s for the Ti alloy (in figure 5.23) then the aluminium alloy adopted the same type of behaviour that the titanium alloy exhibited at the lower velocities, i.e. that of an increasing angle towards the midpoint of the bending edge and then a drop in the angle at the exiting edge. Further experiments were carried out on the aluminium alloy at two higher velocities, 65 and 70 mm/s (in figure 5.24), here the bend angle continued to show the same pattern as that at 60 mm/s.

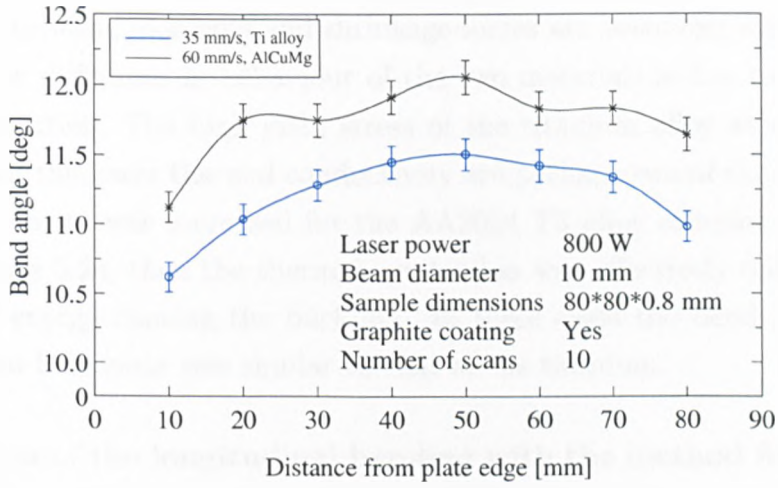


Figure 5.23: Bend angle with in plate location at high traverse velocity

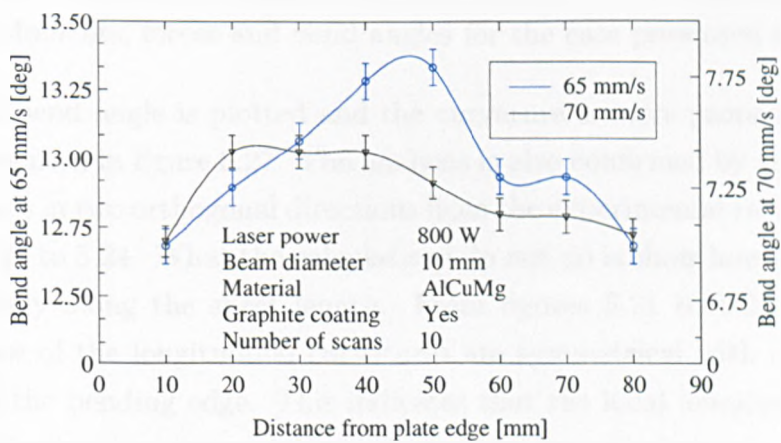


Figure 5.24: Bend angle with in plate location at high traverse velocity

These results indicate that at low traverse velocities the bend angle is increasing over the entire length of the bending edge for the aluminium alloy. This also occurs up to a point for the titanium alloy. However the latter always shows a drop off in the angle after the midpoint along the bending edge. It is probable that the longitudinal bending moments and shrinkage forces are becoming significant. The reason for the difference in behaviour of the two materials is due to the differing thermal properties. The high yield stress of the titanium alloy at elevated temperatures and the lower thermal conductivity are perhaps two of the main factors. When the velocity was increased for the AA2024 T3 alloy samples to 65 and 70 mm/s in figure 5.24, then the thermal conduction was effectively reduced, as was the coupled energy causing the buckling. In these cases the bend angle with in plate location behaviour was similar to that of the titanium.

### Investigation of the longitudinal bending with the method from chapter three

Using the parameters in figure 5.23, the thermal simulation was run and the extent of the isotherm defining the elastic-plastic interface was calculated. The width of the plastic zone was found to be 9.38 mm at the surface and it extended 0.8 mm through the thickness. Table 5.2 presents the longitudinal moments and forces for the section using the method of inherent strain from chapter 3. In figure 5.25 the

Longitudinal bending moment (Nm)	Longitudinal shrinkage force (N)	Longitudinal bend angle (deg)
0.1596	14036.21	0.0587723

Table 5.2: Moments, forces and bend angles for the case presented in figure 5.23

longitudinal bend angle is plotted and the curvature is more pronounced than in the case presented in figure 3.27. The analysis is also confirmed by the presence of the curvatures in two orthogonal directions from the experimental results presented in figures 5.21 to 5.24. What the calculations do not do is show how the behaviour changes locally along the sheet length. From figures 5.21 to 5.24 it is obvious that very few of the longitudinal curvatures are symmetrical with respect to the midpoint of the bending edge. This indicates that the local longitudinal bending moment as the sheet traverses underneath the laser beam is changing, otherwise the moment per unit length would be uniform and the longitudinal bending would act about the midpoint of the bending edge. Therefore the longitudinal moment that the laser beam creates at each point in the direction of scanning affects the next moment by adding to it. In the very slow traverse velocity cases presented in figure 5.21, it would appear that there is a linear increase of the longitudinal bending

moment from one end to the other. Another way of interpreting this would be to assume that the transverse bending moment is increasing from the entrance to the exiting edge, therefore there is a greater transverse bend angle per unit length. However that would require the width of the plastic zone to change from the entrance to the exiting edge. It appears that the isothermal zone width is uniform from one side to the other, therefore the contribution of the transverse bending moment should be approximately constant as well. For this reason it is assumed that the longitudinal moment dominates the bending in that direction. When the traverse velocity increases the longitudinal behaviour becomes more parabolic. To account for how each local bending moment affects the next is probably best solved with a numerical rather than an analytical technique. However as a design tool the longitudinal moments could still be estimated with an appropriate distribution function in the analytical solution.

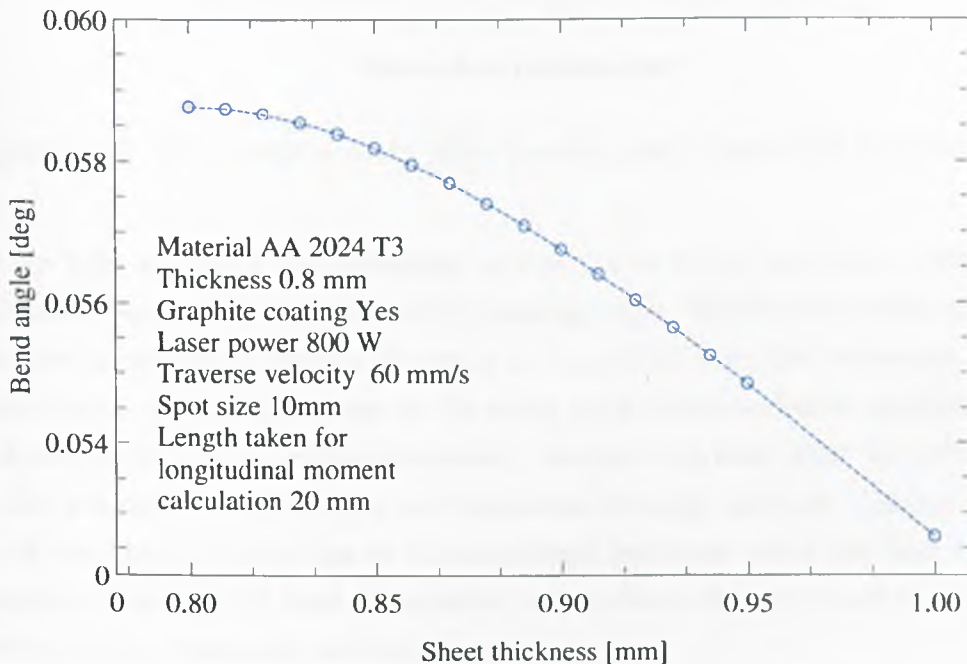


Figure 5.25: Longitudinal bend angle for (for 1 scan) for the case presented in figure 5.23 (for 10 scans = 0.587 degrees)

### Bend angle before and after sectioning

In order to ascertain if any elastic strain was stored in the plate after bending, some initial case aluminium samples were sectioned into eight strips. The cuts were made perpendicular to the axis the laser beam scanned along, running from the laser scan line to the edge of the bent leg of the sample. From figures 5.26 and 5.27 it is evident that there is a difference in bend angles between the sheets

that have been measured before and after sectioning into strips. At the lower scan velocities, the deflection decreased at the entrance edge when the plates were cut out, and the deflection of the strips increased marginally as the exiting edge was approached. This indicates that there is elastic strain held in the plate after the bending like the distortion sometimes found in weldments. As may be seen

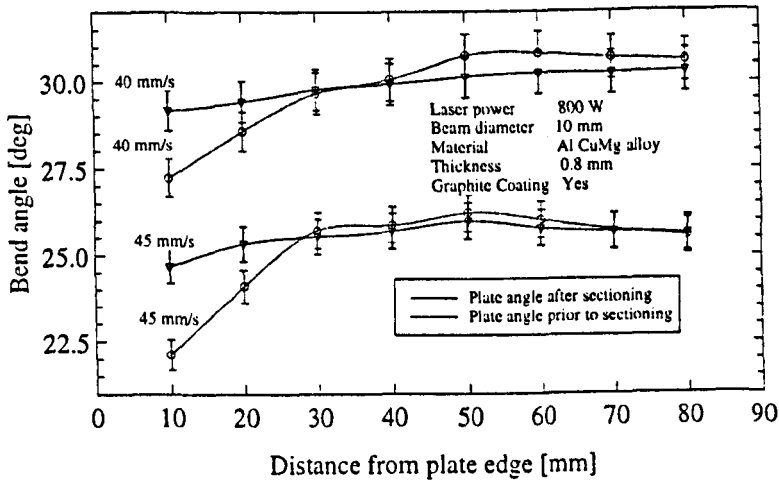


Figure 5.26: Bend angle with in plate location before and after sectioning

in figures 5.26 and 5.27 the deflection of the plates before and after cutting is most similar around the midpoint of the bending edge. When the traverse velocity was further increased to 60 and 70 mm/s in figure 5.27 then the behaviour of the sectioned strips showed a decrease in the angle both before and after the midpoint. At the midpoint, the angle was essentially the same as that prior to sectioning. This also indicates that perhaps the transverse bending moment changes at the edges of the plate. This is due to the restricted heat flow when the heat reaches the edges and has to flow back. This effectively re-heats the plate and changes the behaviour of the transverse bending moment.

If the restraint is increasing towards the midpoint of the bending edge then the contraction of the material in this zone, after cooling, may exert an elastic strain on the material around the midpoint, which would be released upon sectioning and the deflection would be reduced. The question arises as to why the deflection at the exiting edge at the lower traverse velocities should be the same or higher after sectioning given the lower restraint towards the exiting edge. This may be due to a greater ratio of plastic to elastic straining in this zone from the movement of the buckle, the additional restraining moment, and a reduction in the yield stress from the thermal diffusion which has partially heated the material already before the laser beam reaches it.

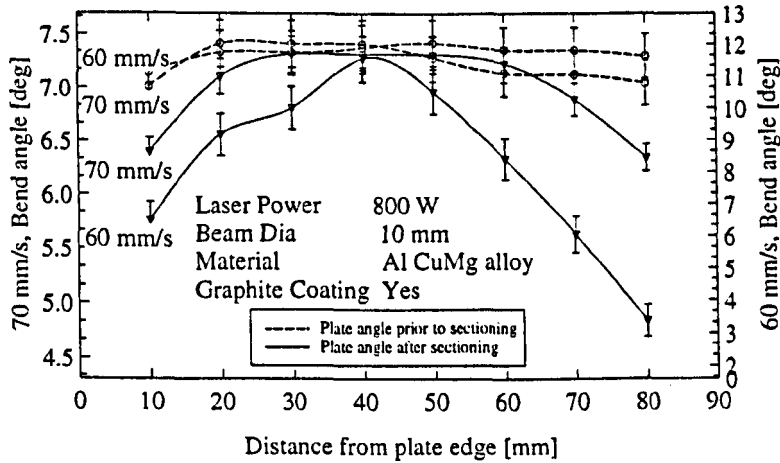


Figure 5.27: Bend angle with in plate location before and after sectioning, high traverse velocity

Variable line energy along the path of irradiation

In an attempt to reduce these edge effects several strategies were examined. The underlying idea was to vary the line energy supplied to the plate surface along the bending edge to balance heat conduction and mechanical restraint effects. This could have been attempted by altering the power density or the interaction time of the laser beam. The interaction time was varied by altering the traverse velocity of the samples relative to the laser beam along the length of the bending edge, as there was no power control available and the response time of the laser may have been too long. As may be seen from figure 5.28 the bend angle was first measured at 30 mm/s for one scan on the titanium alloy, and this showed a 1.15 degree variation from the entrance to the exit of the sample. The second curve shows the

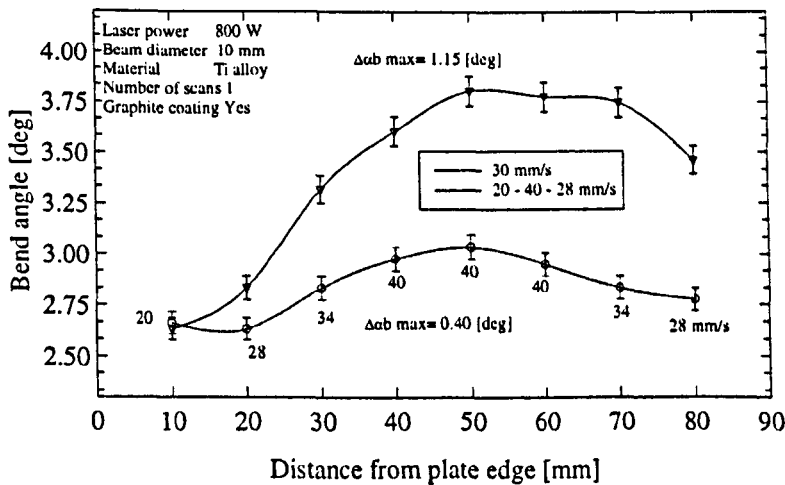


Figure 5.28: Bend angle with varying line energy with location, Ti6Al4V alloy deviation that existed when the average velocity was maintained at approximately

the same level, i.e. 33 mm/s, but it was varied in the range of 20 - 40 - 28 mm/s from the start to finish along the path of irradiation. The velocity was increased to a maximum at the midpoint along the bending edge and then reduced slightly at the exiting edge in an attempt to increase the thermal strain to balance the loss of restraint. Although similar behaviour is evident, the maximum change in the bend angle  $\Delta\alpha_{b,max}$  in this instance was reduced to 0.4 deg.

The initial strategy used for the aluminium alloy in figure 5.29 (curve 1) differed from that used for the titanium alloy in that a larger velocity range of 27 - 57 mm/s from the exiting edge to the midpoint of the bending edge was employed. This

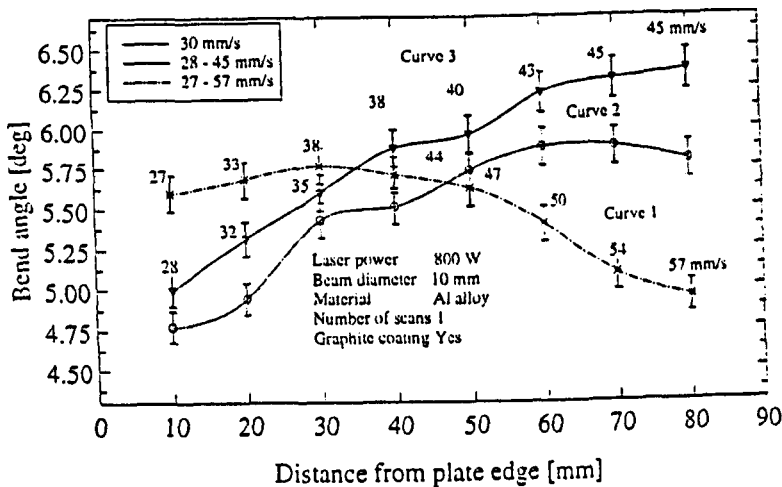


Figure 5.29: Bend angle with varying line energy with location, AA 2024 T3 alloy

strategy was adopted because the thermal conductivity of the aluminium alloy is much higher and the yield stress is significantly reduced at elevated temperatures, this could result in pronounced effects at the exiting edge. This first strategy did not improve the working accuracy by much when compared to the second curve in figure 5.29 which was the normal operating conditions of a constant traverse velocity at 30 mm/s. Since there was a large drop in the angle at the exiting edge in curve one, another strategy was used where the traverse velocity range was decreased slightly. Again it may be seen from figure 5.29 (curve 3) that the angle has increased towards the exiting edge, and the behaviour is similar to that found at the constant velocity. The CNC tables did not allow for a suitable intermediate velocity profile between the previously described two and no further improvement was achieved on the aluminium alloy. The operating range where the traverse velocity should be adjusted for the aluminium alloy is very critical and relatively large changes are incurred by small changes in the velocity, and hence the line energy profile.

Another possible solution to the problem would be to put the heat into the

sheet instantaneously with a high speed scanning system. Then the entire laser scan line would be heated almost at the same time and the moving buckle effect would be relieved. However such a system was not available at the time and its debatable if it would alleviate the geometrical restraint factor - i.e. the changing rigidity of the sheet with distance from the edge or Poisson's ratio.

### 5.2.3 Laser forming a dish shape - A case study in 3-D geometry forming

In this work a moving gaussian laser beam was used for spatial forming a dish shape. By irradiating an area with a moving laser beam symmetrical irradiation over an area is not given implicitly. The objective of this work was to laser form a dish structure symmetrically. This requires:

- Geometrical symmetry should be reached as soon as possible again after the initial irradiations,
- A symmetrical temperature distribution over the plate surface should be realised,
- Any pre-orientation bend should be avoided,
- The laser beam parameters, particularly the irradiation angle of incidence and the irradiation spot diameter, should be held constant.

Concerning geometrical symmetry the idea is to reach as many symmetry lines as soon as possible. With radial lines this is achievable not before three irradiation lines, because two lines which are directly opposite contradict avoiding a pre-orientation bend. Two lines create a folded edge across the irradiated plate which would be detrimental to the entire forming of a smooth and axi-symmetrical dome. The following lines would support a further bending of this folded edge. At least three radial lines in an offset angle of 120 degrees are required.

The temperature dependent parameters, for instance the yield stress, the thermal expansion coefficient or the thermal diffusivity pose another problem. To achieve a symmetrical forming along several lines of irradiation the material properties should alter the same amount. This is only obtainable by the creation of a symmetrical temperature field.

As the coupled energy is highly dependent on the irradiation angle, this angle should be held constant at 90 degrees along each line of irradiation, perpendicular to the surface in order to ensure the coupled energy is constant. This requires that

variable laser power or constant power and variable z-axis movement is available to maintain a constant irradiation spot diameter incident on the surface.

These strategies do not fulfill the last condition because striving for it requires extensive knowledge of the bend angle development *a priori* or on-line correctional movement and sensing to fulfill this condition. The experience in laser bending of 3d-structures is few and as these are the first steps in setting up a knowledge base, the fulfillment of the last requirement did not lie within the scope of this work. It is problematic to retain a perpendicular irradiation and constant spot size since this requires the availability of at least three controllable axes. Along with the movement of the workpiece (requests two axes) a minimum of five axes is required. These requirements could not be met with the CNC-system used.

Due to the difficulties in complying with all four requirements listed above not all of them could be achieved in this study. The following irradiation strategies approach the requirements[63]:

- (a) 3-, 5- and 7-star systems (radial lines)
- (b) Offset systems (radial lines)
- (c) Dividing systems (radial lines)
- (d) Circle line systems (circumferential lines)

### Radial line systems

As suggested by Hennige [42] 3-, 5- and 7-star systems, offset systems and dividing systems can be used for forming the circular plates with radial lines using the upsetting mechanism (i.e. a homogeneous strain through the thickness direction). The overall forming develops as a result of the sequence of the irradiations in relation to the initial and inter-stage geometries.

The strategies presented here deal with the problem of which sequence the lines of irradiation should be distributed on the sample in order to fulfill the conditions described previously. With radial line strategies there is the possibility of either beginning the irradiation at the outside or the inside of the sample (i.e. radius min or max).

### 3-, 5- and 7-star systems

This method divides the 360 degree sample into sectors of the same angle: Using three, five or seven dividing steps the lines of irradiation in the first series look like a 3-, 5- or 7-pointed star. The next step is to rotate this "star" with a certain

offset angle and continue with the laser scans until the sample surface is irradiated completely. The scan patterns are illustrated in figure 5.30 to 5.35.

Radial circle bow lines which lead tangentially into a radial line were implemented (see figure 5.31) as well. A stabilising support of the circular bend was expected, comparable with a torsion effect because of the circular shrinkage. The radii of the circle bows were varied to adjust the curvature.

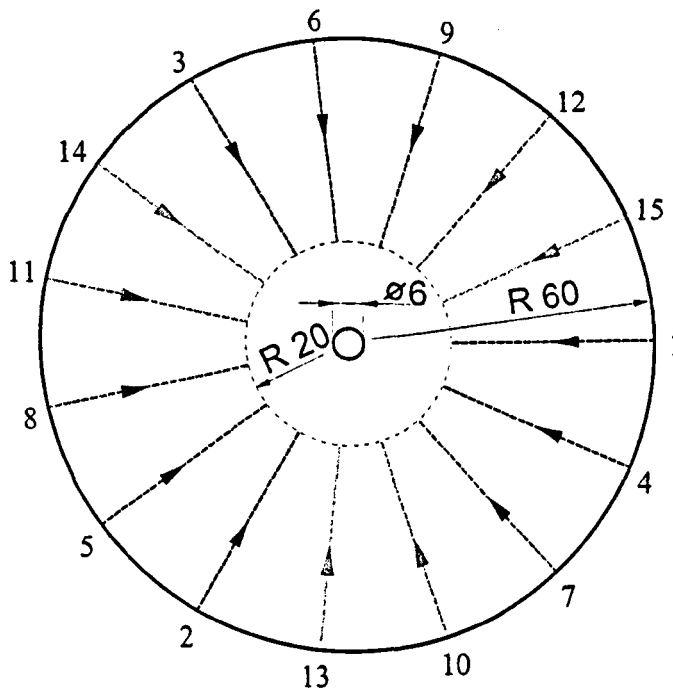


Figure 5.30: 3-star system with radial lines (outside-in)

### Forming result - Radial 3-, 5- and 7-star systems

With radial lines irradiation may start at the outside or at the inside of the sample. At an early stage in the experiments it became obvious that it was better to begin at the outside. Starting from the inside-out tended to distort the samples and cause them to be asymmetrical. This may be due to a larger volume of material being heated and influencing the forming result when the irradiation began from the inside rather than from the outside. Using the latter the heat flows into a smaller volume which is stiffer towards the centre. Starting the process from the outside may be considered to be more symmetrical, assisting a regular forming. It should be noted that the 3-star system reaches mechanical symmetry after just three scan lines, the 5-star system after five lines and the 7-star system after seven lines. Three lines achieve mechanical symmetry as soon as possible. However the heat input is more evenly distributed over the sample the higher the order of the star.

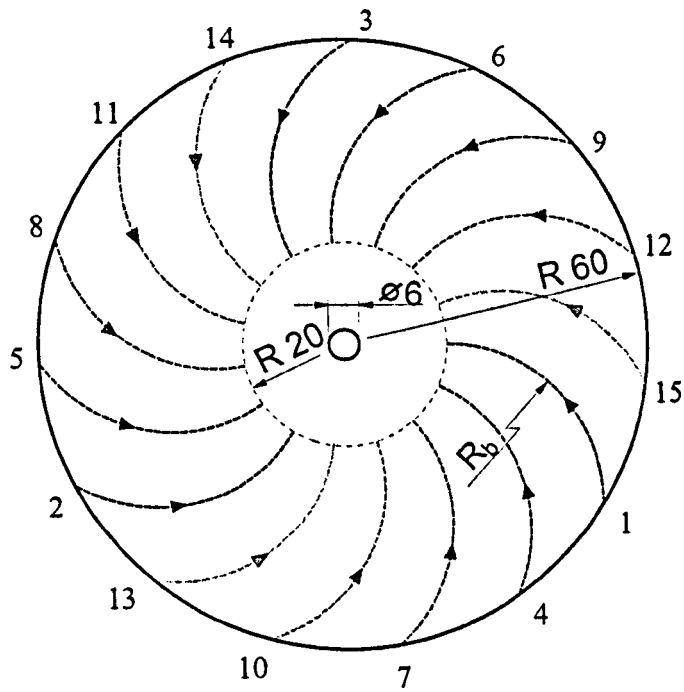


Figure 5.31: 3-star system with circle bow lines (outside-in)

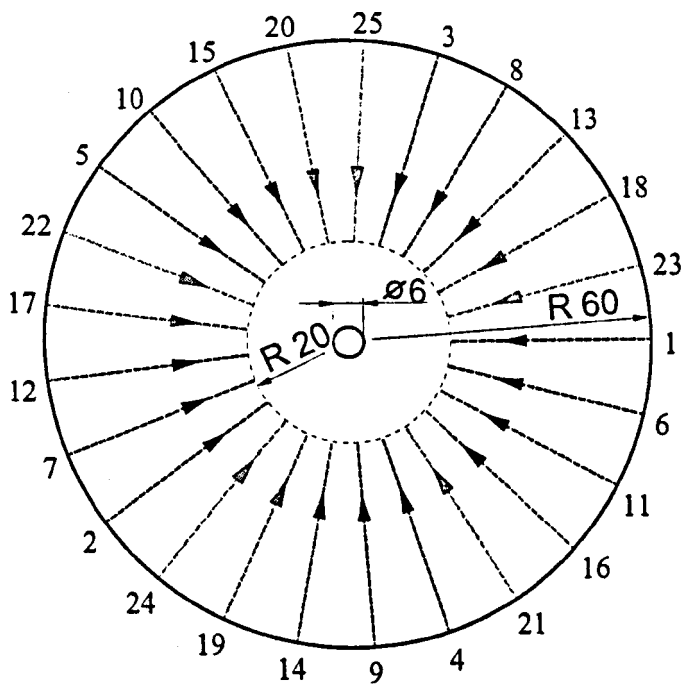


Figure 5.32: 5-star system with radial lines (outside-in)

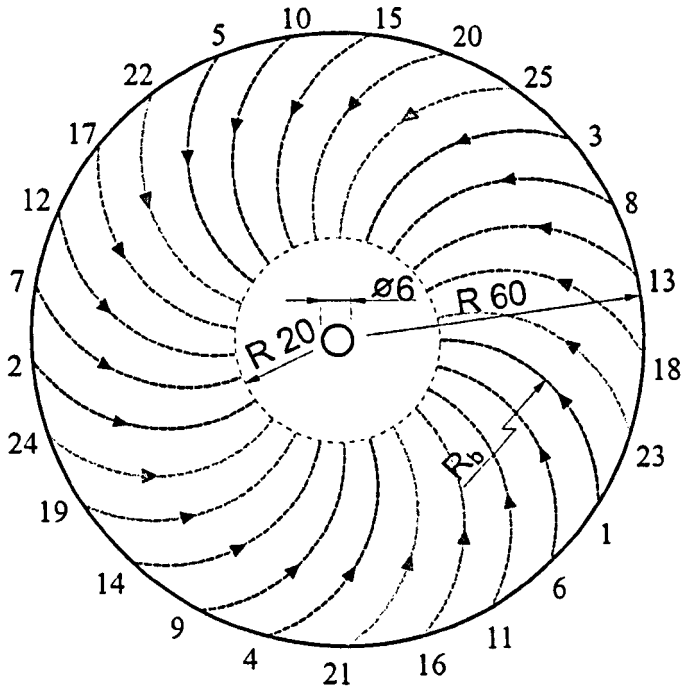


Figure 5.33: 5-star system with circle bow lines (outside-in)

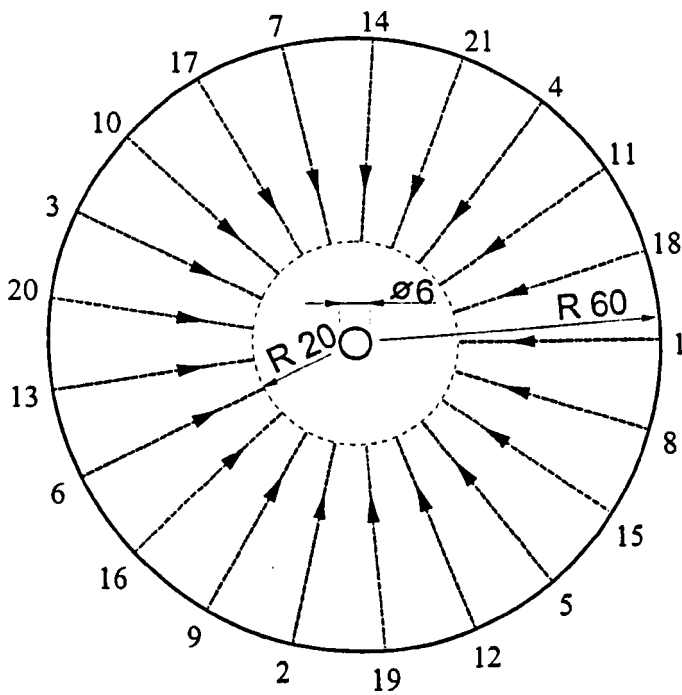


Figure 5.34: 7-star system with radial lines (outside-in)

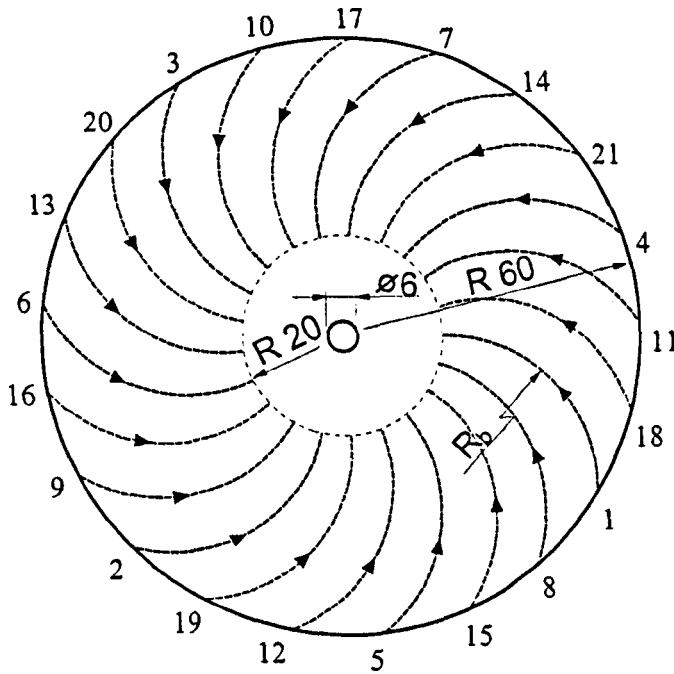


Figure 5.35: 7-star system with circle bow lines (outside-in)

Figure 5.36 illustrates the forming result from a 3-star system. Three well-rounded corners are apparent. They are due to the irradiation principle of rotating the 3-star after three lines with an offset angle. This results in an uneven heat distribution. As a result the samples are not particularly round. The maximum forming (maximum z-co-ordinate) decreases from 3 to 7-star systems as shown in figures 5.36 to 5.38). For subsequent scans the three rounded corners bend up more easily because once the three bending edges emerge the local restraint against bending is decreased and a pre-bending stress is available to assist further scans. Additionally the change in the incident laser beam profile in these areas may augment the energy input. With 5 and 7-star systems the decrease of restraint is not as pronounced due to the fact that more bending edges exist, which diminish any local stress.

The 5 and 7-star strategies present the same typical rounded corners in the inner areas, shaped like a pentagon or hexagon respectively (figures 5.37 and 5.38), whereas the outer areas do not show these features so markedly. The contour lines in that area indicate a saddling and folding which is due to the asymmetry in the irradiation pattern of a 5 or 7 pointed star.

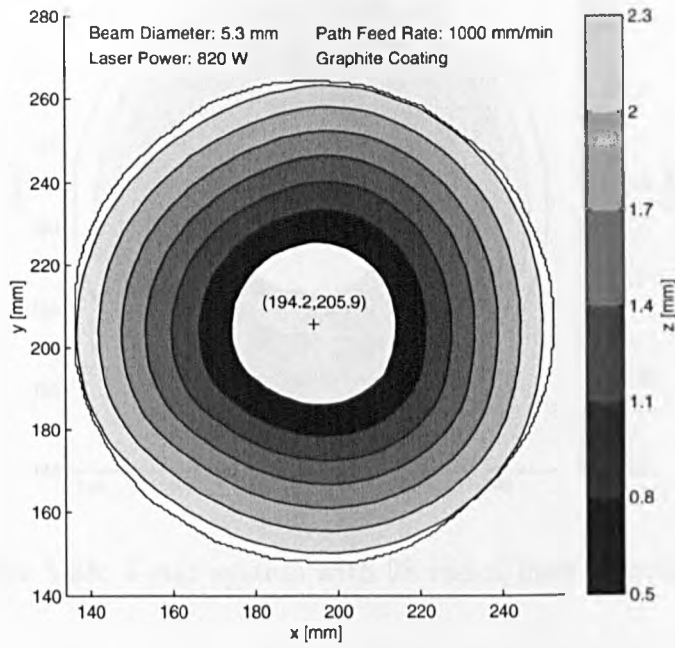


Figure 5.36: 3-star system with 27 radial lines (outside-in)

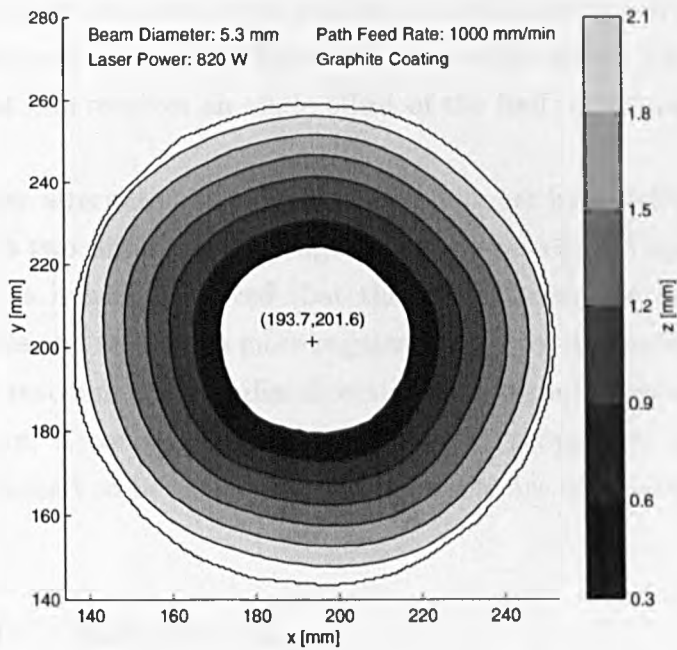


Figure 5.37: 5-star system with 30 radial lines (outside-in)

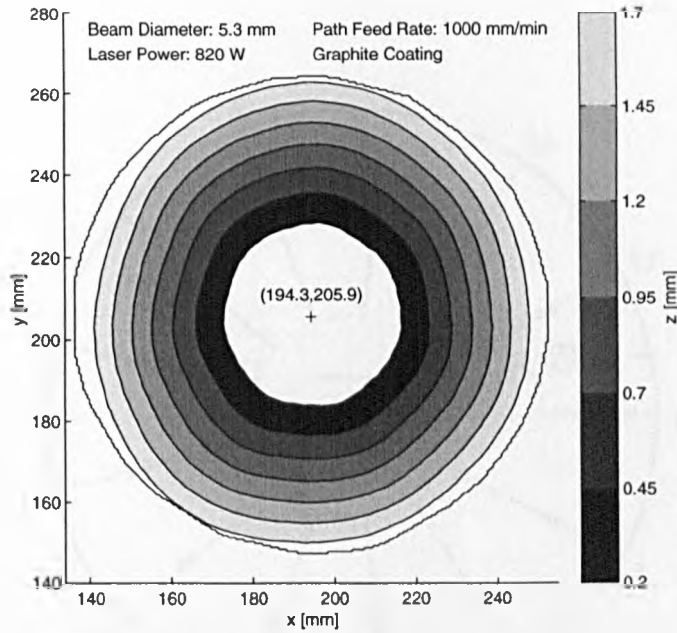


Figure 5.38: 7-star system with 28 radial lines (outside-in)

Due to the lack of roundness at the edges, the surface waviness and the saddling effects, the 3, 5 and 7-star systems did not result in a symmetrical forming.

### Offset systems

The offset method alternates the side between the irradiation lines. The circular plate is divided by an odd number of sectors to avoid directly opposite lines. Even numbers would result in opposite lines and a pre-orientation. After the first scan every subsequent line receives an angle offset of the half sector angle to avoid this problem.

Offsetting may alternate between shorter and longer irradiation lines and circle bow lines. Up to two different line lengths may be selected in each case. Shorter lines were used as it was perceived that they would generate more symmetrical temperature fields and result in a more regular forming of the material. Accounting for the changing restraint in the radial direction, which causes less shrinkage around the circumference, a compensation with a greater proportion of lines near the circumference seemed to be necessary. The systems are illustrated in figures 5.39 to 5.42.

### Forming result - Offset systems

Unfortunately the temperature fields generated with offsetting are not symmetrically distributed over the plate surface because two opposing warmer zones and two colder zones result. The latter are irradiated within the last lines of irradi-

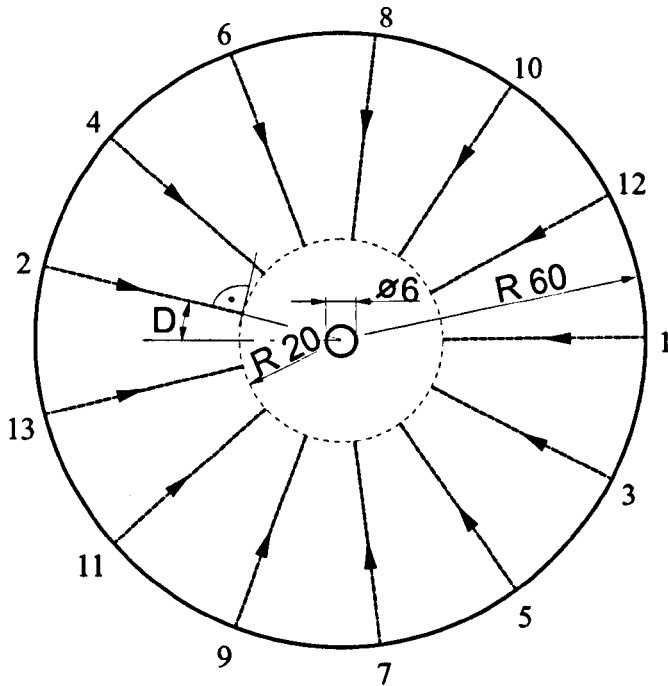


Figure 5.39: Offset system with radial lines (outside-in)

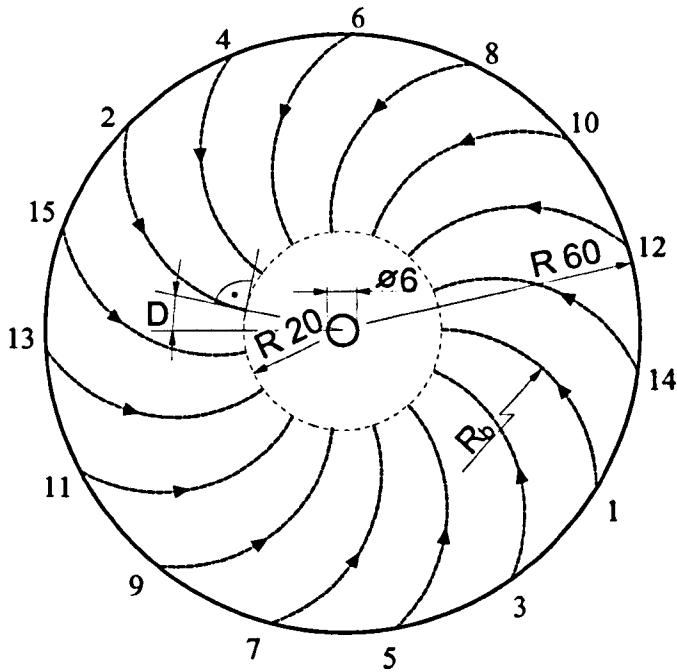


Figure 5.40: Offset system with circle bow lines (outside-in)

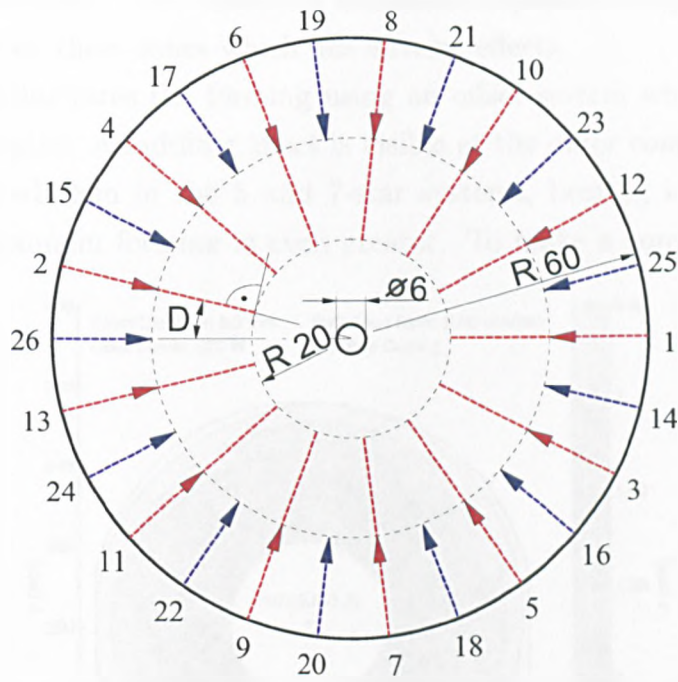


Figure 5.41: Offset system with two radial line types (outside-in)

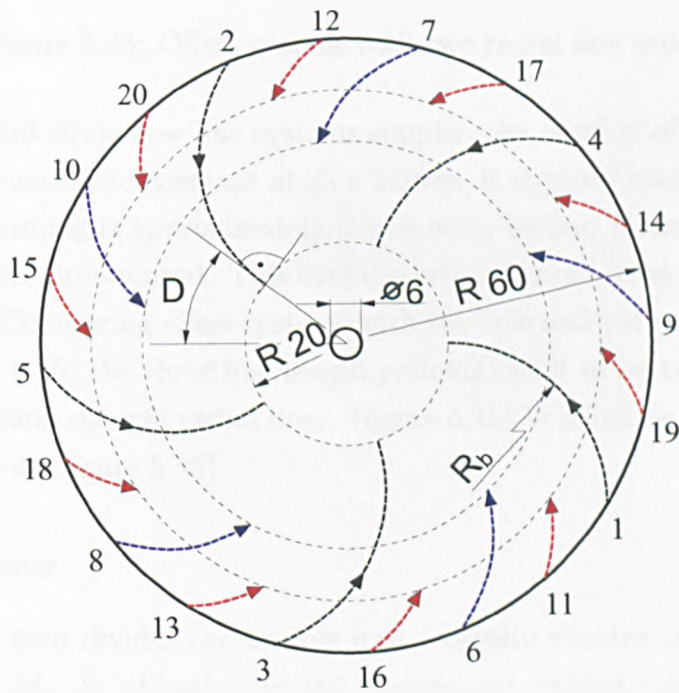


Figure 5.42: Offset system with three circle bow line types (outside-in)

ation. Unless the final line of irradiation is reached mechanical symmetry is not completely given either. This results in different temperature dependent material properties between these zones which has adverse effects.

Figure 5.43 illustrates the forming using an offset system with radial lines of two different lengths. A saddling effect is visible at the outer contours. The effect is less pronounced than in the 5 and 7-star systems, bearing in mind that the comparative maximum forming is even greater. To make a comparison between

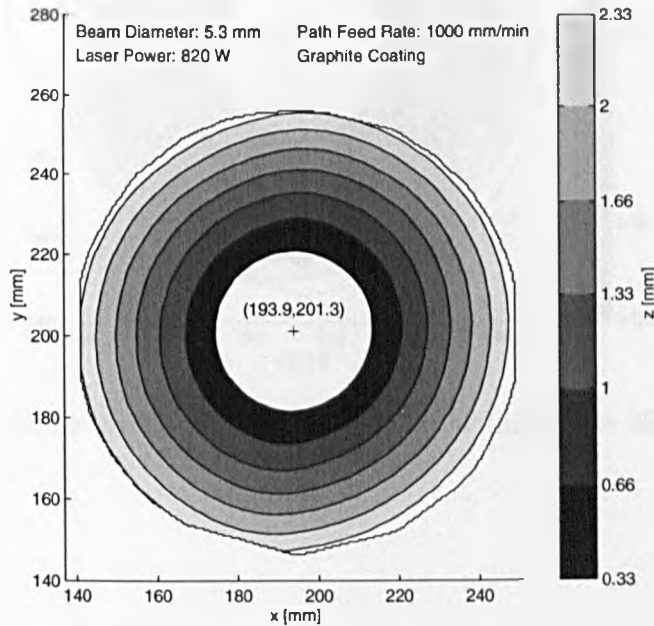


Figure 5.43: Offset system with two radial line types

straight radial and circle bow line systems simpler, the number of irradiation lines in each case has been held constant at  $25 \times 2$  lines. It appears from figure 5.44 that the maximum forming is approximately the same as before. However the saddling effect is even more pronounced. This oval distortion is marked at the inside of the sample as well. Comparing offset systems with two line and with three line lengths (figure 5.45 and 5.46) the three line length systems result in better symmetry. No saddling arose using straight radial lines. (figure 5.45) With circle bow lines a little saddling occurred. (figure 5.46)

### Dividing systems

The dividing system divides the sample into a certain number of sectors, for example 3, 6, 12, 24, etc. Firstly the 360 degrees are divided into 3 sectors - the first three lines of irradiation. The next three lines are placed exactly between those lines. When finished with scanning the "in between" lines, the next lines are chosen where the material is expected to be coolest. In common with offsetting,

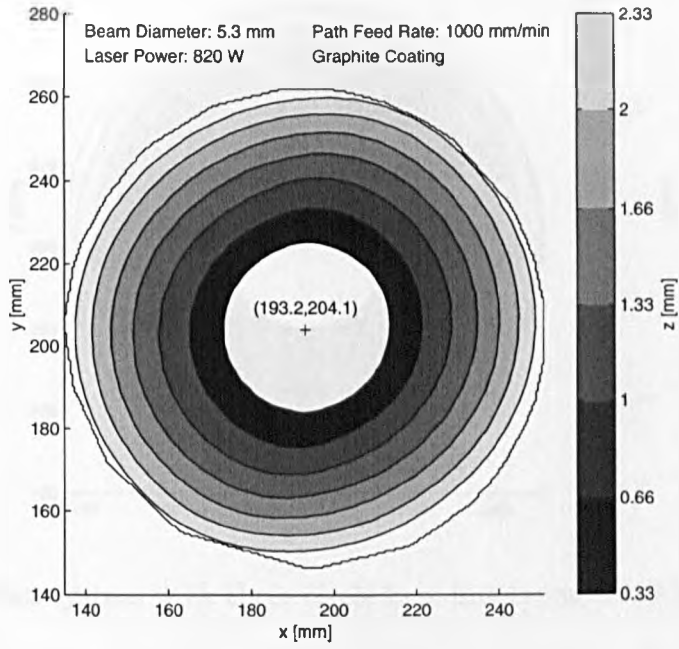


Figure 5.44: Offset system with two circle bow line types 25 x 2outside-in

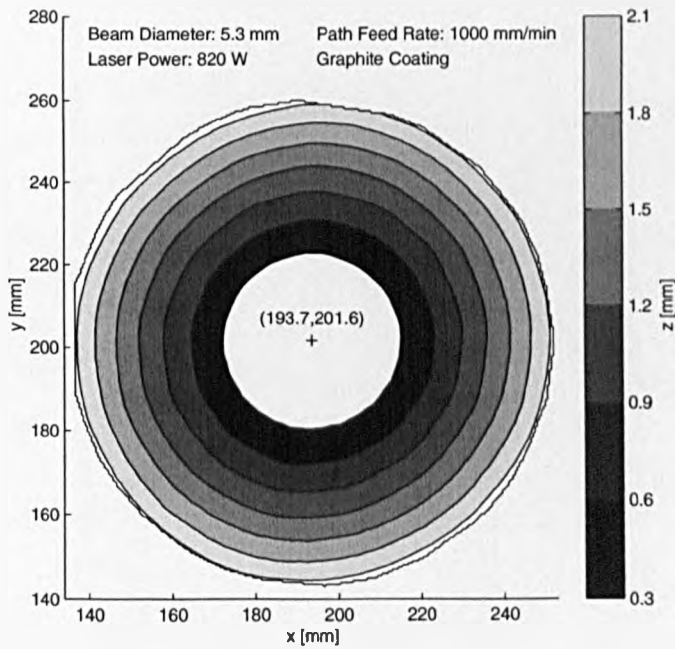


Figure 5.45: Offset system with three radial line types, 13x3 lines (outside-in)

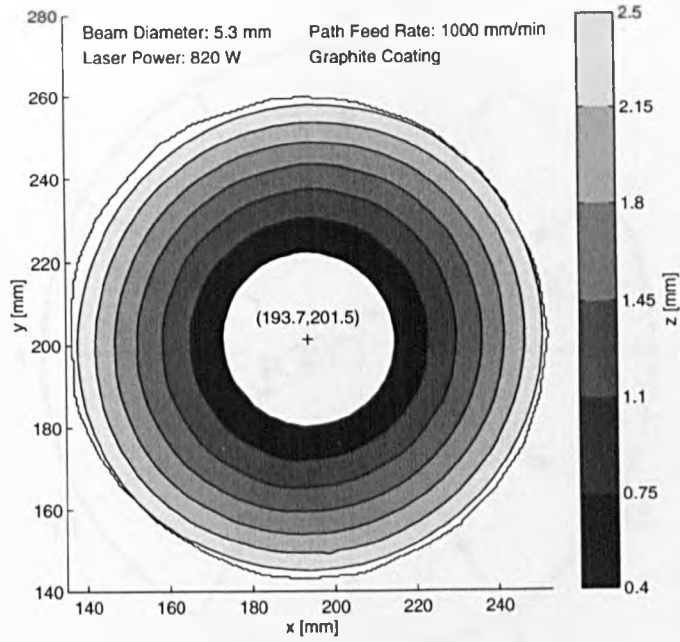


Figure 5.46: Offset system with three circle bow line types, 13x3 lines (outside-in) circle bow lines of varying line lengths were implemented. The scan patterns are shown in figures 5.47 to 5.50.

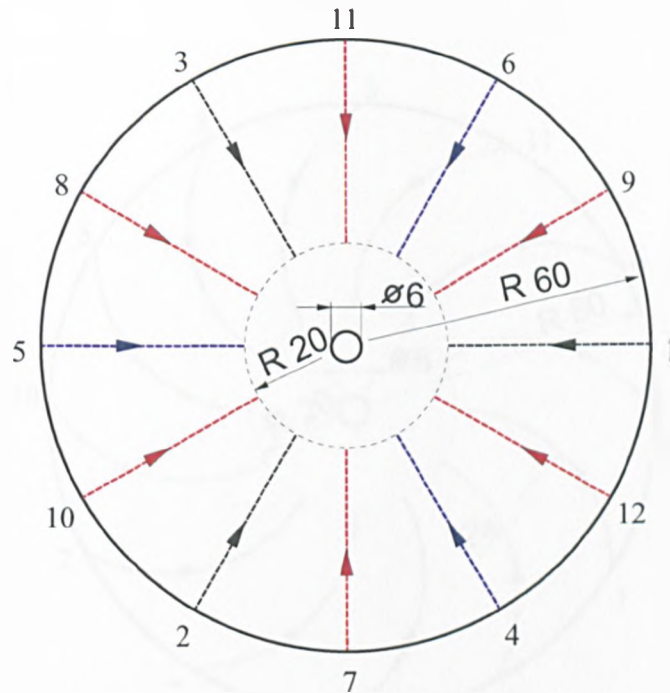


Figure 5.47: Dividing system with radial lines (outside-in)

### Forming result - Dividing systems

The advantage of the dividing system is the generation of an almost symmetrical temperature field and complete geometrical symmetry after every third line of irradiation. The disadvantage is that successive opposite lines cannot be avoided. The method yielded the best results with the upsetting mechanism, straight radial lines and circle bow lines having equal success. Figures 5.51 to 5.54 illustrate the forming results for radial and circle-bow line dividing systems. The outer contour lines fit almost exactly into a circle, which indicates the high degree of symmetry. This highlights that the most important prerequisite for a regular, axi-symmetrical forming is the attainment of symmetry as quickly as possible.

However it appears 12 lines of one line type are too few, a marked radial waviness is very much in evidence (figure 5.53). The waviness diminishes as soon as circle bow lines are used (Figure 5.54). It is worth noting the difference in the maximum forming between straight radial lines (figures 5.51 and 5.53) and circle bow lines (figures 5.52 and 5.54). The maximum forming is much larger with circle bow lines. An explanation may be the greater energy input from the longer irradiation paths of curves compared with straight lines. More of the surface is heated by the laser spot, and the material gets warmer, the average yield stress of the material decreases, and finally the overall resistance to the forming diminishes.

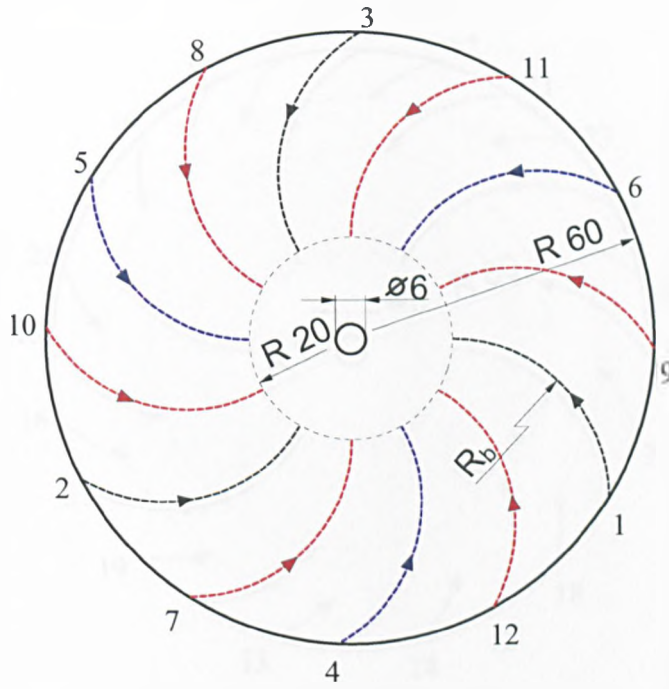


Figure 5.48: Dividing system with circle bow lines (outside-in)

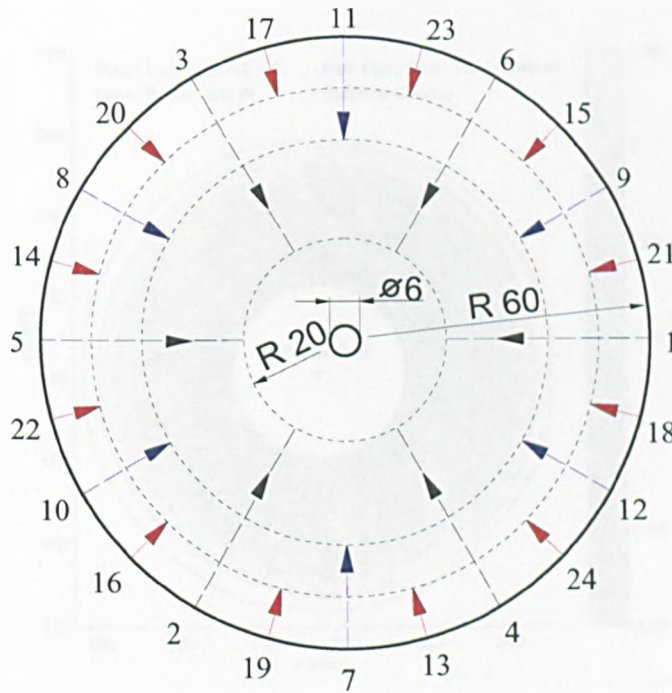


Figure 5.49: Dividing system with three radial line types (outside-in)

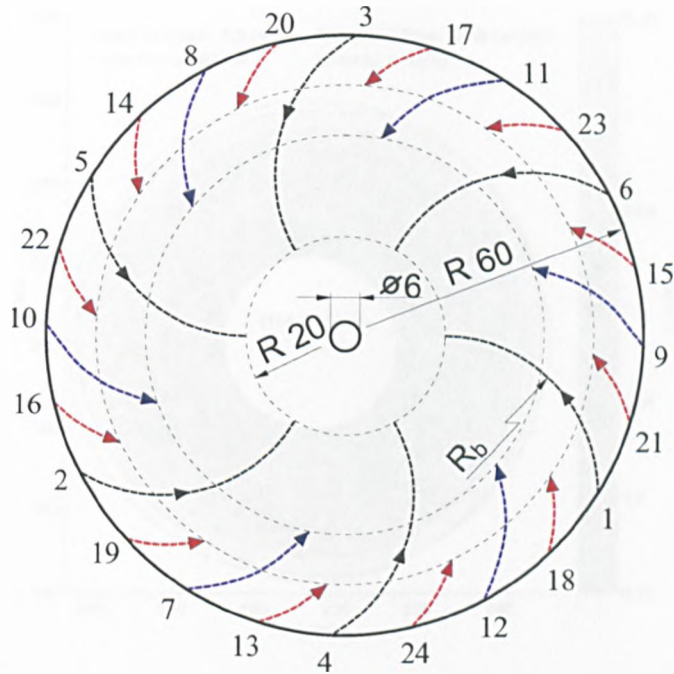


Figure 5.50: Dividing system with three circle bow line types (outside-in)

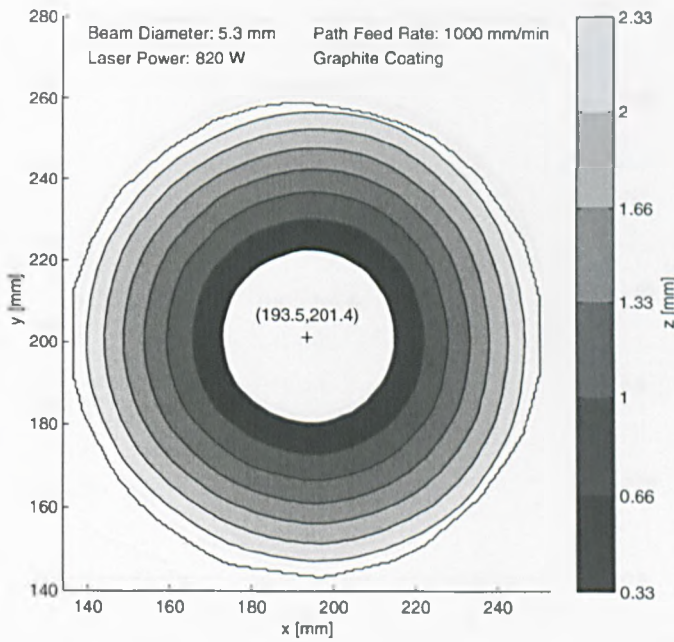


Figure 5.51: Dividing system with two radial line types, 24x 2 lines (outside-in)

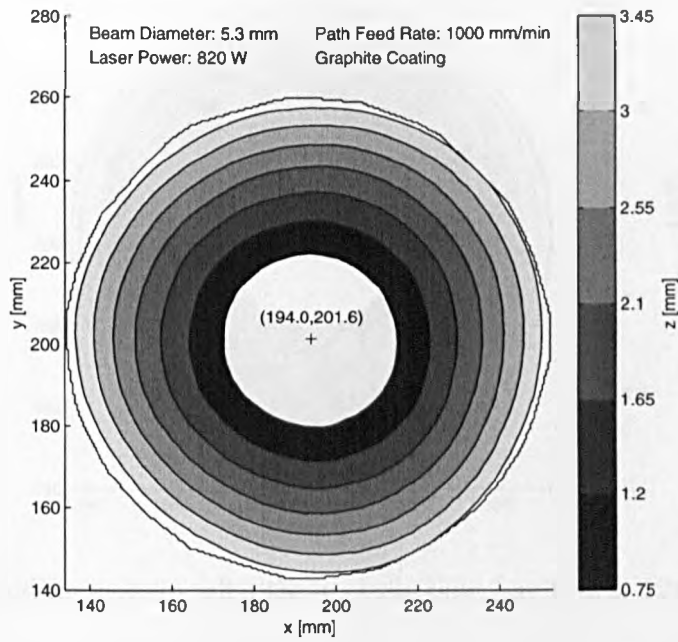


Figure 5.52: Dividing system with two circle bow line types, 24x 2 lines (outside-in)

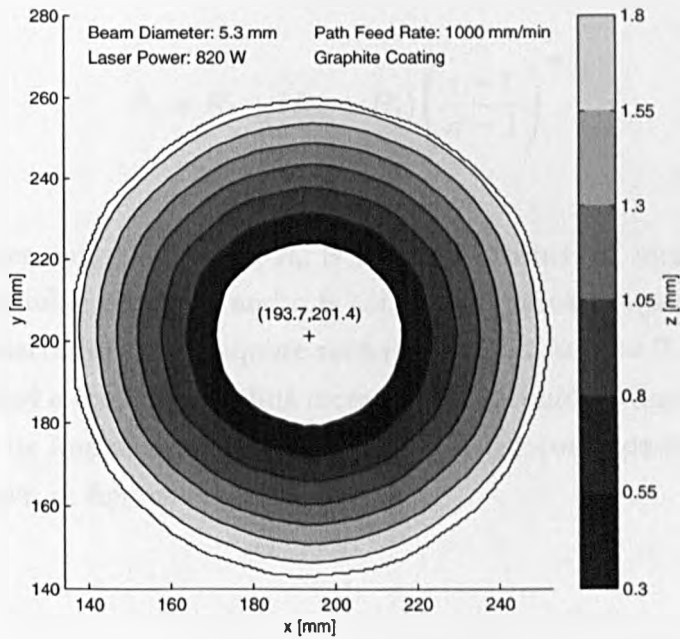


Figure 5.53: Dividing system with three radial line types, 12x 3 lines (outside-in)

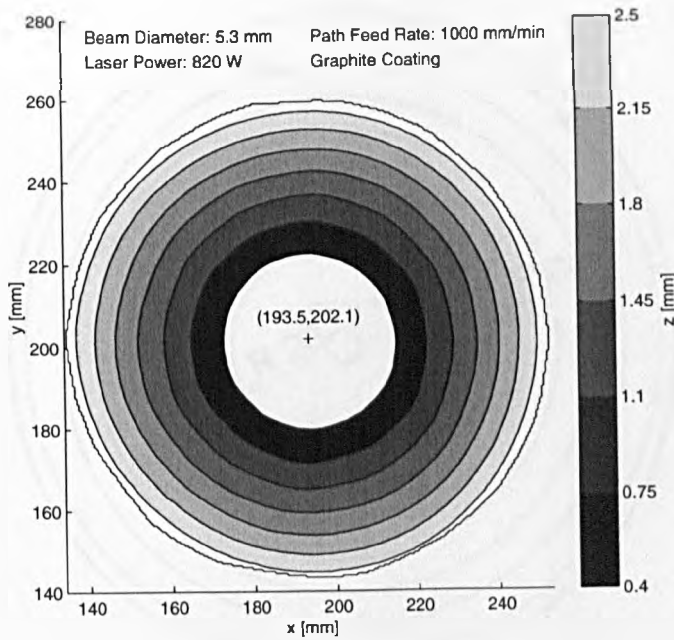


Figure 5.54: Dividing system with three circle bow line types, 12x3 lines (outside-in)

### Circle line systems

An obvious way of forming an axi-symmetrical workpiece such as a circular plate is to irradiate it with circular laser scans. Circle line systems were implemented. The radii of the circles and the density of the lines were altered by the following formula:

$$R_i = R_1 + (R_n - R_1) \left( \frac{i-1}{n-1} \right)^\alpha \quad (5.3)$$

where:

$R_1$  is the inner radius (20 mm),  $R_n$  is the outer radius (57 mm),  $i$  is the radius index,  $n$  is the number of circles and  $\alpha$  is the radius increase exponent. Due to the CNC-system constraints only a square root radius increase  $\alpha = 0.5$ , a linear radius increase  $\alpha = 1$  and a quadratic radius increase  $\alpha = 2$  could be implemented. Many functions could be implemented if the CNC controller could deal with them. The systems are shown in figures 5.55 to 5.57.

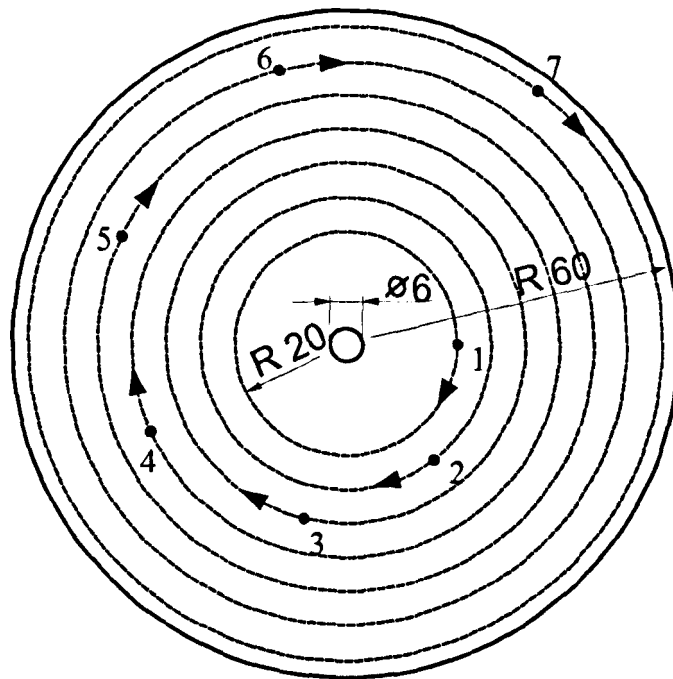


Figure 5.55: Circle line system with linear radius increase (inside-out)

### Forming result - Circle line systems

With circle lines only a small straining was achieved when irradiating from the outside-in. This may be due to a smaller decrease of the yield stress beginning at the circumference compared with starting from the inside. If the sample is irradiated from the inside the heat flow is much larger towards the outer areas (which are irradiated next) because of the greater local temperature difference and because there is a greater volume for heat to flow to in comparison to the inner regions. Ultimately this reduces the yield stress and the restraint is less.

When irradiating from the outside-in another effect becomes dominant. The first lines of irradiation reach very high temperatures because there is very little material around the circumference for the heat to flow to, this results in the heat flowing backwards in the negative radial direction to the inner regions. As the last inner circles are applied, where the restraint for geometrical reasons is greater, the yield stress due to the accumulated high temperature is less, but the realisation of a steep temperature gradient is not possible. This is because even the layers away from the laser beam in the depth direction of the sample are hot from the conduction effects. That is another reason why only small strains develop.

Figures 5.58 to 5.60 indicate that circle line systems yield very good roundness. Irradiation along circular paths generates implicitly well-rounded shapes. Using the formula given in 5.3, the series of radii were calculated. Firstly, figure

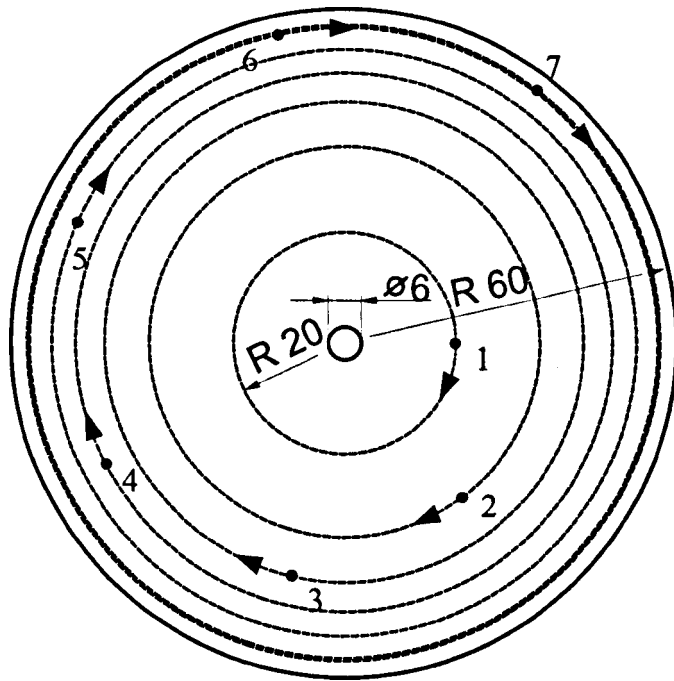


Figure 5.56: Circle line system with square root radius increase (inside-out)

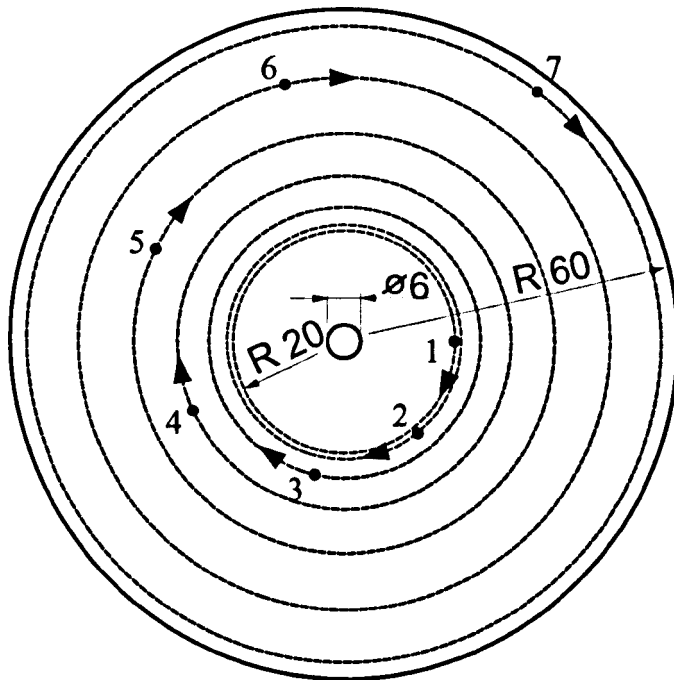


Figure 5.57: Circle line system with quadratic radius increase (inside-out)

5.58 shows the forming for a linear radius increase. The outer contour lines fit excellently into the surrounding circle. Figure 5.59 illustrates the forming using a

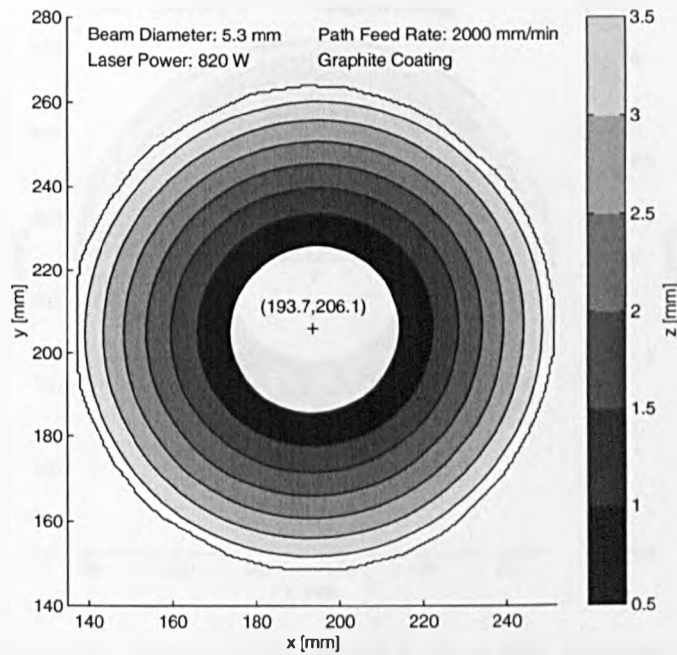


Figure 5.58: Circle line system with linear radius increase, 10 lines (inside-out)

square root radius increase. According to figure 5.56 the lines become more and more dense from the inside to the outside. As before the outer contour lines fit the surrounding circle, which indicates the roundness. The roundness is also apparent in figure 5.60 which presents the results from a quadratic radius increase, where the lines become less and less dense from the inside to the outside (refer to figure 5.57).

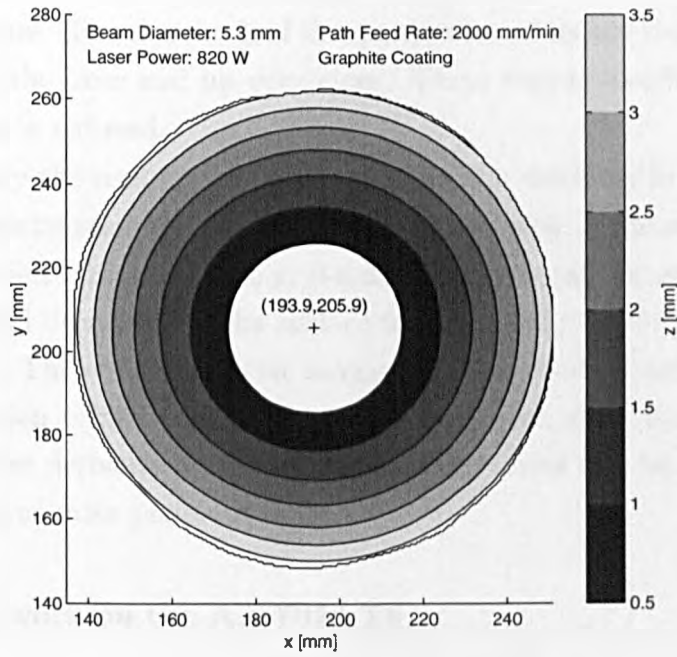


Figure 5.59: Circle line system with square root radius increase, 10 lines (inside-out)

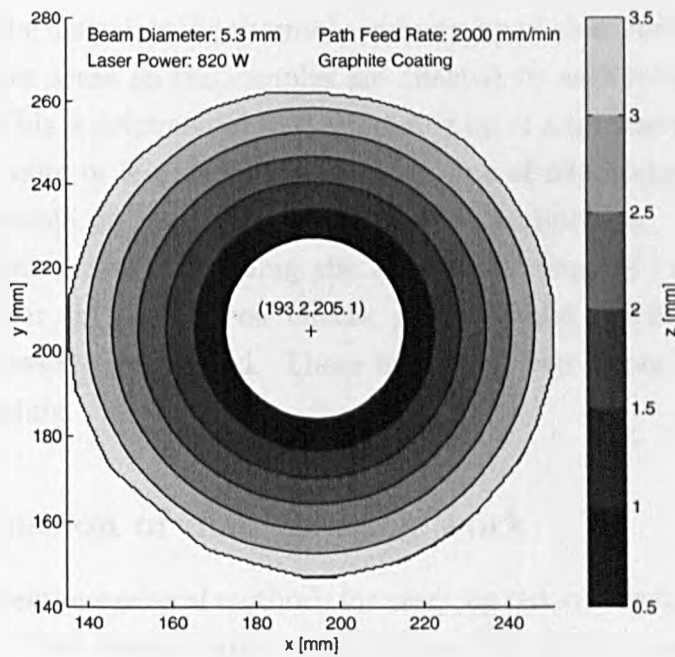


Figure 5.60: Circle line system with quadratic radius increase, 10 lines (inside-out)

The linear radius increase resulted in maximum forming. One reason for this is the more even heat input over the sample surface because of the successive equi-spacing of the lines. The drawback of the quadratic and square root radius increase systems is that the lines end up very close. These regions overheat very quickly and the forming is reduced.

Unfortunately the contour plots cannot show the waviness in the radial direction which occurs inherently if circle line systems are used. If the waviness profile in the radial direction is required, the grid-data has to be transformed a second time. The radial partial derivative of the surface function,  $\partial z(r, \psi)/\partial r$  is a mark for the radial waviness. The circumferential waviness is described by another description via the calculation of the tangential partial derivative,  $\partial z(r, \psi)/\partial \psi$ . After the calculation of the derivatives, the significant derivatives can be displayed in the same manner in contour plots.

### Dish forming work on the AA 7075 T6

The results on the AA 7075 T6 aluminium alloy samples were not promising. In every case after only a few lines of irradiation, a marked saddling effect occurred. This is attributed to the differing material properties. The thermal conductivities of CR4 steel and the AA7075 alloy are approximately 33 and 108 W/m K respectively. The specific heat capacity of the aluminium alloy is approximately 20% higher than the steel.

Comparing the materials the thermal conductivity of aluminium is much higher. As a result, larger areas on the samples are affected by each irradiation, the heat flows "faster". This is detrimental to the building up of a symmetrical temperature field, as this is more or less dependent on each line of irradiation having as little influence as possible on the surrounding material properties. Additionally the effect of guillotining and trepanning the aluminium samples (whereas the steel samples were laser cut) has adverse effects, i.e. a certain amount of pre-bending and residual stresses are incurred. These influences were superimposed onto the actual laser bending.

### 5.2.4 Discussion of dish forming work

In the previous sections several methods for carrying out symmetrical laser forming were described. That was the aim of this study. The *dividing systems* and *circle line systems* are superior to the others. The 3, 5 and 7-star systems resulted in an unbalanced heat distribution, and apart from pre-bending effects, offset systems have the same disadvantage.

With dividing systems it appears to be very important to fulfill the geometrical symmetry condition as soon as possible at each increment of forming. At the earliest this is possible after every third line of irradiation. The heat should be distributed over the sample as evenly as possible to achieve a uniform change in the temperature dependent material properties. The expected detrimental effects of pre-bending (when directly opposite lines are irradiated) seem to be less important even though these lines arise after every third line employing dividing systems.

However it is possible to shape axi-symmetrical structures with the use of radial lines, employing the upsetting mechanism, by building up the irradiation sequence using "3-stars," three lines with a 120 degrees offset, to be continued in the next step with a rotation of the 3-star. That is the best possibility for fulfilling the symmetry requirement with these systems.

## 5.3 Metallurgy and Mechanical Properties

### 5.3.1 The metallurgical changes which may occur to AA2024 - T3 due to laser forming

After achieving the exotic composition and the mechanical properties of this alloy, as outlined in chapter four, it would be expected that further local heat treatment from the scanning laser beam would have some effects. A high temperature zone results from the scanning laser beam. However the cold surrounding material cools this high temperature zone quickly, as it acts as a heat sink and the thermal conduction is high in this alloy. With repeated scanning the integral time that the material remains at temperature is long and metallurgical and mechanical property changes are likely. The possible changes are summarised next.

#### Heating to 503 K

A large amount of plastic deformation is a feature of this alloy from cold rolling. In combination with this initial plastic deformation, if the temperature reaches that of recovery, i.e. 503 K, the dislocations arrange into a substructure of cells. Dissolution into solid solution of less than 0.5% of the copper should take place and this would lower the hardness locally. The high cooling rate causes the saturated solid solution to precipitate out as GP zones during ageing if left at room temperature, recovering the loss in hardness. [60]

### Heating to 623 - 683 K

When the temperature reaches that for recrystallisation, i.e. 623 - 683 K, and the material is exposed to this temperature for long enough, recrystallisation takes place after recovery. The percentage of copper that dissolves into solid solution falls now between 1.0 and 2.0%. Recrystallisation is dynamic as the material is experiencing plastic deformation with the accompanying increases in the dislocation density from the forming process. If recrystallisation is fully accomplished, grain growth may be initiated if the temperature remains high for long enough. [60]

### Heating to 788 - 823 K

When the temperature exceeds the solvus temperature, i.e. 788 - 823k, solution heat treatment proceeds and the alloying elements go into solid solution. If the quench rate is sufficiently high, after cooling these regions stay highly saturated and this facilitates re-ageing at room temperature. Continued heating with the laser may precipitate transition particles such as GP(2),  $\Theta'$  and S'. [60]

### Heating to the Eutectic temperature

If the temperature exceeds the eutectic temperature, regions of the material that have a higher than average composition may partially melt and undergo hot tearing.[60]

### Heating above the melting temperature

Above the melting point the material melts and then rapidly re-solidifies resulting in a cast structure.[60]

A number of these processes may take place simultaneously at various radial distances from the centre of the laser beam and at various depths through the thickness of the material.

## 5.3.2 AA 2024 T3 - Optical micrographs

In figure 5.61 the "as-received" material is presented [64]. An elongated grain structure and a smooth interface between the Alclad and the alloy substrate is present. The elongated grains result from cold-working after solution heat treatment and quenching. Large dark particles are possibly  $\text{Cu}_2\text{FeAl}_7$  constituents and the lighter particles are possibly  $\text{CuAl}_2$ . In figure 5.62, recrystallisation of the surface layer underneath the Alclad has taken place down to 100  $\mu\text{m}$ . The aluminium clad did not recrystallise as the temperature was not high enough for this to occur.

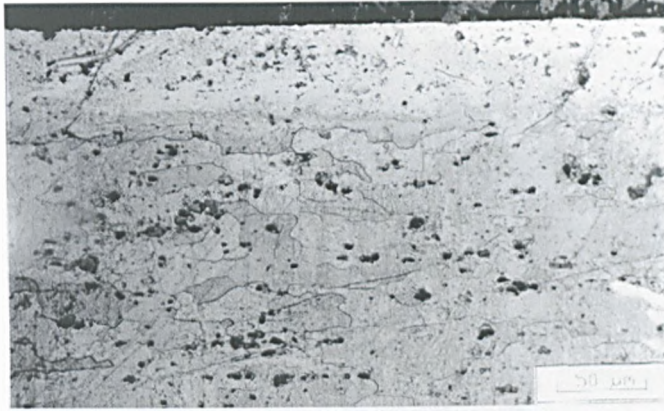


Figure 5.61: The as-received material, x400

	Laser Power (W)	Spot size (mm)	Traverse velocity (mm/s)	Number of scans
Figure 5.62	500	5	25	1
Figure 5.63	500	5	25	1
Figure 5.64	500	1	80	10
Figure 5.65	250	1	20	10
Figure 5.66	500	1	40	10
Figure 5.67	250	1	10	10
Figure 5.68	250	1	10	10
Figure 5.69	250	5	15	5

Table 5.3: Table of parameters used for AA2024 T3 micrographs

The AED value was  $4.0 \text{ J/mm}^2$ . Here the AED value refers to the *average energy density* which the material was exposed to. It is defined by:

$$AED = \frac{nsP}{Dv} \quad (5.4)$$

where:

$ns$  is the number of scans,  $P$  is the laser power,  $D$  is the spot size, and  $v$  is the traverse velocity of the sheet relative to the beam. The units of AED are  $\text{J/mm}^2$ . The higher the AED value, the greater the thermal load the material has experienced.

A recrystallised and elongated grain structure is illustrated in figure 5.63. In this case the grain size is smaller compared to the as-received size. This happened as there was less time for recrystallisation to occur fully. The elongation is due to the previous lamination of the material and the presence of Mn and Fe based dispersoids accentuate this feature. The large dark spots are possibly Fe or Si based constituents remaining from the cast structure. The clad surface is distorted but

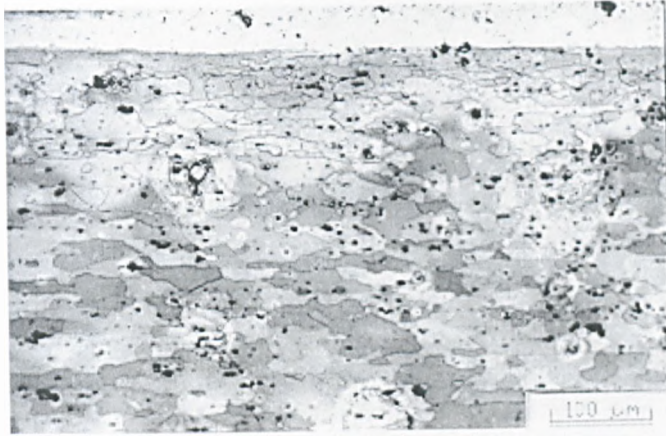


Figure 5.62: Recrystallisation of the upper region of the sheet under the clad layer, x200

the interface with the core alloy looks smooth. In figure 5.64, the Alclad surface

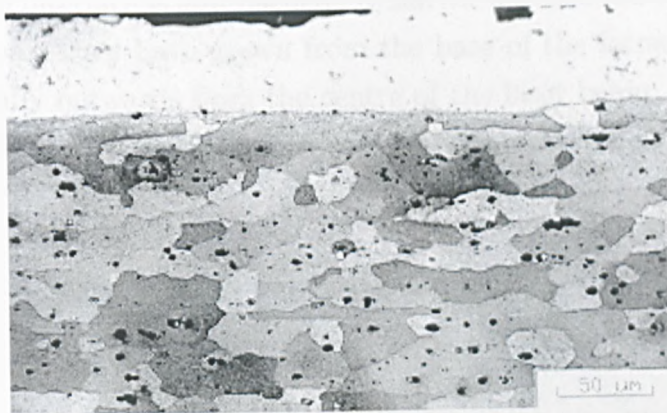


Figure 5.63: Recrystallisation of the upper region of the sheet under the clad layer, x 400

is irregular and the interface is not smooth. Underneath the clad there is severe partial melting of the recrystallised grains which are the dark boundaries visible around the grains. They correspond to the eutectic composition and produce hot tearing between grain boundaries, notably all of them are orientated horizontally. Recrystallisation into finer and less elongated grains is visible up to  $100\ \mu\text{m}$  below the interface. The smaller grain size may be attributed to an incomplete dynamic recrystallisation due to the very rapid heating/cooling cycle. The AED value was  $62.5\ \text{J}/\text{mm}^2$ .

The Alclad layer partially melted at the interface with the alloy substrate forming a dendritic cast structure in figure 5.65. Copper from the core diffused up to the surface of the clad and hot tears of some the grains formed. Underneath the interface the alloy melted slightly. The heat affected zone (HAZ) extends towards the

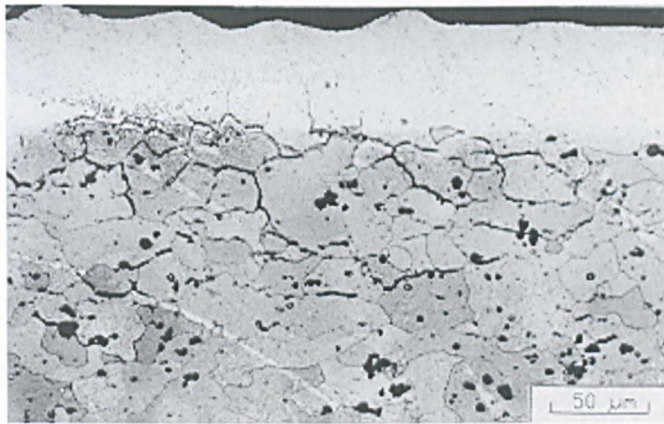


Figure 5.64: Irregular Alclad-substrate interface and severe partial melting of recrystallised grains

bottom showing small recrystallised grains affected by partial melting, particularly as the resolidified interface is approached. Dendritic and cellular structures are visible in this region. They have grown from the base of the former grains and are distributed radially outwards from the centre of the laser beam, following its flux distribution. The AED value was  $125 \text{ J/mm}^2$ . Large recrystallised grains with pre-

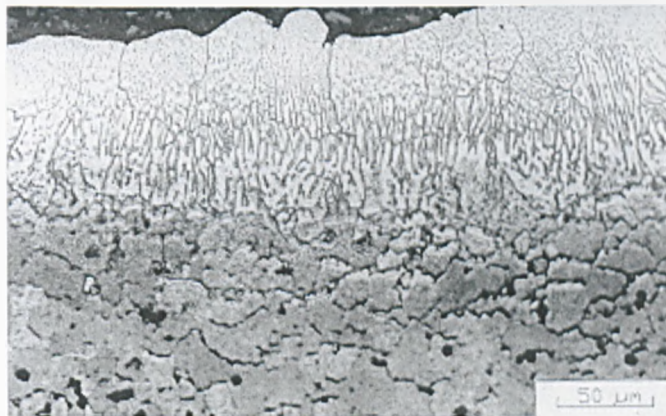


Figure 5.65: Fusion of the alclad with the substrate showing a dendritic cast structure and partial melting of recrystallised grains towards the lower regions

cipitates at their grain boundaries (visible as small dots) may be seen in figure 5.66. Some of the grains have diameters greater than  $100 \mu\text{m}$  and they probably grew during an early secondary recrystallisation induced by the rapid heating/cooling cycle. Larger dark spots may be constituent particles, lighter spots are possibly dispersoids of Mg and Mn. The AED value was  $125 \text{ J/mm}^2$ .

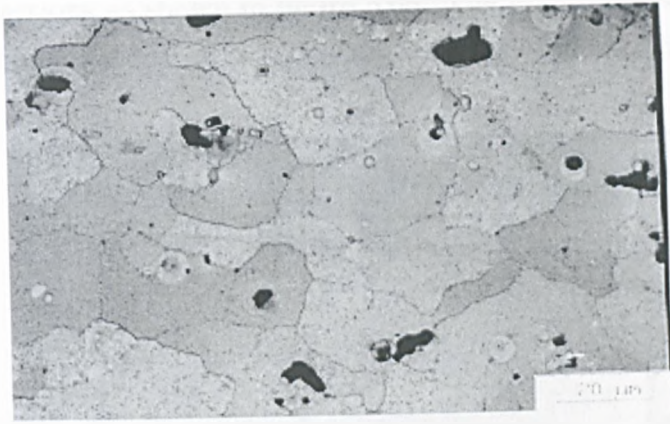


Figure 5.66: Large recrystallised grains with precipitates at the grain boundaries, and constituent particles, visible as dark spots

### 5.3.3 AA 2024 T3 - SEM images

The microstructural changes occurring at the interface of the resolidified material (left) and the former grain structure (right) are shown in figure 5.67. The small recrystallised grains partially melted around their boundaries. The cast structure formed during resolidification shows dendrites growing from the base of the former grains. The AED value used was 250 J/mm<sup>2</sup>. A grain that has partially melted,

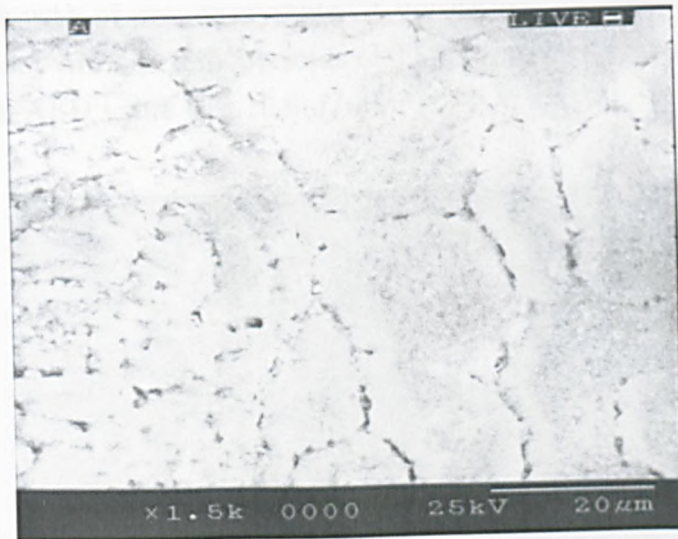


Figure 5.67: Microstructural changes at the interface of the resolidified material and the previous grain structure

as well as the associated hot tear around its boundary is shown in figure 5.68. A constituent round particle (Cu-Mg-Fe) of approximately 4 μm in diameter is visible. A copper depleted zone is observed surrounding the melted grain boundary and the constituent particle. Evidently partial melting occurs with ease at triple grain

boundary intersections as shown in figure 5.68. The grain boundary is filled with the eutectic composition and it is prone to cracking. A subgrain structure which

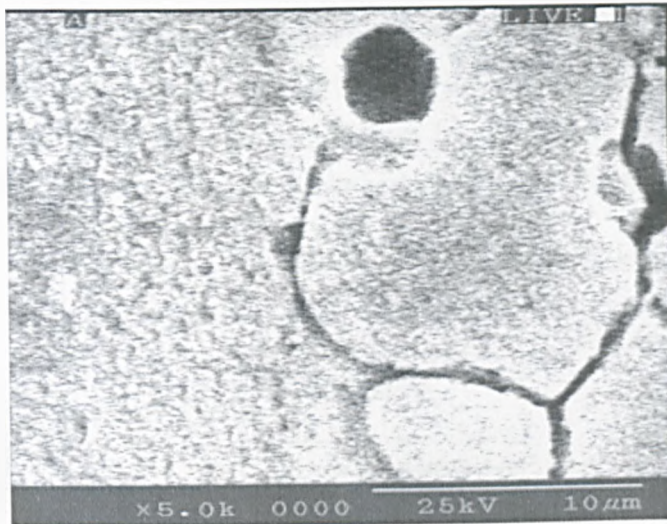


Figure 5.68: Partial melting and hot tearing of a grain

formed during the early stages of dynamic recrystallisation is shown in figure 5.69. It resulted from the high thermal load and the plastic deformation from the forming process. This behaviour was arrested as the interaction time was not long enough to sustain the growth of proper crystals. A constituent particle of  $4\mu\text{m}$  length is visible and possibly Mn based dispersoids of  $0.5$  to  $1\mu\text{m}$  are present at the subgrain boundaries. The AED value was  $16.6 \text{ J/mm}^2$ .

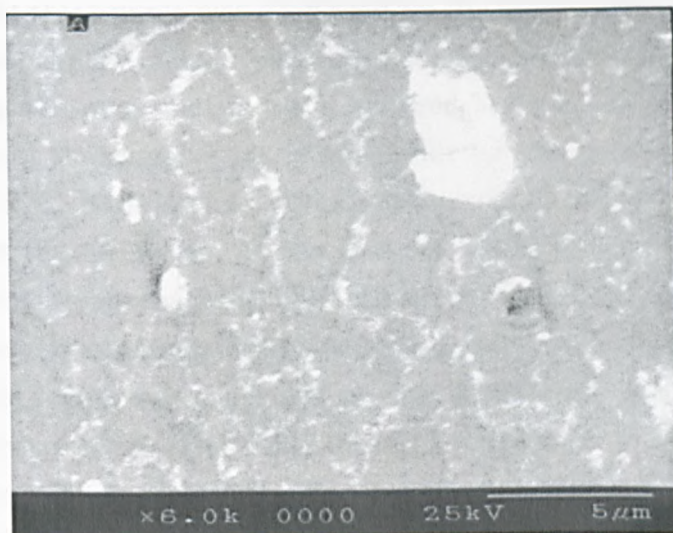


Figure 5.69: Formation of a subgrain structure during the early stages of dynamic recrystallisation

### 5.3.4 AA 2024 T3 - Microhardness graphs

The Vickers hardness of the as-received material was measured across the thickness of the material. This profile is shown in figure 5.70. It may be observed that the hardness level is fairly constant across the thickness of the sheet. However the sudden drop in hardness at the top and bottom layers is due to the change to the almost pure Al cladding. The average Vickers hardness is  $150.90 \pm 2.70$  Hv. In some of the following graphs, the Alclad points are not included. The hardness

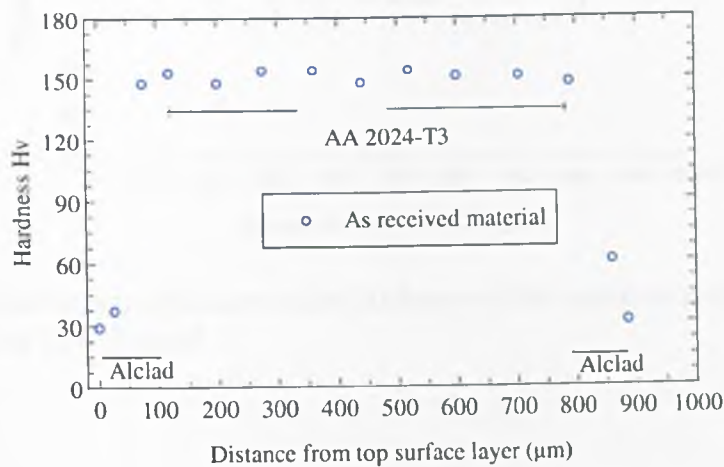


Figure 5.70: Hardness profile across the thickness of the as-received material

profile of the sample in figure 5.71 is almost the same as the "as-received" condition. The interaction time was very small and the temperature was not high enough to anneal the microstructure fully. The reduced amount of recrystallisation of the grain structure of this sample was confirmed by the light microscopy results. The drop in hardness near the alclad - alloy interface may be attributed to a depletion of the copper in the alloy matrix, as it diffused towards the alclad layer. The hardness profile of the samples are quite similar for similar interaction times as shown in figure 5.72. Both laser treated samples exhibit maximum micro-hardness at  $400 \mu\text{m}$  below the surface and then a decrease towards the as-received value as the bottom layers are approached. The increase in hardness towards the peak T6 temper value may be due to artificial ageing. Recrystallisation of smaller grains in the upper-middle region was confirmed by light microscopy results. The bottom region did not recrystallise. This could mean that the temperature field there was lower than the minimum recrystallisation temperature for the AA 2024 T3 alloy. The net result for this region was that the hardness approached the as-received value again. The drop in hardness at the top surface is associated with the Alclad layer. The high temperature there promotes copper and magnesium diffusion into the clad and lowers the hardness.

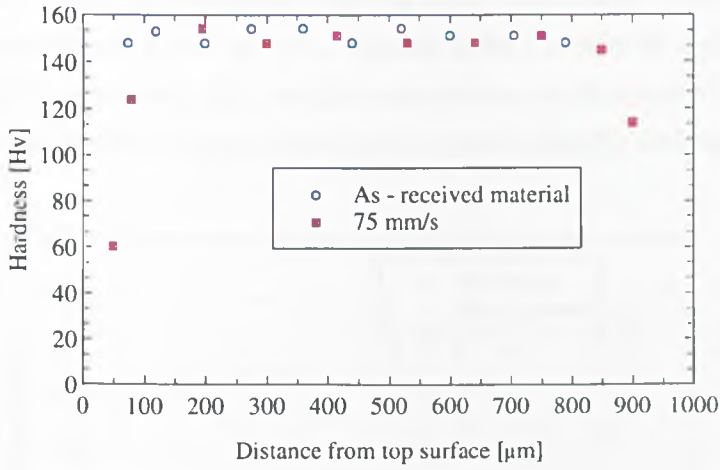


Figure 5.71: Hardness profile across the thickness of the material scanned 10 times, with an AED of  $10.6 \text{ J/mm}^2$

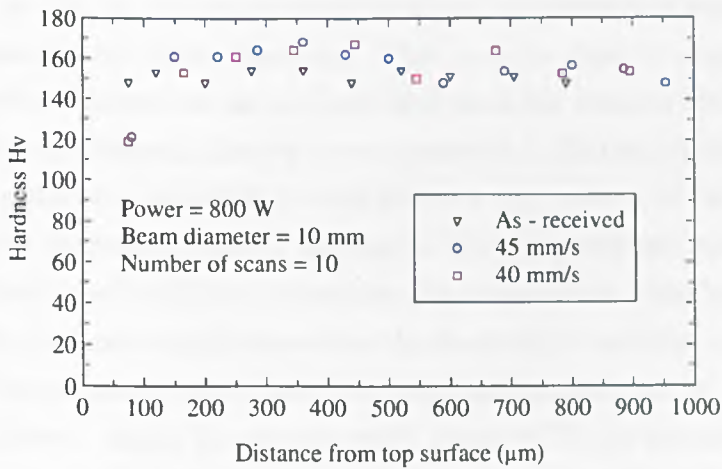


Figure 5.72: Hardness profiles across the thickness for samples with an AED of 17 and  $20 \text{ J/mm}^2$

There is an increase in the hardness profile in the upper regions of the sample illustrated in figure 5.73 just below the Alclad layer. The higher AED value of  $25 \text{ J/mm}^2$  was used. The hardness increase is due to the finer grain size after recrystallisation. This was confirmed by the light microscopy. The effect of a T6 temper may have played a role as well. Approaching the middle zone the hardness converges to the as-received value as the temperature is diminished in this region. In addition, as the strain is proportional to the power density and interaction time,

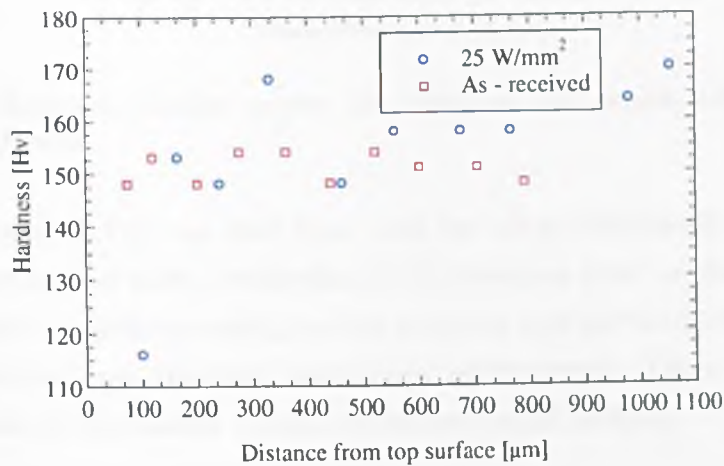


Figure 5.73: Hardness increase due to finer grain size after recrystallisation for an AED of  $25 \text{ J/mm}^2$

increases in these lead to an increase in the strain of the lower layer by cold working up to a point (as long as the temperature gradient mechanism is sustainable), and hence an increase in the micro-hardness. This may be used to explain the sharp increase in hardness above the as-received level near the bottom clad layer. There is a steep drop in hardness at the top zone in sample 1 (30 mm/s), figure 5.74. The hardness approaches the as-received value towards the bottom of the sample. This may be due to a decreasing partial melting in the recrystallised structure. These features were confirmed by light microscopy. The interaction time for sample three was less and the hardness profile resembles the as-received material along the entire depth. If the temperatures were lower recrystallisation and partial melting would have been inhibited. Again in common with figure 5.73 the increase in hardness at the bottom region of sample 1 is caused by strain hardening. It has been shown that the bend angle is inversely proportional to the scanning velocity [14], therefore for sample 1 the strain hardening is higher compared to that of sample 3. The sample in figure 5.75 exhibits a lower hardness level than the as-received material up to the middle region. The micro-hardness increases with depth to a maximum of 160 Hv (higher than the as received value). This is attributed to strain hardening

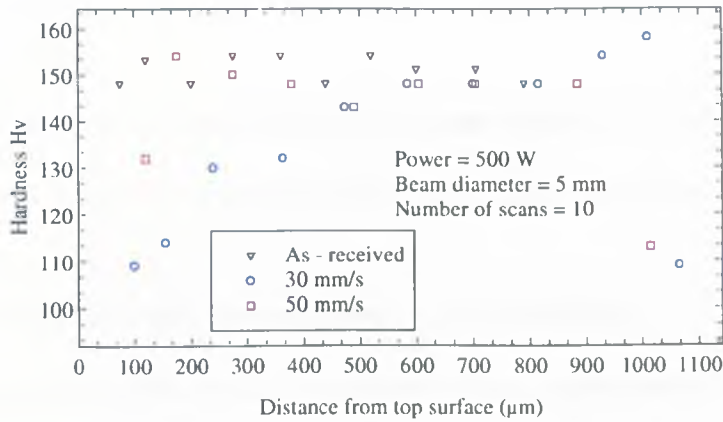


Figure 5.74: Hardness profiles across the thickness for sample with an AED of 33.33 and 20  $J/mm^2$

at the lower layers. The top clad layer and the alloy underneath it melted and partial melting ensued with a reduction of the hardness level to below 100 Hv. In the fusion zone, complete recrystallisation occurred and partial melting of the top region was evident from the light microscopy observations. There was a reduced recrystallisation of the middle region and lesser partial melting.

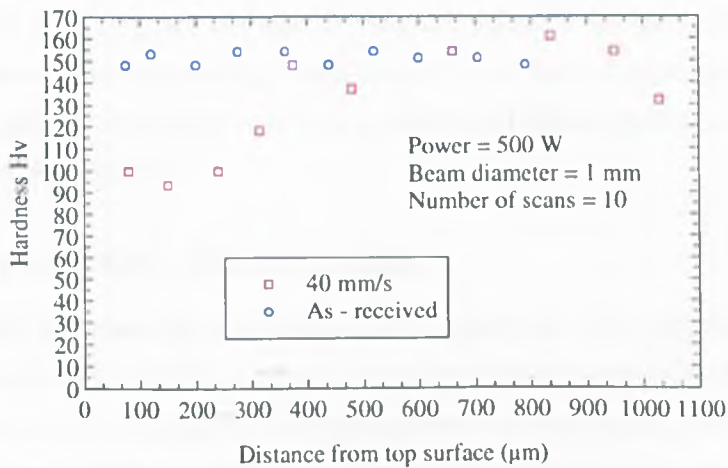


Figure 5.75: Hardness profiles across the thickness for a sample with an AED of 125  $J/mm^2$

### 5.3.5 Discussion of the metallurgy and mechanical properties of laser bent AA 2024

#### Optical and SEM micrographs

For AED values up to 25  $J/mm^2$  no damage occurred to the microstructure of the material. In some cases recrystallisation of the top region of the sheet occurred.

For AED values between 25 and 133 J/mm<sup>2</sup>, a variety of microstructural changes took place, including:

- (a) Recrystallisation of finer grains in the upper region of the sheet,
- (b) Presence of subgrain structures and dispersoid precipitation at grain boundaries,
- (c) Partial melting around recrystallised grain boundaries,
- (d) Melting and resolidification of the upper region, underneath the Alclad layer.

Partial melting and the associated hot tearing of the grain boundaries was the main form of damage observed. It is important to note that it is impossible to identify this effect by observing the integrity of the alclad layer. The alclad layer has a higher melting point and it may be unaffected, masking the damaged alloy structure underneath it. For AED values between 133 and 250 J/mm<sup>2</sup>, the clad layer and the substrate fuse together.

Recrystallised grains suffer from partial melting taking place at triple grain boundary intersections. Constituent particles of various sizes most possibly made of Cu, Mg, Fe and Si, appear at grain boundaries. The formation of a subgrain structure inside former grain occurs. A cast structure is formed after resolidification of the fusion zone containing dendrites growing from former grains.

Other less significant results of the metallurgical investigation on the AA 2024 T3 are given in Appendix D.

### **Mechanical properties - Microhardness**

AED values that preserve an acceptable microstructure, i.e. < 25 J/mm<sup>2</sup>, result in hardness values which remain constant across the depth direction of the bend and which are close to the average value of the as-received material. (150.9 + / - 2.7 Hv) Some AED values result in samples with hardness levels above and slightly below that number. The systematic error associated with these measurements was quite high as +/- 5 Hv units. This was due to the inaccuracy involved in positioning the indenter of the Vickers hardness testing machine. Apart from this error the change in hardness in laser forming of the AA 2024 may be explained by recrystallisation and precipitation theory. The major contributing factors are:

- (a) Recrystallisation of small sized grains
- (b) Nucleation at intermediate temperatures (473 to 773 K) of small amounts of transition particles such as  $\Theta'$  and  $S'$  from previously formed saturated solid solution regions, similar to a T6 temper,

(c) Full recrystallisation and grain growth of the previous structure.

Increasing the AED value further causes partial melting ( $> 25J/mm^2$ ) or fusion ( $> 133J/mm^2$ ) and an irreversible decrease in the hardness across the heat affected and fusion zones results.

### 5.3.6 Metallurgical changes which occur in $\alpha - \beta$ Ti6Al4V due to laser forming

#### Heating above 1228 K

The rapid heating of the Ti6Al4V may result in the formation of martensite, especially after prolonged high temperature processing above the beta transus. The pick-up of oxygen and nitrogen may occur, resulting in a surface structure which is composed mainly of alpha-phase, since oxygen and nitrogen are alpha stabilisers. Oxygen is readily absorbed and produces an oxygen enriched layer commonly called "alpha case". This layer is detrimental because of the very brittle nature of the oxygen-enriched alpha structure. At 1228 K, the alpha structure can extend 200 to 300 $\mu m$  below the surface. To check for the alpha case, the samples were etched with 5ml of HF, 20ml of lactic acid and 20ml of glycerol or a 4% HF solution. Alpha case presents itself as light grey, dark grey indicates its absence.

### 5.3.7 $\alpha - \beta$ Ti6Al4V - Optical micrographs

In figure 5.76 the "as-received" microstructure of the mill-annealed  $\alpha - \beta$  Ti6Al4V is presented. Dark globular particles of beta in a matrix of alpha can be observed [65]. In the cases where metallurgical changes took place these changes were usually the

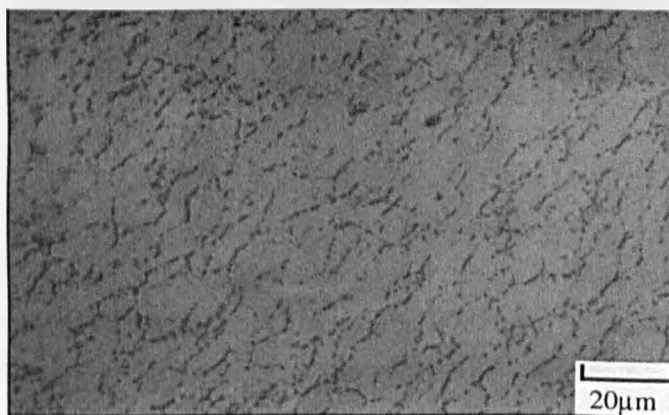


Figure 5.76: The as-received microstructure of the Ti6Al4V

formation of acicular plates of martensite ( $\alpha'$ ) and retained beta. These large plates

are illustrated in figure 5.77. Figure 5.78 illustrates the most extreme case of large

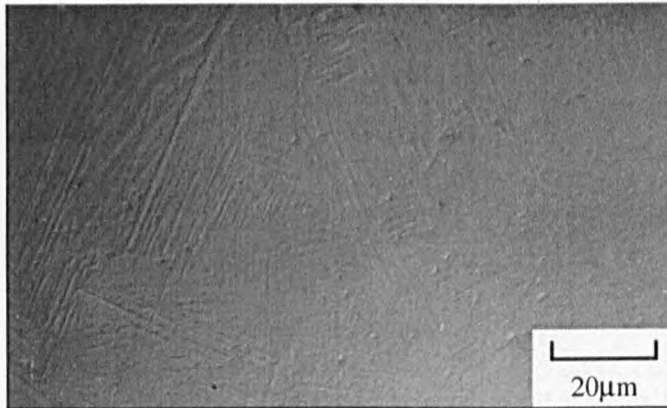


Figure 5.77: Formation of acicular plates for large energy input, processing in air plate formation. In this instance the sample was heated rapidly and then forced cooled with a jet of air. The plates formed at the lower surface of the material are approximately four times smaller than those at the laser irradiated surface. In the samples that exhibited these changes the amount of plate-like formation

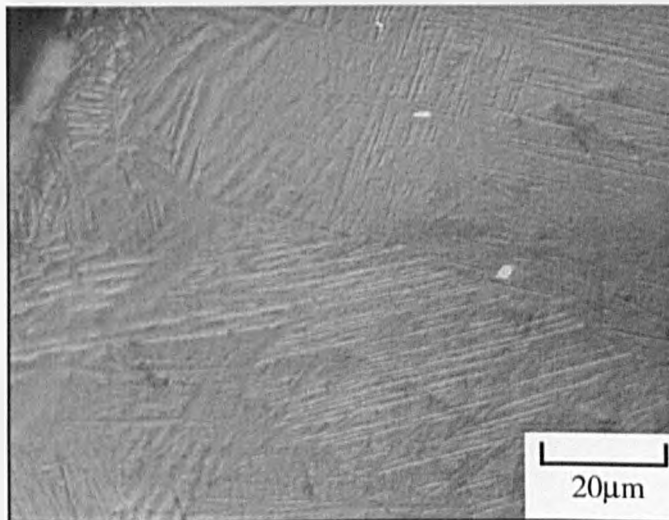


Figure 5.78: Formation of large acicular plates for large energy input, processing in air

decreased radially out from the centre of the laser spot. This formation reflected the temperature distribution of the heat affected zone (HAZ). The length and breadth of this transformed zone (if present) increased with increasing energy input, as shown in figure 5.79. The volumetric change associated with this transformation had a negative effect on the bending rate. This was accompanied by the formation of a hard and brittle alpha case described later which locally increased the material strength, albeit at the expense of the ductility. The bending process itself caused

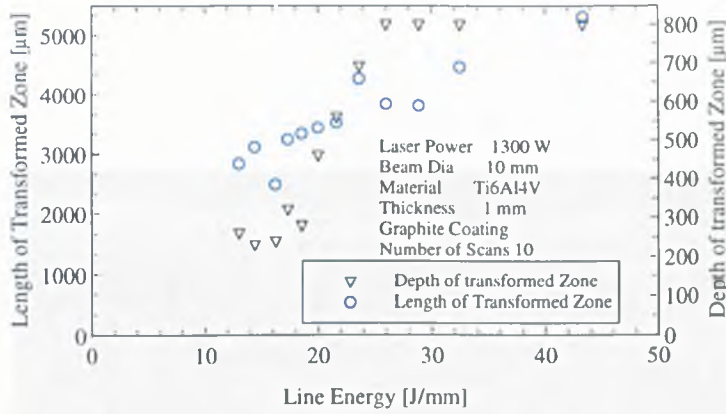


Figure 5.79: Length and depth of transformed zone v laser input energy

an increase in the sample thickness which contributed to the decreased bending rate, as discussed in section 5.2.1. The increase is shown in figure 5.80. The thickness increase is accompanied by a change in volume for this alloy. Figure



Figure 5.80: Thickness increase in the laser irradiated zone,  $\alpha - \beta$  Ti6Al4V alloy

5.81. shows the average plate size increase with increasing laser energy at the surface of the material. Depending on the processing parameters employed a hard

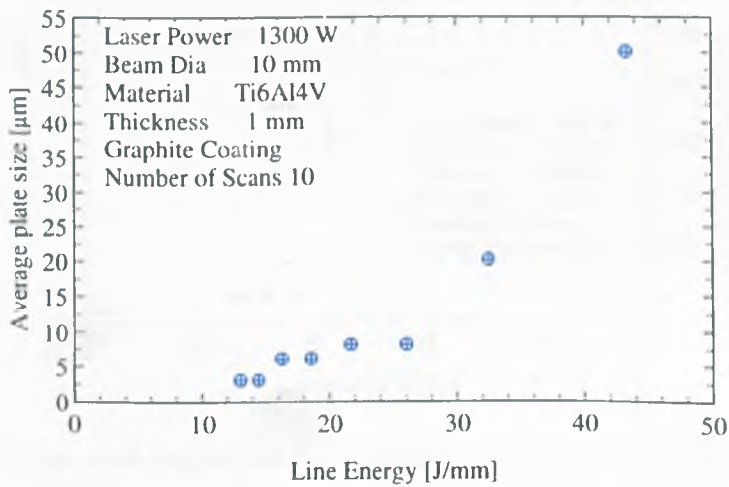


Figure 5.81: Plate size with increasing line energy,  $\alpha - \beta$  Ti6Al4V alloy

and brittle alpha case formed in some instances (see figure 5.82). Figure 5.83 shows how this formation varied with the energy input parameters. It was found

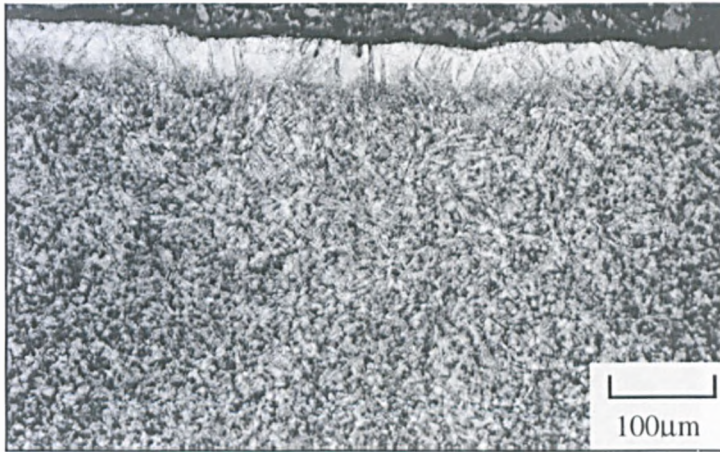


Figure 5.82: Alpha case formation processing in air, Ti6Al4V

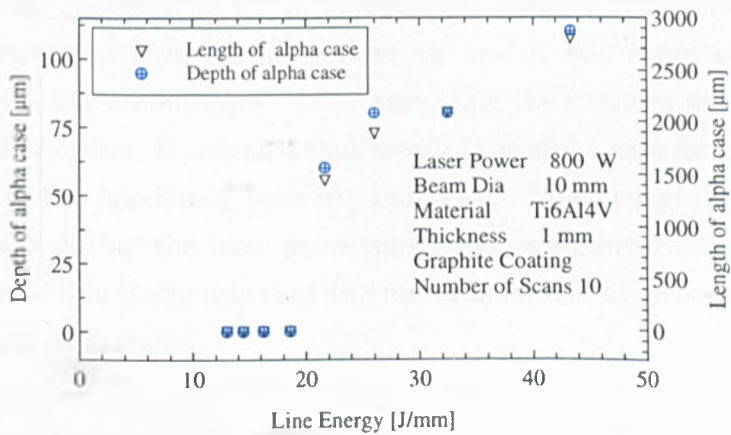


Figure 5.83: Alpha case formation with increasing energy input and processing in air, Ti6Al4V

that if these metallurgical changes did occur that annealing treatments could be used to put the material into a more serviceable condition, as shown in figure 5.84 which illustrates the typical diffusional transformation to the Widmanstatten structure. The plate like  $\alpha$  shown here is not as fine as structures shown in figures 5.77 and 5.78. Here the cooling rate was much reduced, as the material was cooled slowly in the furnace. After the material was air cooled after heating above the

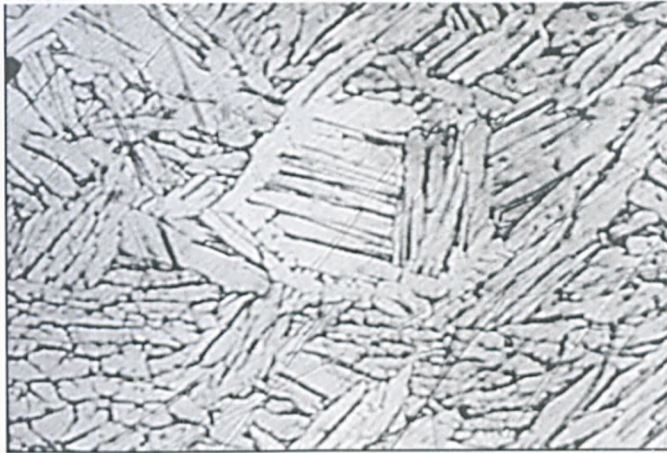


Figure 5.84: Microstructure after the annealing treatment showing the typical Widmanstatten structure

beta transus the  $\alpha$  was much finer, due to the much higher quench rate. This resulted in a structure of acicular  $\alpha$  (transformed  $\beta$ ) and prior  $\beta$  grain boundaries. The dimensions of the sample were checked before and after the treatment and surprisingly there appeared to be no dimensional change, or stress relieving. The annealing experiments were carried out in air and it was expected that further alpha case formation would occur. After annealing the samples were etched again with the 4% HF solution. It revealed that most of the alpha case formation from the annealing was in the previously laser irradiated area which suggests that the effect of oxygen uptake during the laser processing stage is augmented upon annealing. The conclusion of this study was that the material should be processed in an inert atmosphere such as argon.

### 5.3.8 Microhardness graphs

The microhardness level of the as received material was measured across the sample thickness and averaged to 342Hv. After laser bending the measurements were repeated across the sample thickness, the points of measurement being slightly different due to the increase in the sheet thickness in the bent area. In figure 5.85 it may be observed that there is a slight increase in hardness at the sample surface

which was irradiated. This may not be surprising given the possibility for the alpha case formation here, especially with the large energy input. In most of the other micro-hardness measurements no appreciable increases were observed, refer to Appendix E.

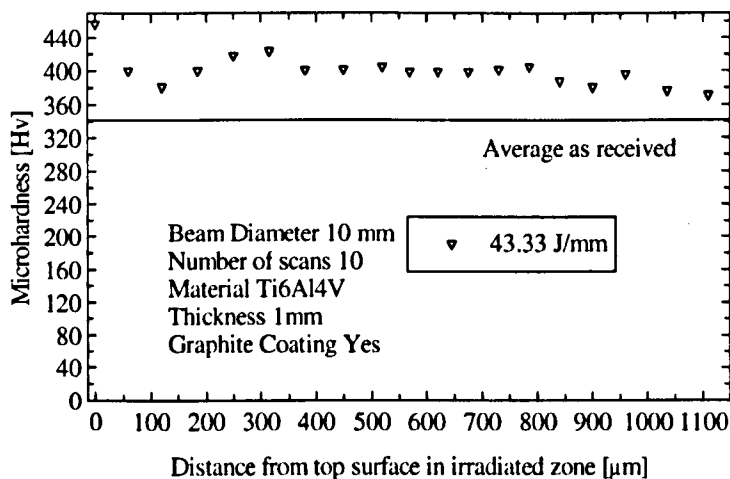


Figure 5.85: Increase in microhardness at the sample surface in the presence of an alpha case

### 5.3.9 Discussion of the metallurgy and mechanical properties of laser bent $\alpha - \beta$ Ti6Al4V

#### Optical micrographs

In most cases changes occurred to the microstructure of the Ti6Al4V alloy. The changes resembled the characteristic Widmanstatten microstructure of titanium alloys. After laser treatment the phases that were present included acicular martensite ( $\alpha'$ ) and retained beta. The bulk of the associated plate like structure was contained within the radial extents of the laser spot. Therefore, radially outwards in this region there is a decrease in the formation of transformed beta.

In figure 5.78 the most extreme case of needle formation is shown. This is due to the very long interaction time due to the slow traverse velocity, and the forced air cooling directly opposite the laser line. The slower the velocity, the greater the integral time at elevated temperatures, and thus the possibility of transformation is increased. For a traverse velocity of 10mm/s and a bending edge length of 80mm, the time the laser takes to scan across the entire edge is 8 seconds. Since the cooling of the material was assisted by a jet of air, as well as the self quenching due to the cooler surrounding material, there is a high possibility for a diffusionless transformation to take place. The increase in volume observed in the material at

the bend edge is assisted by the volumetric expansion associated with the formation of martensite. It had a negative effect on the bending rate as discussed in section 5.1.1, (figure 5.1).

### **Mechanical properties - Microhardness**

A surprising result from the microhardness tests was that there was no increase in hardness at the lower layers of the sheet due to strain hardening, reported first by Sprenger et al.[40] Some experimental error is to be expected in taking manually positioned micro-hardness measurements. This systematic error was approximated to 2.5%. This is not significant when considering the gross changes expected due to strain hardening. The only change that can be identified from the microhardness tests on the alloy is that a hard and brittle layer called an alpha case is formed due to the uptake of oxygen. For some specimens the alpha case extended deeply into the heat affected zone, and increased the hardness there.

The microhardness of specimens annealed in an air atmosphere was found to be up to 560 Hv on the alpha case. On the laser formed only samples, Vickers Hardness numbers that were this high were not found. On the laser formed samples, the maximum hardness was 480Hv on the alpha case for samples which had been repeatedly scanned (30 times) with the laser beam. This indicates that oxygen uptake is augmented with increasing the number of laser scans in an air atmosphere over the same track. It is detrimental to the material.

In non alpha case zones no significant changes in microhardness were found, i.e. there was no evidence of strain hardening. Sprenger et al [40] carried out experiments on Ti6Al4V in the 2.8mm gauge. In that work the samples were scanned 80 times and beyond and reportedly bent via the temperature gradient mechanism. No explanation of the micro-hardness in the upper layers of the material was presented. Micro-hardness as high as 620 Hv was found for the sheets that had been scanned many times in that work. It is the authors belief that this was due to the formation of alpha case, which extended more deeply into the material with increasing scans. However it should be noted that the material in that investigation was almost 3 times thicker and strain hardening is more pronounced for thicker sheets.

Samples bent to small angles (approx 8 deg) exhibited microstructural changes which were not critical. No alpha case formed in those samples.

## 5.4 Integrated 2D process demonstration

### 5.4.1 The demonstrator part

As described previously the culmination of the fundamental investigation on the 2D forming was the demonstration of the process [65]. The part had to be produced within geometrical tolerances and had to be metallurgically and mechanically acceptable. The required demonstrator part is illustrated in figure 5.86.

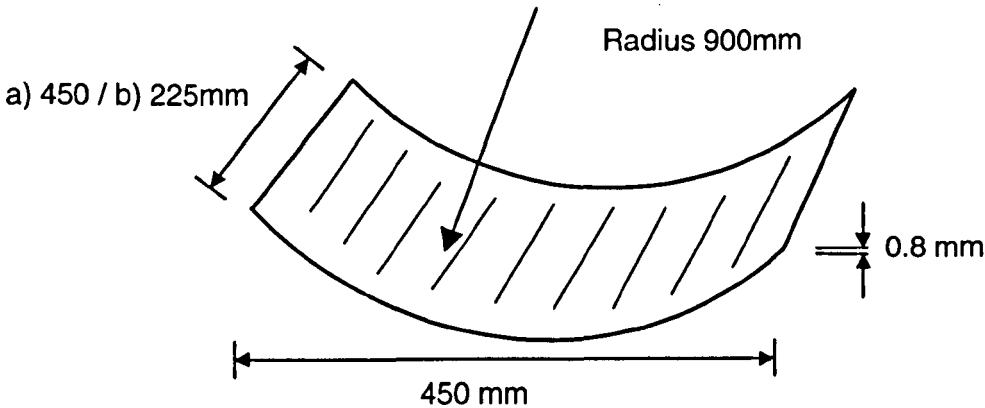


Figure 5.86: Required demonstrator part

### 5.4.2 Initial forming strategy

As described in chapter four the chosen demonstrator has a very shallow radius of curvature. Given that this material possesses much initial plastic deformation and residual stress from upstream processes such as cold rolling, springback is often a limiting factor in cold forming it in terms of the repeatability of the maximum radius achievable. In figure 5.87, the vertical deflection required at each transverse point along the radius of curvature of the demonstrator is illustrated. Starting with an initially flat sheet and working with laser scans starting at one edge and approaching the opposite edge, via an offset displacement between the lines, the first line of irradiation is required to vertically displace the “starting edge” of the sheet by just some microns. Assuming that a linear decrease in the radius is obtained by offsetting the lines an equal amount each time in the transverse direction, it seems reasonable to assume that if the first edge deflection can be quantified and stabilised, that the linear offsetting of the lines should result in the specified radius by the time the opposite edge has been reached. This was one of the first themes of investigation in the early stages of the demonstrator part work at the *Sowerby Research Centre*. In an earlier study, some small tokens of a

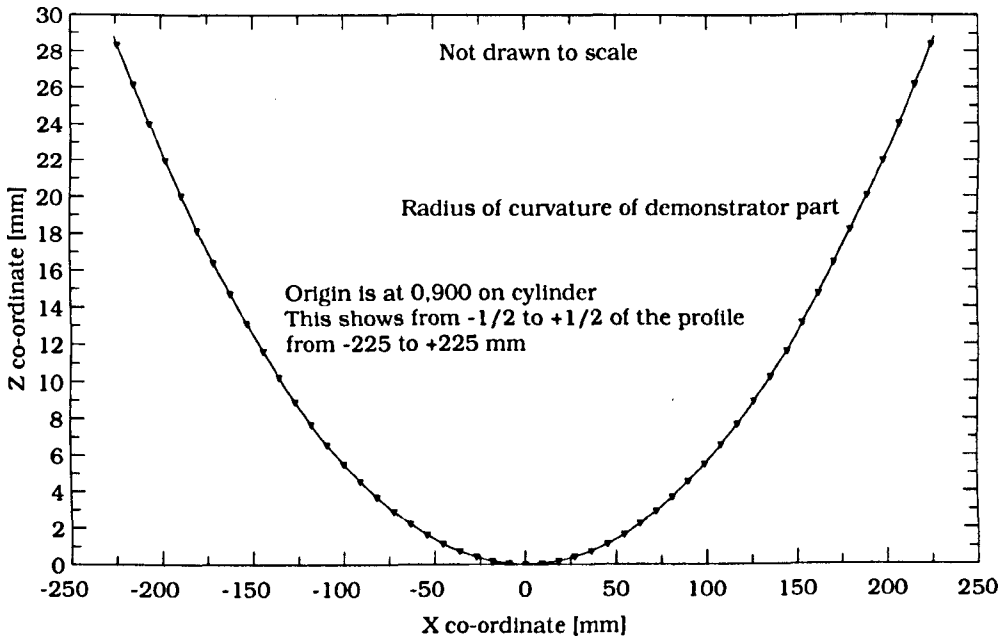


Figure 5.87: Required deflection at each point along the curvature

laser drilled titanium alloy were laser formed into a model of a leading edge of an aircraft wing. In that study the lines of irradiation were linearly offset from each other, and once the initial deflection at the edge had been stabilised by adjusting the input laser energy, it was possible to form a smooth and reproducible radius of curvature using the linear offset. The major question which remained to be answered after this work concerned the transferability of this information to the larger AA 2024 T3 samples. This is discussed next.

### 5.4.3 Influence of the part size

The initial experimentation on the large tokens of AA2024 T3 indicated that the laser processing parameters used on the smaller aluminium alloy tokens were not transferable. At an early stage in this work it became obvious that the size of the part was hampering the symmetry of the forming. Significant curvatures appeared both at and away from the laser irradiated zone. The lateral dimensions of the demonstrator part were scaled up when compared to the small tokens, however the thickness of the sheet was maintained at 0.8 – 1mm in both cases. Therefore the aspect ratio of the sheet was radically changed. The laser stripe measurement system was not employed for profiling these samples as they were too badly distorted. A photograph of one of them is illustrated in figure 5.88. An instability existed along the midpoint of the bending edge in most cases. When the laser beam reached the midpoint of the bending edge quite a violent longitudinal bend-

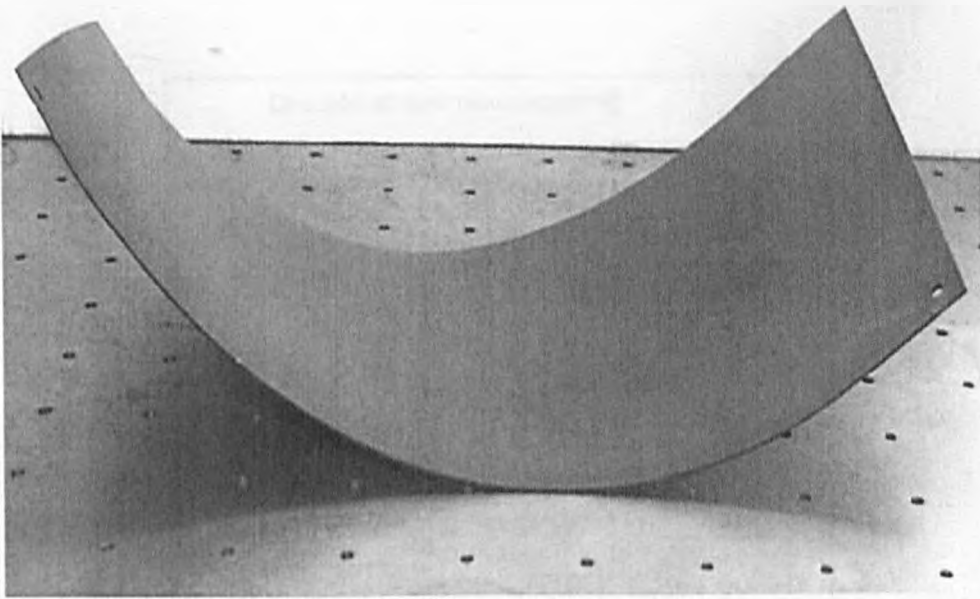


Figure 5.88: Distortion of demonstrator part

ing reversal took place, as schematically illustrated in figure 5.89. The amount of counterbending away from the laser beam became very pronounced with these large samples. After the initial bends the sheet deflected off the simply supporting table. The counterbending played havoc with the forming, there were sudden and violent changes in the direction of the curvature, even a number of seconds after the entire forming operation had taken place. This seemed to correspond to the bifurcation of equilibrium states often seen in structures which are mechanically loaded. In that case a constant external load is applied to a structure, yet there appears to be several equilibrium states that the structure can adopt (displacements), even if there are only very slight disturbances. The disturbance in the laser forming case may be the self quenching of the part in air and the return towards the ambient temperature values of the mechanical properties. That disturbance seems enough to shift the displacements substantially.

The counterbending effects were diminished by placing a wooden block underneath the sheet so that it contacted the lower surface at a point tangential to the sheet as shown in figure 5.90.

This prevented the sheet from counterbending at the point tangential to the wooden block. It provided a reaction force which was transmitted back to the forming and augmented the positive forming towards the laser beam. However it increased the plastic restraining as well. The sheet bent positively by more than in the case of the free counterbending, but once the sheet had reached the maximum positive bend angle, it dropped off again slightly due to the plastic restraining

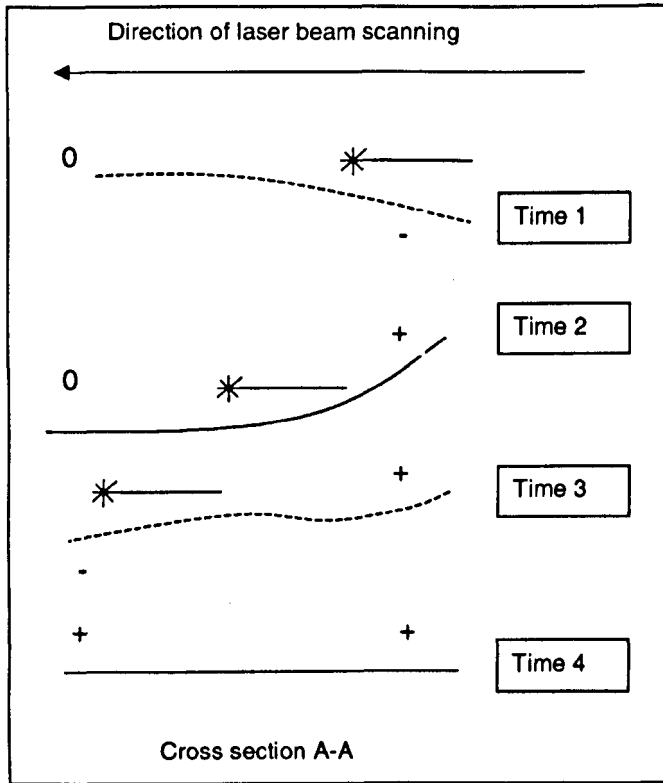


Figure 5.89: Schematic of longitudinal bending along bending edge from start to end of process

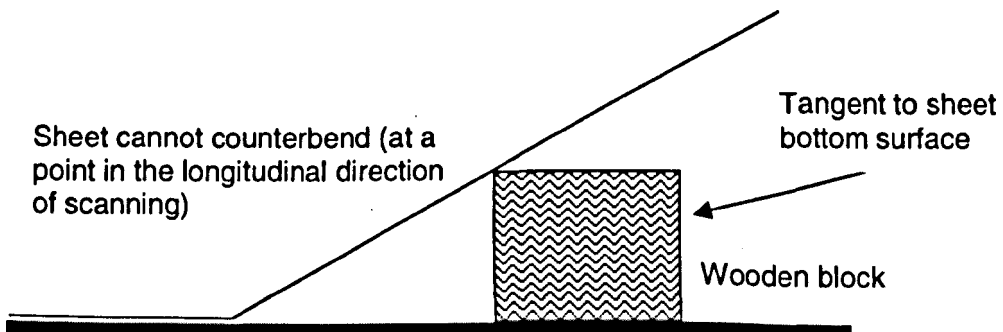


Figure 5.90: Arresting the counterbending

from the build up of tensile stresses in the plastically compressed zone (plastic restraining is outlined in chapter two).

The plastic restraining in this case may have been the result of gravity and of a large amount of thermally induced strain from the large laser beam diameter. It was necessary to employ the large laser beam diameter to ensure that the surface remained smooth. If a small laser beam of the order of the sheet thickness had been employed, this would have resulted in a faceted surface, i.e. discrete bends visible along the curvature which are not smooth. The disadvantage of the large laser beam is the bulk conduction away from the beam, which leads to an elastic straining far away from the laser beam, but which may cause a plastic restraining near the centre of the laser beam. The success of the “wooden block” system was not complete. The main problem was that the transverse and longitudinal bending moments lifted part of the sheet off the wooden block as the sample traversed underneath the beam. That resulted in counterbending in some places, similar to that shown in figure 5.89.

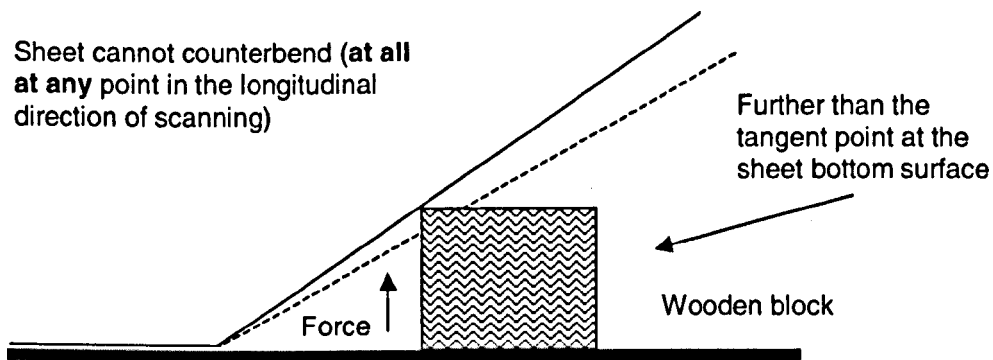


Figure 5.91: Force exerted by block underneath the sheet past the tangential point of contact

To overcome this problem the wooden block was pushed underneath the sheet slightly further than the tangential point as shown in figure 5.91. This pre-bent the sheet elastically slightly, and removed the possibility for counterbending anywhere along the length of the bending edge. Having performed these operations an improvement in the stability of the bending of the larger sheet was gained. However the reaction force that the wooden block provided was difficult to keep uniform. That was because at each increment of forming the wooden block had to be moved further underneath the sheet as it bent up. This resulted in an uneven distribution of the reaction force, as the block was moved underneath the sheet from one edge to the other, and using a linear offset for the laser lines the deflection was changing non-linearly for each laser scan line.

The net result was that the radius of curvature was changing at each scan line

analogously and it was not possible to form a cylinder of radius 900mm. As the aspect ratio of the sheet was found to be one of the major limiting variables, the sheet dimensions were reduced to 450x225 x0.8mm in an attempt to stabilise the process. This halved the length of the bending edge but maintained the transverse width of the sheet at the same level as previously. Initial trials using the same energy input parameters showed that the possibility of the transverse instability had been greatly diminished. The counterbending effects were still apparent but the violent flipping from one equilibrium position to another had been circumvented. The wooden block was used to some degree, but again it was very difficult to implement repeatably for the reasons described previously.

Of note in the forming of the smaller sheet was the forming that was taking place on either side of the laser scan line. Working from one edge of the sheet to the other was causing significant deflections on either side of the laser scan line despite the sheet being built in at one end. In order to overcome this problem a pneumatic clamping device was constructed which clamped the part rigidly against the supporting table on one side of the laser line as shown in figure 5.92. The other

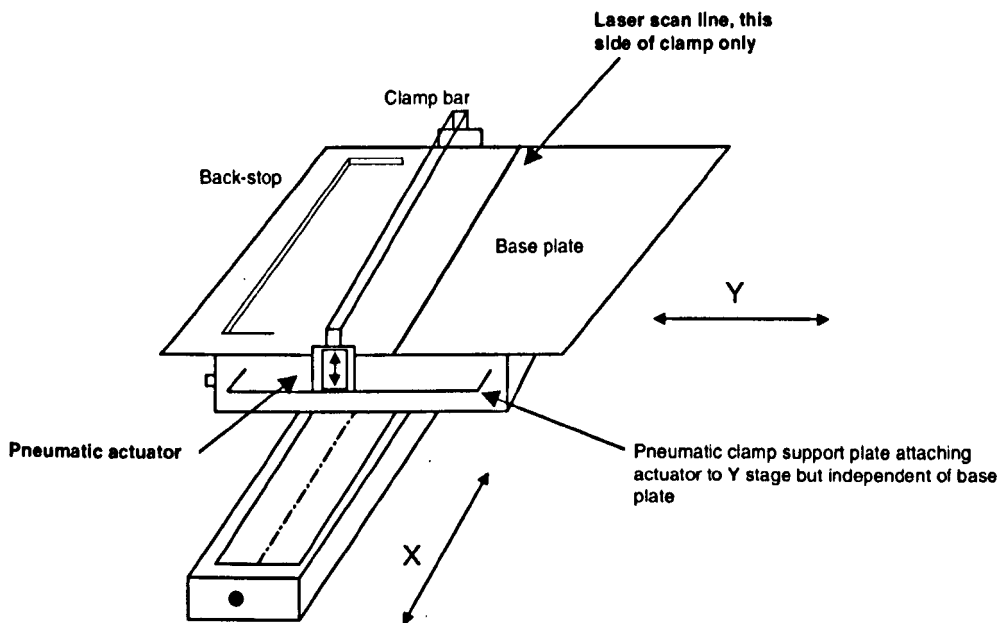


Figure 5.92: Pneumatic clamping arrangement

side of the line was free to rotate in the positive  $Z$  direction, but inhibited from counterbending by the wooden block. With these procedures it was possible to form the required radius in one increment of forming.

The geometrically accurate laser formed sample is illustrated in figure 5.93. It was formed under the conditions in table 5.4. At least three almost identical radii were produced and delivered to the sponsors throughout British Aerospace. These

Parameter	AA 2024 T3
Spot size	10.0 mm
Laser power	500 W
Velocity	80000 counts/s
Line offsets	15000 counts
Graphite coating	yes

Table 5.4: Laser process parameters for the 2-D forming of demonstrator part

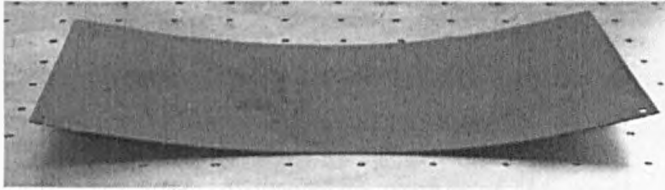


Figure 5.93: Geometrically accurate demonstrator part

sheets were profiled with the laser stripe measurement system. Example plots of the information from the stripe measurement system are shown in figures 5.94 to 5.102.

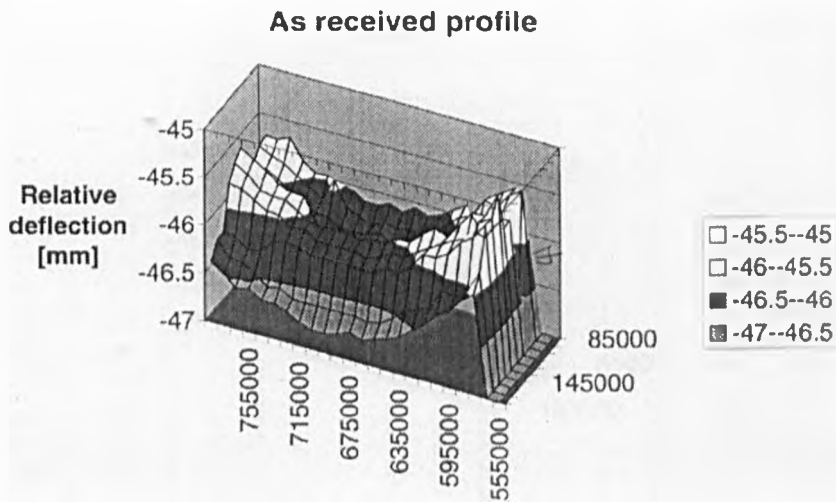


Figure 5.94: As received profile of the sheet

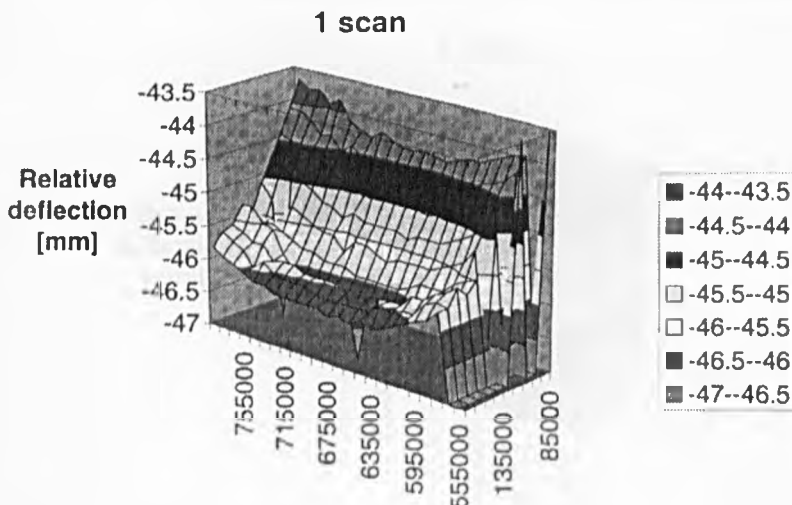


Figure 5.95: Profile after 1 laser scan line

A further three sheets with a smaller radius of 600 mm were produced and the process seemed to stabilise the smaller the radius was on these large sheets. On large sheets forming very small deflections in the springback zone of conventional forming is not the incremental process first thought. Instead it was possible to form the tighter radii with improved stability. The tighter radii facilitated the use of a greater energy input per scan line than in the case of the larger radii, i.e. forming larger angles per scan. The larger bend angles pre-bent the part considerably for subsequent scans, thereby increasing the strength of the part, and reducing counterbending and longitudinal distortion problems. Having described these effects it was still possible to form very shallow radii on large parts, even larger than the 900mm specified. However this was achieved at the expense of repeatability.

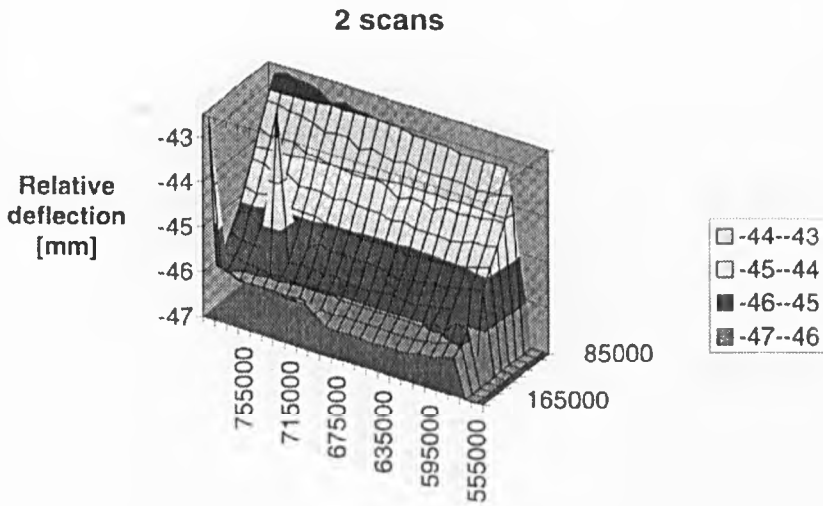


Figure 5.96: Profile after 2 laser scan lines

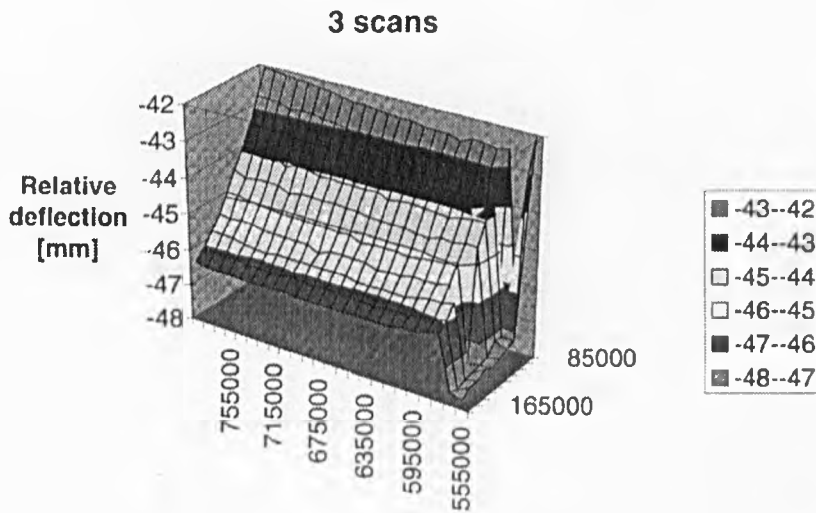


Figure 5.97: Profile after 3 laser scan lines

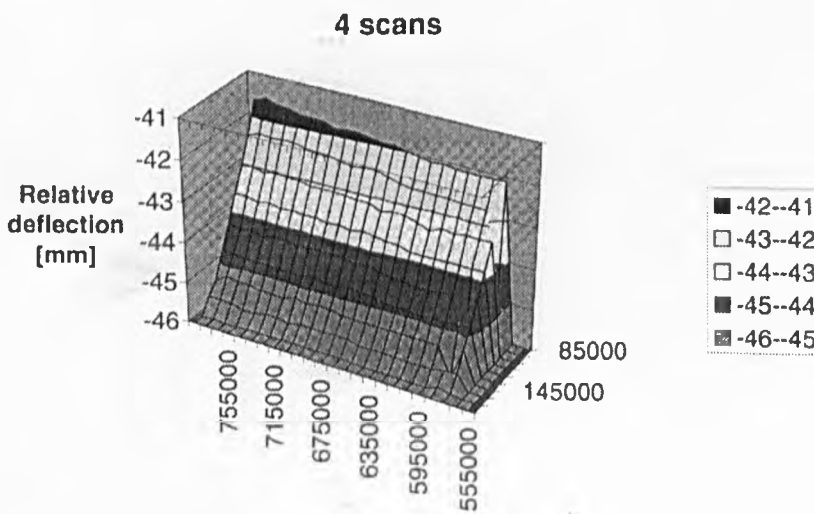


Figure 5.98: Profile after 4 laser scan lines

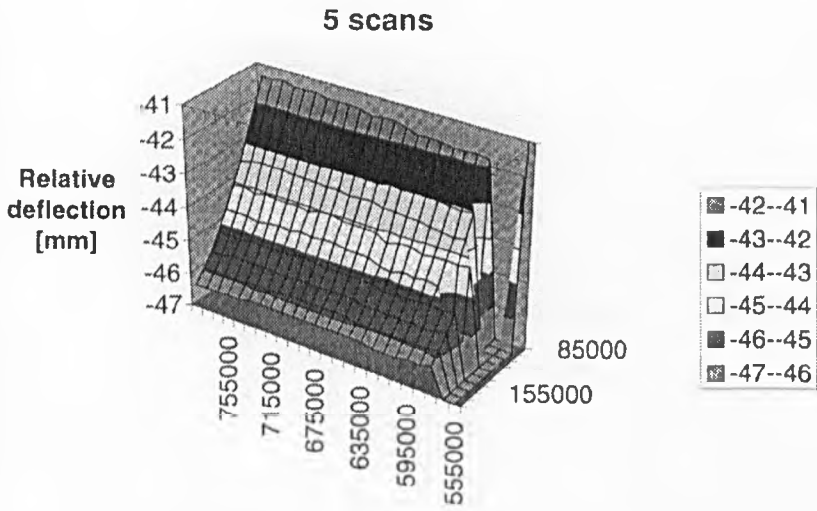


Figure 5.99: Profile after 5 laser scan lines

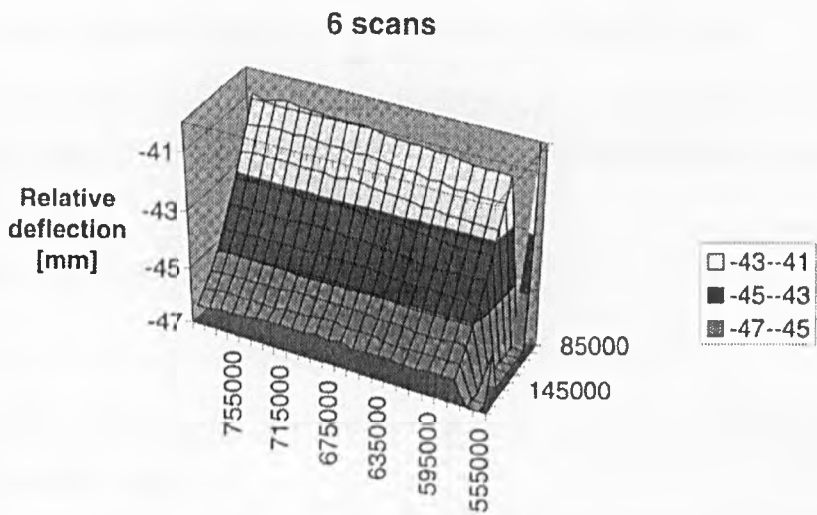


Figure 5.100: Profile after 6 laser scan lines

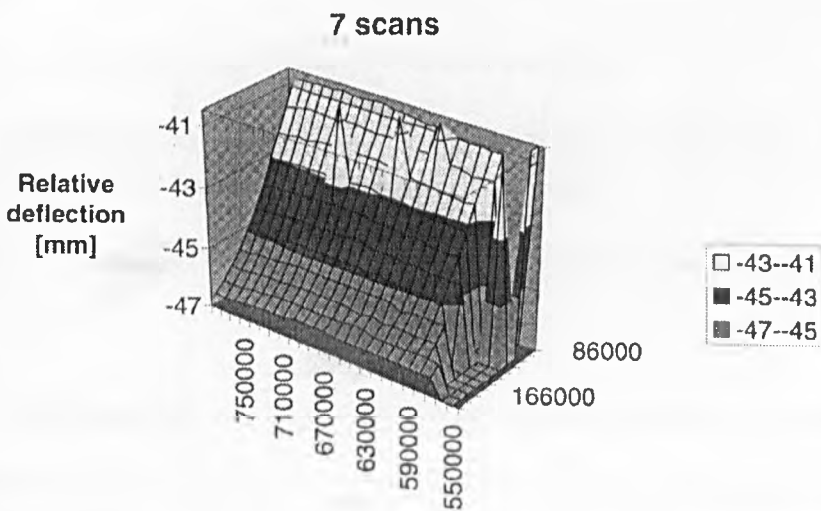


Figure 5.101: Profile after 7 laser scan lines

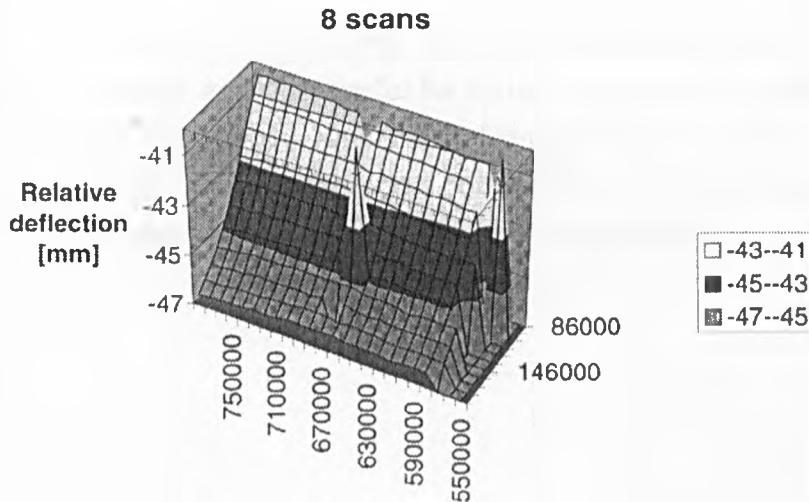


Figure 5.102: Profile after 8 laser scan lines

#### 5.4.4 2-D Laser forming system requirements

Having established a stable laser forming of the specified geometry it is possible to name the important laser forming system components that are required for this task:

- Laser stripe measurement system,
- Pneumatic clamping on the “clamp” side of the sheet,
- A vertical movement stage to bring either the sheet or the stripe measurement system into range,
- Lateral translational stages to move the part around under the stationary beam,
- Cooling system for part at each stage of forming,
- A computer interfaced with these components and an algorithm which automates what was achieved manually in this study,
- A knowledge based system which learns from both the automatic and manual intervention.

#### 5.4.5 Conclusion of 2-D process demonstration work

Clearly there are very complicated dependencies for the previously described forming task. This work has shown the significance of the part dimensions and has addressed the counterbending effects. The decisions at each increment of the forming

were carried out manually and manual intervention was used here. Some machine learning capability would be useful for future process development given the stochastic nature of the process, and ways of improving the control of the force applied underneath the sheet could form a future study as well. This is especially important if forces have to be applied around a 3-D geometry.

# Chapter 6

## Conclusions and Future Work

### 6.1 Conclusions

#### 6.1.1 Process Mechanics

This work has described the forces and moments acting in laser bending operations on sheet material. Primarily they include transverse and longitudinal bending moments and shrinkage forces. Previous analytical routes have looked at transverse bending moments only. It was shown that the superposition of these forces and moments could be used as a first step towards shape prediction in laser forming, without the need for a computationally expensive thermoelastic-plastic analysis. The analysis depends on the ability to calculate the extents of the “inherent strain” zone. In this work an elliptical distribution was used to idealise the geometry of the zone. This was confirmed by the thermal analysis using the solution to the three dimensional heat conduction equation. This work lead to improved understanding of the process mechanics.

#### 6.1.2 Energy Influences on laser forming of sheet material

An investigation into the factors influencing the laser forming process on the alloys Ti6Al4V and Al2024 was carried out. The influence of the energy parameters on the process was investigated. The effect of varying the energy supplied to the plate surface was examined by altering the traverse velocity of the plate for a constant laser power and spot size in each experiment. Conclusions from the experimental energy study showed that:

- (a) Plastic strain development was critically dependent on the energy supplied to the workpiece surface.

- (b) When the laser beam was of the order of 12 times the sheet thickness the temperature gradient mechanism was active on the 1.0mm gauge  $\alpha - \beta$  Ti6Al4V alloy, the buckling mechanism on the aluminium alloy. On the titanium alloy, an optimum point in the energy input - bend angle curve existed. This was due to the volumetric changes from the phase transformation effects on the titanium alloy for large energy inputs. This optimum point was not evident on the aluminium alloy and the bend angle decreased monotonically with decreasing energy input. On the aluminium alloy, the exponent relating processing velocity to bend angle in the low velocity range was found to be 0.54, higher than the quoted analytical value of 0.33 available in the literature. This indicates that the temperature gradient mechanism may have played a role (the theoretical exponent for it being 1), and that as the velocity is increased slightly on the aluminium alloy, regardless of the spot size, there is a transition from the BM to the TGM.
- (c) When the laser beam diameter was of the order of 1-5 times the sheet thickness the temperature gradient mechanism was active on both materials. The extent of the plastic zone was greatly reduced and the bend angles were smaller. In this regime good correlation with analytical models was possible.

### 6.1.3 Geometrical influences on laser forming of sheet material

The geometrical investigation looked at sheet dimension effects, decreasing bend rates, longitudinal bending, spatial forming of a curved part and forming of a predefined radius of curvature. The study led to some conclusions:

- (a) For increasing sheet thickness (by the laser forming process itself) on the Ti6Al4V alloy it was shown that there was a large reduction in the achievable bend angle for subsequent scans.
- (b) The decreasing bend angle rate with increasing number of scans over the same track was evident. This was attributed to a partial burn-off of the graphite coating used to increase the absorptivity of the samples, thickening of the bending edge, the formation of a hard and brittle alpha case in some instances on the titanium alloy, volumetric changes on the titanium alloy (as described in the previous section) and strain hardening of the outer side of the bending edge.
- (c) The influence of the plate dimensions was addressed. It was concluded that for increasing plate width there is a large variation in the stability of the

bending process, but for increasing length there is not a significant change in the bend angle, at least up to the maximum plate length which was investigated.

- (d) Longitudinal bending and edge effects were apparent in most samples which were produced. These effects were pronounced when the plate was heated slowly and the beam diameter on the surface was large compared to the thickness of the sample, and less pronounced for high traverse velocities and smaller beam diameters (but still evident). A variable line energy along the path of irradiation may be used to minimise such effects.
- (e) For 3-D forming thermal and mechanical symmetry should be maintained as much as possible at each increment of the process to ensure a smooth and symmetrical forming. Irradiation strategies were developed to do this to produce a dish shape from a circular plate. The most dominant parameter was found to be the spatial sequence of irradiation. Spatial sequences were implemented accordingly to circumvent distortion.
- (f) For forming a 2-D predefined radius of curvature it was found that the aspect ratio of the sheet was critical to the achievable and stable radius. The information from the initial study on the small AA Al2024 T3 tokens of dimensions 80 x 80 x 0.8mm was not transferable to the larger demonstrator part of 450 x 450 x 0.8mm, or to the successfully formed part of dimensions 450 x 225 x 0.8mm. The thickness of the sheet was not scaled with the lateral dimensions and this resulted in the flexibility of the sheet hampering the stability of the forming process for certain radii. For the predefined radius of 900mm (which is very shallow) a stable forming could not be achieved on the 450 x 450 x 0.8mm sheet. When the radius was decreased to circa 600mm the forming was stabilised. The 900mm radius was achieved on a smaller and less flexible part of dimensions 450 x 225 x 0.8mm. However in common with the former case, the stability of the process was questionable. Decreasing the radius and increasing the bend angle rate favoured a more stable forming. As the radius is increased the bend angle per scan line must be reduced accordingly, and the elastic recoverable share of the bending is increased effectively in order to fulfill this requirement. As the elastic recoverable share of the bending was increased it was concluded that the process became more and more unstable on the aluminium alloy. This task was automated to the extent that once the program instructions were downloaded the machinery would produce and measure one complete increment of the process.

### 6.1.4 Metallurgical and mechanical property implications

Metallurgical and mechanical analyses of the laser formed samples were carried out in order to determine the level of microhardness of the samples and changes to the microstructure. The conclusion of these investigations brought some important facts to light:

- (a) In the case of the aluminium alloy the as received microstructure could be maintained when an average energy density (AED) of less than  $25 \text{ J/mm}^2$  was used for forming. In some cases at this energy level subgrain structures were present and incomplete recrystallisation of small grains in the upper region of the sheet occurred.
- (b) For AED values between 25 and  $133 \text{ J/mm}^2$  full recrystallisation occurred which contrasted with the microstructure of the as received material. In this processing envelope segregation of dispersoids at grain boundaries occurred and partial melting of the previously recrystallised grains.
- (c) When the AED exceeded this level a cast dendritic structure resulted from melting underneath the pure aluminium clad layer. For very large AED values the clad layer and the substrate layer fused together.
- (d) Some fluctuation of the micro-hardness level was found in the laser formed AA 2024 T3 which had been exposed to an AED of  $< 25 \text{ W/mm}^2$ . The slight oscillatory nature of the microhardness about the as-received value, around this AED value, can be explained by recrystallisation and precipitation theory for this alloy. The contributing factors are:
  - (a) Recrystallisation of small sized grains
  - (b) Nucleation at intermediate temperatures (473 to 773 K) of small amounts of transition particles such as  $\Theta'$  and  $S'$  from previously formed saturated solid solution regions, similar to a T6 temper
  - (c) Full recrystallisation and grain growth of the previous structure
- (e) Increasing the AED value further caused partial melting ( $> 25 \text{ J/mm}^2$ ) or fusion ( $> 133 \text{ J/mm}^2$ ) and an irreversible decrease in the hardness across the heat affected and fusion zones.
- (f) In the case of the Ti6Al4V alloy, a limited processing envelope was identified where the material could be laser formed.

- (g) In the cases where metallurgical changes took place to the titanium alloy, these changes were usually the formation of acicular plates of martensite  $\alpha'$  and retained beta. In the samples that exhibited these changes the amount of plate-like formation decreased radially out from the centre of the laser spot. This formation reflected the temperature distribution of the heat affected zone (HAZ). The length and breadth of this transformed zone (if present) increased with increasing energy input.
- (h) Depending on the processing parameters employed a hard and brittle alpha case formed in some instances on the Ti6Al4V.
- (i) It was found that if these metallurgical changes did occur to the titanium alloy, that the as received properties could be regained via annealing treatments. The microhardness level of the as received material was measured across the sample thickness and averaged to 342Hv. After laser bending a slight increase in hardness at the sample surface which was irradiated was evident. The conclusion of the study was that the material should be processed in an inert atmosphere such as argon. By doing so alpha case formation would be inhibited and the microhardness level would not be increased by the uptake of oxygen.

## 6.2 Future work

This work has described some major issues in laser forming. In terms of practical laser forming the two primary concerns are geometrical accuracy and metallurgical / mechanical property integrity.[66]

### 6.2.1 Spatial forming in 3D

Many one dimensional bends were made in this work, a case study was made on 2D forming of a predefined radius of curvature and an investigation was made into spatial forming of an axi-symmetric structure - a dish shape. This provided a starting point in establishing rules about laser forming certain geometries. This work should be extended in further studies to establish spatial irradiation patterns for laser forming any feasible geometry. It is recommended that the saddle, the twisted shape, and the pillow should be investigated next. They have axi-symmetry and curvatures in several directions. They are generic shapes or primitives which could be modified slightly to yield near net shape parts.

An important aspect of the proposed work would be the investigation of the spatial scan patterns to achieve such geometries. The shape prediction capability will be of prime importance. It is not obvious how to laser form arbitrary 3D shapes from sheet metal. Simulation, perhaps using the method of inherent strain and large elastic deformation analysis used in this work, along with improved understanding of the high temperature mechanical properties of the materials investigated would facilitate this.

### 6.2.2 Closed loop control

It is unlikely that a large variety of the proposed geometries can be laser formed in an open loop. The irradiation angle of incidence and the spot profile change as the forming geometry translates and rotates in relation to the laser processing head. Therefore some correctional movements must be implemented in a closed loop system to maintain known energy input. The laser stripe measurement system could serve the dual purpose of measuring the geometry and the distance and angle that the processing head is from the workpiece. Additionally the measurement information should be used to construct rules about what the laser forming machine should do after each increment of forming automatically. Examples of this would be to increase or decrease the rate of forming, depending on how close the curvature is to the required curvature, and change the direction of scanning if a curvature is developing in the wrong location.

### 6.2.3 Other alloys

The suitability of other alloys for laser forming could form another study. In this work two aerospace alloys were investigated. The work concentrated on the AA 2024 T3. It may be possible to take a T4 temper aluminium which is heat treated and naturally aged and laser form it more readily than the T3 temper. The T3 temper is cold rolled after heat treatment and possesses much initial plastic deformation and residual stress. It may be possible to laser form 7xxx series aluminium alloys in the heat treated and artificially aged T6 state which are very difficult to form conventionally (in that state). If that is possible heat treatment after forming would not be required, as is conventionally. On the titanium alloy, work could be carried out to assess the possibility of shrouding the part from oxygen to prevent oxidation and the formation of a hard and brittle alpha case on the sheet surface. It is recommended that future work on 3D forming would examine CR4 mild steel or similar. This would facilitate examining the effect of spatial irradiation patterns on geometry in the absence of complicated metallurgical effects

which affect the process mechanics themselves; as in the case of the previously described alloys.

# Appendix A

## Counterbending model - Yau 97

The counter-bending angle away from the laser beam was described again using the two-layer geometry-strain approach. Considering figure A.1 the counter-bending

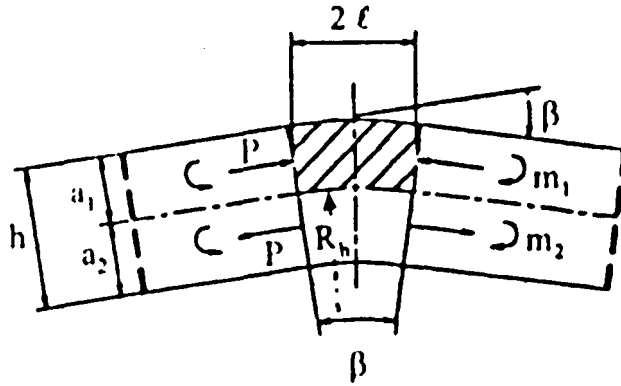


Figure A.1: Geometry of Yau's two layer model

angle is:

$$\beta_B = \frac{2l}{R_h} = \frac{2l(1 + \epsilon_1)}{R_h + Z_1} = \frac{2l(1 + \epsilon_1)}{R_h - Z_2} \quad (\text{A.1})$$

which may be rearranged as:

$$\frac{4l}{s_0}(\epsilon_1 - \epsilon_2) \quad (\text{A.2})$$

The thermal expansion of the heated zone is restricted by the cold surrounding material which causes a compressive force,  $F$ . The thermally induced strain of the upper layer was then given by:

$$\epsilon_1 = \alpha_{th}\Delta T + \frac{s_1}{2R_h} - \frac{F}{Es_1b} \quad (\text{A.3})$$

and the strain of the lower layer was given by:

$$\epsilon_2 = -\frac{s_2}{2R_h} + \frac{F}{Es_2b} \quad (\text{A.4})$$

Substituting the last two equations into the equation for  $\beta$  yields:

$$\beta_B = \frac{4l}{s_0} \left[ \alpha_{th} + \frac{s_0}{2R_h} - \frac{F}{Eb} \left( \frac{1}{s_1} + \frac{1}{s_2} \right) \right] \quad (\text{A.5})$$

The total bending moment is equal to the sum of the upper and lower layer components and is given by:

$$M = M_1 + M_2 = F \frac{s_1}{2} + F \frac{s_2}{2} = \frac{Fs_0}{2} \quad (\text{A.6})$$

Applying the previously described elastic bending moment theory to both layers gives:

$$M_1 = \frac{E}{R_h} I_1 = \frac{E}{R_h} \int_0^{s_1} bz^2 dz = \frac{E}{R_h} \left[ \frac{bs_1^3}{3} \right] \quad (\text{A.7})$$

By the same procedure the bending moment for the lower layer,  $M_2$  is equal to:

$$M_2 = \frac{E}{R_h} \left[ \frac{b(s_2)^3}{3} \right] \quad (\text{A.8})$$

Substituting  $M_1$  and  $M_2$  gives:

$$\frac{Fs_0}{2} = \frac{E}{R_h} \left( \frac{bs_1^3}{3} \right) + \frac{E}{R_h} \left( \frac{b(s_2)^3}{3} \right) \quad (\text{A.9})$$

which is equal to:

$$\frac{Fs_0}{2} = \frac{bE}{3R_h} (s_1^3 + (s_0 - s_1)^3) \quad (\text{A.10})$$

Then by substitution of A.10 into A.5  $\beta_B$  is found to be:

$$\beta_B = \frac{4l}{s_0} \left[ \alpha_{th} \Delta T + \frac{s_0}{2R_h} - \frac{2}{3R_h s_0} (s_1^3 + s_2^3) \left( \frac{1}{s_1} - \frac{1}{s_2} \right) \right] \quad (\text{A.11})$$

Using equation A.1 the last equation can be rearranged to give:

$$\alpha_{th} \Delta T = \frac{\beta}{3ls_0} \left( s_0^2 + (s_2)^2 + \frac{s_0^3}{s_2} + \frac{s_2^3}{s_1} \right) \quad (\text{A.12})$$

If  $m$  is the thickness ratio between the upper and lower layers equation A.11 can

be described by:

$$\alpha_{th}\Delta T = \left[ \frac{\beta}{3ls_0} \left( s_2^2(1+m)(m^2 + \frac{1}{m}) \right) \right] \quad (\text{A.13})$$

and finally the counter-bending angle is expressed by:

$$\beta_B = \frac{3l\alpha_{th}\Delta T}{s_0} \frac{m(1+m)}{1+m^3} \quad (\text{A.14})$$

In Yau's model it is assumed that the positive bending towards the laser beam commences at the end of the heating cycle and at the beginning of the cooling cycle, positive bending is denoted by  $\eta$ . Considering the geometry and strains presented in figure A.1 again the positive bending angle is derived as follows:

$$\eta_B = \frac{2l}{R_c} = \frac{2l(1+\epsilon_1)}{R_c - Z_1} = \frac{2l(1+\epsilon_1)}{R_c + Z_2} \quad (\text{A.15})$$

which may be rearranged as:

$$\frac{4l}{s_0}(\epsilon_2 - \epsilon_1) \quad (\text{A.16})$$

The strain due to the contraction is described by:

$$\epsilon_1 = \frac{F}{Es_1b} - \frac{s_0}{2R_c} - \alpha_{th}\Delta T \quad (\text{A.17})$$

$$\epsilon_2 = -\frac{F}{Es_2b} + \frac{s_2}{2R_c} \quad (\text{A.18})$$

Substituting equations A.17, A.18 into A.16 gives:

$$\alpha_{th}\Delta T = \frac{F}{bE} \left( \frac{1}{s_1} + \frac{1}{s_2} \right) \quad (\text{A.19})$$

According to Yau since no external force is applied the bending moment during cooling must equal the previous bending moment:

$$Ml = Fl\frac{s_1}{2} + Fl\frac{s_2}{2} = \frac{Fs_0}{2} \quad (\text{A.20})$$

and  $Fl = F$

If the plastic moment occurs at  $z \geq \frac{s_1}{2}$  and  $z \geq \frac{s_2}{2}$  then:

$$Ml = \int_{-\frac{s_2}{2}}^{\frac{s_1}{2}} \frac{E}{R_c} bz^2 dz + \int_{\frac{s_1}{2}}^{s_1} Ybz dz + \int_{-\frac{s_2}{2}}^{-s_2} Ybz dz \quad (\text{A.21})$$

and

$$\frac{Fs_0}{2} = \frac{Eb}{24R_c}(s_1^3 + s_2^3) + \frac{3Yb}{8}(s_1^2 + s_2^2) \quad (\text{A.22})$$

which may be rearranged to:

$$\frac{P}{b} = \frac{2}{h} \left[ \frac{E}{24R_c}(s_1^3 + s_2^3) + \frac{3Y}{8}(s_1^2 + s_2^2) \right] \quad (\text{A.23})$$

Substituting equation A.23 into equation A.22,  $m = \frac{s_1}{s_2}$  and  $\eta_B = \frac{2l}{R_c}$ ,  $\eta$  is finally found from:

$$\eta_B = \frac{6l}{s_0 E} \frac{(1+m)}{(1+m^3)} (4Em\alpha_{th}\Delta T - 3Y(1+m^2)) \quad (\text{A.24})$$

The final bending angle was expressed by the positive bending angle less the counter-bending:

$$\alpha_b = \eta_B - \beta_B = \frac{3l}{s_0} \frac{(1+m)}{(1+m^3)} \left[ 7m\alpha_{th}\Delta T - 6(1+m^2)\frac{Y}{E} \right] \quad (\text{A.25})$$

Yau uses the same approach to the temperature field that Vollertsen adopted in his work. [16]

# Appendix B

## Energy input parameters

### B.1 Energy input - bend angle tables

10 mm Beam Diameter, 0.8 mm Ti6Al4V						
Laser	Traverse	Beam	Angle for	Angle for	Line	Line Energy
Power [W]	Velocity [mm/s]	Diameter [mm]	1 scan	10 scans	Energy W/mm	at max angle, 1st scan, W/mm
			deg	deg		
1300	30	10	1.83856	28.0576	43.33	
1300	35	10	3.6391	29.5532	37.14	
1300	40	10	3.2109	26.885	32.50	
1300	45	10	4.6422	23.3643	28.89	
1300	50	10	5.6822	21.1564	26.00	
1300	55	10	6.0507	30.1137	23.64	23.64
1300	60	10	4.8812	24.5604	21.67	
1300	65	10	3.7703	17.7447	20.00	
1300	70	10	2.5308	21.4052	18.57	
1300	75	10	1.3462	20.1531	17.33	
1300	80	10	0.7849	11.4751	16.25	
1300	90	10	0.4836	9.7593	14.44	
1300	100	10	0.1129	8.6428	13.00	
1300	110	10	0.2257	2.9195	11.82	
1000	20	10	2.920	29.42	50.00	
1000	25	10	3.319	27.83	40.00	
1000	30	10	5.143	24.65	33.33	
1000	35	10	7.069	24.13	28.57	28.57
1000	40	10	6.899	24.5604	25.00	
800	10	10	4.01557	30.5406	80.00	
800	20	10	5.3813	16.8568	40.00	
800	22.5	10	6.89925	21.4548	35.56	35.56
800	25	10	6.67326	23.1709	32.00	
800	27.5	10	3.8559	21.8508	29.09	
800	30	10	4.44296	23.6534	26.67	
800	32.5	10	2.38785	16.4888	24.62	
800	35	10	0.89946	12.8439	22.86	
800	37.5	10	0	0.910926	21.33	
800	40	10	0	2.6509	20.00	
500	7.5	10	7.0686	26.43	66.67	
500	10	10	6.5036	21.36	50.00	
500	12.5	10	7.9134	24.75	40.00	40.00
500	15	10	3.8559	23.80	33.33	
500	16.25	10	2.1819	20.05	30.77	
500	17.5	10	0	5.48	28.57	
500	20	10	0	2.86	25.00	
250	1	10	6.164		250.00	
250	2.5	10	7.2378	26.885	100.00	
250	3.75	10	7.5759	26.2433	66.67	66.67
250	5.00	10	4.1752	11.8597	50.00	
250	6.25	10	0	6.67	40.00	
250	7.50	10	0.3438	3.09	33.33	
250	10.00	10	0	0.00	25.00	

5 mm Beam Diameter, 0.8 mm Ti6Al4V						
Laser	Traverse	Beam	Angle for	Angle for	Line	Line Energy
Power [W]	Velocity [mm/s]	Diameter [mm]	1 scan	10 scans	Energy W/mm	at max angle,
			deg	deg		1st scan, W/mm
1000	50	5	3.6619	27.9377	20.00	20.00
1000	70	5	2.6909	25.4357	14.29	
1000	80	5	1.0312	15.9075	12.50	
1000	90	5	0.5156	6.1641	11.11	
800	50	5	4.2321	24.655	16.00	16.00
800	60	5	2.2906	17.4322	13.33	
800	70	5	1.3175	13.1702	11.43	
800	80	5	1.1457	8.4186	10.00	
800	90	5	0.9166	5.1995	8.89	
800	100	5	0	2.405	8.00	
500	20	5	2.91955	25.4544	25.00	
500	25	5	4.46	25.4544	20.00	20.00
500	30	5	2.74808	19.9509	16.67	
500	35	5	1.6039	10.2595	14.29	
500	40	5	0.5729	10.2595	12.50	
500	45	5	0.802	4.0611	11.11	
500	50	5	0.5729	2.11898	10.00	
500	55	5	0.46866	2.51938	9.09	
250	5	5	3.4907	16.8043	50.00	
250	6.25	5	3.4907	20.4856	40.00	40.00
250	7.5	5	3.2623	18.2008	33.33	
250	10	5	0.3438	9.5366	25.00	

3.5 mm Beam Diameter, 0.8 mm Ti6Al4V						
Laser	Traverse	Beam	Angle for	Angle for	Line	Line Energy
Power [W]	Velocity [mm/s]	Diameter [mm]	1 scan	10 scans	Energy W/mm	at max angle,
			deg	deg		1st scan, W/mm
250	10	3.5	1.8328	15.1896	25.00	
250	15	3.5	2.9295	17.8486	16.67	16.67
250	20	3.5	1.8328	5.4268	12.50	
250	25	3.5	0	2.1189	10.00	
250	30	3.5	0.34377	1.6039	8.33	

10 mm Beam Diameter, 1.0 mm Ti6Al4V						
Laser	Traverse	Beam	Angle for	Angle for	Line	Line Energy
Power [W]	Velocity [mm/s]	Diameter [mm]	1 scan	10 scans	Energy W/mm	at max angle,
			deg	deg		1st scan, W/mm
1300	30	10	3.5421	28.5462	43.33	
1300	35	10	5.1371	28.0576	37.14	37.14
1300	40	10	4.6764	25.9661	32.50	
1300	45	10	4.2094	28.2358	28.89	
1300	55	10	1.9873	22.9284	23.64	
1300	60	10	2.4164	21.1066	21.67	
1300	70	10	1.16867	7.7447	18.57	

5 mm Beam Diameter, 1.0 mm Ti6Al4V						
Laser	Traverse	Beam	Angle for	Angle for	Line	Line Energy
Power [W]	Velocity [mm/s]	Diameter [mm]	1 scan	10 scans	Energy W/mm	at max angle,
			deg	deg		1st scan, W/mm
1000	50	5	2.8052	25.4685	20.00	20.00
1000	70	5	1.9788	11.8599	14.29	
1000	80	5	0.9739	5.0859	12.50	
1000	90	5	0.1718	2.51938	11.11	
800	50	5	2.4622	14.0901	16.00	16.00
800	60	5	1.71835	6.6732	13.33	
800	70	5	1.3748	5.31322	11.43	
800	80	5	1.1457	2.6337	10.00	
800	90	5	0.7448	1.6038	8.89	
800	100	5	0.401	1.3748	8.00	
500	20	5	3.6619	27.6995	25.00	25.00
500	25	5	2.4622	20.1531	20.00	
500	30	5	1.5466	7.63217	16.67	
500	35	5	1.14576	3.833	14.29	
500	40	5	0.7448	2.91955	12.50	
500	45	5	0.401	1.89007	11.11	
500	50	5	0.5729	1.54661	10.00	
500	55	5	0.40106	1.1457	9.09	
250	5	5	3.2623	11.6401	50.00	
250	6.25	5	3.4907	13.2245	40.00	40.00
250	7.5	5	0.7448	3.6049	33.33	
250	10	5	0	0	25.00	

3.5 mm Beam Diameter, 1.0 mm Ti6Al4V						
Laser	Traverse	Beam	Angle for	Angle for	Line	Line Energy
Power [W]	Velocity [mm/s]	Diameter [mm]	1 scan	10 scans	Energy W/mm	at max angle,
			deg	deg		1st scan, W/mm
250	10	3.5	2.8264		25.00	25.00
250	15	3.5	1.7756		16.67	
250	20	3.5	1.3178		12.50	
250	25	3.5	0.6302		10.00	
250	30	3.5	0.34377		8.33	

10 mm Beam Diameter, 3.0 mm Ti6Al4V						
Laser	Traverse	Beam	Angle for	Angle for	Line	Line Energy
Power [W]	Velocity [mm/s]	Diameter [mm]	1 scan	10 scans	Energy W/mm	at max angle,
			deg	deg		1st scan, W/mm
1000	10	10	2.5375	melt	100.00	
1000	15	10	3.0338	melt	66.67	66.67
1000	20	10	1.6039	29.423	50.00	
1000	25	10	1.3748	27.834	40.00	
1000	30	10	0.80208	24.6511	33.33	
1000	35	10	0.9167	24.1324	28.57	
1000	40	10	0.9739	24.5604	25.00	
500	5	10	3.2623	8.6988	100.00	100.00
500	6.25	10	1.6611	5.5403	80.00	
500	7.5	10	1.203	5.7673	66.67	
500	8.75	10	0.5729	1.4894	57.14	
500	10	10	0	1.3748	50.00	

5 mm Beam Diameter, 3.0 mm Ti6Al4V						
Laser	Traverse	Beam	Angle for	Angle for	Line	Line Energy
Power [W]	Velocity [mm/s]	Diameter [mm]	1 scan	10 scans	Energy W/mm	at max angle, 1st scan, W/mm
			deg	deg		
250	5	5	2.2906	5.59711	50.00	50.00
250	6.25	5	1.203	2.2906	40.00	
250	7.5	5	0.9739	1.20303	33.33	

10 mm Beam Diameter, 0.8 mm Al2O24						
Laser	Traverse	Beam	Angle for	Angle for	Line	Line Energy
Power [W]	Velocity [mm/s]	Diameter [mm]	1 scan	10 scans	Energy W/mm	at max angle,
			deg	deg		1st scan, W/mm
1300	40	10	1.8442	31.0899	32.50	
1300	50	10	1.2775	34.0193	26.00	
1300	60	10	3.6106	37.3436	21.67	
1300	70	10	3.9015	38.0964	18.57	18.57
1300	80	10	2.2906	34.6832	16.25	
1300	90	10	2.5937	25.641	14.44	
1300	100	10	3.2052	29.3795	13.00	
1300	110	10	1.8042	24.7969	11.82	
1300	125	10	1.5008	16.3306	10.40	
1300	140	10	0.9396	6.3905	9.29	
1300	150	10	0	0.77917	8.67	
1000	20	10	5.4836	48.4926	50.00	50.00
1000	25	10	4.42017	43.9499	40.00	
1000	30	10	4.8471	40.2646	33.33	
1000	35	10	4.41447	40.7613	28.57	
1000	40	10	4.8528	40.2312	25.00	
1000	45	10	4.4202	36.5754	22.22	
1000	50	10	4.8983	37.5963	20.00	
1000	55	10	3.3366	35.2985	18.18	
1000	60	10	2.8967	29.2488	16.67	
1000	65	10	2.4107	23.316	15.38	
1000	70	10	2.405	26.0586	14.29	
1000	75	10	1.4664	17.9005	13.33	
1000	80	10	0.9911	15.323	12.50	
1000	90	10	0.9716	9.815	11.11	
1000	100	10	0.67605	4.8812	10.00	
1000	110	10	0	0.481273	9.09	
800	15	10	5.5177	19.5448	53.33	53.33
800	20	10	4.5227	27.7892	40.00	
800	25	10	3.86731	32.9836	32.00	
800	30	10	4.0212	38.7644	26.67	
800	35	10	3.2281	37.3436	22.86	
800	40	10	3.2224	32.9836	20.00	
800	45	10	2.9024	27.2485	17.78	
800	50	10	2.6852	22.4466	16.00	
800	55	10	1.5409	16.594	14.55	
800	60	10	0.7906	9.2578	13.33	
800	65	10	0	10.5919	12.31	
800	70	10	0.4836	4.4543	11.43	
800	75	10	0.4774	0.4774	10.67	
500	10	10	3.0338	12.8983	50.00	
500	12.5	10	2.9616	11.5851	40.00	
500	15	10	3.20521	12.5167	33.33	33.33
500	17.5	10	2.4851	12.3528	28.57	
500	20	10	2.2334	10.1485	25.00	
500	25	10	1.83283	6.9557	20.00	
500	27.5	10	2.0217	7.1814	18.18	
500	30	10	0.1146	4.4031	16.67	
250	0.5	10	3.485	12.8438	500.00	500.00
250	1	10	2.1189	5.2428	250.00	
250	2.5	10	0.916654	2.17619	100.00	
250	5	10	0.8594	1.9473	50.00	

## B.2 Energy input - bend angle plots

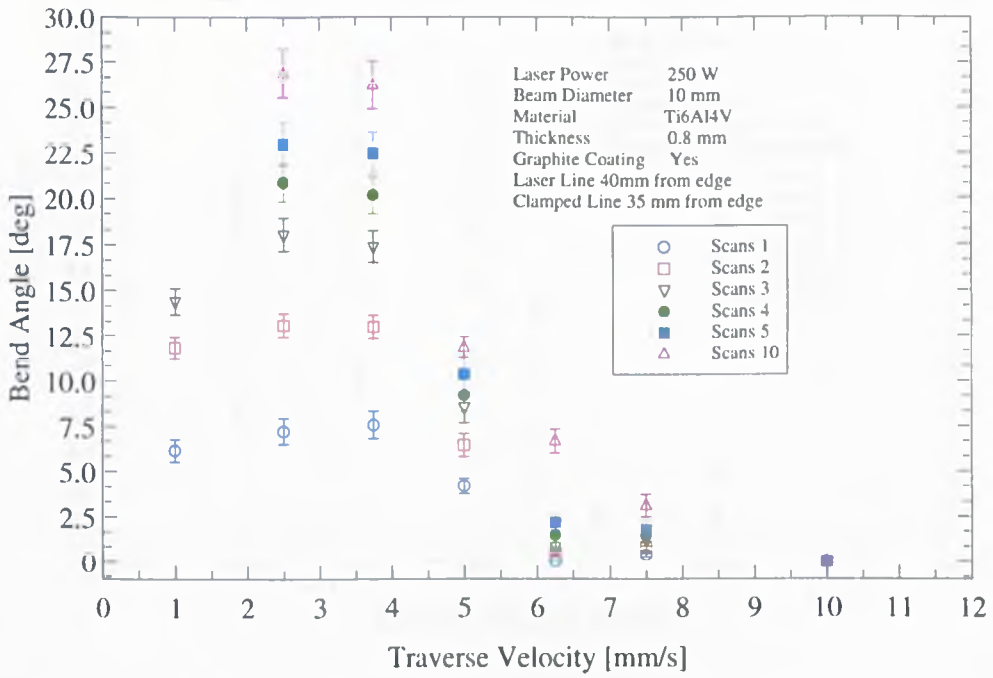


Figure B.1: Bend angle with decreasing energy input

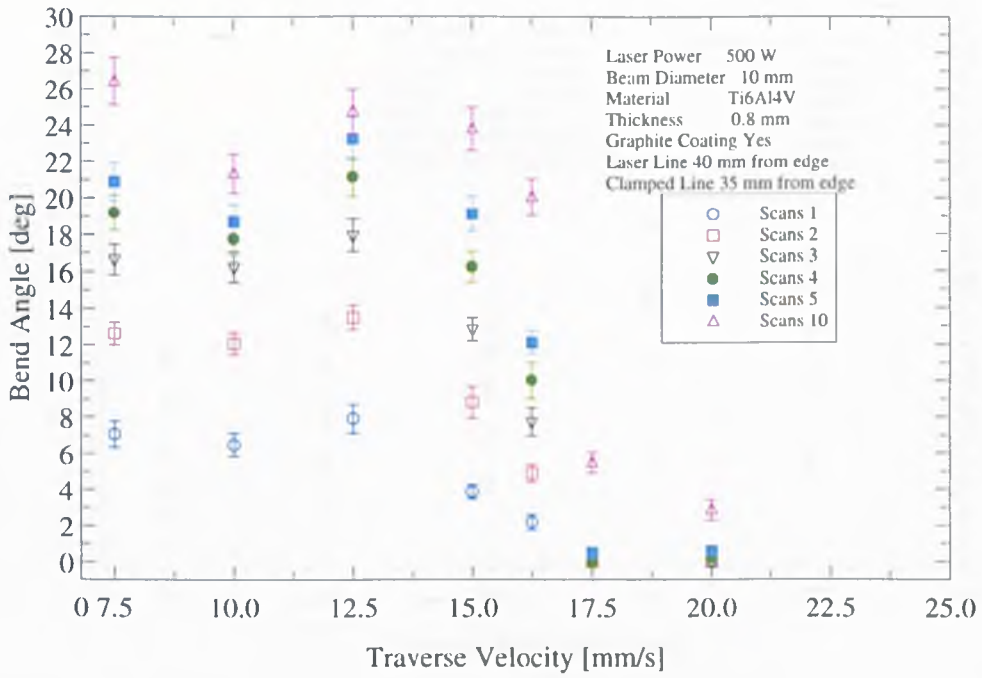


Figure B.2: Bend angle with decreasing energy input

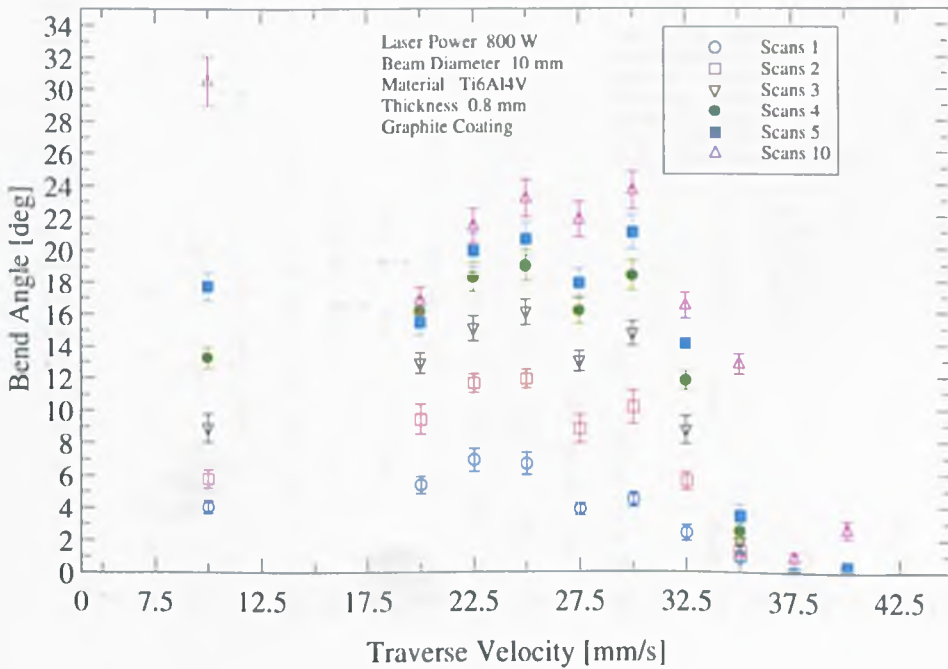


Figure B.3: Bend angle with decreasing energy input

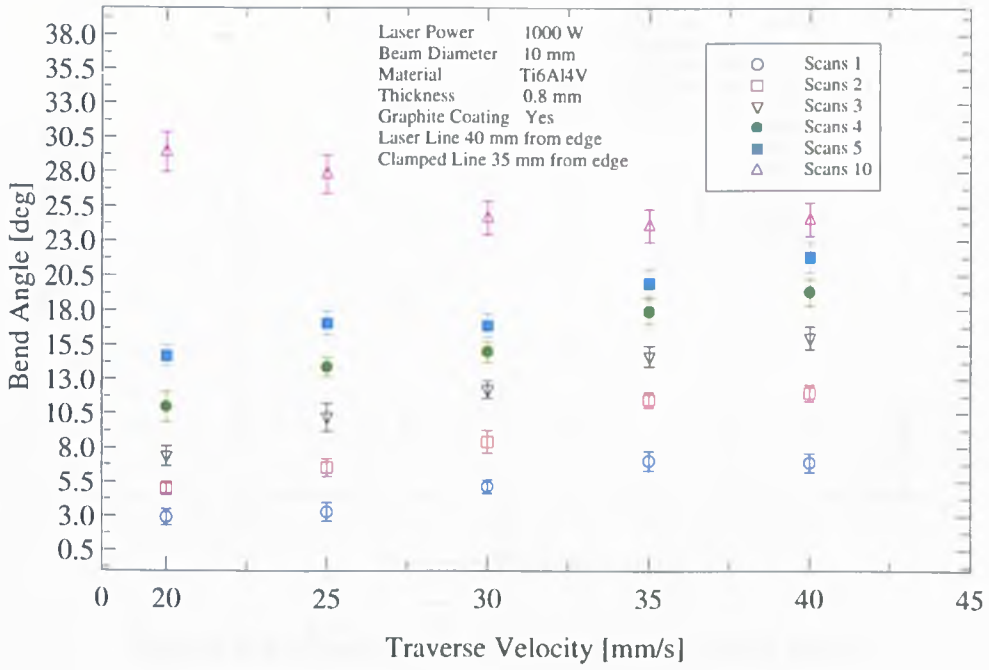


Figure B.4: Bend angle with decreasing energy input

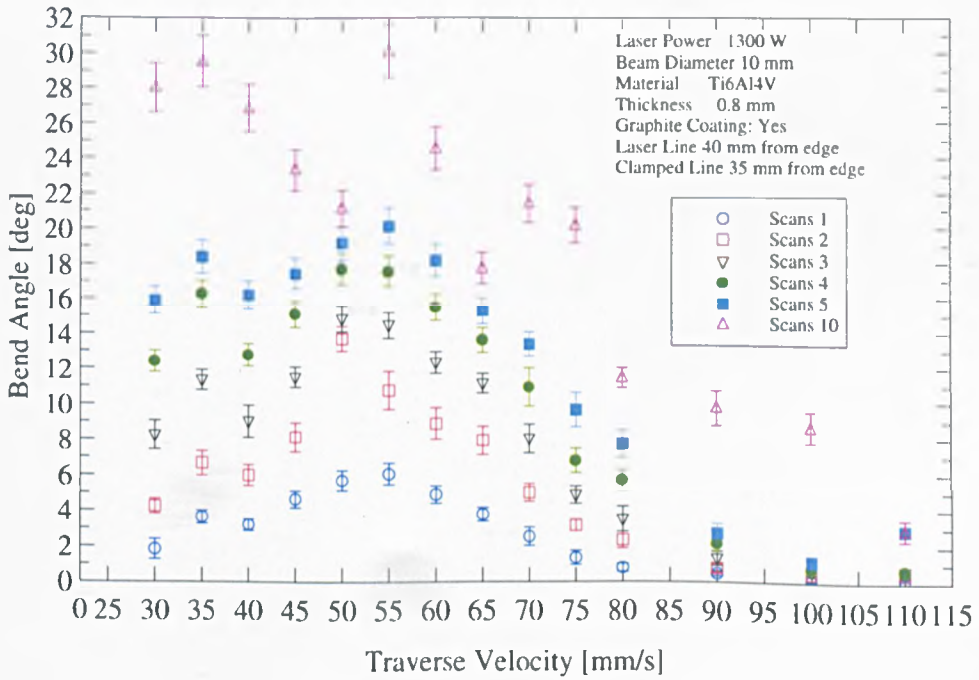


Figure B.5: Bend angle with decreasing energy input

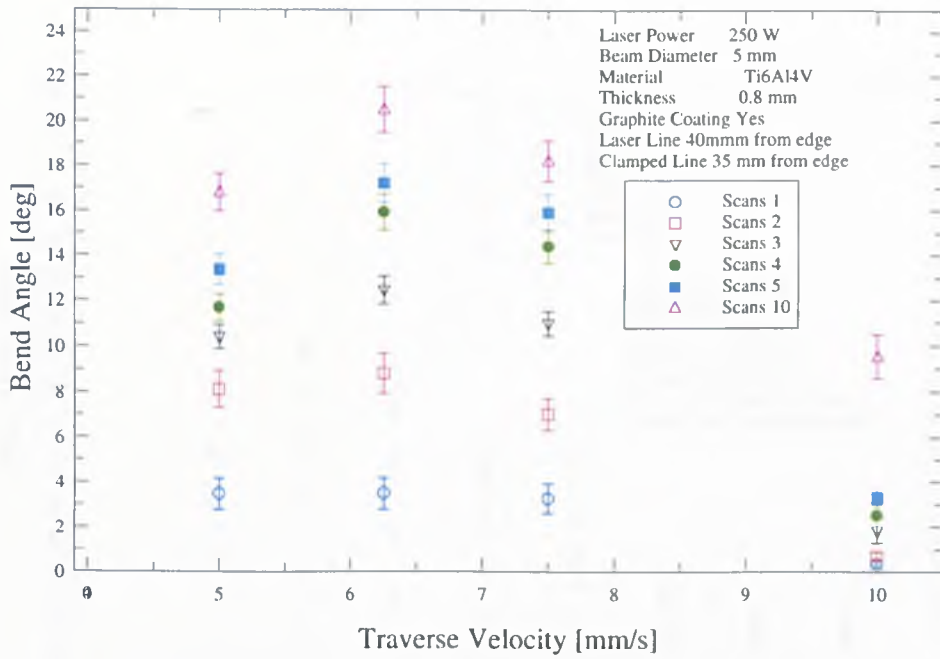


Figure B.6: Bend angle with decreasing energy input

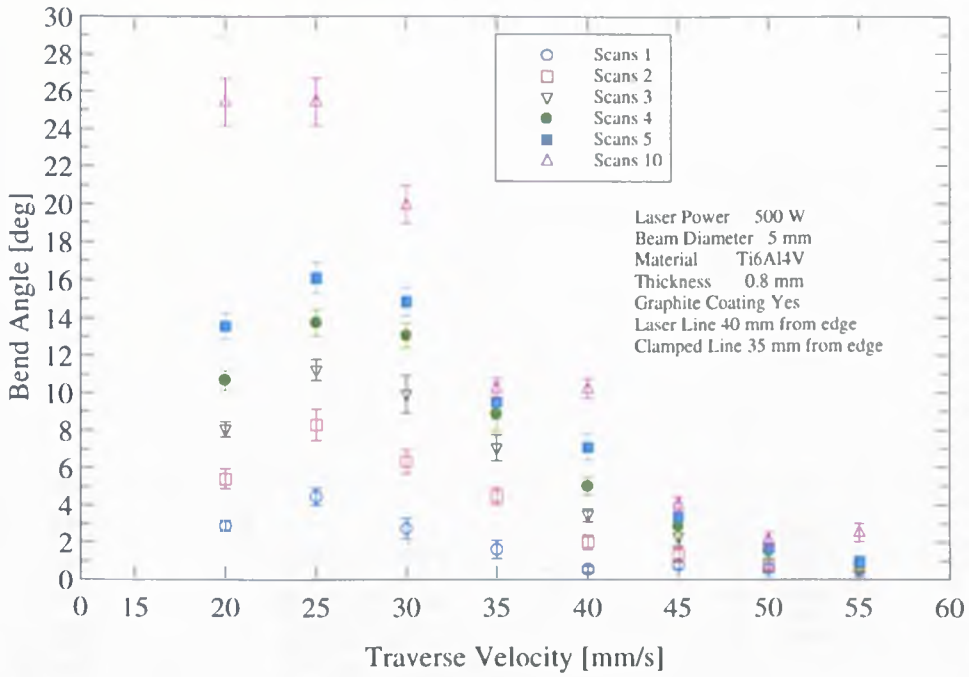


Figure B.7: Bend angle with decreasing energy input

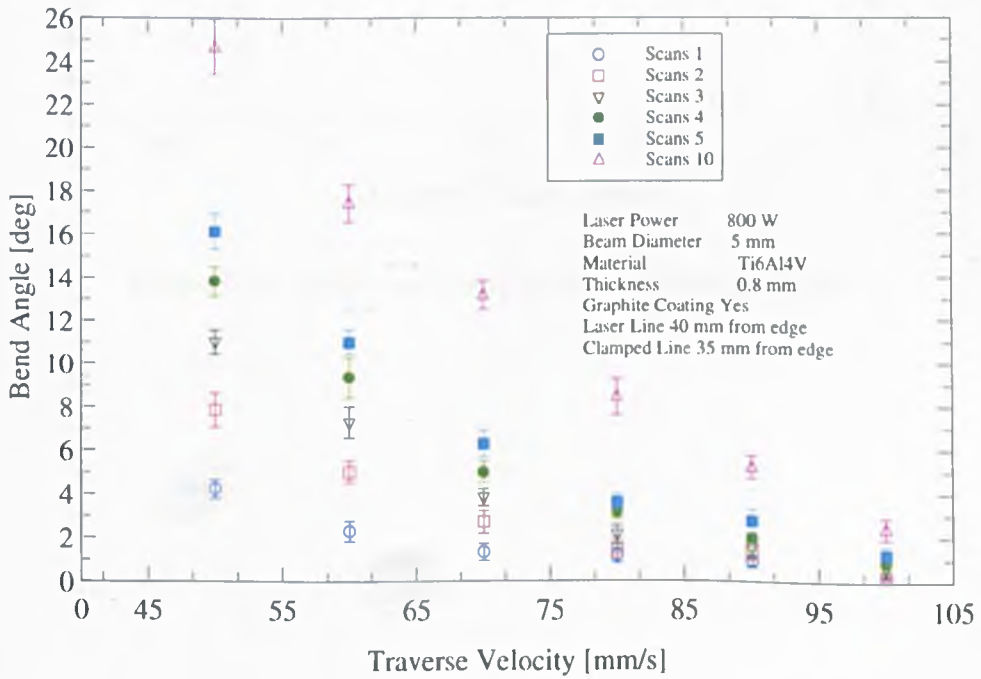


Figure B.8: Bend angle with decreasing energy input

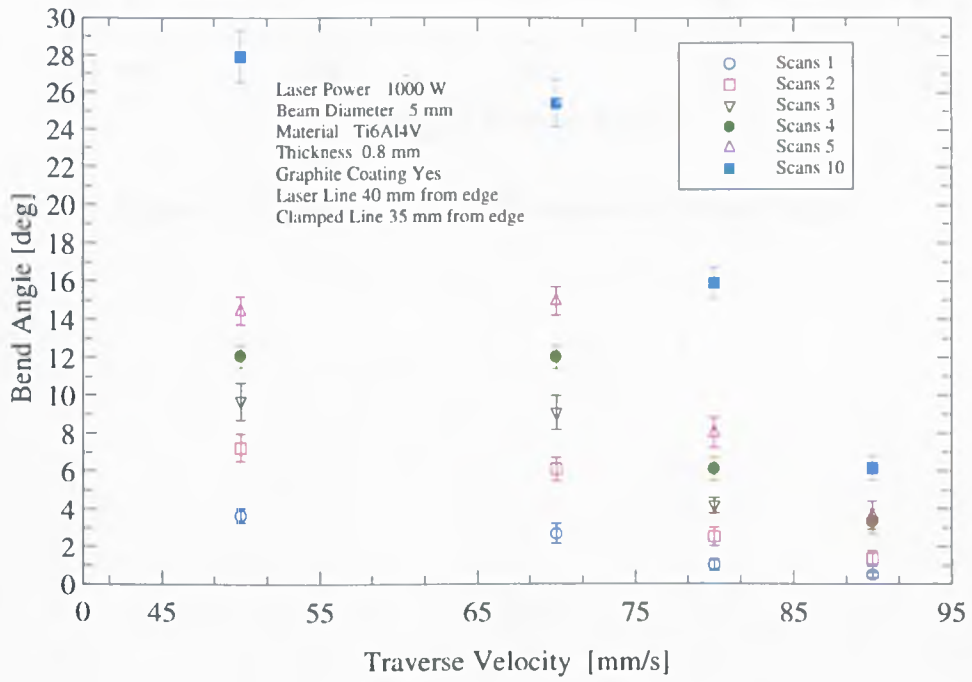


Figure B.9: Bend angle with decreasing energy input

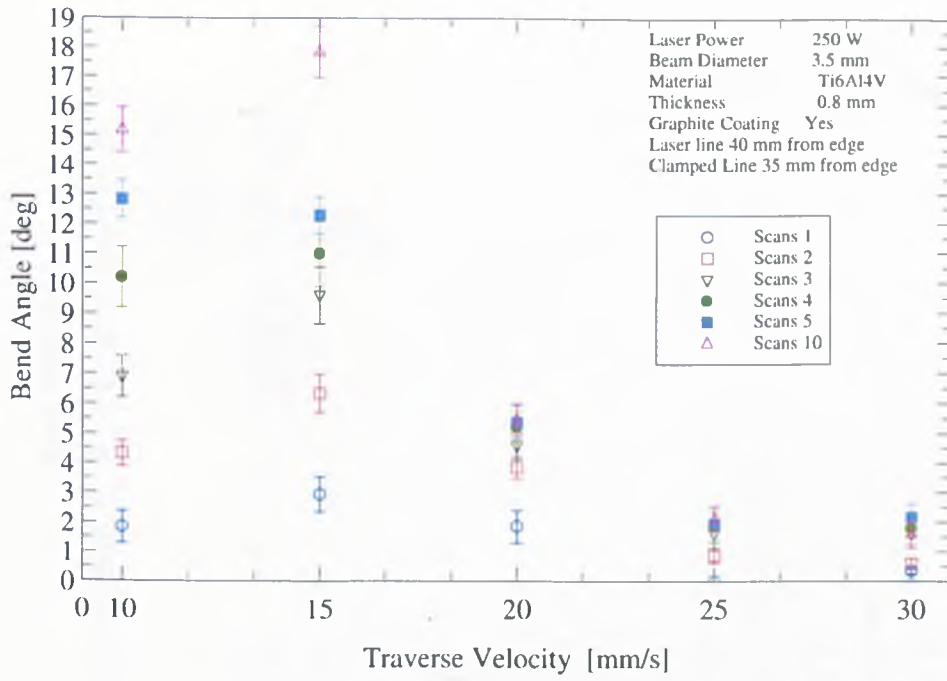


Figure B.10: Bend angle with decreasing energy input

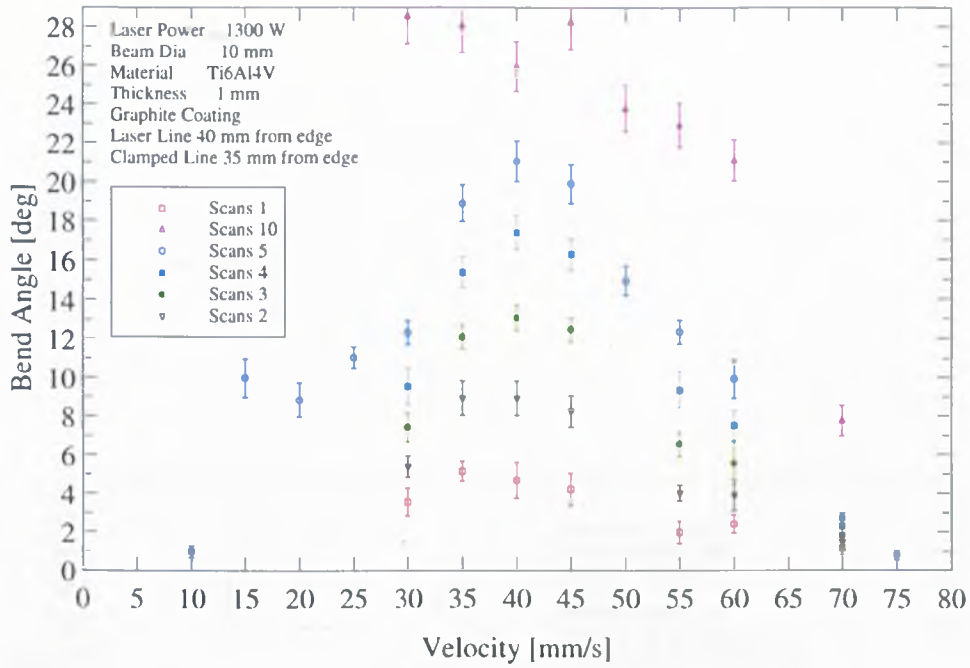


Figure B.11: Bend angle with decreasing energy input

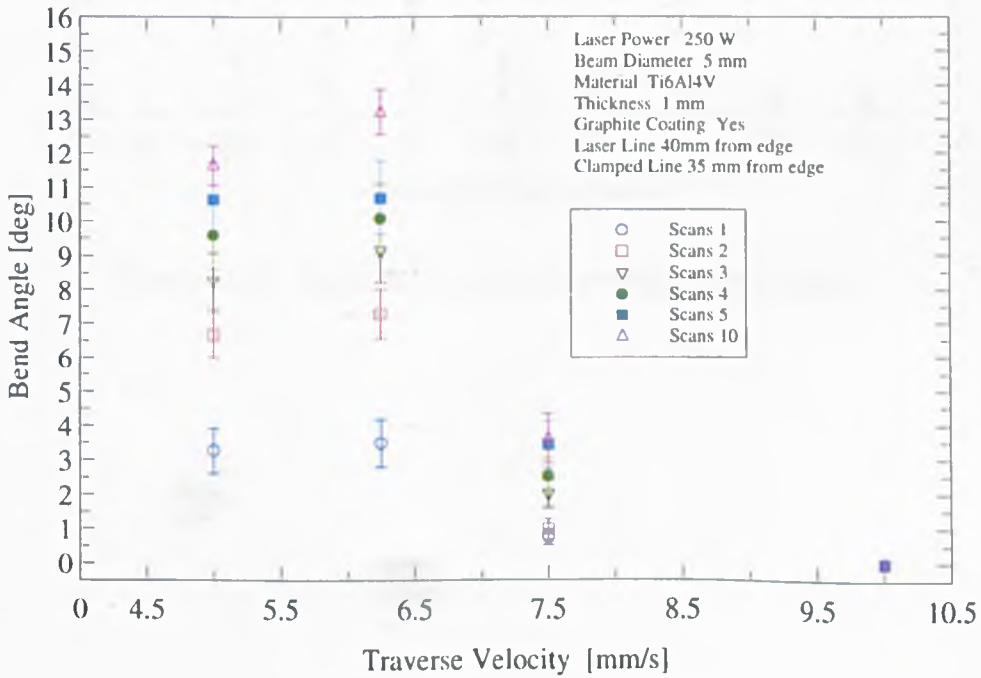


Figure B.12: Bend angle with decreasing energy input

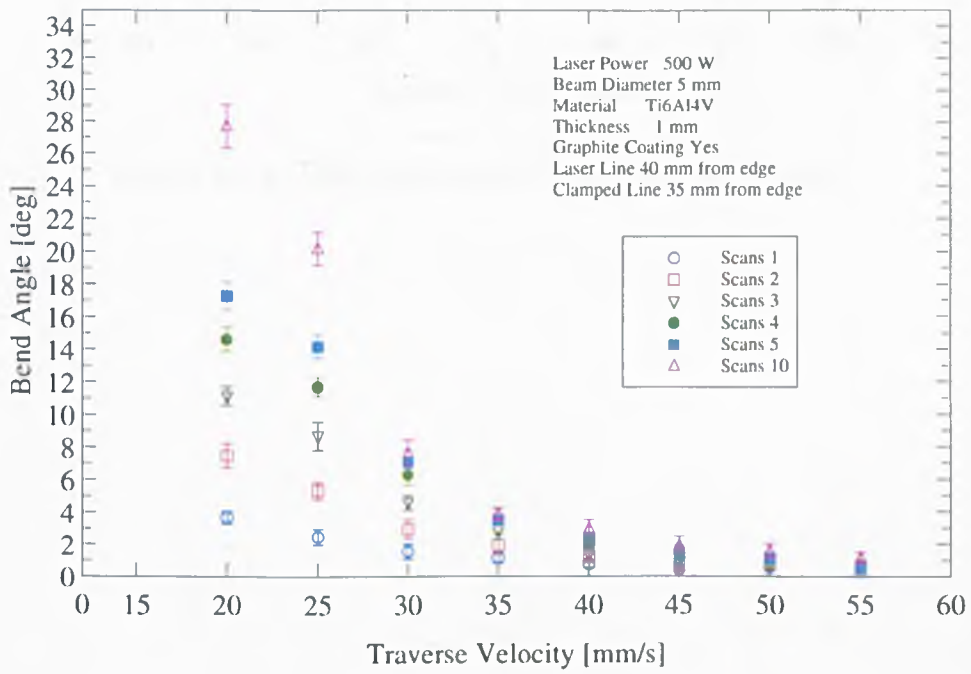


Figure B.13: Bend angle with decreasing energy input

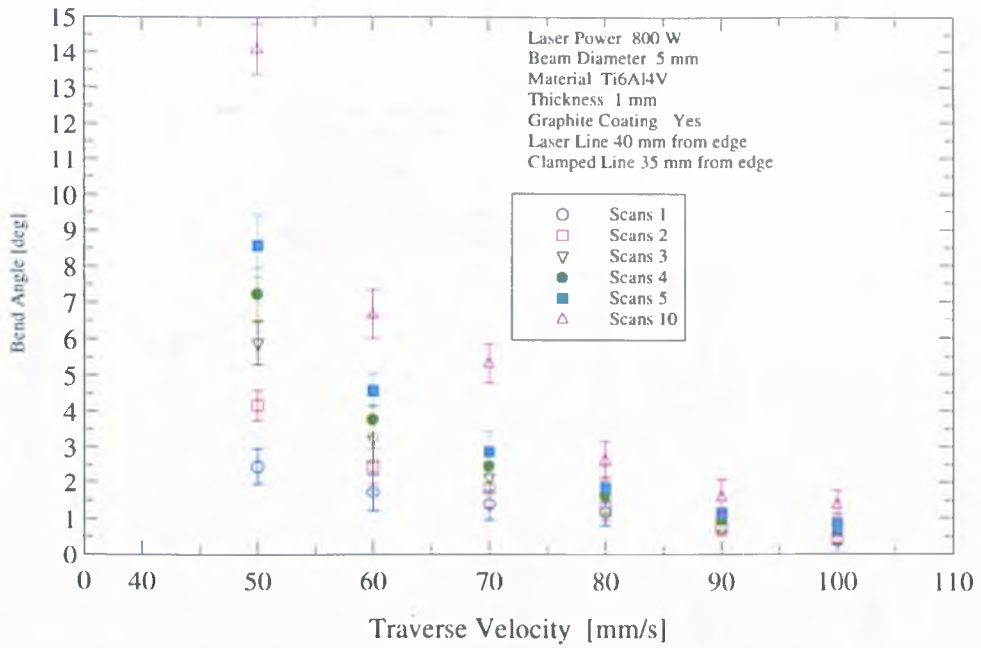


Figure B.14: Bend angle with decreasing energy input

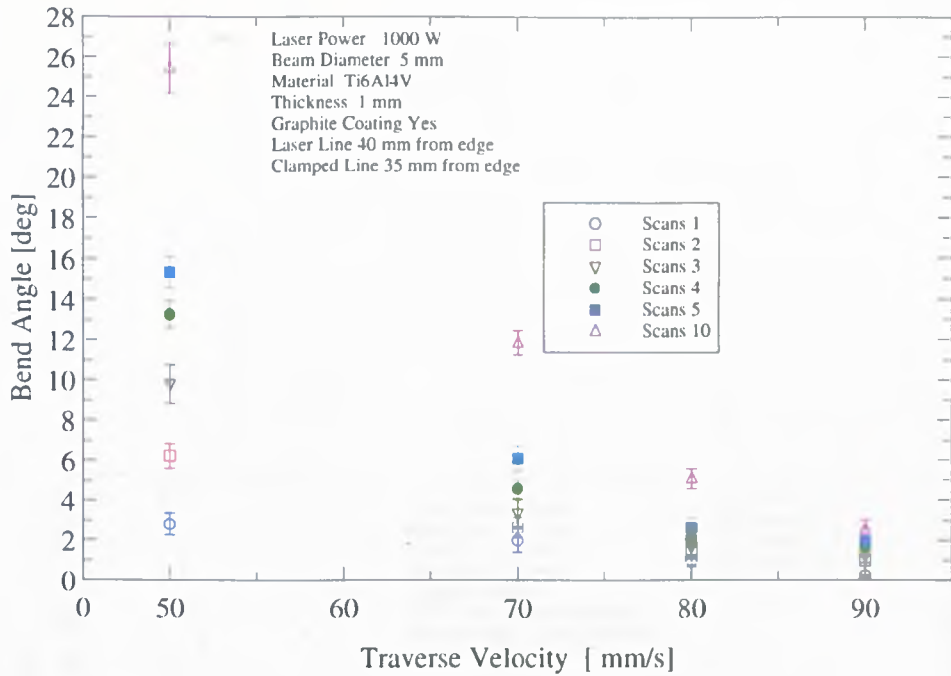


Figure B.15: Bend angle with decreasing energy input

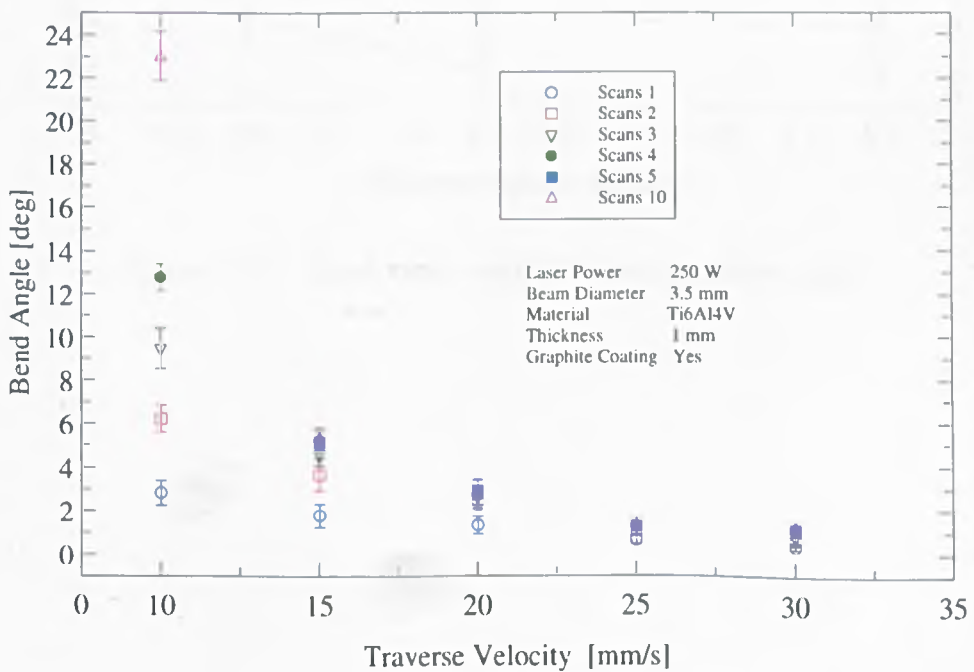


Figure B.16: Bend angle with decreasing energy input

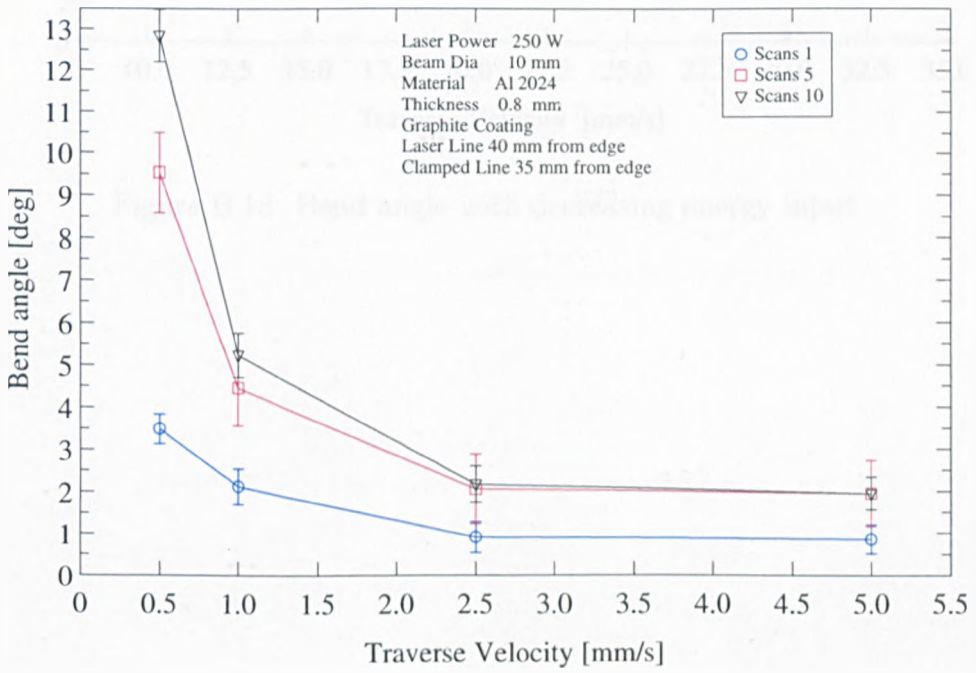


Figure B.17: Bend angle with decreasing energy input

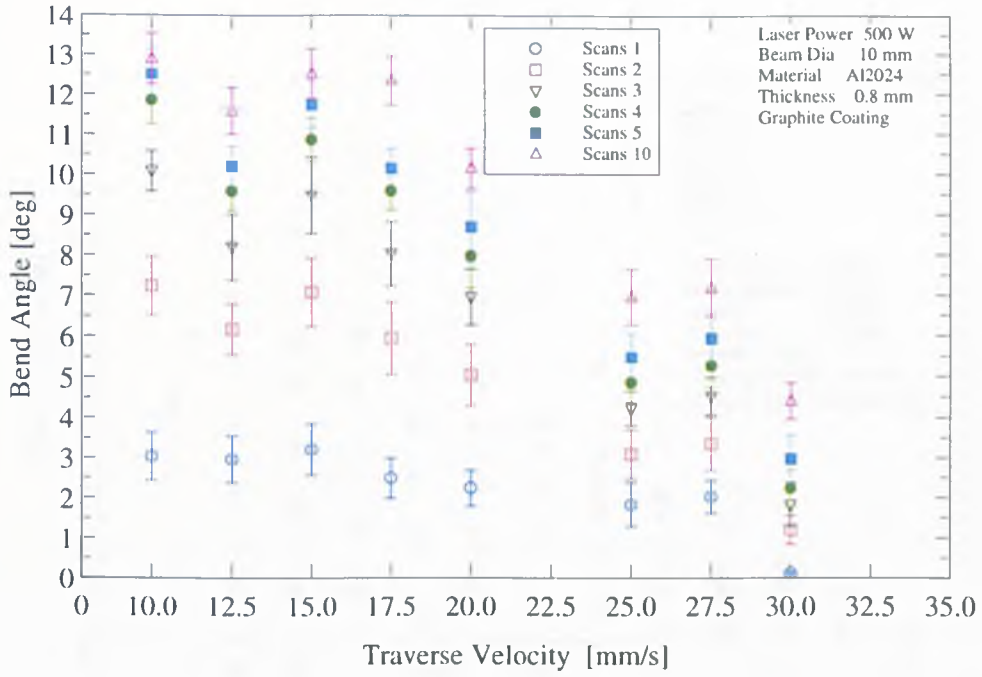


Figure B.18: Bend angle with decreasing energy input

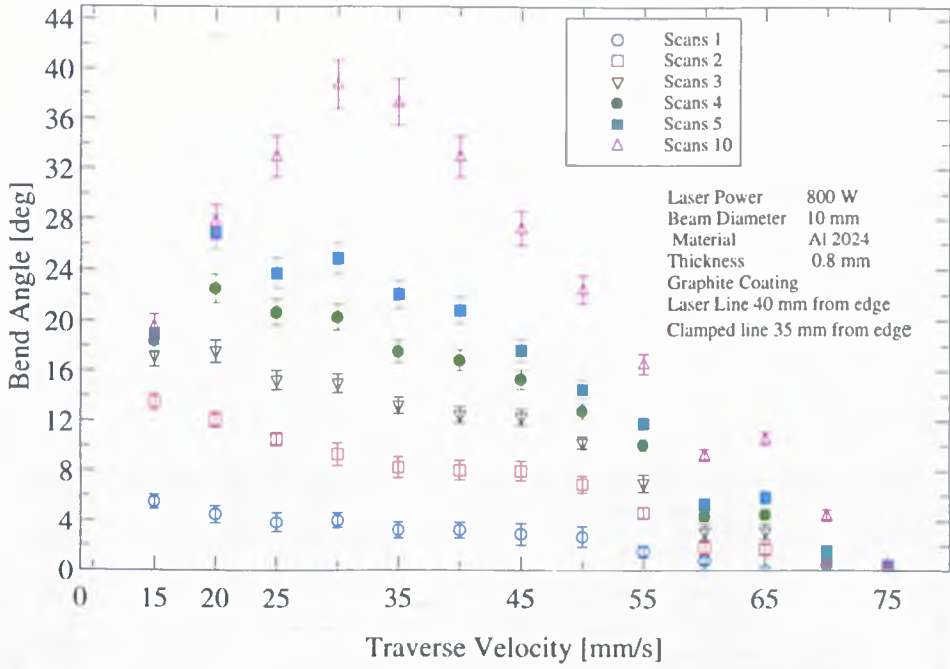


Figure B.19: Bend angle with decreasing energy input

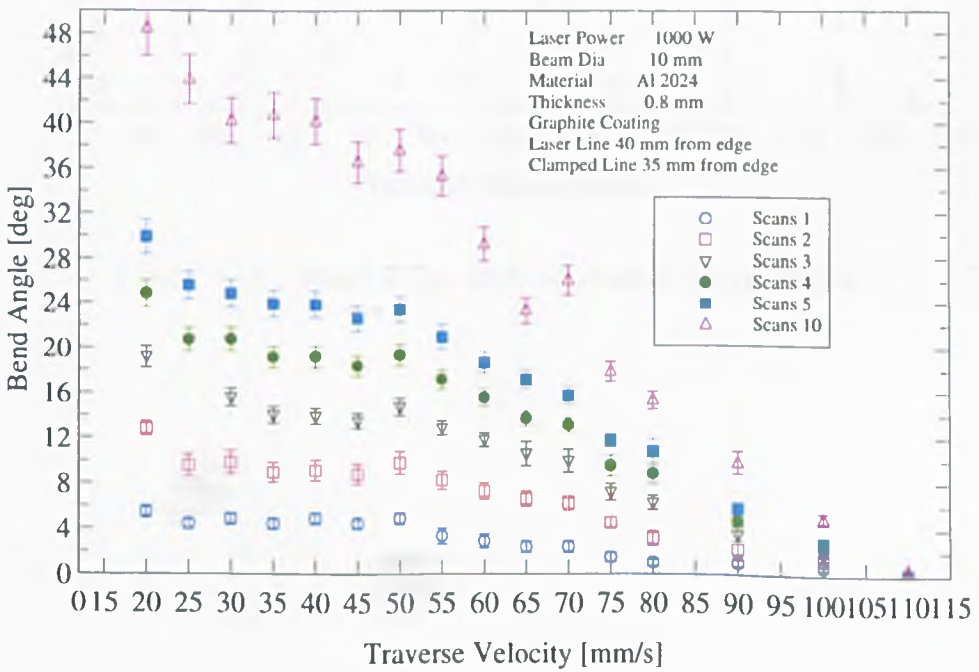


Figure B.20: Bend angle with decreasing energy input

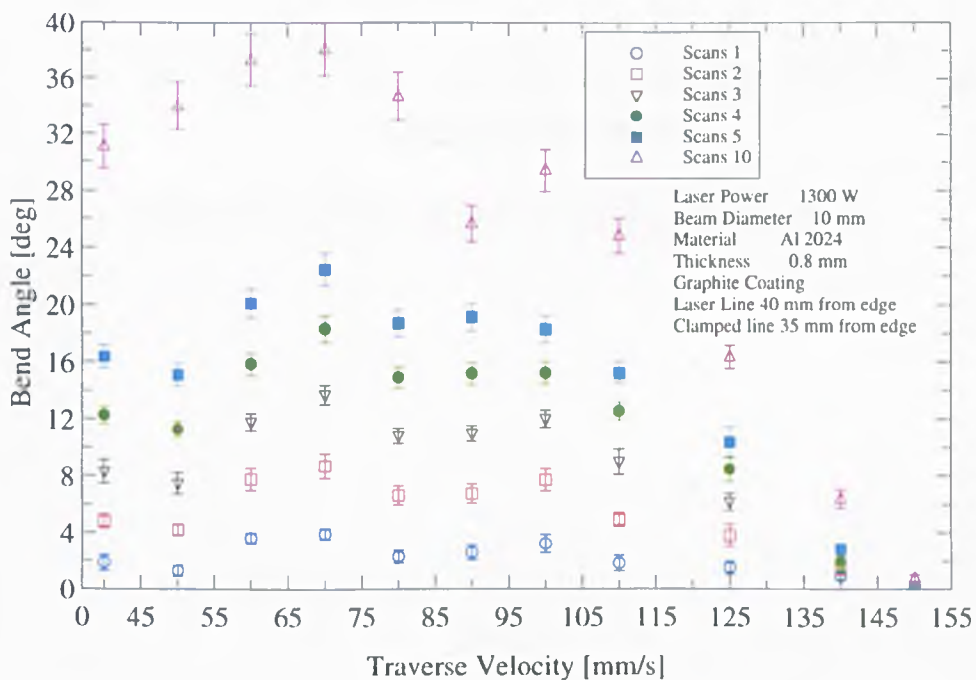


Figure B.21: Bend angle with decreasing energy input

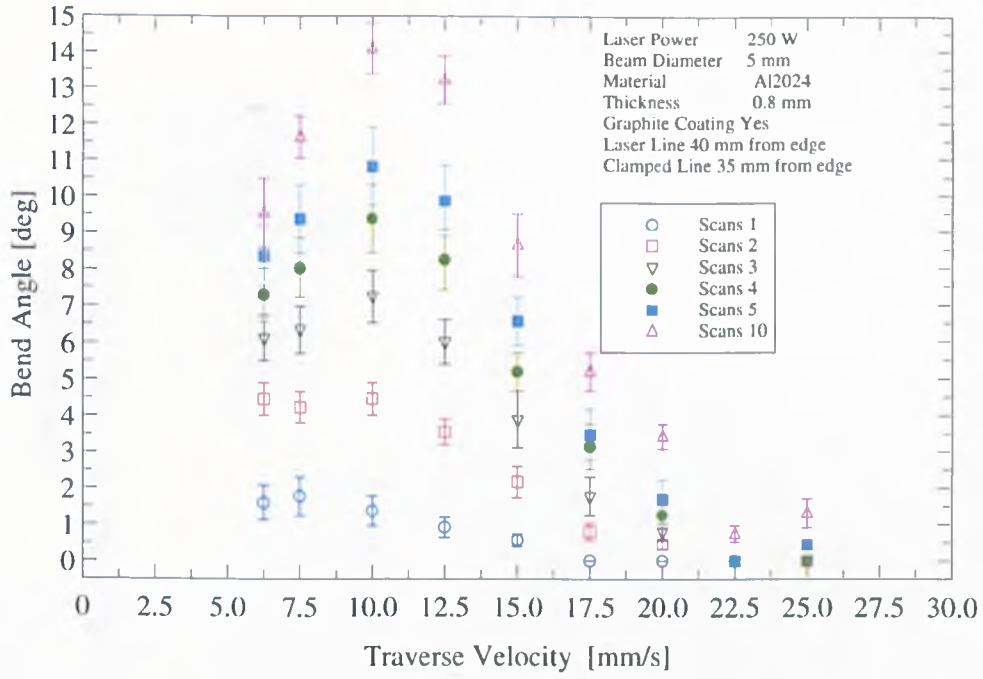


Figure B.22: Bend angle with decreasing energy input

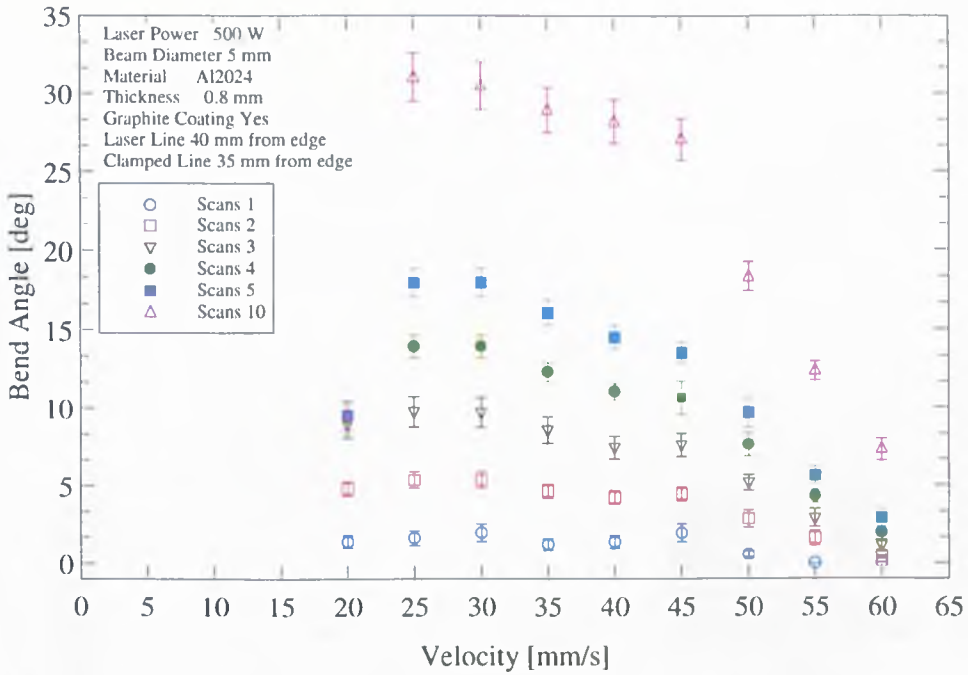


Figure B.23: Bend angle with decreasing energy input

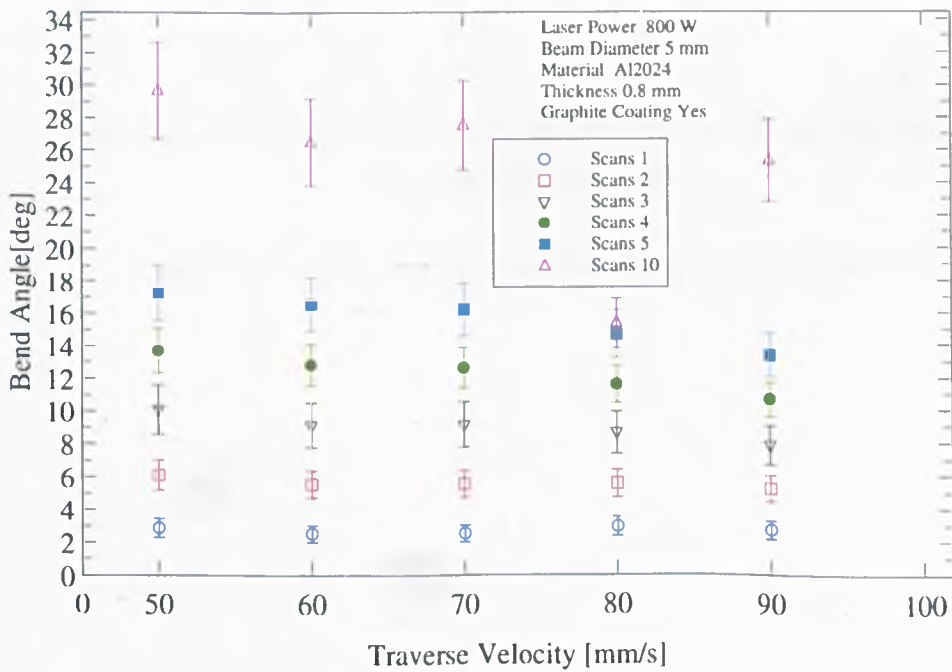


Figure B.24: Bend angle with decreasing energy input

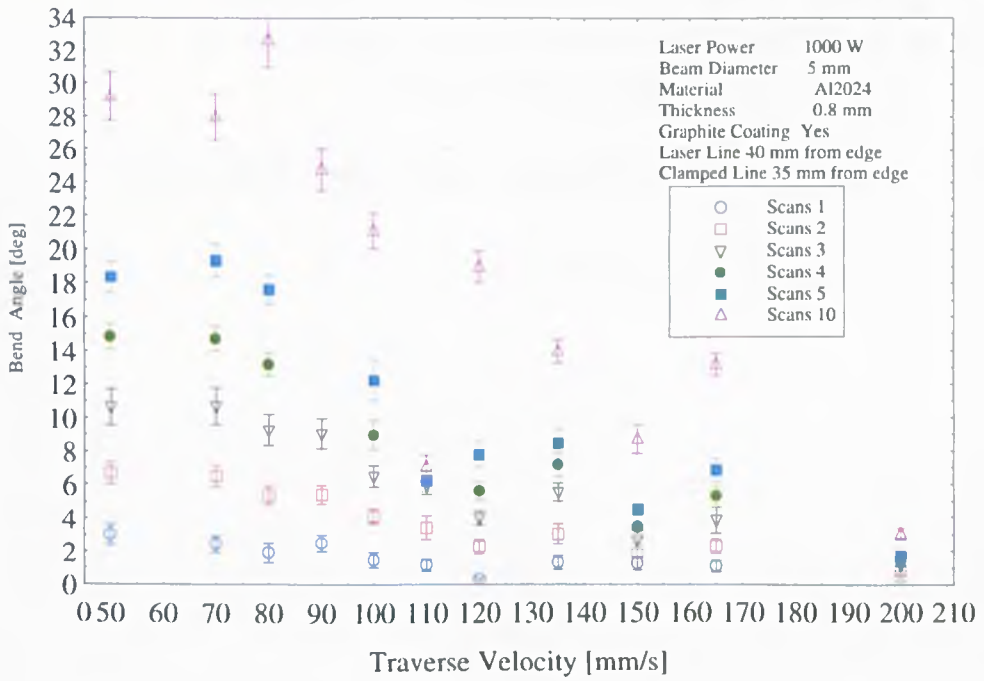


Figure B.25: Bend angle with decreasing energy input

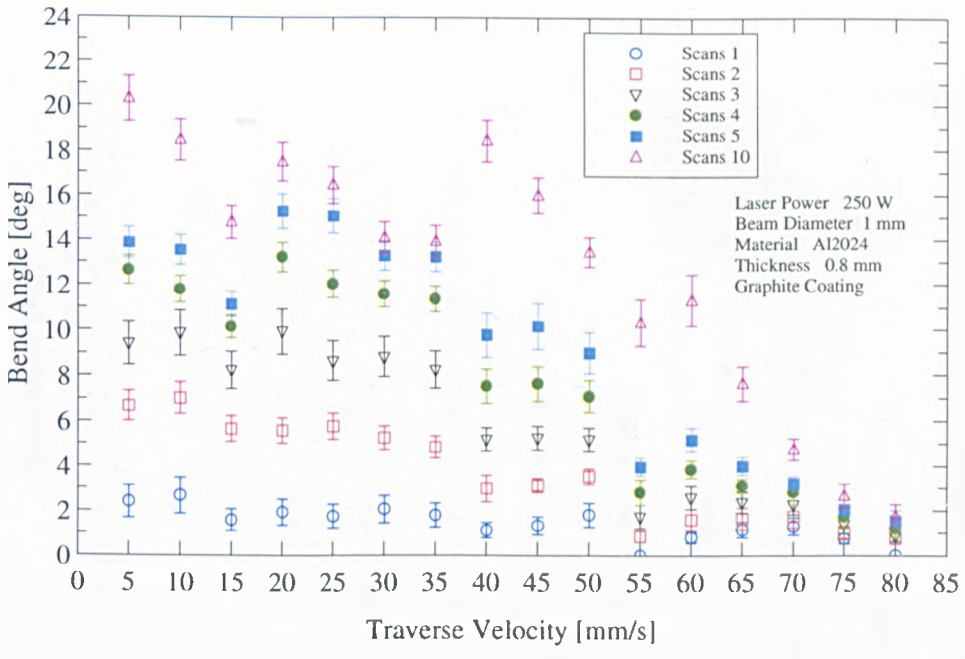


Figure B.26: Bend angle with decreasing energy input

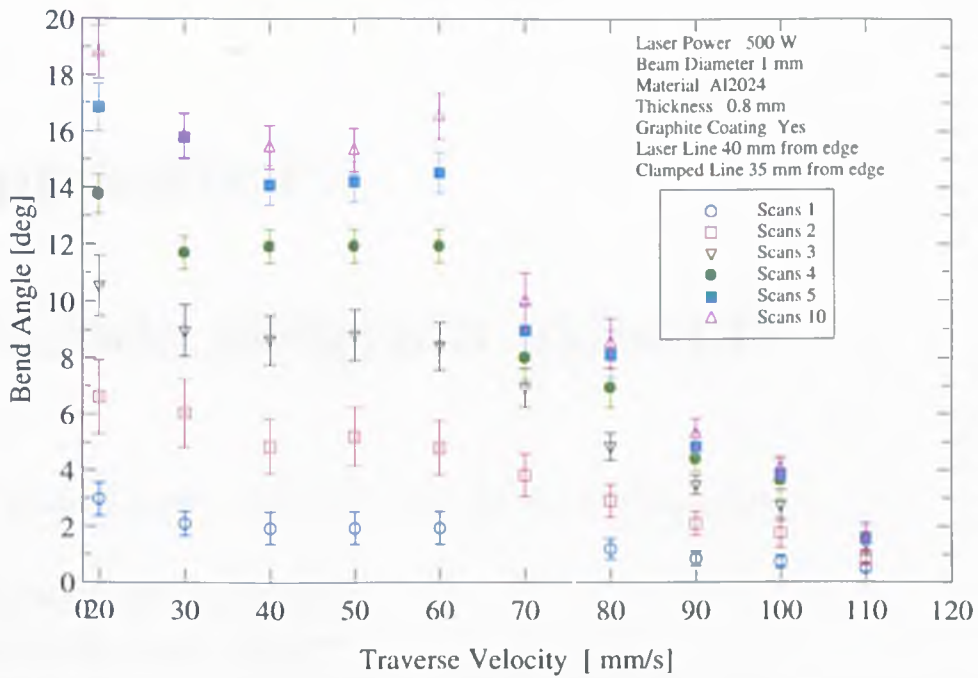


Figure B.27: Bend angle with decreasing energy input

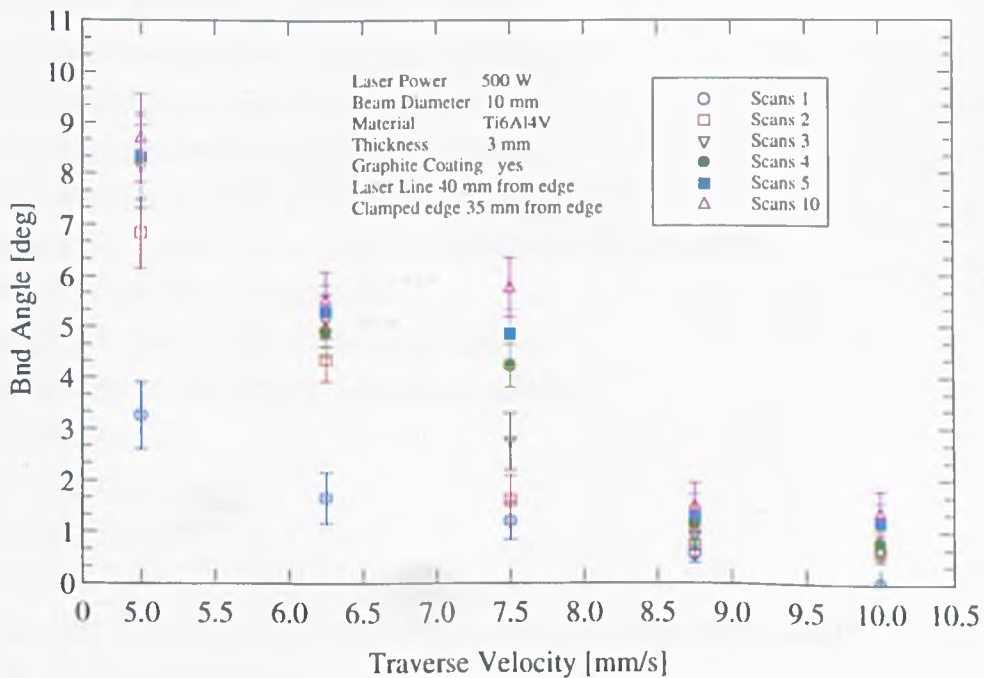


Figure B.28: Bend angle with decreasing energy input

# Appendix C

## G-Code program example

This is an example of one of the codes for the dividing system.

```
N100 L1=20 (inner radius)
N105 L2=62 (outer radius)
N110 L3=12 L4=0 (number of sectors: 3, 6, 12, 24, 48, ... and accumulated angle)
N115 L5=L2 L6=0 (x and y position for starting irradiation)
N120 L7=3 (test variable)
N125 L8=-360 (offset between 2 different division levels)
N130 L11=0 (offset for same division level)
N135 L9=0 (irradiation counter per 3-star)
N140 L10=0 (irradiation counter per line type)
N145 L100=3 (line types L100=2 or 3)
N150 L101=0 (general irradiation counter)
N155 L102=2*L3 L103=3*L3 L104=L100-1*2*L3
(numbers of irradiation for special offsets and exit number)
N200 G71 G94 G90 (initialisation)
N300 G59 X-250 Y-180 Z-200 (origin offset)
N400 G01 X0 Y0 Z0 F2000 (moving to offset)
N500 M70 (laser)
N600 M57 (laser)
N700 M59 (laser)
N1000 G79 L10=L3 N3500 (leave if one line type ready)
N1100 G90 G01 XL5 YL6 F2000 (move to irradiation start point)
N1200 M55 (shutter open)
N1300 G90 G01 EAL4 EXL1 F1600 (irradiation line)
N1400 M54 (shutter closed)
N1500 L9=L9+1 (irradiation counter)
```

N1600 G79 L9=3 N2200 (jump if offset needed)  
N1700 L4=L4-120 (next angle)  
N1800 G79 L4=L4-360 N2000 (angle between -360;360 degrees?)  
N1900 L4=L4+360 (if not ...)  
N2000 L5=CL4\*L2 L6=SL4\*L2 (start point co-ordinates: cosine, sine)  
N2100 G79 N1000 (next irradiation of 3-star)  
N2200 L10=L10+L9  
N2300 L9=0  
N2400 G79 L10=L7 N2700  
N2500 L4=L4+L11 (offset between lines of same division level)  
N2600 G79 N1700  
N2700 L8=L8/2  
N2800 L4=L4+L8 L11=-360/L7 (offset between two division levels)  
N2900 L7=L7\*2  
N3000 G79 N1800  
N3500 L101=L101+L10 (increase general irradiation counter)  
N3600 L7=3 L9=0 L10=0 L11=0 (reset variables for next loop)  
N3700 G79 L101=L104 N6000 (leave if ready)  
N3800 G79 L101=L102 N4500 (get offset after 2\*L3 lines)  
N3900 G79 L101=L103 N5000 (get offset after 3\*L3 lines) (else offset after L3 lines)  
N4000 L4=L8 (extra offset)  
N4100 L1=L2-L1/2+L1 (new inner end radius)  
N4200 G79 N5500  
N4500 L4=1.5\*L8 (extra offset)  
N4600 L1=L2-L1/2+L1 (new inner end radius)  
N4700 G79 N5500  
N5000 L4=0.5\*L8-180 (extra offset, inner end radius stays the same)  
N5500 L8=-360 (reset)  
N5600 L5=CL4\*L2 L6=SL4\*L2 (next start point)  
N5700 G79 N1100 (jump back to irradiation loop)  
N6000 M58 (laser)  
N6100 G90 G59 X0 Y0 Z0 (offset cancellation)  
N6200 G01 X0 Y0 Z0 F2000 (homing)  
N6300 M02 (end)

# Appendix D

## Metallurgy AA 2024 T3

### D.1 Processing parameters - AA 2024 T3

Sample ID	Velocity mm/s	Number of scans	Process specifications
47	15	5	Power = 250 W Beam diameter = 5 mm Scanned back and forth Natural air convection cooled No time allowed in between scans
48	15	10	
49	15	20	
50	15	30	
51	15	40	
1	30	10	Power = 500 W Beam diameter = 5 mm Forced air convection cooled 2 min. allowed in between scans
2	40	10	
3	50	10	
F1	25	10	Power = 500 W Beam diameter 5 mm Natural air convection cooled 2 min. allowed in between scans
F2	50	10	
F3	100	10	
F4	25	10	Power = 650 W Beam diameter 10 mm Natural air convection cooled 2 min. allowed in between scans
F5	50	10	
F6	100	10	

Sample ID	Velocity mm/s	Number of scans	Process specifications
53	25	1	Power = 500 W Beam diameter = 5 mm Forced air convection cooled
32	50	1	
24A	10	10	Power = 800 W Beam diameter = 10 mm Forced air convection cooled
24B	20	10	
24C	25	10	
24E	35	10	
25B	45	10	
25C	50	10	
26A	65	10	
26C	75	10	
8	75	1	Power = 250 W Beam diameter = 1 mm Forced air convection cooled
34A	10	10	
34C	20	10	
35A	30	10	
35C	40	10	
35E	50	10	
36B	60	10	
284	20	10	Power = 500 W Beam diameter = 1 mm Forced air convection cooled
286	40	10	
288	60	10	
290	80	10	
292	100	10	
293	110	10	
66	50	1	Power = 500 W Beam diameter = 2,3,3 mm respectively Forced air convection cooled
86	100	10	
98	100	10	
108	100	1	

Sample ID	Region	Microstructure description
1	Top	Full recrystallization, small size equiaxed grains, partial melting
	Middle	Half recrystallized structure, some partial melting
	Bottom	Elongated grain structure, reduced partial melting
2	Top	Full recrystallization, equiaxed grains, partial melting
	Middle	Half recrystallized structure, reduced partial melting
	Bottom	Elongated grain structure
3	Top	Full recrystallization, equiaxed grains, some partial melting
	Middle	Half recrystallized grain structure
	Bottom	Elongated grain structure
8	Top	Elongated grain structure
	Middle	Not available
	Bottom	Elongated grain structure
24B	Top	Some recrystallization of grain structure
	Middle	Elongated grains, reduced recrystallization of structure
	Bottom	Not available
24C	Top	Some recrystallization of grain structure
	Middle	Elongated grain structure
	Bottom	Elongated grain structure
24E	Top	Some recrystallization of grain structure
	Middle	Elongated grain structure
	Bottom	Elongated grain structure
25B	Top	Some recrystallization of grain structure
	Middle	Elongated grain structure
	Bottom	Elongated grain structure
25C	Top	Some recrystallization of grain structure
	Middle	Elongated grains, reduced recrystallization of grain structure
	Bottom	Elongated grain structure
26A	Top	Reduced recrystallization of grain structure
	Middle	Elongated grain structure
	Bottom	Elongated grain structure
26C	Top	Reduced recrystallization of grain structure
	Middle	Not available
	Bottom	Not available
32	Top	Reduced recrystallization of grain structure
	Middle	Elongated grain structure
	Bottom	Elongated grain structure
34A	Top	Alclad fused with alloy, full recrystallized, partial melting
	Middle	Full recrystallized structure, partial melting
	Bottom	Not available
34C	Top	Alclad fused with alloy, full recrystallized, partial melting
	Middle	Full recrystallized structure, grain growth, partial melting
	Bottom	Not available

Sample ID	Region	Microstructure description
35A	Top	Alloy fused below Alclad, Full recrystallization, partial melting
	Middle	Early recrystallization, subgrain structure, some partial melting
	Bottom	Not available
35C	Top	Full recrystallization of structure, some partial melting
	Middle	Full recrystallization of structure
	Bottom	Not available
35E	Top	Full recrystallization, reduced grain growth, reduced partial melting
	Middle	Full recrystallization of structure
	Bottom	Not available
36B	Top	Full recrystallization, reduced grain growth
	Middle	Full recrystallization of structure
	Bottom	Not available
47	Top	Half recrystallized, grain growth, some partial melting
	Middle	Elongated grains, reduced recrystallization, reduced partial melting
	Bottom	Elongated grain structure
48	Top	Full recrystallized, partial melting
	Middle	half recrystallized, some partial melting
	Bottom	Elongated grain structure
49	Top	Full recrystallized, grain growth, reduce partial melting
	Middle	half recrystallized structure
	Bottom	Elongated grain structure
50	Top	Full recrystallized, severe partial melting
	Middle	Not available
	Bottom	Elongated grain structure
51	Top	Full recrystallized, severe partial melting
	Middle	Half recrystallized, partial melting
	Bottom	Elongated grains, some recrystallization, some partial melting
53	Top	Half recrystallization, elongated grains
	Middle	Elongated grain structure
	Bottom	Elongated grain structure
66	Top	Fusion zone below Alclad, full recrystallization, partial melting
	Middle	Half recrystallized, partial melting
	Bottom	Not available
86	Top	Fusion zone of Alclad and alloy, full recrystallization, partial melting
	Middle	Half recrystallized, partial melting
	Bottom	Elongated grains, partial melting
98	Top	Half recrystallized, some partial melting
	Middle	Reduced recrystallization, reduced partial melting, subgrain structure
	Bottom	Elongated grain structure
108	Top	Not available
	Middle	Not available
	Bottom	Elongated grain structure
284	Top	Full fusion zone of Alclad and alloy
	Middle	Full recrystallized, severe partial melting
	Bottom	Half recrystallized, some partial melting, some elongated grains

Sample ID	Region	Microstructure description
286	Top	Half fusion zone Alclad and alloy, full recrystallized, partial melting
	Middle	Full recrystallized, , grain growth , some partial melting
	Bottom	Half recrystallized, reduced partial melting
288	Top	Half Fusion zone Alclad and alloy
	Middle	Recrystallized grain structure
	Bottom	Elongated grain structure
290		Half recrystallized below Alclad layer, partial melting
		Some recrystallization of grain structure, reduced partial melting
		Not available
292	Top	Half recrystallized below Alclad layer, partial melting
	Middle	Reduce recrystallization of grain structure, reduced partialmelting
	Bottom	Not available
293	Top	Reduced recrystallization only below Alclad layer
	Middle	Elongated grain structure
	Bottom	Not available

# Appendix E

## Mechanical properties Ti6Al4V

### E.1 Processing Parameters

I.D.	Specimen Number	LASER PARAMETERS				TRANSFORMED ZONE		Alpha case ?
		Power (W)	B.D (mm)	Velocity (mm/s)	No. of scans	Length of Zone at surface (microns)	Depth (microns)	
1	JS 2.6	250	5	10	1	2550	1000	?
2	JS 3.4	250	5	10	1	2540	1000	?
3	JS4.6	250	5	10	5	2490	1000	yes
4	JS10.4	250	5	10	5	2290	860	yes
5	JS20.4	500	5	30	15	1560	400	yes
6	JS21.5	500	5	40	15	1950	400	yes
7	JS 22.5	250	5	50	15	1810	310	?
8	JS5.4	250	5	15	10	1950	1000	yes
9	JS6.4	250	5	15	20	2150	1000	yes
10	JS7.4	250	5	15	30	2120	950	yes
11	JS 9.4	250	5	15	30	1680	270	yes
12	37B	1300	10	30	10	5300	800	yes
13	37D	1300	10	40	10	4450	800	yes
14	37E	1300	10	45	10	3810	800	yes
15	38A	1300	10	50	10	3830	800	yes
16	38B	1300	10	55	10	4260	690	no
17	38C	1300	10	60	10	3520	560	no
18	38D	1300	10	65	10	3440	460	no
19	38E	1300	10	70	10	3340	280	no
20	39A	1300	10	75	10	3240	320	no
21	39B	1300	10	80	10	2480	240	no
22	39C	1300	10	90	10	3110	230	no
23	39D	1300	10	100	10	2830	260	no
24	Ti 39	800	10	30	1	2610	800	no
25	Ti 7	800	10	30	1	2980	490	no
26	Ti 8	800	10	35	1	1830	380	no
27	Ti 9	800	10	40	1	0	0	no
28	Ti 10	800	10	45	1	0	0	no
29	Ti 11	800	10	50	1	0	0	no
30	Ti 12	800	10	55	1	0	0	no
31	Ti 18	800	10	30	5	4380	800	no
32	Ti 17	800	10	35	5	3640	590	no
33	Ti 16	800	10	40	5	2790	300	no
34	Ti 15	800	10	45	5	2310	210	no
35	Ti 14	800	10	50	5	1580	130	no
36	Ti 13	800	10	55	5	1230	120	no
37	40E	800	10	40	10	0	0	no

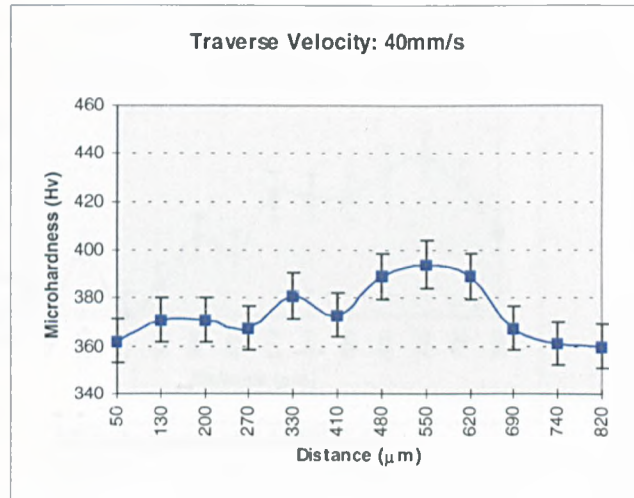
## E.2 Micro-hardness graphs

Laser parameters:

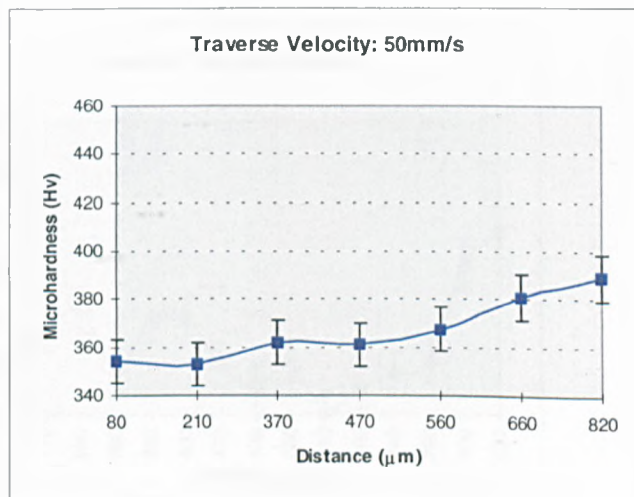
Power 1300W

Beam Diameter 10mm

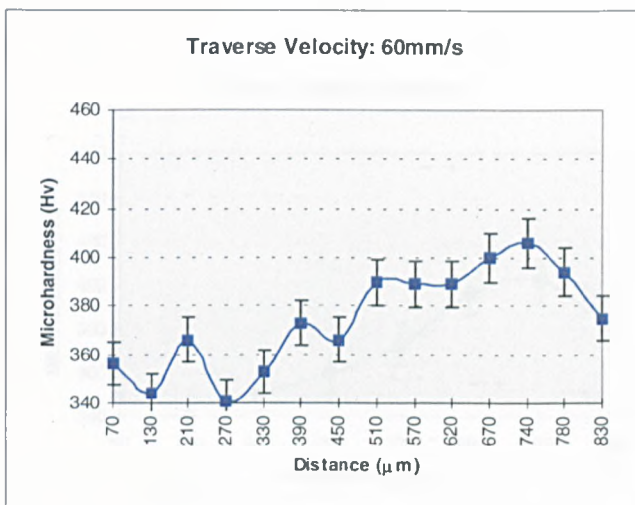
Number of scans: 10 (for first 6 figures)



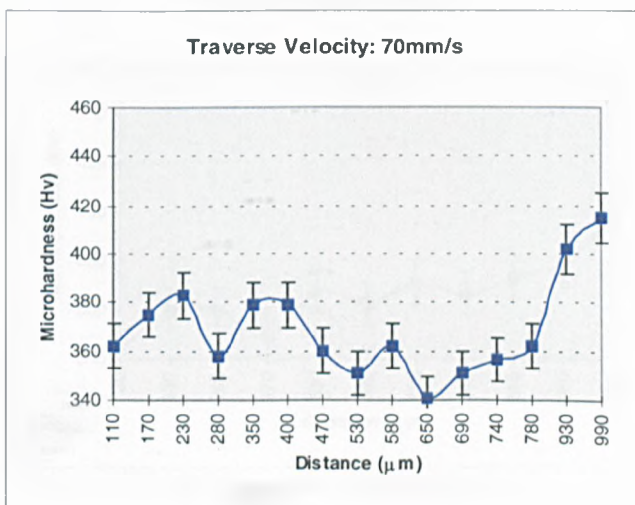
Microhardness of SAMPLE 13



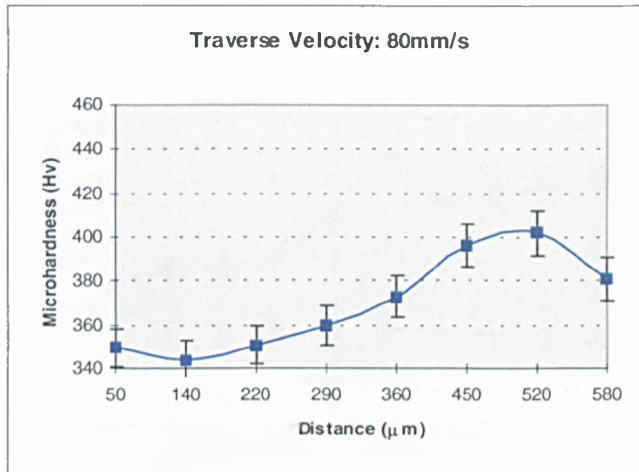
Microhardness of SAMPLE 15



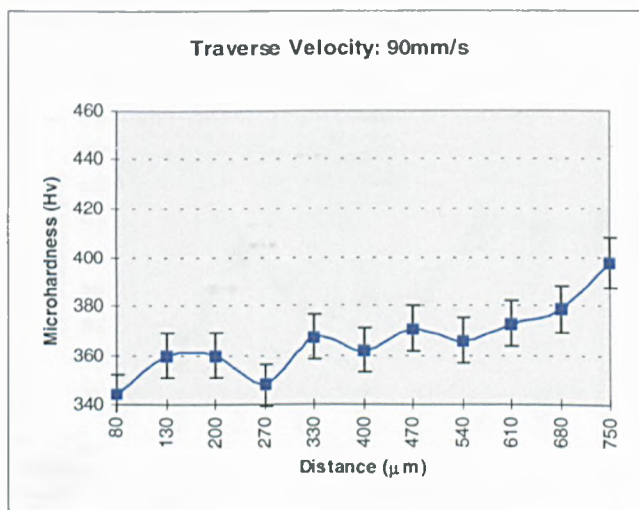
Microhardness of SAMPLE 17



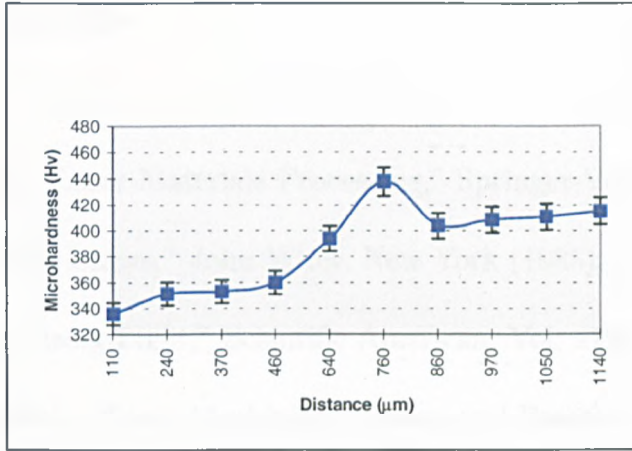
Microhardness of SAMPLE 19



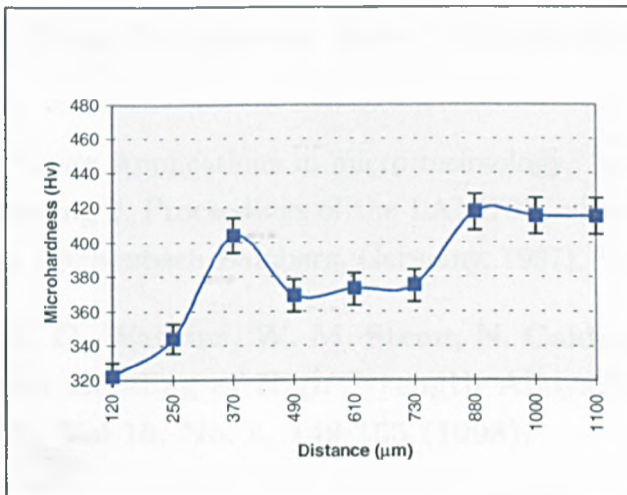
Microhardness of SAMPLE 21



Microhardness of SAMPLE 22



Microhardness of SAMPLE 9  
Power 250W; B.D.5mm; Velocity 15mm/s; 20scans



Microhardness of SAMPLE 5  
Power 500W; B.D.5mm; Velocity 30mm/s; 15 scans

# References

- [1] W. M. Steen, "Laser Materials Processing," Springer-Verlag (1991)
- [2] J. Eloy, "Power Lasers," John Wiley, New York (1985).
- [3] A. Schalow, "Laser Light," Scientific American, Vol. 219, 120-136 (1968).
- [4] G. Chryssolouris, "Laser Machining, Theory and Practice," Mechanical Engineering Series, Springer-Verlag, p.58 (1991).
- [5] J. Ready, "Lasers-Their Unusual Properties and Their Influence on Applications," Lasers in Modern Industry, Society of manufacturing Engineers Marketing Services Dept., Dearborn, MI, 17-38 (1979).
- [6] Coherent, Inc. Staff, Lasers: Operation, equipment, Application, and Design, McGraw-Hill, New York (1980).
- [7] R. E. Holt, "Flame Straightening Basics," Welding Engineer, 49-53 (June 1960).
- [8] W. Hoving, "Laser Applications in micro technology," in Laser Assisted Net Shape Engineering 2, Proceedings of the LANE'97, edited by M. Geiger and F. Vollertsen, (Meisenbach Bamberg, Germany, 1997), Vol. 2, pp.69-80.
- [9] J. Magee, K. G. Watkins, W. M. Steen, N. Calder, J. Sidhu, and J. Kirby, "Laser Bending of High Strength Alloys," Journal of Laser Applications, Vol.10, No. 4, 149-155 (1998).
- [10] Y-C. Hsiao, H. Shimizu, L. Firth, W. Maher, K. Masabuchi, "Finite Element Modelling Of Laser Forming," in Proceedings of the International Congress On Applications of Lasers and Electro-Optics, (ICALEO97), (San Diego, U.S.A, 1997), Section A. pp.31-40.
- [11] M. Geiger, F. Vollertsen, G. Deinzer, "Flexible straightening of Car Body Shells by Laser Forming," SAE Paper 930 279 (1993).

- [12] H. Hanebeuth, Chr. Hamann, "Suitability of CuCoBe-alloys for laser beam bending," in *Laser Assisted Net Shape Engineering 2*, Proceedings of the LANE'97, edited by M. Geiger and F. Vollertsen, (Meisenbach Bamberg, Germany, 1997), Vol. 2, pp. 367-374.
- [13] F. Vollertsen, "Mechanisms and models for laser forming" in *Laser Assisted Net shape Engineering*, Proceedings of the LANE'94, edited by M. Geiger and F. Vollertsen, (Meisenbach Bamberg, Germany, 1994), Vol. I, pp. 345-360.
- [14] F. Vollertsen, "Laser forming, Mechanisms, Models, Applications" in *LFT Erlangen monograph* (1995).
- [15] Y. Namba, "Laser Forming of Metals and Alloys". In *Proceedings of Laser Advanced Materials Processing (LAMP87)*, (Osaka, Japan, 1987), pp. 601-606.
- [16] F. Vollertsen, "An analytical model for laser bending," *Lasers Eng.* 2, 261-276 (1994).
- [17] F. Vollertsen, M. Rodle, "Model for the Temperature Gradient Mechanism of laser Bending," in *Laser Assisted Net Shape Engineering*, Proceedings of the LANE'94, edited by M. Geiger and F. Vollertsen, (Meisenbach Bamberg, Germany, 1994), Vol. I, pp. 371 - 378.
- [18] H. Frackiewicz, "Laser Metal Forming Technology," in *Fabtech International'93*, Proceedings of the FABTECH INTERNATIONAL conference, (Illinois1993), pp. 733 - 747.
- [19] Z. Mucha, J. Hoffman, W. Kalita, and S. Mucha, "Laser Forming of Thick Free Plates,". in *Laser Assisted Net shape Engineering 2*. Proceedings of the LANE'97, edited by M. Geiger and F. Vollertsen, (Meisenbach Bamberg, Germany, 1997), Vol. 2, pp. 383-392.
- [20] M. Geiger, F. Vollertsen, "The Mechanisms of Laser Forming," *CIRP ANNALS* Vol. 42, 1, 301 - 304 (1993).
- [21] H. Arnet, F. Vollertsen, "Extending laser bending for the generation of convex shapes," *Proceedings of the Institution of Mechanical Engineers Vol 209, Part B: Journal of Engineering Manufacture*, 433 - 442 (1995).
- [22] F. Vollertsen, I. Komel, and R. Kals, "The laser bending of steel foils for microparts by the buckling mechanism - A model," *Model. Simul. Mater. Sci. Eng.* 3, 107 - 119 (1995).

- [23] J. Kraus, "Basic processes in laser bending of extrusions Using the Upsetting Mechanism," in *Laser Assisted Net Shape Engineering 2, Proceedings of the LANE'97*, edited by M. Geiger and F. Vollertsen, (Meisenbach Bamberg, Germany, 1997), Vol. 2, pp.431-438.
- [24] A. Moshaiov, J. G. Shin, "Modified Strip Model for Analysing the Line Heating Method (Part 2): Thermo-Elastic-Plastic Plates," *Journal of Ship Research*, Vol. 35, No. 3, 266-275 (Sept. 1991).
- [25] C. L. Yau, K. C. Chan, W. B. Lee, "A New Analytical Model for Laser Bending," in *Laser Assisted Net Shape Engineering 2, Proceedings of the LANE'97*, edited by M. Geiger and F. Vollertsen, (Meisenbach Bamberg, Germany, 1997), Vol. 2, pp. 357-366.
- [26] W. W. Duley, *Laser Processing and Analysis of Materials*. Plenum Press (1983).
- [27] L. P. Welsh, J. A. Tuchman, I. P. Herman, "The importance of Thermal Stress and Strains Induced in Laser Processing with Focused Gaussian Beams," *Journal of Applied Physics*, Vol. 64, 6274-6286 (1988).
- [28] Y. Iwamura, E. F. Rybicki, "A transient Elastic -Plastic thermal Stress analysis of flame forming," *Transactions of ASME, Journal of Engineering for Industry*, 163-171 (February 1973).
- [29] A. Moshaiov, "The mechanics of the flame bending process: Theory and Applications," *Journal of Ship Research* , Vol. 31, No.4, 269-281 (1987).
- [30] T. Suhara, "Study on Thermo Plastic working: Bending of Beam of Rectangular Cross Section," *Journal of Zosen Kyokai*, Vol. 103, 233-243 (1958).
- [31] M. Araki, N. Inoue, M. Horioka, M. Ando, "On Angular Distortion of Hull Steel Plates by Line Heating Methods," *Journal of the Society of Naval Architects of Japan*, Vol. 133, 343-348 (1973).
- [32] F. Vollertsen, M. Geiger, W. M. Li, "FDM- and FEM- simulation of laser forming: a comparative study," *Advanced Technology of Plasticity*, edited by Z. R. Wang, Y. He, III, 1793-1798 (1993).
- [33] M. Geiger, S. Holzer, F. Vollertsen, "Laserstrahlbiegen - Simulation eines 3 - dimensionalen, thermomechanischen Prozesses," in *Metal Forming Process Simulation in Industry*, edited by B. Kropli and, E. Luckey, (Monchengladbach, Germany, 1994, pp. 335 - 352.

- [34] N. Alberti, L. Fratini, F. Micari, "Numerical simulation of the laser bending process by a coupled thermal mechanical analysis," in *Laser Assisted Net Shape Engineering, Proceedings of the LANE'94*, edited by M. Geiger and F. Vollertsen, (Meisenbach Bamberg, Germany, 1994), Vol. I, pp. 327 - 336.
- [35] N. Alberti, L. Fratini, F. Micari, M. Cantello, G. Savant, "Computer Aided Engineering of a laser assisted bending processes," in *Laser Assisted Net Shape Engineering 2, Proceedings of the LANE'97*, edited by M. Geiger and F. Vollertsen, (Meisenbach Bamberg, Germany, 1997), Vol. 2, pp.375-382.
- [36] S. Holzer, H. Arnet, M. Geiger, "Physical and Numerical modelling of the Buckling Mechanism," in *Laser Assisted Net Shape Engineering, Proceedings of the LANE'94*, edited by M. Geiger and F. Vollertsen, (Meisenbach Bamberg, Germany, 1994), Vol. I, pp. 379 - 386.
- [37] Y. Namba, "Laser Forming in Space". *Proceedings of the International Conference on Lasers'85*, edited by C. P. Wang, (STS Press, McLean 1986), pp. 403-407.
- [38] K. Scully, "Laser line Heating," *Journal of Ship Production* Vol. 3, No.4, 237 - 246 (1987).
- [39] K. Masabuchi, "Studies at M.I.T related to Applications of Laser Technologies to Metal Fabrication," in *Proceedings of Laser Advanced Materials Processing (LAMP'92)* (Niigata, Japan, 1992), pp. 939 - 946.
- [40] A. Sprenger, F. Vollertsen, W. M. Steen, and K. G. Watkins, "Influence of strain hardening on laser bending" *Manuf Syst.* 24, 215-221 (1995).
- [41] H. Frackiewicz, W. Trampczynski, W. Przetakiewicz, "Shaping of tubes by Laser Beam," in the *Proceedings of the 25th International Symposium on Automotive Technology and Automation (ISATA 25th, 1992)*, pp.373 - 380.
- [42] T. Hennige, "Laser forming of spatially curved parts," in *Laser Assisted Net Shape Engineering 2, Proceedings of the LANE'97*, edited by M. Geiger and F. Vollertsen, (Meisenbach Bamberg, Germany, 1997), Vol. 2, pp. 409-420.
- [43] F. Vollertsen, "Applications of lasers for flexible shaping processes," in *Schlus- seltechnologie Laser: Herausforderung an die Fabrik 2000, Proceedings of the 12th International Congress (LASER95)*, edited by M. Geiger, (Meisenbach Bamberg, Germany, 1995), pp.151-162.

- [44] F. Klocke, A. Demmer, C. Dietz, "Laser Assisted Metal Forming," in Laser Assisted Net Shape Engineering 2, Proceedings of the LANE'97, edited by M. Geiger and F. Vollertsen, (Meisenbach Bamberg, Germany, 1997), Vol. 2, pp.81-92.
- [45] H. K. Tonshoff, A. H. Berndt, A. R. Rosenthal, "Laser Based Cutting, Tensioning and Straightening of Saw Blades - A Flexible Production Line," in Laser Assisted Net Shape Engineering, Proceedings of the LANE'94, edited by M. Geiger and F. Vollertsen, (Meisenbach Bamberg, Germany, 1994), Vol. 1, pp.337-344.
- [46] W. Hoving, "Accurate manipulation using laser technology," in the Proceedings of the European Symposium on Laser and Optics and Manufacturing, (Munich, Germany, 1997), SPIE Vol. 3097, (1997), pp. 284-295.
- [47] A. Huber, B. Muller, F. Vollertsen, "A measuring device for small angles and displacements," in Laser Assisted Net Shape Engineering 2, Proceedings of the LANE'97, edited by M. Geiger and F. Vollertsen, (Meisenbach Bamberg, Germany, 1997), Vol. 2, pp. 409-420.
- [48] J. Widlaszewski, "Precise laser bending," in Laser Assisted Net Shape Engineering 2, Proceedings of the LANE'97, edited by M. Geiger and F. Vollertsen, (Meisenbach Bamberg, Germany, 1997), Vol. 2, pp.393-398.
- [49] M. Pridham, G. Thompson, "Laser forming: a force for the future," *Materials World*, Vol. 2, (Nov 1994).
- [50] M. Pridham, G. Thompson, "Laser forming," *Manufacturing Engineer*, p.24 (June 1995).
- [51] G. Thompson, M. Pridham, "A Feedback Control System for Laser Forming," *Mechatronics* Vol. 7, No.5, 429-441 (1997).
- [52] J. E. Jones, V. L. Rhoades, J. C. Jones, A. C. Beck, P. Oberly, P. Sewell, D. D. Schwemmer, D. Stompro, T. Whipple, "Use of the Flexible Laser Automated Intelligent Real-Time (FLAIR) System for Laser Thermal Forming, Presented at the International Conference on the Industrial Applications of Lasers in Manufacturing, (Minneapolis, U.S.A, April 1998).
- [53] R. J. Blake, R. M. Pearson, A. B. Revell, W. E. Simon, "Laser Thermal Forming of Sheet Metal Parts Using Desktop Laser Systems," in Proceedings of the International Congress On Applications of Lasers and Electro-Optics, (ICALEO97), (San Diego, U.S.A, 1997), Section E. pp.66-75.

- [54] Y. Ueda, H. Murakawa, A. Rashwan, Y. Okumoto, R. Kamichika, "Development of Computer Aided Process Planning System for Plate Bending by Line-Heating (Report II) - Practice for Plate Bending in Shipyard Viewed from Aspect of Inherent Strain, Transaction of JWRI, (1992), Vol. 21, NO. 1, pp. 123-133.
- [55] C. Jang, S. Seo, D. Ko, "A study on The Prediction of Deformations of Plates Due to Line Heating Using a Simplified Thermal Elasto-Plastic Analysis," Journal of Ship Production, Vol. 13, No. 1, Feb. 1997, pp. 22-27.
- [56] S. P. Timoshenko, J. N. Goodier, "Theory of Elasticity." Third Edition, *McGraw - Hill*, 1970.
- [57] S. V. Patankar, "Numerical Heat Transfer and Fluid Flow," Taylor and Francis, 1980.
- [58] R. Ducharme, "CEMWAM/PT5/EU091, No. 1," British Aerospace contractor report, March 1997, unpublished work.
- [59] W. Heckel, M. Geiger, "In-Process Measurement Of Bending Angles Based On The Principle Of Light Sectioning," ISPRS Commission V publication, (1994)
- [60] E. Hatch, "Aluminium: Properties and physical metallurgy," American Society of Metals, 1984.
- [61] J. Magee, K. G. Watkins, W. M. Steen, N. Calder, J. Sidhu, J. Kirby, "Laser Forming of Aerospace Alloys," Proceedings of ICA-LEO 97, Vol. 83, Part 2, section e-156 (1997), pp.156-165.
- [62] J. Magee, K. G. Watkins, W. M. Steen, N. Calder, J. Sidhu, and J. Kirby, "Edge effects in laser forming," in Laser Assisted Net shape Engineering 2. Proceedings of the LANE'97, edited by M. Geiger and F. Vollertsen, (Meisenbach Bamberg, Germany, 1997), Vol. 2, pp.399-408.
- [63] J. Magee, K.G. Watkins, T. Hennige, "Symmetrical laser Forming," To appear in the Proceedings of ICALEO 99, San Diego, USA.
- [64] J. Ramos, J. Magee, F. Noble, K. G. Watkins, W. M. Steen, "The Microstructure of Laser bent Aluminium Alloy AA2024-T3", Proceedings of ICALEO98 , Vol. 85, Part 2, section e-178 (1998), pp.178-185.

- [65] J. Magee, K. G. Watkins, W. M. Steen, R. L. Cooke, J. Sidhu, "Development Of An Integrated Laser Forming Demonstrator System For The Aerospace Industry", Proceedings of ICALEO98 , Vol. 85, Part 2, section e-141 (1998), pp.141-150.
- [66] J. Magee, K. G. Watkins, W. M. Steen, "Advances in Laser Forming," Journal of Laser Applications, Vol.10, No.6,(1998), pp.235-246.

## Acknowledgements

I express my thanks to Professor William Steen for giving me the opportunity to do this work and to Dr Ken Watkins for his tutelage and supervision. I acknowledge that this work was carried out with funding from British Aerospace. I thank Dr Jagjit Sidhu, Dr Stewart Williams and Dr Len Cooke of the Sowerby Research centre British Aerospace for project management, facilities and assistance. I am grateful to Dr Graeme Scott of the Sowerby Research centre for practical assistance there, Mr Jason Kirby of Airbus for material supplies, and Dr Neil Calder for stimulating interest in laser forming in British Aerospace and the University of Liverpool. I thank Hans Reger, Jorge Ramos, and Joanne Stockton for the data they generated on the projects I supervised. I appreciate the help from the laser group and the discussions with my colleagues in the mechanical engineering department which assisted me with my investigation. Most importantly I am thankful to my family for their love, encouragement and support.

LIVERPOOL  
UNIVERSITY  
LIBRARY

